



# Fabrication techniques for femtosecond laser textured and hyperdoped silicon

## Citation

Franta, Benjamin Andrew. 2016. Fabrication techniques for femtosecond laser textured and hyperdoped silicon. Doctoral dissertation, Harvard University, Graduate School of Arts & Sciences.

## Permanent link

<http://nrs.harvard.edu/urn-3:HUL.InstRepos:33493373>

## Terms of Use

This article was downloaded from Harvard University's DASH repository, and is made available under the terms and conditions applicable to Other Posted Material, as set forth at <http://nrs.harvard.edu/urn-3:HUL.InstRepos:dash.current.terms-of-use#LAA>

## Share Your Story

The Harvard community has made this article openly available.  
Please share how this access benefits you. [Submit a story](#).

[Accessibility](#)

# Fabrication techniques for femtosecond laser textured and hyperdoped silicon

A thesis presented

by

Benjamin Andrew Franta

to

The Harvard John A. Paulson School of Engineering and Applied Sciences

in partial fulfillment of the requirements

for the degree of

Doctor of Philosophy

in the subject of

Applied Physics

Harvard University

Cambridge, Massachusetts

April 2016

©2016 - Benjamin Andrew Franta

All rights reserved.

Thesis advisor

**Eric Mazur**

Author

**Benjamin Andrew Franta**

# **Fabrication techniques for femtosecond laser textured and hyperdoped silicon**

## **Abstract**

This thesis presents a range of advances in the fabrication of femtosecond laser textured and hyperdoped silicon, a material platform with potential applications in photovoltaics, photodetectors, light-emitting diodes, lasers, and potentially other optoelectronic devices.

After providing background and a review of the state of hyperdoped black silicon research in Chapter 1, we explore a range of fabrication approaches in Chapter 2, including laser texturing near and below the melting threshold of silicon, laser texturing and hyperdoping using scanned pulses, fabrication with thin films, control of the dopant concentration on textured substrates, and removal of surface material using chemical etching.

In Chapter 3, we review the material microstructure of hyperdoped black silicon, including the morphology, the presence and origin of high-pressure material phases, and the incorporation of dopants from thin films.

In Chapter 4, we explore the use of laser annealing to increase the crystallinity of hyperdoped black silicon, addressing a longstanding challenge in the field. We show that nanosecond laser annealing can be used on a wide variety of textures—from at least 10 micrometers in size to sub-micrometer in size—to produce high



---

crystallinity and high optical absorptance simultaneously. Furthermore, we see that nanosecond laser annealing can reactivate the sub-bandgap absorptance after it has been deactivated by thermal annealing. We close Chapter 4 by exploring the use of fs laser pulses to anneal hyperdoped black silicon.

Finally, in Chapter 5, we discuss advances in the thesis, outstanding challenges in the research field, and an outlook for applications.

# Contents

|  |          |
|--|----------|
| Title Page . . . . .   | i        |
| Abstract . . . . .   | iii      |
| Table of Contents . . . . .  | v        |
| Citations to previously published work . . . . .   | ix       |
| Acknowledgments . . . . .  | xi       |
| Dedication . . . . .   | xiv      |
| <b>1 Introduction to thesis</b>  | <b>1</b> |
| 1.1 Content and layout of thesis . . . . .   | 1        |
| 1.2 Introduction to hyperdoped black silicon . . . . .   | 4        |
| 1.2.1 Interest in hyperdoped black silicon . . . . .   | 4        |
| 1.2.2 Properties and fabrication of hyperdoped black silicon . . . . .   | 5        |
| 1.3 Recent advances in hyperdoped silicon research . . . . .   | 7        |
| 1.3.1 Introduction . . . . .   | 7        |
| 1.3.2 Observing the intermediate band . . . . .  | 7        |
| 1.3.3 Measuring electron lifetime, carrier mobility, and absorption<br>coefficient to derive a figure of merit . . . . . | 8        |
| 1.3.4 Understanding dopant deactivation . . . . .  | 10       |
| 1.3.5 Observing sub-bandgap photoresponse . . . . .  | 12       |
| 1.3.6 Measuring the doping process . . . . .   | 13       |
| 1.3.7 Controlling the doping profile . . . . .   | 14       |
| 1.3.8 Characterizing the material microstructure . . . . .   | 15       |
| 1.3.9 Controlling the crystallinity . . . . .  | 16       |
| 1.4 Outstanding challenges in hyperdoped black silicon research . . . . .  | 17       |
| 1.4.1 Introduction . . . . .   | 17       |
| 1.4.2 Crystallinity . . . . .  | 18       |
| 1.4.3 Doping concentration . . . . .   | 19       |
| 1.4.4 Hyperdoped layer thickness . . . . .   | 20       |
| 1.4.5 Optical path length enhancement . . . . .  | 21       |
| 1.4.6 Thermal stability . . . . .  | 22       |
| 1.4.7 Embedded hyperdoped layer architecture . . . . .   | 22       |

|          |  |           |
|----------|--|-----------|
| <b>2</b> | <b>Advances in femtosecond laser processing of silicon</b>           | <b>24</b> |
| 2.1      | Introduction to chapter . . . . .                                    | 24        |
| 2.2      | Laser texturing near the single-pulse melting threshold . . . . .    | 26        |
| 2.2.1    | Introduction . . . . .   | 26        |
| 2.2.2    | Methods . . . . .  | 26        |
| 2.2.3    | Results . . . . .  | 28        |
| 2.2.4    | Discussion . . . . .   | 33        |
| 2.2.5    | Conclusions . . . . .  | 42        |
| 2.3      | Laser texturing below the single-pulse melting threshold . . . . .   | 43        |
| 2.3.1    | Introduction . . . . .   | 43        |
| 2.3.2    | Methods . . . . .  | 43        |
| 2.3.3    | Results . . . . .  | 44        |
| 2.3.4    | Discussion . . . . .   | 47        |
| 2.3.5    | Conclusions . . . . .  | 54        |
| 2.4      | Initiation of surface textures . . . . .                             | 55        |
| 2.4.1    | Introduction . . . . .   | 55        |
| 2.4.2    | Methods . . . . .  | 56        |
| 2.4.3    | Results . . . . .  | 56        |
| 2.4.4    | Discussion . . . . .   | 65        |
| 2.4.5    | Conclusions . . . . .  | 73        |
| 2.5      | Fabrication with scanned pulses . . . . .                            | 74        |
| 2.5.1    | Introduction . . . . .   | 74        |
| 2.5.2    | Methods . . . . .  | 77        |
| 2.5.3    | Results . . . . .  | 78        |
| 2.5.4    | Discussion . . . . .   | 81        |
| 2.5.5    | Conclusions . . . . .  | 86        |
| 2.6      | Low-fluence fabrication with selenium thin films . . . . .           | 88        |
| 2.6.1    | Introduction . . . . .   | 88        |
| 2.6.2    | Methods . . . . .  | 88        |
| 2.6.3    | Results . . . . .  | 89        |
| 2.6.4    | Discussion . . . . .   | 90        |
| 2.6.5    | Conclusions . . . . .  | 95        |
| 2.7      | Controlling the dopant concentration in hyperdoped black silicon . . | 96        |
| 2.7.1    | Introduction . . . . .   | 96        |
| 2.7.2    | Methods . . . . .  | 97        |
| 2.7.3    | Results . . . . .  | 98        |
| 2.7.4    | Discussion . . . . .   | 100       |
| 2.7.5    | Conclusions . . . . .  | 105       |
| 2.8      | Surface cleaning with hydrofluoric acid . . . . .                    | 106       |
| 2.8.1    | Introduction . . . . .   | 106       |
| 2.8.2    | Methods . . . . .  | 106       |
| 2.8.3    | Results . . . . .  | 107       |

|          |   |            |
|----------|---|------------|
| 2.8.4    | Discussion . . . . .  | 108        |
| 2.8.5    | Conclusions . . . . .   | 112        |
| 2.9      | Conclusions of chapter . . . . .  | 112        |
| <b>3</b> | <b>The material microstructure of hyperdoped black silicon</b>  | <b>118</b> |
| 3.1      | Introduction to chapter . . . . .   | 118        |
| 3.2      | The origins of pressure-induced phase transformations during the surface texturing of silicon using femtosecond laser irradiation . . . . . | 119        |
| 3.2.1    | Introduction . . . . .  | 119        |
| 3.2.2    | Measuring pressure-induced phases . . . . .   | 120        |
| 3.2.3    | Conclusions . . . . .   | 125        |
| 3.3      | Improving dopant incorporation during femtosecond-laser doping of Si with a Se thin-film dopant precursor . . . . .                         | 127        |
| 3.3.1    | Introduction . . . . .  | 127        |
| 3.3.2    | High fluence regime . . . . .   | 128        |
| 3.3.3    | Low fluence regime . . . . .  | 132        |
| 3.3.4    | Conclusions . . . . .   | 133        |
| 3.4      | Conclusions of chapter . . . . .  | 135        |
| <b>4</b> | <b>Laser annealing of hyperdoped black silicon</b>  | <b>136</b> |
| 4.1      | Introduction to chapter . . . . .   | 136        |
| 4.2      | Nanosecond laser annealing of 10-micrometer surface textures . . . . .  | 138        |
| 4.2.1    | Introduction . . . . .  | 138        |
| 4.2.2    | Methods . . . . .   | 139        |
| 4.2.3    | Results . . . . .   | 144        |
| 4.2.4    | Discussion . . . . .  | 151        |
| 4.2.5    | Conclusions . . . . .   | 160        |
| 4.3      | Nanosecond laser annealing of 1-micrometer surface textures . . . . .   | 162        |
| 4.3.1    | Introduction . . . . .  | 162        |
| 4.3.2    | Methods . . . . .   | 162        |
| 4.3.3    | Results . . . . .   | 162        |
| 4.3.4    | Discussion and conclusions . . . . .  | 163        |
| 4.4      | Nanosecond laser annealing of sub-micrometer surface textures . . . . .   | 165        |
| 4.4.1    | Introduction . . . . .  | 165        |
| 4.4.2    | Methods . . . . .   | 166        |
| 4.4.3    | Results . . . . .   | 168        |
| 4.4.4    | Discussion . . . . .  | 169        |
| 4.4.5    | Conclusions . . . . .   | 176        |
| 4.5      | Femtosecond laser annealing of hyperdoped black silicon . . . . .   | 176        |
| 4.5.1    | Introduction . . . . .  | 176        |
| 4.5.2    | Methods . . . . .   | 177        |
| 4.5.3    | Results . . . . .   | 180        |

|          |                                   |            |
|----------|-----------------------------------|------------|
| 4.5.4    | Discussion . . . . .              | 181        |
| 4.5.5    | Conclusions . . . . .             | 188        |
| 4.6      | Conclusions of chapter . . . . .  | 188        |
| <b>5</b> | <b>Conclusions of thesis</b>      | <b>191</b> |
| 5.1      | Advances in this thesis . . . . . | 191        |
| 5.2      | Outstanding challenges . . . . .  | 194        |
| 5.3      | Outlook . . . . .                 | 197        |
|          | <b>Bibliography</b>               | <b>201</b> |

# Citations to previously published work

Parts of this dissertation cover research reported in the following articles:

1. Franta, B., Pastor, D., Gandhi, H., Rekemeyer, P.H., Gradecak, S., Aziz, M.J., & Mazur, E. (2015). Simultaneous high crystallinity and sub-bandgap optical absorptance in hyperdoped black silicon using nanosecond laser annealing. *Journal of Applied Physics* 118:225303.
2. Mazur, E., Franta, B., Pastor, D., Gandhi, H., & Raymond., A. (2015). Laser doping and texturing of silicon for advanced optoelectronic devices. *Proc. CLEO Pacific Rim*.
3. Smith, M.J., Sher, M.-J., Franta, B., Lin, Y.-T., Mazur, E., & Gradecak, S. (2014). Improving dopant incorporation during femtosecond-laser doping of Si with a Se thin-film dopant precursor. *Applied Physics A* 114.
4. Smith, M.J., Sher, M.-J., Franta, B., Lin, Y.-T., Mazur, E., & Gradecak, S. (2012). The origins of pressure-induced phase transformations during the surface texturing of silicon using femtosecond laser irradiation. *Journal of Applied Physics* 112:0835518.
5. Franta, B., Sher, M.-J., Lin, Y.-T., Phillips, K., & Mazur, E. (2012). Femtosecond laser hyperdoping and micro/nanotexturing of silicon for photovoltaics. *Proc. SPIE* 8243, 82431D.
6. Franta, B., Pastor, D., Aziz, M., & Mazur, E. (Patent application, filed Nov. 2015). Creation of hyperdoped semiconductors with concurrent high crys-

tallinity and high sub-bandgap absorptance using nanosecond laser annealing.

PCT/US2015/060385.

# Acknowledgments

A huge number of people have helped me along the way during this PhD. First, I want to thank the Mazur group for providing such a fun and interesting place to work. I especially want to thank Eric Mazur—for encouraging me as a prospective student, taking me on as a member of his lab, giving me encouragement and freedom to pursue my research interests, providing a huge range of professional development opportunities, allowing me to become a better teacher by assisting with his AP50 course, and for allowing me to pursue my various interests in graduate school. As all of Eric’s graduate students know, he is one of a kind in so many great ways.

I want specially to thank Virginia Casas for keeping everything running in miraculous fashion. (And always with a great sense of humor!)

I want to thank all of the graduate students, professors, visiting researchers, and everyone else I’ve collaborated with on hyperdoped black silicon research over the years: Matt Smith, Paul Rekemeyer, Renee Sher, Yu-Ting Lin, Kasey Phillips, Hemi Gandhi, David Pastor, Prof. Mike Aziz, Prof. Silvija Gradecak, Prof. Thierry Sarnet and everyone at LP3 at Aix-Marseille University, and anyone I might have forgotten.

I want to thank the Harvard University Center for the Environment for providing a great program for learning about energy, environment, and climate. I especially want to thank Prof. Dan Schrag for allowing me to assist with and learn from his course on energy and climate and for his support over the years.

I want to thank the Belfer Center for Science and International Affairs at the Harvard Kennedy School of Government for allowing me to work as a pre-doctoral research fellow for two years. I especially want to thank Prof. David Keith for allowing



## *Acknowledgments*

---

me to work under his auspices and for his support over many years.

I want to give a big thank you to my friends, colleagues, and mentors in the Philippines. First to Dr. Gemma Narisma, Director Toni Loyzaga, and everyone else at Manila Observatory and Ateneo de Manila University. I also want to thank Dr. Hilly Quiaoit, Engr. Dexter Lo, and everyone else who was so generous during my fieldwork around Xavier University and elsewhere. And I am incredibly grateful to the Camachos for being such a welcoming, nice, and fun family to live with. (Even with dengue and chikungunya...it was great!)

I want to thank USAID and NSF for supporting my research in the Philippines through the Research and Innovation Fellowship program.

I want to thank the wide cast of characters I've met through climate activism, especially those who've worked so hard to create the fossil fuel divestment movement. Much of what I understand about leadership I've learned from working with them.

I want to thank Prof. Naomi Oreskes, who has been a great inspiration and extraordinarily generous with her time, mentorship, and support.

I want to thank the Harvard-Radcliffe Collegium Musicum and Dr. Andy Clark for allowing me to be part of their incredible community of artists.

I want to thank my physics professors at Coe College in Cedar Rapids, Iowa for being such incredibly positive influences in my life: Steve "Doc" Feller, Mario Affatigato, and Jim Cottingham. They set me on a path of loving to learn about the world.

Finally, I want to thank my family for tolerating long distance, (occasional) grad school stress, and a mostly unintelligible subject (don't worry; most of the time I don't

## *Acknowledgments*

---

understand it either). They've encouraged me to pursue my interests—wherever those interests go—which is a great gift.

*To all my friends who always wanted a thesis about hyperdoped black silicon  
dedicated to them*

# Chapter 1

## Introduction to thesis

### 1.1 Content and layout of thesis

This thesis focuses on experimental fabrication techniques for laser-processed black silicon and hyperdoped black silicon. The thesis is organized into five chapters. Chapter 1 is an overview of current hyperdoped black silicon research. Chapters 2–4 contain 13 experimental sections, each of which examines a separate aspect of laser fabrication and is mostly self-contained. Chapter 5 concludes the thesis and provides a future outlook for hyperdoped black silicon research.

Chapter 1 provides an introduction to hyperdoped black silicon. The basic background of black silicon, hyperdoped silicon, and hyperdoped black silicon are discussed in Section 1.2. Many excellent introductions and reviews of hyperdoped black silicon already exist [1–4], so only a basic background is presented here, and we move on to provide a review of major recent advances (Section 1.3) and outstanding challenges in the field (Section 1.4). With this state of the field laid out, we move on

to the experimental chapters (Chapters 2–4).

Chapters 2–4 contain a series of mostly self-contained experimental sections. The first seven experimental sections (Sections 2.2–2.8) report experimental results not yet published. The next two experimental sections, Sections 3.2 and 3.3 in Chapter 3, discuss the main results from two journal articles in which I participated as a co-investigator [5,6]. The final four experimental sections, Sections 4.2–4.5 in Chapter 4, contain content from a journal article in which I participated as the lead investigator [7] as well as additional content not before published.

We now unpack the content of the experimental sections in more detail. Chapter 2 begins with an investigation of the laser texturing of silicon in air near the melting threshold fluence (Section 2.2). We begin with texturing using stationary pulses at the melting threshold in air because we expect the silicon modification process to be relatively simple here compared to in the sections that follow, avoiding the effects of incubation, ablation, laser scanning, and unusual ambient gases. Thus, this first section serves as a point of reference for the following sections. Next, in Section 2.3, we move to fluences below the melting threshold, again using stationary pulses, in order to consider incubation effects produced by fs laser irradiation of silicon. We then move to irradiation conditions that allow us to observe the initiation of surface texturing by ripple-like structures, which gives us a phenomenological understanding of how such surface texturing occurs, from initial nanometer-scale effects on the surface to fully-developed surface textures (Section 2.4).

In Section 2.5, we move from irradiating silicon with stationary pulses to using scanned pulses. We link the surface modification effects of stationary pulses with

scanned pulses quantitatively, and we use a high-throughput fabrication system to explore a range of fabrication parameters. In Section 2.6, we consider fabrication with Se thin films at low irradiation fluences, again using scanned pulses.

We conclude Chapter 2 by examining some additional fabrication techniques. The first, in Section 2.7, is to explore how to control the dopant concentration in hyperdoped black silicon by separating the laser texturing and laser doping steps. Then, in Section 2.8, we use hydrofluoric acid to remove surface oxide debris and amorphous silicon after laser texturing.

Chapter 3 reports the main results from two journal articles in which I participated as a co-investigator [5, 6]. Section 3.2 discusses mechanisms that give rise to pressure-induced silicon phases during fs laser texturing of silicon. Section 3.3 discusses the surface texture, microstructure, and dopant incorporation produced by fs laser irradiation of Se thin films on silicon when using high and low laser fluences.

Chapter 4 describes laser annealing of hyperdoped black silicon. Sections 4.2 and 4.3, which contain content from a previously published journal article [7], describe ns laser annealing of black silicon with surface textures around 10 micrometers and 1 micrometer in size, respectively. Section 4.4 describes ns laser annealing of sub-micrometer surface structures. And finally, Section 4.5 discusses the use of infrared fs laser pulses to anneal hyperdoped black silicon.

We conclude with Chapter 5, which discusses the main advances in the thesis, outstanding challenges in the field, and an outlook for hyperdoped black silicon applications.

## **1.2 Introduction to hyperdoped black silicon**

### **1.2.1 Interest in hyperdoped black silicon**

This thesis focuses on results from experiments with silicon processed with femtosecond (fs) laser pulses. This process and the materials it produces have been the topic of academic and industrial research for over a decade [8].

Interest in fs laser processed silicon focuses largely on two areas. First, fs laser irradiation of silicon produces self-organized surface structures that have strong anti-reflective and light-trapping properties. Such strongly textured silicon materials are generally termed “black silicon” due to their black appearance to the eye [9–11]. Black silicon may be useful in applications in which efficient light absorption is desirable, such as in photovoltaics [12]. The fabrication of black silicon with laser pulses is attractive because it may be more economical than black silicon fabrication with other methods, such as nanowire growth or reactive ion etching [2].

The second appeal of fs laser irradiation of silicon is that the process can introduce supersaturated concentrations of dopants into the silicon surface in a thin layer [1]. Dopants at such high concentrations can alter the band structure of the host material [13], producing a band of energy states within the bandgap called an intermediate band [14, 15]. Because the intermediate band allows for absorption of photons with energies less than the bandgap energy, there is interest in using intermediate band materials—in this case, heavily doped materials—for photovoltaics and photodetectors that are sensitive to long wavelengths [16]. Silicon that is doped heavily enough to produce an intermediate band is doped above the solid solubility limit,

and thus is often described as supersaturated or “hyperdoped.” When the silicon is heavily textured as well as hyperdoped, it is called hyperdoped black silicon.

### **1.2.2 Properties and fabrication of hyperdoped black silicon**

Here, we provide some further background to hyperdoped black silicon, pointing out its important properties and discussing how it is fabricated.

Hyperdoped black silicon is silicon that is both supersaturated with low-solubility dopants (i.e., “hyperdoped”) and that possesses a light-trapping surface (the “black” in black silicon). Supersaturation with dopants increases the intrinsic optical absorptance coefficient, particularly to photon energies below the bandgap energy [17], and a light-trapping surface increases the optical path length within the material and can lower the optical reflectance of the surface [10]. These properties in combination make hyperdoped black silicon a strong absorber of photon energies both above and below silicon’s bandgap energy, including in the visible and infrared regions of the electromagnetic spectrum. The strong broadband absorptance in hyperdoped black silicon has aroused interest for its potential use in silicon-based infrared photodetectors [18, 19] and intermediate band photovoltaics [16].

Various methods exist for fabricating hyperdoped black silicon, in addition to methods for fabricating silicon that is hyperdoped but optically flat and methods for fabricating black silicon that is not hyperdoped. Hyperdoped black silicon can be fabricated by irradiating silicon with femtosecond [4] or nanosecond [8] laser pulses in the presence of dopants, which are typically in the form of a gas [4] or a thin film [6, 20, 21]. Laser irradiation parameters are used that both 1) hyperdope the silicon through a



process of silicon melting, dopant diffusion into the melt, and solute trapping during rapid resolidification of the silicon, and 2) produce self-organized surface structures on the nanometer and micrometer scales that have light-trapping properties. Silicon that is hyperdoped but optically flat can be fabricated by pulsed laser melting of ion implanted silicon [22,23] or by laser irradiation of silicon using irradiation parameters that hyperdope the silicon but avoid the formation of self-organized surface structures [24]. Black silicon that is not hyperdoped can be fabricated by chemical etching of silicon [9,25], by direct laser texturing [26,27], or by laser irradiation of silicon using irradiation parameters that produce self-organized surface structures without the presence of dopants [11,28]. Each of these fabrication methods presents its own challenges, and sometimes the fabrication approach can affect the fundamental properties of the hyperdoped material. For example, fs laser irradiation and ion implantation can both produce flat hyperdoped silicon, but the material microstructure, dopant uniformity, and dopant gradient (which affects internal electric fields) [29] can differ between the fabrication methods. Thus, developing understanding of and improvements in fabrication methods is central to understanding the physical properties of hyperdoped silicon—and central as well to creating useful devices.

Next, in Section 1.3, we discuss major areas of recent progress in hyperdoped black silicon research, and in Section 1.4, we enumerate major outstanding challenges in the field.

## **1.3 Recent advances in hyperdoped silicon research**

### **1.3.1 Introduction**

Over the past decade, some major advances have been made in understanding the properties of hyperdoped silicon—intrinsic properties of hyperdoped silicon as well as incidental material properties resulting from the fs laser irradiation process. Many of these properties are important for device design. In this section, we review some of the major recent advances in the field. Observing the intermediate band, measuring the electron lifetime, carrier mobility, and absorption coefficient, and understanding dopant deactivation and reactivation are advances in understanding the intrinsic properties of hyperdoped silicon. Observing sub-bandgap photoresponse is an advance in fabricating hyperdoped silicon devices. And measuring the doping process, controlling the dopant profile, characterizing the material microstructure, and controlling the crystallinity are advances in laser fabrication of hyperdoped black silicon.

### **1.3.2 Observing the intermediate band**

The concentration range of chalcogen (sulfur, selenium, and tellurium) dopants that yields an intermediate band in crystalline silicon has been measured as  $<0.4$  atomic % ( $2 \times 10^{20} \text{ cm}^{-3}$ ), as illustrated in Figure 1.3.1, with doping above this concentration yielding a metallic band structure [13]. The presence of an intermediate band in hyperdoped silicon below this critical doping concentration is supported by density functional theory [13], temperature-dependent conductivity [30], and x-ray emission spectroscopy [31]. Determining the doping concentration yielding a true intermediate

band—rather than a metallic band structure—is important for interpreting material properties and for device design, because a metallic band structure is not expected to produce significant photovoltage or photocurrent in a device. A large fraction of hyperdoped black silicon reported in the literature contains doping concentrations around 1 at. % [4], which is too high for intermediate band formation. Thus, controlling the doping concentration in laser doping is an important challenge.

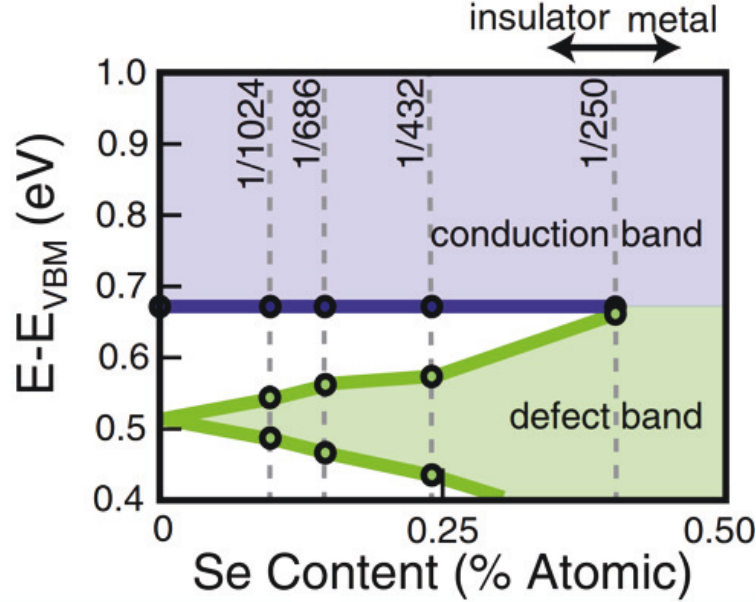


Figure 1.3.1: Density functional theory calculation of an intermediate band from Se in silicon. Beyond 0.4 at. %, the band structure becomes metallic. From [13].

### 1.3.3 Measuring electron lifetime, carrier mobility, and absorption coefficient to derive a figure of merit

Progress has been made in determining three intrinsic properties of hyperdoped silicon as a function of doping concentration: electron lifetime, carrier mobility, and optical

absorption coefficient.

The lifetime of photogenerated carriers in laser-doped silicon helps to determine the carrier transport length within the laser-doped layer. To measure the photogenerated electron lifetime in silicon doped with sulfur or selenium, femtosecond laser pulses were used to generate free carriers in the doped layer. The THz transmission through the material, which is a function of the number of free carriers, was then measured as a function of time [32]. This revealed that the carrier lifetime in hyperdoped silicon is on the order of picoseconds and decreases as the dopant concentration is increased, consistent with the expected effects of Shockley-Read-Hall recombination, as shown in Figure 1.3.2 below.

Carrier mobilities [29,33] and absorption coefficients [17,34] in chalcogen-hyperdoped crystalline silicon have also been measured, as shown in Figure 1.3.3 below.

To extract photogenerated carriers, a balance exists between dopant concentration and doping layer thickness. Greater doping concentration increases the optical absorptance but decreases the carrier lifetime and mobility. Greater doped layer thickness also increases the optical absorptance but decreases the fraction of carriers that can be extracted before recombination. For a given doped layer thickness, a figure of merit can be calculated that indicates the fraction of extractable carriers as a function of doping concentration [15]. By maximizing the figure of merit, one can determine the doping concentration that maximizes the photogenerated carrier extraction rate.

The lifetime values measured indicate that the optimal dopant concentration for balancing optical absorption and carrier transport in sulfur-hyperdoped silicon

is around 0.03 atomic % ( $1.4 \times 10^{19} \text{ cm}^{-3}$ ) [32], as shown in Figure 1.3.4, which is more than two orders of magnitude greater than the equilibrium solubility limit for chalcogens in silicon of 0.0001 atomic % ( $5 \times 10^{16} \text{ cm}^{-3}$ ) [35]. At this dopant concentration, the optical absorption coefficient is only about  $300 \text{ cm}^{-1}$  [34], suggesting that light-trapping techniques are likely be necessary to obtain strong optical absorption.

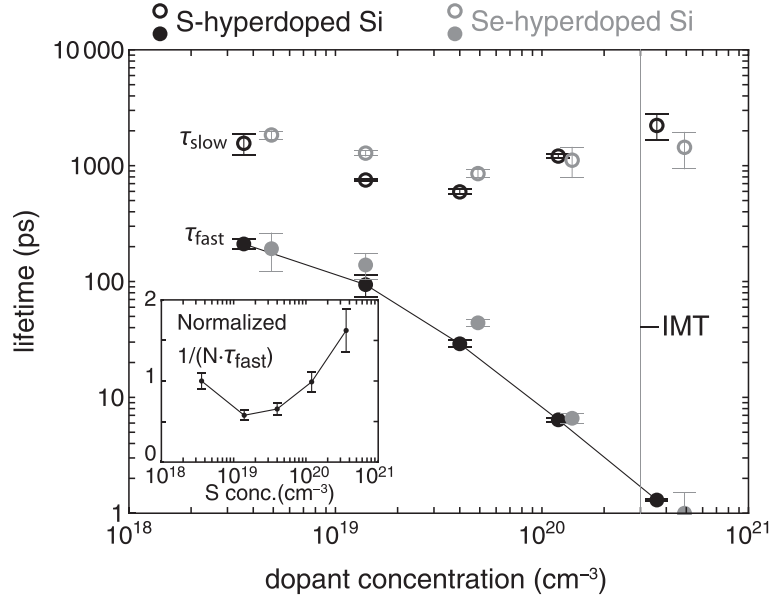


Figure 1.3.2: The electron lifetime ( $\tau_{fast}$ ) in silicon doped with sulfur or selenium as a function of dopant concentration. The inset shows that at high doping concentration, the trapping rate increases faster than the trap density. From [32].

### 1.3.4 Understanding dopant deactivation

Thermal annealing increases the crystallinity of hyperdoped black silicon and can improve electrical rectification at the homojunction between the hyperdoped layer and the substrate, but thermal annealing also deactivates the sub-bandgap optical absorbance of the material in a manner consistent with the dopants diffusing to optically

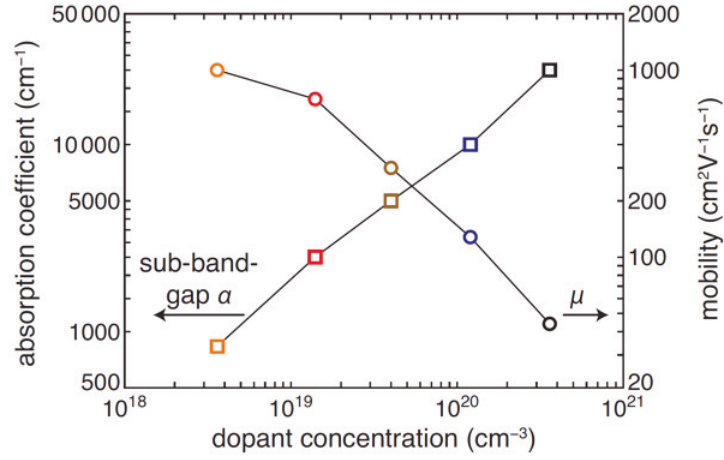


Figure 1.3.3: The optical absorption coefficient (left axis) and photogenerated electron mobility (right axis) as a function of doping concentration. From [32] and references therein.

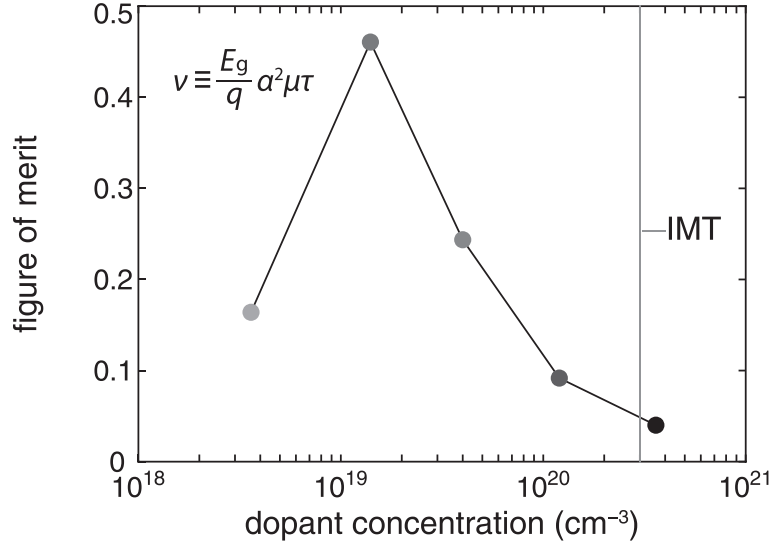


Figure 1.3.4: The figure of merit, which incorporates the carrier lifetime, the carrier mobility, and the optical absorption coefficient and which indicates the fraction of photogenerated carriers that can be extracted from a hyperdoped layer of given thickness, as a function of doping concentration. From [32].

inactive sites in the silicon lattice (with diffusion lengths  $< 1$  micrometer) [8, 36].

After deactivation, the sub-bandgap optical absorptance can be reactivated partially

by heating and fast cooling, as shown in Figure 1.3.5 [37]. The sub-bandgap absorptance can be almost entirely reactivated by nanosecond laser annealing [7]. Understanding the thermal deactivation and reactivation of sub-bandgap absorptance is important for understanding the non-equilibrium conditions required for the supersaturated dopants to be optically absorbing, as well as in considering thermal treatments in device design.

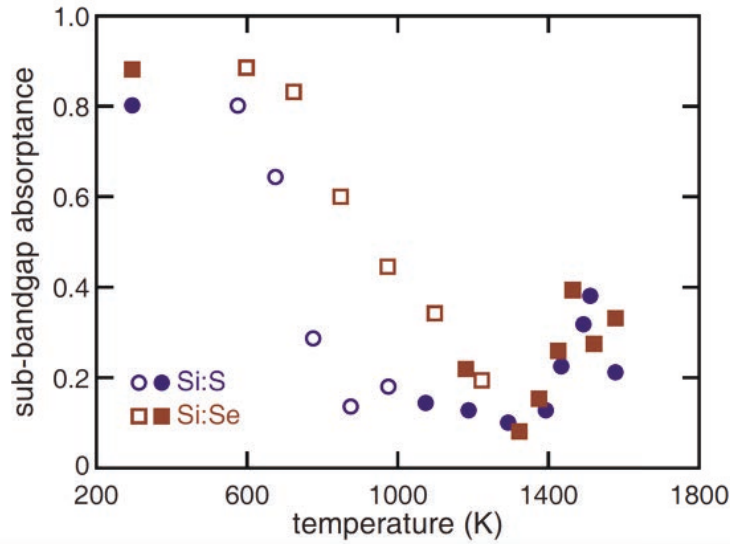


Figure 1.3.5: Deactivation of sub-bandgap optical absorptance with increasing annealing temperature. After high-temperature treatment and fast cooling, the sub-bandgap absorptance reactivates. From [37].

### 1.3.5 Observing sub-bandgap photoresponse

Recently, sub-bandgap optoelectronic response has been observed both in flat crystalline silicon hyperdoped with gold and in sulfur-hyperdoped black silicon, demonstrating that hyperdoping can indeed produce sub-bandgap optoelectronic response in semiconductor materials, as shown below [38, 39]. The response is small, as shown

in Figure 1.3.6, but it demonstrates the principle of sub-bandgap photoresponse in intermediate band devices, and performance might be improved with the addition of light trapping, selection of new dopants, or improved device architecture.

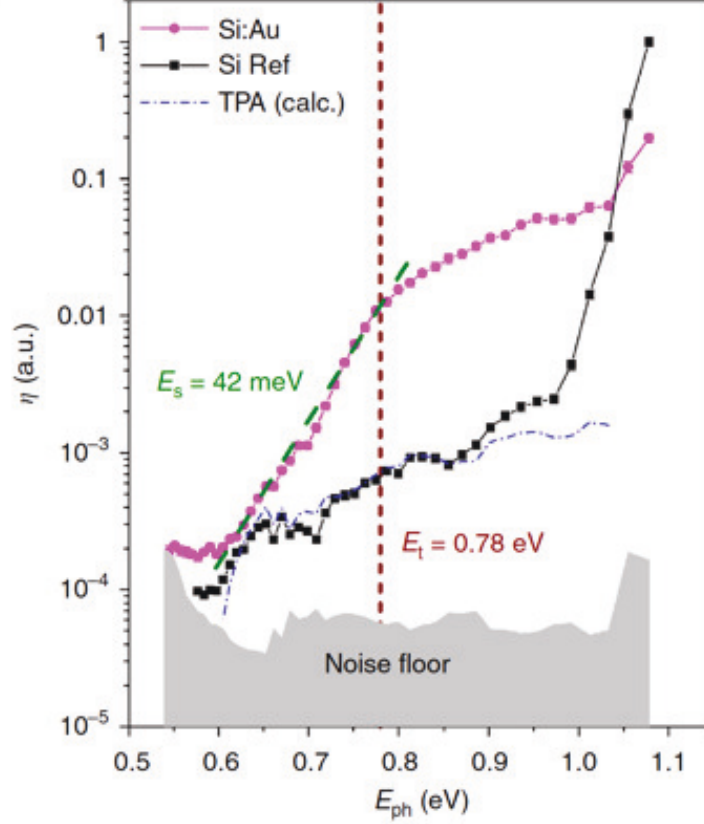


Figure 1.3.6: Increased sub-bandgap optoelectronic response in gold-hyperdoped silicon (pink circles) compared to silicon reference (black squares). From [38].

### 1.3.6 Measuring the doping process

To fabricate hyperdoped devices using laser doping, the doping concentration and doped layer depth must be controlled. It is important to control the dopant concentration as it affects the balance between carrier lifetime and optical absorption, and



because very high dopant concentrations (e.g.,  $> 0.4$  at. % selenium in silicon [13]) can produce a metallic band structure that is not useful for photoconductive or photovoltaic devices. Similarly, the doped layer thickness influences the fraction of extractable photogenerated carriers. However, the doping concentration and depth are sensitive to the laser irradiation and dopant precursor conditions (e.g., dopant gas pressure). Thus, measuring the laser doping process under a range of conditions is important for controlling the hyperdoped material properties.

Sher et al. [40] measured the evolution of doping profiles pulse by pulse and also investigated the effect of gas pressure on dopant incorporation. The results (shown in Figure 1.3.7) provide an empirical guide for controlling the dopant profile using fs laser irradiation and gas pressure, albeit with a small number of pulses ( $< 10$  pulses). Using these data, investigators can tailor the doping concentration and doped layer thickness using fs laser pulses.

### **1.3.7 Controlling the doping profile**

Methods have also recently been developed to control the shape of the doping profile. This is important because the dopant concentration gradient can generate internal fields that assist or impede carrier transport [29].

Lin et al. [41] doped a silicon wafer with a single laser pulse, then used additional laser pulses in a non-dopant environment to melt the surface repeatedly, which progressively smoothed the dopant concentration gradient through diffusion, as shown in Figure 1.3.8. With enough laser pulses, the dopant concentration profile was transformed from steeply graded to nearly flat within the top 50 nm of the

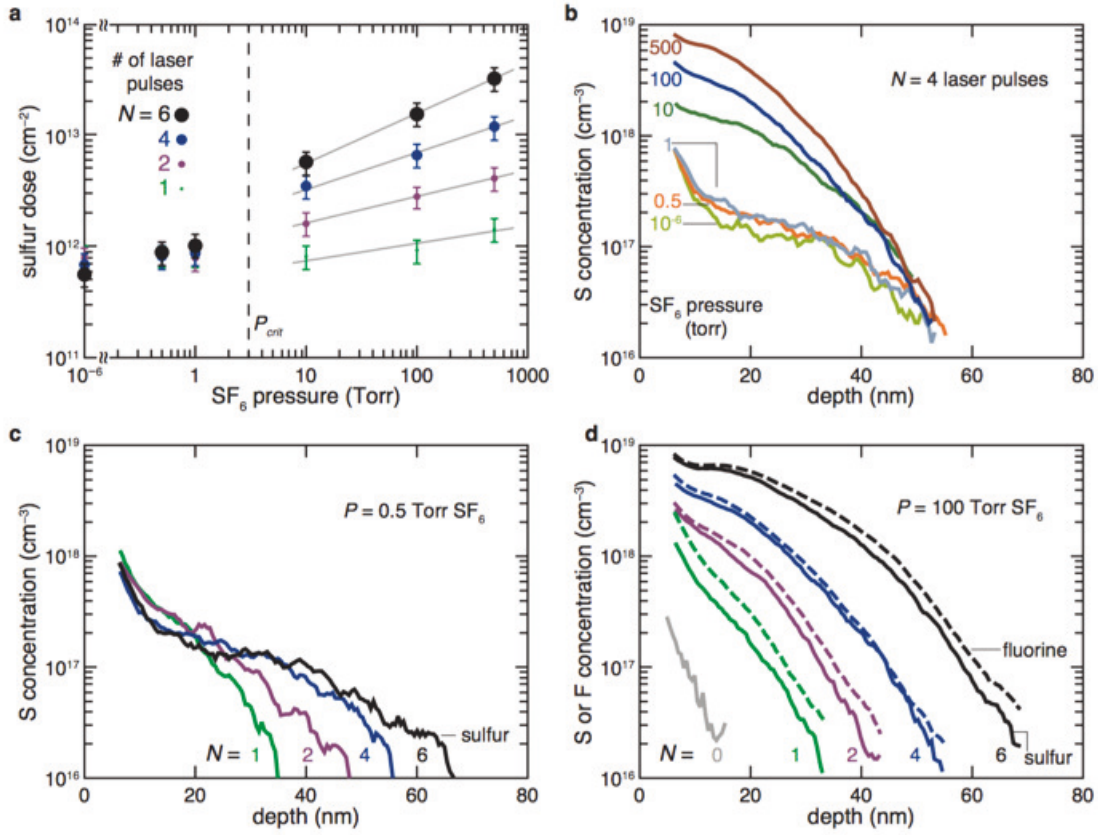


Figure 1.3.7: Doping profiles produced by a small number of fs laser pulses on silicon (pulse fluence of  $2.5 \text{ kJ/m}^2$ ). The dopant gas pressure and number of pulses are both important for controlling the dopant concentration and depth. From [14].

surface.

### 1.3.8 Characterizing the material microstructure

Femtosecond laser irradiation of silicon generates a complex material microstructure, with amorphous silicon, polycrystalline silicon, pressure-induced silicon phases, and doped regions. The details of this microstructure are expected to affect the electronic properties of laser-processed devices. Thus, understanding how the microstructure

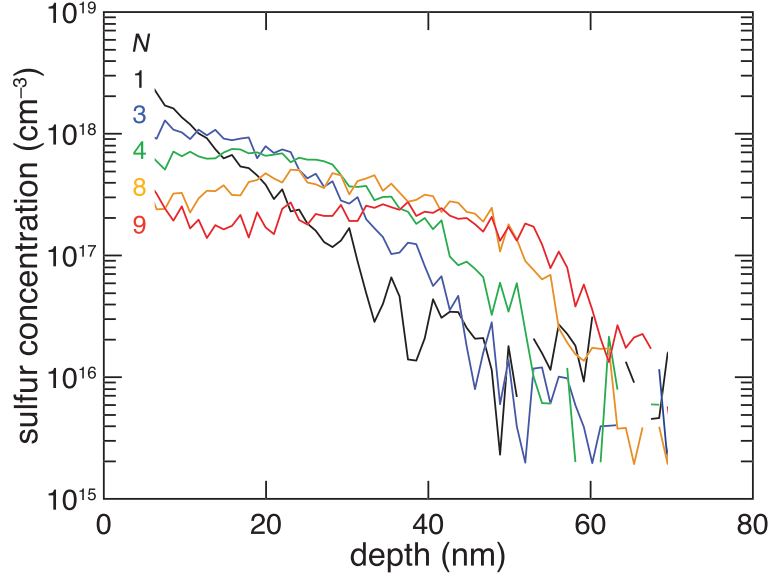


Figure 1.3.8: The concentration of sulfur introduced into silicon with a femtosecond laser pulse as a function of depth. Sulfur is introduced with the first pulse ( $N=1$ ). Subsequent pulses in a non-dopant environment reduce the dopant concentration gradient through diffusion. From [41].

forms is important for choosing irradiation conditions and understanding the properties of resultant devices.

Recent work with Raman spectroscopy and transmission electron microscopy as revealed which material phases are present in laser-processed silicon and spatial distribution of these phases [42]. Additional studies have investigated the physical mechanisms responsible for these microstructures and the structures formed under various dopant and laser fluence conditions [5,6]. A detailed discussion of this work is presented in Chapter 3.

### 1.3.9 Controlling the crystallinity

Finally, methods have been developed to control the material crystallinity. Laser-doped silicon should be highly crystalline in order to make dopants optically and

electrically active and to improve carrier mobility and lifetime. It can be useful to achieve high crystallinity without use of thermal annealing, because thermal annealing causes the dopants to diffuse and the sub-bandgap optical absorptance to drop [36].

To achieve high crystallinity without dopant diffusion, pulsed laser annealing can be used [7]. This process, which is discussed in detail in Chapter 4, results in both high crystallinity and high sub-bandgap absorptance. Additionally, if the sub-bandgap absorptance is deactivated through thermal annealing, laser annealing can be used to almost fully reactivate the sub-bandgap absorptance.

## **1.4 Outstanding challenges in hyperdoped black silicon research**

### **1.4.1 Introduction**

In this section, we consider some of the most important outstanding challenges in hyperdoped black silicon research: obtaining appropriate crystallinity, doping concentration, hyperdoped layer thickness, optical path length enhancement, thermal stability, and device architecture. In some of these areas, such as crystallinity and doping concentration, progress has recently been made; in others, such as fabricating an embedded hyperdoped layer structure, little work has thus far been done. A major overarching challenge is to address each area simultaneously with the others. Progress in hyperdoped black silicon research might depend not only on advancing the scientific understanding of the material and device physics, but also the practical understanding of how to design fabrication processes in order to achieve many desired

properties simultaneously.

### **1.4.2 Crystallinity**

One of the classic challenges of laser-textured and laser-doped silicon is the poor crystallinity resulting after irradiation. Amorphous material forms due to melting and fast resolidification, and various pressure-induced phases can also be formed [5]. Removing the defective material through chemical etching can be problematic due to a flattening of the surface texture [43] or a removal of the doped layer. Thermal annealing to recover crystallinity can be problematic for devices and also deactivates the sub-bandgap absorption of the dopant (depending on the dopant species) [36]. Co-doping with nitrogen can be used to increase the crystallinity of hyperdoped black silicon [44], but some amorphous silicon is still formed, and this necessitates the inclusion of nitrogen impurities in the material.

The demonstration of the effectiveness of ns laser annealing for recovering crystallinity while maintaining the sub-bandgap optical absorptance of the material [7] substantially resolves the issue of poor crystallinity in hyperdoped silicon (Chapter 4). However, the use of ns laser annealing may not be practicable in all situations. Thus, this remains an important research area for the development of laser-hyperdoped devices and, more immediately, for the adoption of laser texturing in photovoltaics manufacturing [45] as a potential replacement for chemical and reactive ion etching for texturization.

### 1.4.3 Doping concentration

For intermediate band devices, the dopant concentration should not exceed the critical threshold for metallic band structure formation. For chalcogens in silicon, this critical threshold (what we in this thesis call the semiconductor-to-metal transition limit) appears to be around 0.4 at. % [13]. Meeting this requirement presents two challenges. The first is that when laser-doping, it is difficult to control the doping concentration. Indeed, essentially all hyperdoped textured silicon reported in the literature—for over a decade—appears to contain doping concentrations in excess of this limit [1]. Doping below this limit using laser irradiation is possible but requires the use of few laser pulses, which is insufficient to generate a highly textured surface [14, 24]. Thus, fabricating hyperdoped black silicon with fs lasers presents a catch-22: If enough laser pulses are used to generate a highly textured surface, then the dopant concentration is typically too high, and if fewer laser pulses are used to keep the dopant concentration in the proper range, then a highly textured surface is typically not formed. We begin to address this challenge in Section 2.7 by separating the laser texturing and laser doping steps. However, this challenge requires much more attention.

The second challenge presented by the need to keep the doping concentration below the semiconductor-to-metal transition limit is that such doping concentrations yield sub-bandgap absorption coefficients that are relatively low (e.g., around  $10^5$ – $10^6$   $\text{m}^{-1}$ ) [34], requiring optical path lengths of 1–10 micrometers for strong absorption. Hyperdoped layer thicknesses of this depth, however, are expected to strongly inhibit carrier extraction would be difficult to fabricate. Thus, it appears that efficient intermediate band optoelectronic devices would require the use of light-trapping effects for

strong absorption to occur. This indicates that the simplest approach for controlling the doping concentration—ion implantation of flat surfaces—may not be suitable for fabricating efficient hyperdoped devices. However, it may be possible to carry out ion implantation of light-trapping surface.

#### **1.4.4 Hyperdoped layer thickness**

The thickness of the hyperdoped layer should be less than the carrier transport lengths to allow for carrier extraction. The transport length depends on the carrier mobility, the built-in field, and the carrier lifetime. The built-in field, in turn, depends on the hyperdoped layer thickness. Thus, the transport length is a function of the hyperdoped layer thickness. If the built-in field is 1 V and is uniformly distributed across the hyperdoped layer (an optimistic assumption), and if we assume a carrier lifetime of 100 ps [32], an electron mobility of  $200 \text{ cm}^2/(\text{V}\cdot\text{s})$ , and a hole mobility of around 1% of the electron mobility, then we can estimate the electron and hole drift lengths as a function of hyperdoped layer thickness, shown in Figure 1.4.1. In chalcogen-hyperdoped silicon, we expect electrons to be extractable from hyperdoped layers greater than 1 micrometer thick (due to their relatively high mobility). However, we estimate that holes can only drift through about 150 nm of hyperdoped material before recombining. The required hyperdoped layer thickness for hole extraction may be reduced further when considering that the built-in field might not extend to the center of the hyperdoped layer, so that holes must diffuse to the edge of the hyperdoped layer to undergo drift. Our estimate here is similar to the transport length measured for holes in sulfur-hyperdoped silicon of around 100 nm under an internal

field produced by the dopant concentration gradient [29]. Measuring the efficiency of carrier extraction as a function of hyperdoped layer thickness and developing methods to control the hyperdoped layer thickness are important research areas.

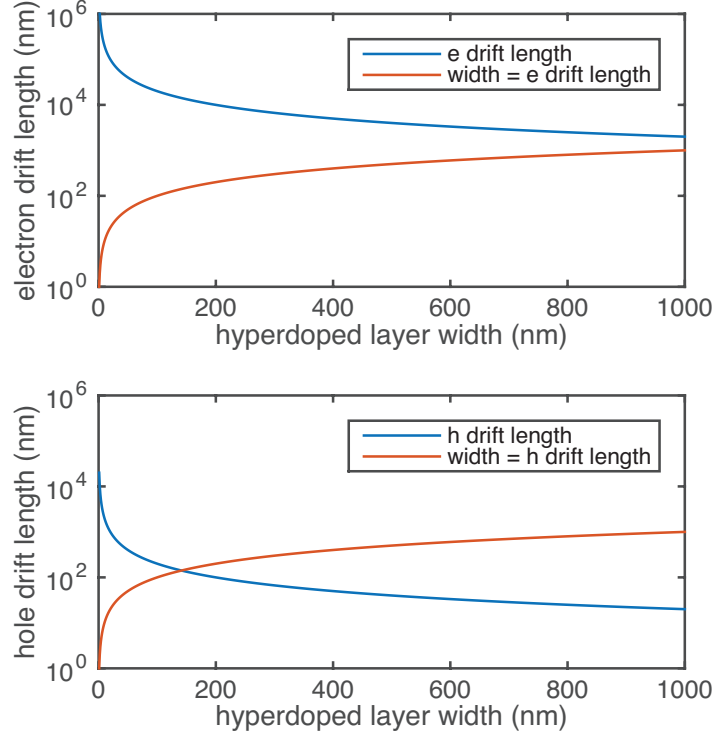


Figure 1.4.1: Estimates of electron (top) and hole (bottom) drift lengths in sulfur-hyperdoped silicon as a function of hyperdoped layer width (thickness). When the “drift length” curve is above the “width = drift length” curve, then we expect the width to be sufficiently small for carrier extraction to occur. We estimate that holes can drift through only about 150 nm of hyperdoped material before recombining (due to the short carrier lifetime and holes’ relatively low mobility).

### 1.4.5 Optical path length enhancement

Because the minority carrier transport length is generally less than the optical absorption depth, optical path length enhancement strategies, such as geometric light



trapping from surface structures or plasmonic light trapping from metal nanoparticles, should be used to increase optical absorption within the hyperdoped layer. With geometric light trapping, optical path length enhancements of up to 50 are predicted, with higher factors potentially attainable using nanophotonic light trapping tuned to the intermediate band absorption wavelength [46]. We discuss this further in Section 2.7.

#### **1.4.6 Thermal stability**

Deactivation of the sub-bandgap optical absorptance from thermal exposure should be avoided in the final device material in order to obtain efficient light absorption [36,37]. Some strategies for avoiding thermal deactivation include the use of dopants with lower thermal diffusivities [47], the avoidance of thermal treatments for obtaining increased crystallinity [44], and the use of laser annealing to increase crystallinity and activate strong sub-bandgap absorptance [7]. Some of the most commonly used dopants, such as sulfur, deactivate quickly under thermal exposure. Improved methods for laser doping with more stable dopants could be useful.

#### **1.4.7 Embedded hyperdoped layer architecture**

The original concept for an intermediate band device envisions an intermediate band layer (e.g., a hyperdoped layer) sandwiched between conventional p-type and n-type layers [16]. Ostensibly, this would preserve the output voltage for photovoltaic devices. It could also increase carrier collection efficiency by reducing the transport distance within the hyperdoped layer in transit to collection electrodes. Thus far,

essentially no work has been published on achieving this design with hyperdoped materials. Fabricating this design might be accomplished by chemical vapor deposition of conventional doped silicon on top of the hyperdoped silicon layer. Prospective challenges of this approach, however, include obtaining acceptable contact resistance between the hyperdoped layer and the deposited silicon and avoiding thermal deactivation of the dopant in the hyperdoped layer during the deposition process, which may require high temperatures.

## Chapter 2

# Advances in femtosecond laser processing of silicon

### 2.1 Introduction to chapter

This chapter consists of seven sections on advances in fs laser processing of silicon. The sections range from understanding the basic mechanisms at play in the silicon texturing process to applied techniques for obtaining desired material properties. The chapter begins by exploring laser texturing of silicon under simple conditions—in air near the single-pulse melting threshold using stationary pulses (Section 2.2). We then move to fluences below the single-pulse melting threshold to illustrate the behavior of incubation effects in laser texturing (Section 2.3). Finally, we use low pulse fluence and low pulse number to observe the generation of surface textures from the earliest, isolated modifications of the surface to fully developed, interconnected textures; additionally, the influence of gas pressure on the texture formation process

provides insight into the basic mechanisms governing the texturing process (Section 2.4).

Having explored the generation of surface textures using stationary pulses, we move to exploring surface texturing using scanned pulses. We use a high-throughput fabrication system to explore the fabrication parameter space of laser-processed silicon experimentally (Section 2.5). We are also able to quantitatively link the understanding of texturing developed in Sections 2.2–2.4 to the texturing threshold we observe using scanned pulses. Next, we expand our study of texturing using scanned pulses to silicon coated with thin films, observing texturing of the surface at fluences far below the silicon melting threshold and surface textures at very high pulse numbers (thousands of pulses) not before observed.

We close Chapter 2 with two sections on fabrication techniques. First, we begin to tackle one of the most challenging problems in laser-doped silicon: how to control the doping concentration while also obtaining high optical absorptance. We separate the laser texturing and laser doping steps and use optical absorptance measurements to observe what appear to be intermediate band formation and the semiconductor-to-metal transition (Section 2.7). Lastly, we explore the use of hydrofluoric acid to remove unwanted material from the surface of textured silicon; we find that it is effective at removing surface debris, which is oxygen-rich, as well as amorphous silicon on the surface, without altering the textured surface morphology (Section 2.8).

## **2.2 Laser texturing near the single-pulse melting threshold**

### **2.2.1 Introduction**

In this section, we investigate laser texturing of silicon at fluences around  $1.5 \text{ kJ/m}^2$ , near the single-pulse melting threshold of silicon. Surface texturing using laser irradiation involves a range of physical mechanisms, including but not limited to melting, mass transport, crystallographic changes, and ablation. We begin our investigation of surface texturing at fluences near the single-pulse melting threshold, because we expect the texturing process to be relatively simple compared to greater and lower fluences, avoiding ablation and structural incubation effects. We also utilize an air atmosphere in this section to avoid the etching effects of fluorine-bearing gases, such as  $\text{SF}_6$ . Thus, the texturing we observe in this section can serve as a point of reference for more complex texturing regimes involving extreme fluences or other gases.

### **2.2.2 Methods**

A silicon wafer was irradiated with a series of stationary 800 nm fs laser pulses without translating the sample. A peak fluence of  $1.5 \text{ kJ/m}^2$  (near the single-pulse melting threshold) and pulse numbers of 200–900 were used in 100 pulse increments. The pulse diameter was 840x1000 micrometers, the pulse duration was 50 fs, and a pulse repetition rate was 100 Hz. To examine the effects of surrounding gas pressure, duplicate samples were prepared in ambient air at atmospheric pressure, 100 Torr, and 20 Torr.

The resultant surface morphology was examined using electron microscopy. The local fluence  $F$  within the modified region was calculated using:

$$F = \frac{P * T}{f * 2\pi d_x d_y} \exp\left(\frac{-x^2}{2d_x^2}\right) \exp\left(\frac{-y^2}{2d_y^2}\right)$$

Where  $P$  is the laser power,  $T$  is the transmittance of the irradiation chamber window (0.95),  $f$  is the laser pulse repetition rate,  $d_x$  and  $d_y$  are the diameters of the laser pulse at  $1/e^2$  of its maximum intensity in the x and y directions, respectively, and  $x$  and  $y$  are the distances from the center of the pulse in the x and y directions, respectively. This equation was used to determine the local fluence at various points in each laser-textured area, including the local threshold fluence for texturing (corresponding to the edge of each textured area).

To characterize the chemical composition of the surface, energy-dispersive x-ray spectroscopy was used. The electron excitation beam was scanned over transects containing both clumps of debris and clean surface area. Elements present on the surface were identified using energy-dispersive x-ray spectroscopy analysis software, and the relative abundance of elements between the debris clumps and clean surface area was determined along each transect.

The presence of amorphous silicon in the laser-irradiated area was measured using Raman spectroscopy. A micro-Raman spectrometer with a 10-mW 632.8-nm HeNe laser was used, with a spot size of about 10 micrometers. First, a baseline was subtracted from Raman spectra by fitting and subtracting a 2nd-degree polynomial through a series of spectral values that are nominally zero for silicon (70, 80, 600,

700, 800, 1100, 1200, 1300, and 1400  $\text{cm}^{-1}$  were used). Then, the spectral area from 460–510  $\text{cm}^{-1}$  (associated with the broad amorphous silicon peak centered at 480  $\text{cm}^{-1}$ ) was divided by the spectral area from 515–525  $\text{cm}^{-1}$  (associated with the sharp crystalline silicon peak centered at 520  $\text{cm}^{-1}$ ). This procedure yields an indicator of amorphous silicon content that is insensitive to variations in overall spectral strength. The amorphous silicon content was mapped out radially over the modified area.

### **2.2.3 Results**

First we report results from the stationary pulse samples fabricated with a peak fluence of 1.5  $\text{kJ}/\text{m}^2$  (the single-pulse melting threshold of silicon), with pulse numbers of 200–900 pulses. All pulse numbers resulted in surface texturing. The surface texture was composed of parallel ripple structures (laser-induced periodic surface structures) about 400 nm in width. After 200 pulses, the ripples appear fully developed and deep (i.e., the crevasses between the ripples are too deep to be imaged by electron microscopy). With increasing pulse number, the ripples become increasingly covered in debris, as shown in Figure 2.2.1.

Varying the gas pressure has a significant effect on the amount and distribution of the surface debris. At atmospheric pressure, the surface debris sits on top of the ripples in clumps. At lower pressures, the surface debris is more uniformly distributed in smaller clumps. At 20 Torr, the lowest gas pressure investigated, very little debris sits on the surface for local fluence values near the onset of surface modification, as shown in Figure 2.2.2.

Because the pulse has a Gaussian profile, the local fluence decreases with dis-

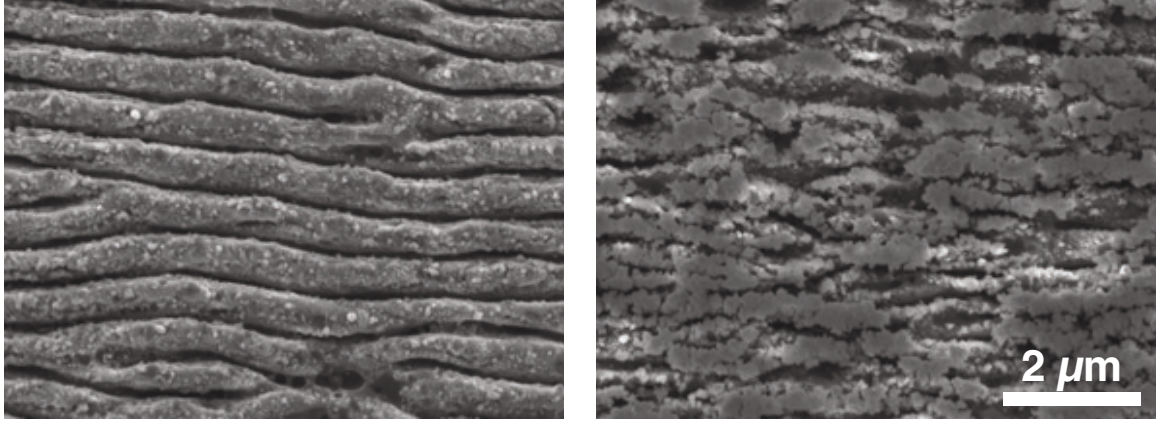


Figure 2.2.1: Scanning electron micrographs showing effect of pulse number on structure of ripples at a local fluence of  $1.4 \text{ kJ/m}^2$  and an air pressure of 20 Torr. Left: 200 pulses. Right: 500 pulses.

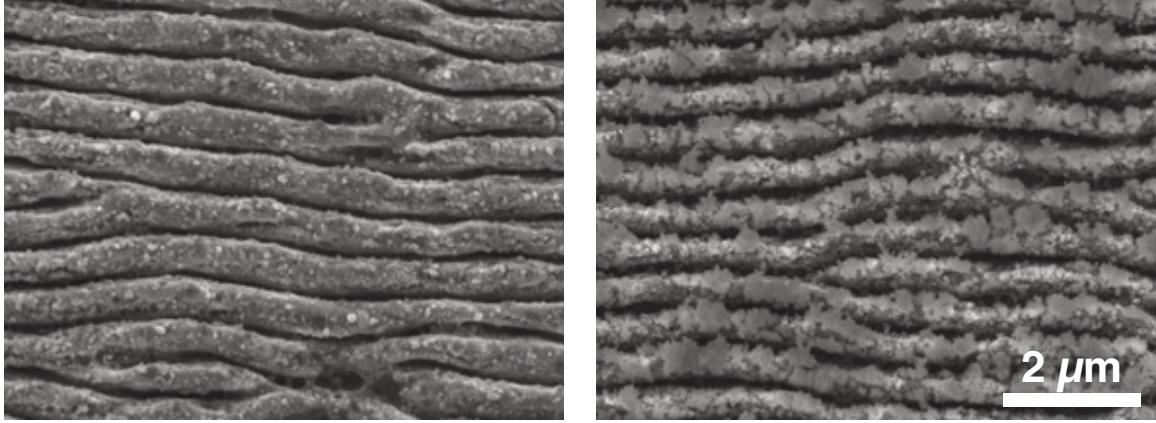


Figure 2.2.2: Scanning electron micrographs showing effect of pressure on surface debris. Local fluence for both images  $1.4 \text{ kJ/m}^2$  with 200 pulses. Left: 20 Torr air. Right: ambient atmospheric pressure (760 Torr).

tance from the center of the pulse. Thus we can examine the effects of a range of local fluence values from a single sample. At local fluences above that associated with the formation of surface ripples, the surface becomes increasingly pitted, bifurcated, and shallow, as shown in Figure 2.2.3. Higher local fluence also resulted in increased amounts of debris on the surface. We can also measure the fluence associated with the onset of surface texturing for a given pulse number, shown in Figure 2.2.4. For



example, with 200 pulses (and a peak fluence of  $1.5 \text{ kJ/m}^2$ ), texturing was observed at local fluences greater than  $1.4 \text{ kJ/m}^2$ . With increasing pulse number, the fluence associated with the onset of surface texturing decreased. For example, at 900 pulses, surface texturing was observed at a local fluence of  $1.0\text{--}1.1 \text{ kJ/m}^2$ . This reduction in threshold fluence was not affected by gas pressure.

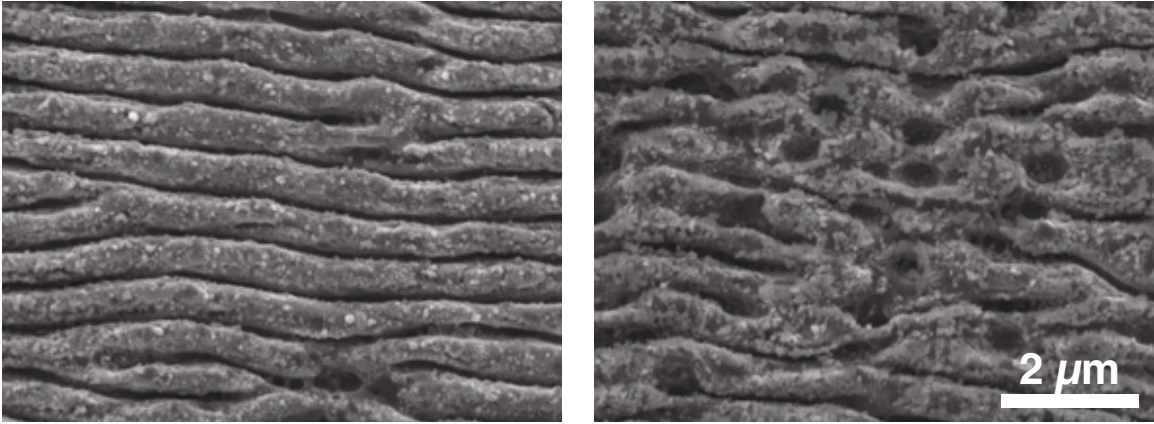


Figure 2.2.3: Effect of local fluence on surface structure after 200 pulses in 20 Torr air. Left: Local fluence of  $1.4 \text{ kJ/m}^2$ . Right: Local fluence of  $1.5 \text{ kJ/m}^2$ .

The most uniform surface ripples were produced at the edge of the circular region textured by the laser pulse, which corresponds to the lowest local fluence sufficient for texturing for a given number of pulses. With increasing pulse number and fluence, the surface ripples become increasingly pitted, bifurcated, and shallow. Increasing pulse number and fluence also produced more surface debris, although surface debris was reduced by using reduced gas pressure. For the pulse numbers we investigated, the most uniform surface ripples were produced within a local fluence range of  $1.3\text{--}1.4 \text{ kJ/m}^2$  with 200–300 pulses, shown in Figure 2.2.5.

We report the results of elemental analysis of the surface by energy-dispersive

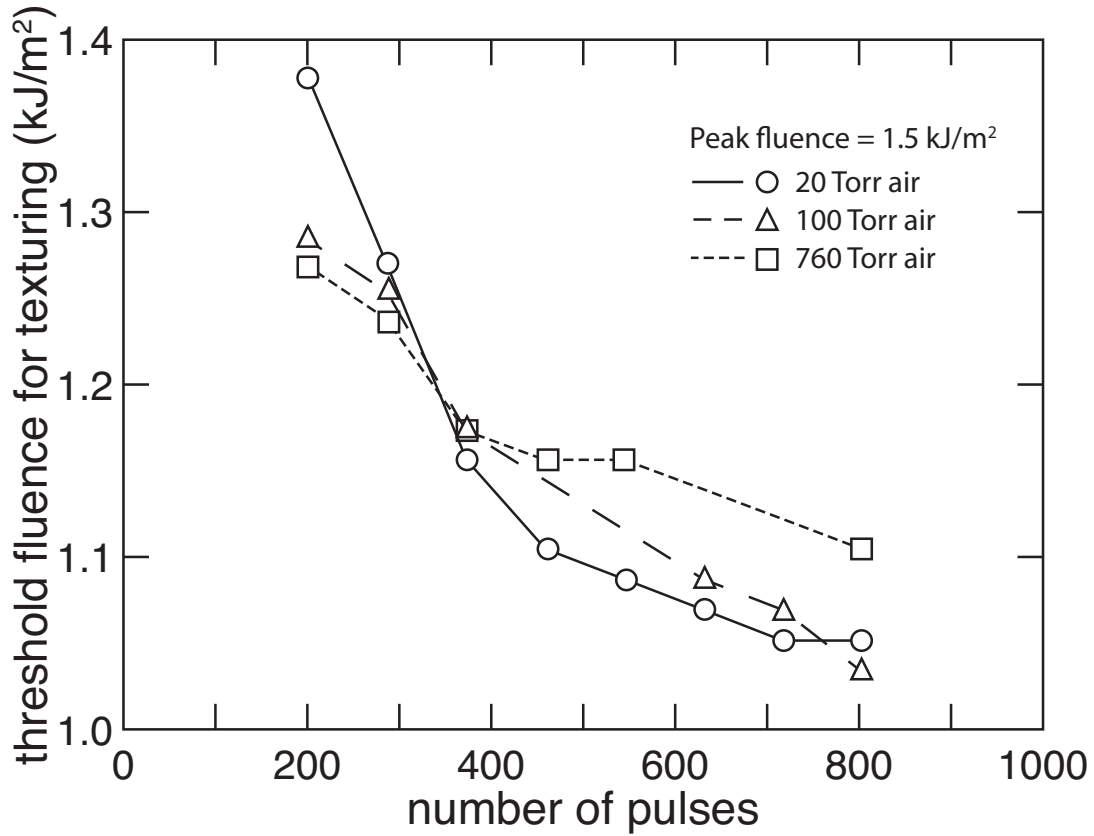


Figure 2.2.4: Reduction in local threshold fluence for texturing with increasing pulse number.

x-ray spectroscopy. In general, silicon and oxygen were detected on the surface, with carbon sometimes detected as well. Surface debris showed high levels of oxygen. In samples without surface debris, oxygen was also detected in the surface of the ripples. Figure 2.2.6 shows the qualitative abundance of these elements along transects over the surface.

We now report the results of Raman spectroscopy, which we used to measure the amorphous silicon content. All samples showed amorphous silicon where texturing occurred, as shown in Figure 2.2.7. Figure 2.2.8 shows the average amorphous silicon signal as a function of distance from the center of the textured area for different gas

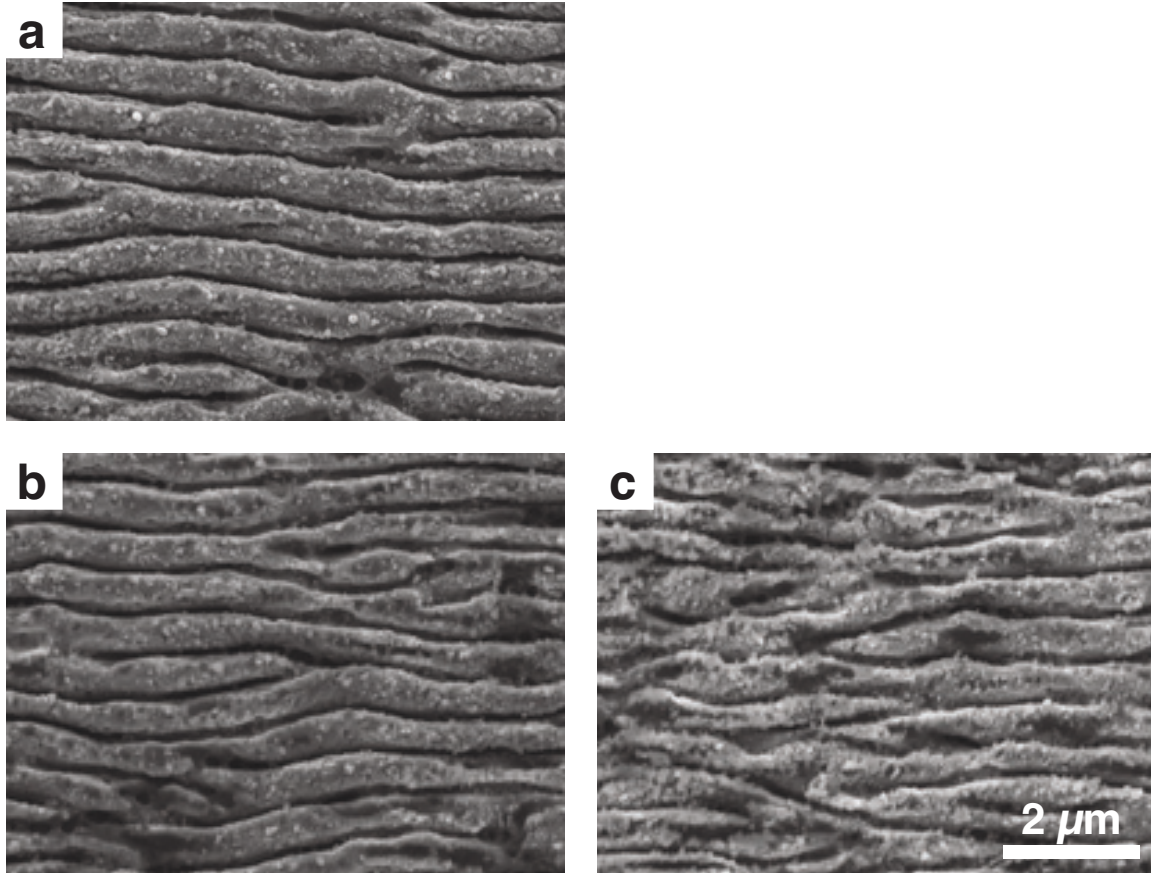


Figure 2.2.5: Surface ripples at the modification threshold. The modification threshold fluence decreases with increasing pulse number. a:  $1.4 \text{ kJ/m}^2$ , 200 pulses. b:  $1.3 \text{ kJ/m}^2$ , 300 pulses. c:  $1.2 \text{ kJ/m}^2$ , 500 pulses. All fabricated in 20 Torr air.

pressure and pulse number parameters. The strength of the amorphous silicon signal was greatest near the edge of the textured area and was essentially uniform over the interior of the textured area. The amorphous silicon signal within the textured area was slightly decreased when pressure and pulse number were both increased.

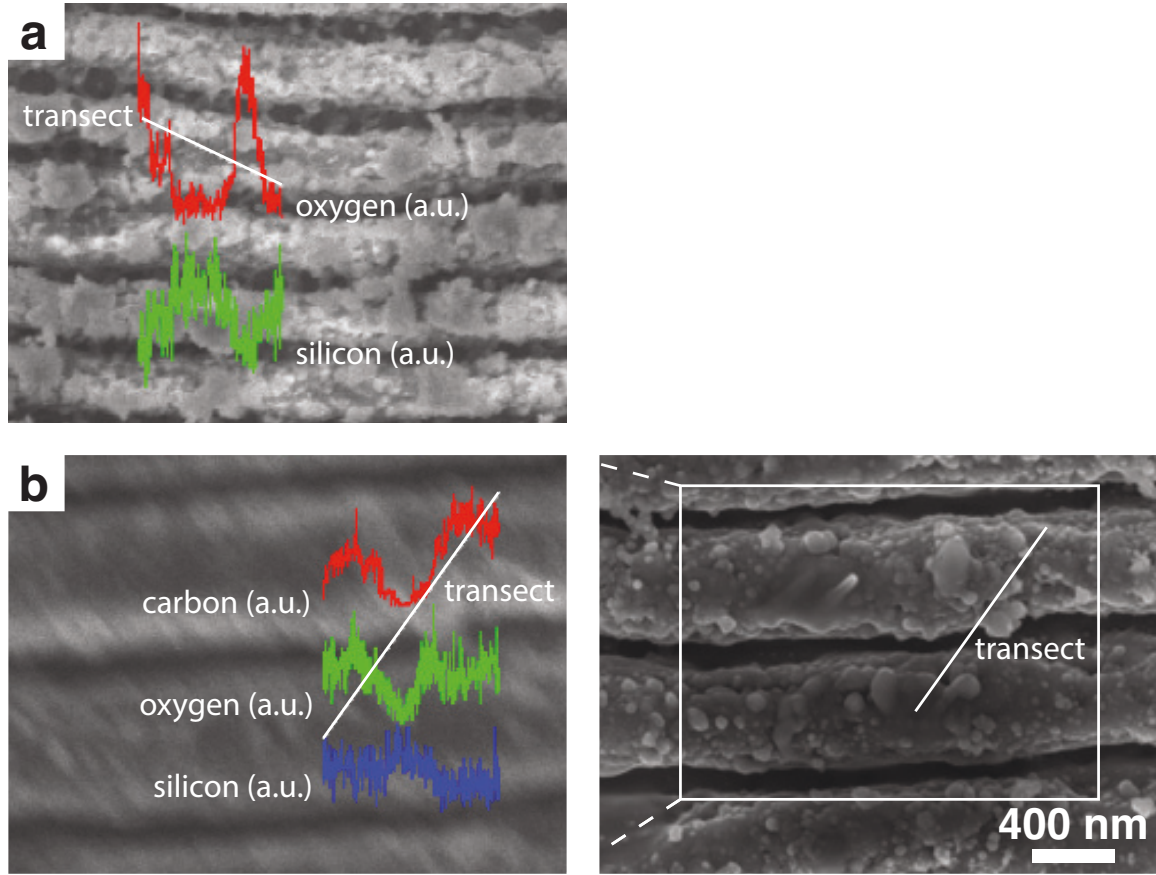


Figure 2.2.6: Elemental analysis of the surface by energy-dispersive x-ray spectroscopy. a: Analysis over a transect indicates that surface debris contains high levels of oxygen (red) and reduced levels of silicon (green) relative to debris-free surface area. Irradiation performed at atmospheric pressure (local fluence of  $1.4 \text{ kJ/m}^2$ , 200 pulses). b: Debris-free surface area (left) shows oxygen (green) and carbon (red) in the surface, with abundance highest at the top surface of the ripples than between the ripples. Measured silicon abundance (blue) indicates that reduced oxygen and carbon content between ripples is not due to reduced signal strength between ripples. Irradiation performed at 20 Torr (local fluence of  $1.4 \text{ kJ/m}^2$ , 200 pulses).

#### 2.2.4 Discussion

First we consider the overall morphology of the surface. We observe a sharp transition from untextured silicon to fully developed laser-induced period surface structures (i.e., ripples). Above the minimum fluence and pulse number combination required

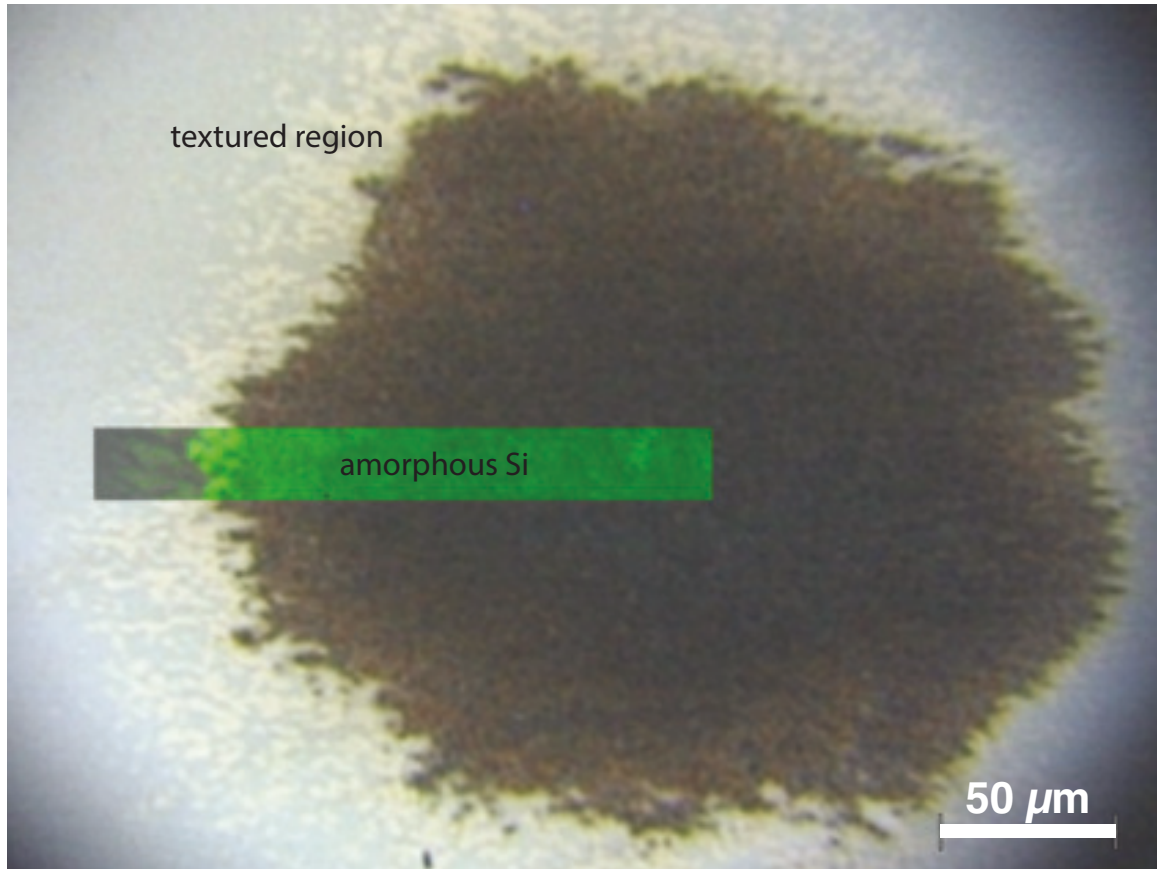


Figure 2.2.7: Optical microscope image of area textured with 200 pulses in 20 Torr air (peak fluence  $1.5 \text{ kJ/m}^2$ ). Amorphous silicon signal intensity from Raman spectroscopy (green) overlaid on image (rectangular region; arbitrary units). Amorphous silicon is observed only with texturing and is most intense near the edge of the textured area.

to produce ripples, the ripples become damaged (i.e., increasingly pitted, bifurcated, shallow, and covered with debris). Thus, the ripples are most uniform immediately after formation. Further irradiation does not further enhance the structure of the ripples. We infer that the ripples are formed from the flat surface during a single melting event or a small number of such events. Further irradiation on the formed ripple structures may cause focusing in the crevasses between the ripples, leading to ablation of material and the development of pits and surface debris. Eventually, the



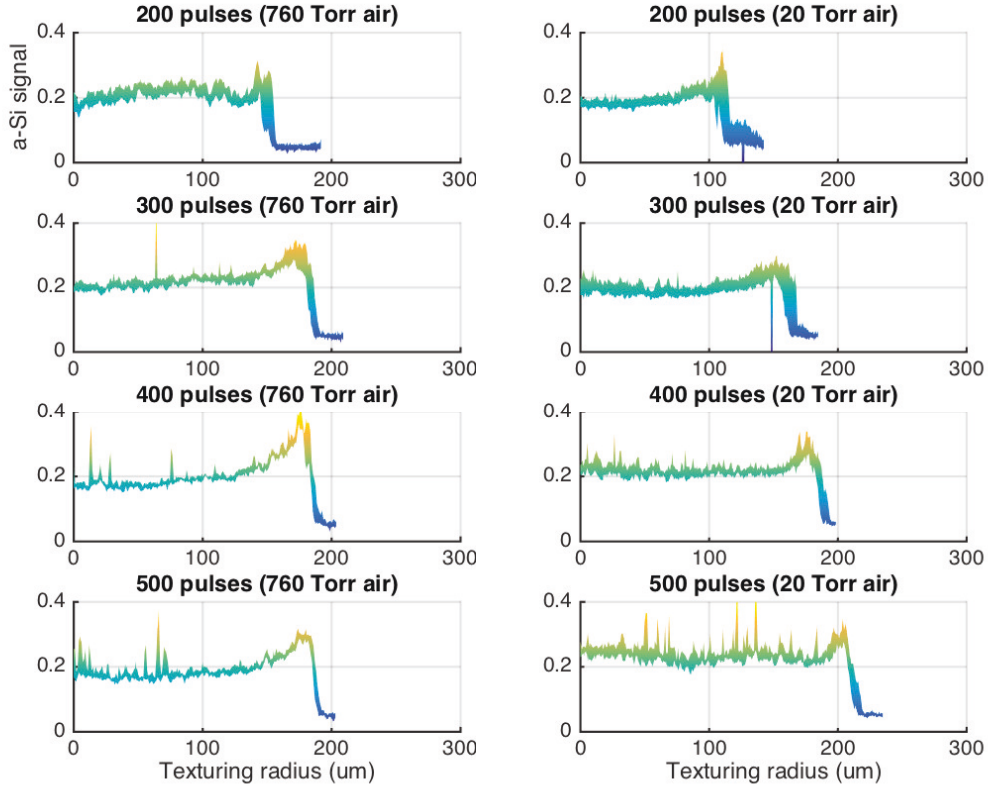


Figure 2.2.8: Amorphous silicon signal as a function of distance from the center of the textured area for various gas pressures and pulse numbers. Amorphous silicon signal is greatest near edge of textured area and decreases to a uniform value within the textured area. The amorphous silicon signal is not significantly affected by pulse number or gas pressure.

ripple structures are largely destroyed, leaving an irregular rough surface. Continued irradiation beyond this point does not appear to re-form the surface ripples, which may be due to the roughness of the surface, which would interfere with an ordered melting and resolidification process.

The ripples we observe are formed at fluences on the melting threshold of silicon. At the melting threshold, we expect the melting depth to be shallow, on the order of tens of nm [6], and we do not expect ablation to occur. Yet the ripples we observe

are 400 nm in size, and the crevasses between them appear to be at least this deep. Thus, we speculate that the ripples are initially formed through a process of melting and material transfer in the molten state to the surface of the ripple structures. The transition from flat silicon to fully developed ripples appears to be abrupt, with very little intermediate morphology apparent. Yet we do not expect the surface ripples to become fully formed in a single melting event, which would involve melting the surface hundreds of nm in depth, either in regular striations or more uniformly. Thus, we infer that the ripples are formed in a series of melting events. It is possible that once melting and surface irregularities occur, feedback processes lead to the formation of fully developed surface ripples after a small number of subsequent melting events.

We can estimate the number of pulses required to transform the initially molten silicon to fully formed surface ripples by examining the outer edges of our textured areas. On the outer edge of our samples irradiated with 400 pulses, we observe a transition zone of about 10 micrometers between flat silicon and fully formed surface ripples, as shown in Figure 2.2.9. Yet, between 300 and 500 pulses, the radius of the textured area increases by about 50 micrometers (from 150 to 200 micrometers), indicating an average growth in the textured area of 250 nm per pulse. This implies that after the initial formation of surface irregularities, about 40 pulses are sufficient to produce a fully formed network of surface ripples. Similarly, on the outer edge of a sample irradiated with 500 pulses, we observe a transition zone of around 5 micrometers, and between 400 and 600 pulses, the textured area increases by only about 25 micrometers, again implying that about 40 pulses yield fully formed surface ripples after the initial formation of surface irregularities. This estimate pertains to

the edge of the textured area, which is just at the threshold for ripple formation. For local fluences above the melting threshold, we expect the number of pulses necessary for ripple formation to be fewer.

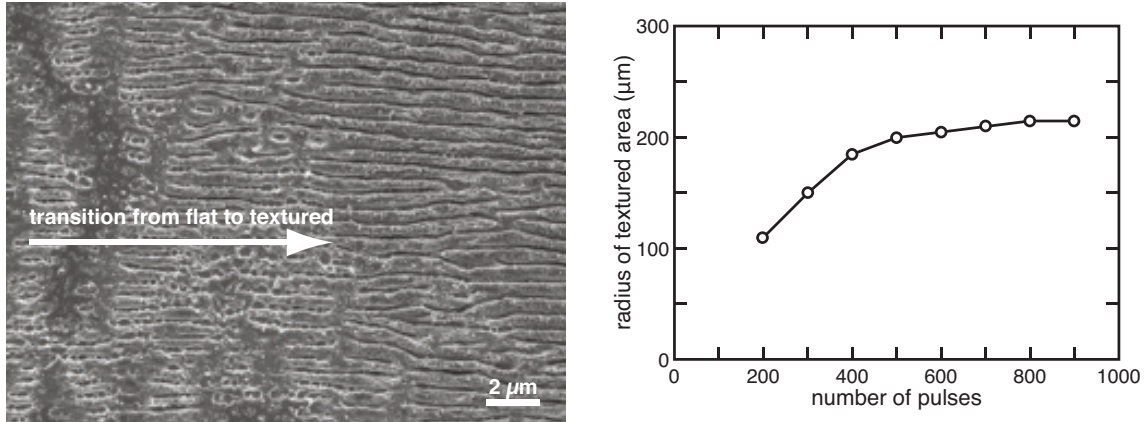


Figure 2.2.9: Transition from flat silicon to fully developed surface ripples. Left: scanning electron micrograph of edge of sample irradiated with 400 pulses in 20 Torr air showing transition zone of about 10 micrometers between flat silicon and fully developed surface ripples. Right: Texturing radius increasing with pulse number (here, for samples irradiated in 20 Torr air).

We comment on the observed reduction in texturing threshold fluence with increasing pulse number. Two factors could be at play here. First, there may be non-thermal incubation effects occurring over many pulses below the single-pulse melting threshold, such as the generation of structural defects, that lead to increased levels of heating with each additional laser pulse such that melting eventually occurs even below the single-pulse melting threshold fluence. Second, because the center of each pulse is at the single-pulse melting threshold, we expect surface texturing to occur there without incubation effects required. The development of surface texturing (i.e., ripples) may lead to an enhancement of the local fluence through light trapping, focusing, or other effects, which could then cause local fluences below the single-pulse



melting threshold to exceed that threshold over some parts of the surface (e.g., at the edge of crevasses between existing ripples). The reduction in texturing fluence with increasing pulse number appears to plateau, which could reflect the maximum local fluence enhancement that can be obtained by the surface ripples. The reduction of threshold fluence with pulse number does not appear to be affected by gas pressure. However, we note that at higher gas pressures, the presence of debris introduces some uncertainty in measuring the radius of the textured area.

We comment on the fact that sharp surface spikes are not generated here, in contrast to some past studies of laser texturing [8]. Here, we irradiate samples in ambient air, which contains nitrogen, oxygen, water vapor, and trace gases. However, black silicon is often fabricated in fluorine-bearing gases, such as  $\text{SF}_6$  and  $\text{NF}_3$  [44,48]. Fluorine-containing plasmas are known to etch silicon [49]. Thus, in the presence of, for example,  $\text{SF}_6$ , surface ripples rapidly develop into conical surface structures with additional laser pulses. However, in the absence of  $\text{SF}_6$  and at the low fluences we examine here, the surface ripples do not develop into conical surface structures with additional irradiation. Rather, after the ripples are initially formed, they become damaged by further irradiation. Thus, the development of the surface morphology with increasing pulse numbers follows a distinct path depending on whether the fabrication atmosphere contains a silicon etchant.

We consider the development of the surface debris. Debris appears to accumulate just outside the edge of the textured area, as shown in Figure 2.2.10. This may be ablated material from the interior of the textured area. The initial surface texturing appears to develop below the debris, at which point the debris is removed from the

surface. This may be due to explosive removal of material as the surface texture is initially formed. As these surface textures develop into fully formed ripples, debris reappears on top of the ripples. This may be due to continued ablation of material from between the ripples, which is then deposited onto the surface. At higher fluence and pulse number, more surface debris is produced, which corresponds with the damaging of the surface ripples. The reduction of surface debris at lower gas pressures might be due to the escape of debris from the surface to the chamber environment during irradiation.

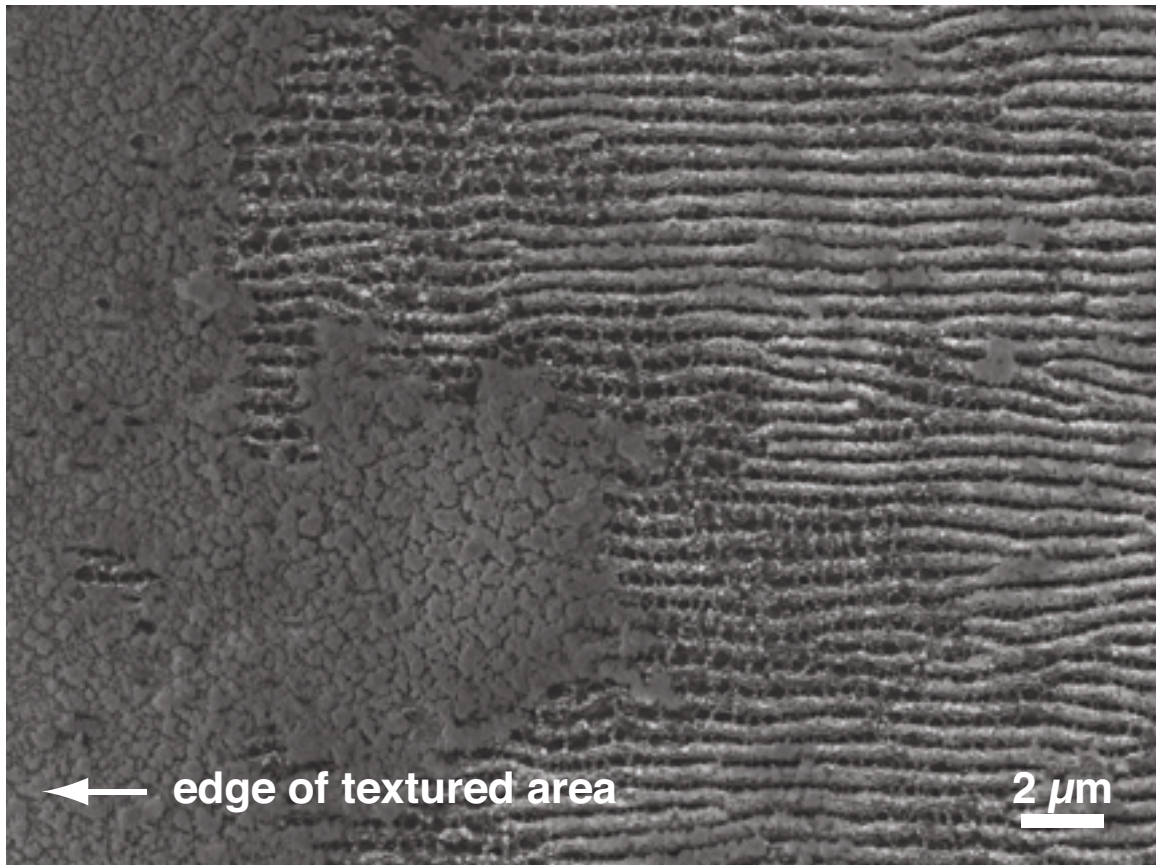


Figure 2.2.10: Scanning electron micrograph showing the accumulation of surface debris just outside of the textured area, and the removal of debris upon texture formation. Sample irradiated with 200 pulses in air at atmospheric pressure.

We now consider the chemistry of the surface debris. Energy-dispersive x-ray spectroscopy shows that the debris is composed of silicon and oxygen, and that the debris is oxygen-rich compared to the surface of the ripples. It is possible that the initial debris is derived from the native oxide on the silicon surface, which is transparent to the irradiation wavelength (800 nm); as the surface texture is formed, the surface oxide could be ablated and redeposited on the surface. With additional irradiation, ablation of the silicon leads to more debris accumulation, and it is reasonable to expect that this ablated material becomes infiltrated with oxygen from the surrounding atmosphere. The large amount of fluffy debris material we observe on the ripple surface, which continues to accumulate with increasing pulse number, could be silica, fumed silica, or some form of hydrated silica, as the air in which the irradiation was performed contained ambient water vapor. The fluffy morphology of the debris is similar to that reported for fumed silica [50].

The surface of the ripples themselves contains oxygen and carbon in addition to silicon, according to energy-dispersive x-ray spectroscopy. The presence of oxygen indicates oxygen infiltration during melting and resolidification. Carbon may derive from contamination during handling. The amounts of oxygen and carbon are greatest on top of the ripples and decrease in the crevasses between the ripples. The reduction in oxygen and carbon signal between the ripples is likely not an artifact of the surface morphology, because the silicon signal intensity actually increases in this region. The infiltration of oxygen into the top surface of the ripples could affect the electronic properties at the surface as well as the chemical stability of the surface (e.g., if treated with hydrofluoric acid).

We turn our attention to the presence of amorphous silicon on the surface. A thin layer of amorphous silicon may be present just outside of the textured area due to localized melting and resolidification [24], although the amorphous silicon signal from Raman spectroscopy in this region is near the noise floor. In contrast, the amorphous silicon signal increases significantly at the onset of texturing. This may be due to an increase in surface area (and thus surface amorphous silicon) upon texturing and/or the formation of pressure-induced amorphous silicon due to continued irradiation of the textured surface [5, 42].

The amount of amorphous silicon detected within the textured surface is roughly uniform, indicating that once the surface texture forms, the amount of amorphous silicon present does not change with continued irradiation, nor does it depend on the local fluence. Within the textured area, the amorphous silicon signal is reduced slightly by continued irradiation and also by increased gas pressure. The reduction of amorphous silicon signal with continued irradiation may be due to the deposition of crystalline grains on the surface or to annealing of amorphous silicon on some parts of the surface. Additionally, the increased gas pressure increases the amount of debris on the surface of the ripples, which might reduce the melting and amorphization produced by subsequent pulses.

Finally, we consider the implications of these results for texturing silicon while avoiding the generation of amorphous material. Here, the presence and amount of amorphous silicon correlated most strongly not with local fluence or pulse number, but rather with the onset of texturing. This indicates that the texturing and amorphization processes are strongly related to each other and that the melting threshold

fluence, it may not be possible to produce surface textures while maintaining high crystallinity.

### **2.2.5 Conclusions**

In this section, we investigated the formation of surface textures using a peak fluence of  $1.5 \text{ kJ/m}^2$  (near the single-pulse melting threshold for silicon). During irradiation, laser-induced period surface structures (ripples) are formed with a spatial period of about 400 nm. After formation, the ripples become damaged (pitted, bifurcated, and shallow) when irradiated with additional pulses. The amount of texturing produced by stationary pulses is greater than the amount produced by scanned pulses with the same nominal fluence and pulse number parameters.

Fluffy debris is present on the surface on top of the ripples and is increased by increased fluence and pulse number. Reducing the ambient gas pressure significantly reduces the accumulation of debris on the surface. The debris is oxygen-rich and may derive from the native oxide on the silicon surface and other ablated material, and may be composed of silica, fumed silica, and/or some form of hydrated silica. Oxygen is also detected within the top surface of the ripples.

The local fluence associated with the onset of surface texturing decreases with increasing pulse number, indicating the presence of non-thermal incubation effects or local fluence enhancement at the edge of the textured area. At the edge of the textured area, we can estimate that after the initial formation of surface irregularities, fully developed surface ripples are formed after about 40 pulses.

Raman spectroscopy showed amorphous silicon throughout the textured area.

The amount of amorphous silicon was greatest at the edge of the textured area, which is associated with the onset of texturing. Increased pulse number and gas pressure decreased the amount of amorphous silicon slightly, which may be due to the presence of debris interfering with melting and resolidification.

Our results indicate that at low fluence, the texturing and amorphization processes are closely linked. It is possible that amorphization is unavoidable in the ripple formation process at fluences near the melting threshold.

## **2.3 Laser texturing below the single-pulse melting threshold**

### **2.3.1 Introduction**

In this section, we expand on Section 2.2 by investigating texturing with a peak fluence of  $1.4 \text{ kJ/m}^2$ , below the single-pulse melting threshold. We examine a wide range of pulse numbers, from 10–8000 pulses. These parameters allow us to observe the incubation of surface modification over many pulses.

### **2.3.2 Methods**

A silicon wafer was irradiated with a series of stationary 800 nm fs pulses without translating the sample. A peak fluence of  $1.4 \text{ kJ/m}^2$  (below the single-pulse melting threshold for silicon) and pulse numbers of 10, 100, 500, 1000, 1500, 2000, 3000, 5000, and 8000 were used. The pulse diameter was 900x1000 micrometers and the

pulse repetition rate was 100 Hz. The irradiation was carried out in ambient air at atmospheric pressure.

The surface morphology of each textured area was examined using scanning electron microscopy. In order to examine the effect of pulse number on the threshold fluence for texturing, the radius of each textured area was measured and converted a local fluence using the fluence equation in Section 2.2.

Irregularly shaped debris on the surface was characterized chemically using energy-dispersive x-ray spectroscopy and structurally using Raman spectroscopy as in Section 2.2.

### **2.3.3 Results**

No surface texturing was observed after 10 or 100 pulses. In the region irradiated with 100 pulses, debris about 10 micrometers in size was observed, shown in Figure 2.3.1. Energy-dispersive x-ray fluorescence identified this object as silicon, and Raman spectroscopy showed that the vibrational mode at  $520\text{ cm}^{-1}$  was shifted to  $500\text{ cm}^{-1}$ .

Surface textures were produced with pulse numbers of 500 and greater. Overall, the surface texture was rippled, similar to that produced in Section 2.2. The surface texture initially formed as a non-periodic network and developed into surface ripples with additional pulses. As in Section 2.2, the surface ripples were covered in surface debris. Figure 2.3.2 shows the transition from a non-periodic surface texture to surface ripples with increasing local fluence at 500 pulses.

The transition from flat silicon to a rippled surface was gradual for local fluences near the single-pulse melting threshold (e.g.,  $1.4\text{ kJ/m}^2$ ). For these fluences, a non-

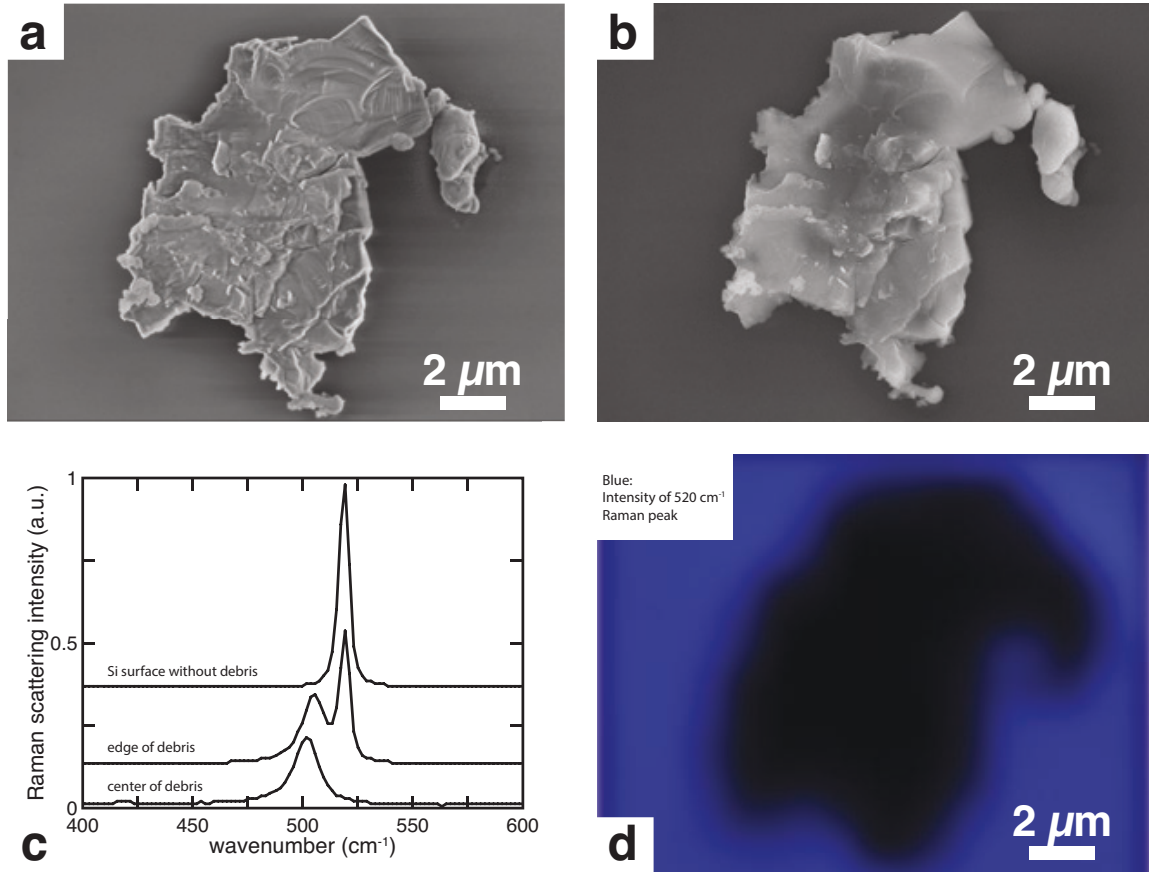


Figure 2.3.1: Debris produced by 100 pulses at a peak fluence of 1.4 kJ/m<sup>2</sup> in air at atmospheric pressure. Scanning electron microscope images produced with sidescattered (a) and backscattered (b) electrons. c: Raman spectra of debris showing shift in silicon vibrational mode from 520 cm<sup>-1</sup> to 500 cm<sup>-1</sup>. d: Intensity of 520 cm<sup>-1</sup> Raman peak on surface, showing a sharp reduction at the edge of the debris.

periodic texture was formed before surface ripples were developed. However, for lower fluences at higher pulse numbers (e.g., local fluence of 1.2 kJ/m<sup>2</sup> with 1000 pulses), the transition was abrupt, with flat silicon transforming directly to rippled silicon, as shown in Figure 2.3.3. At the edge of the textured area, a thin layer of material was typically observed delaminating from the surface.

As in Section 2.2, large amounts of fluffy debris continued to accumulate with



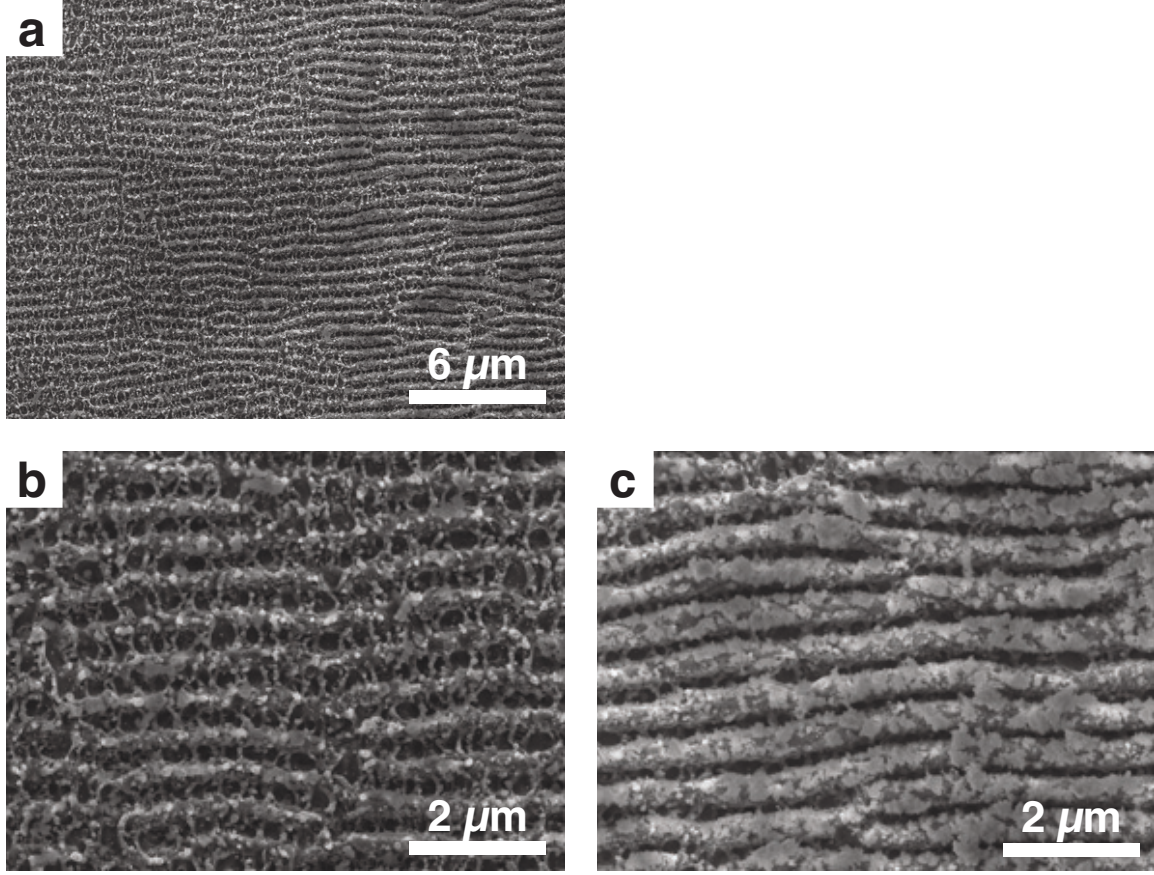


Figure 2.3.2: a: transition between irregular surface texturing and surface ripples after 500 pulses. Left side of frame  $1.35 \text{ kJ/m}^2$ , right side of frame  $1.40 \text{ kJ/m}^2$ . b: Close up of initiation of surface ripple formation from non-periodic network. c: Fully formed surface ripples covered in debris produced with a local fluence of  $1.4 \text{ kJ/m}^2$ .

additional pulses. After 5000 pulses, only a 2-micrometer-wide region at the edge of the textured area remained uncovered by debris, shown in Figure 2.3.4. After 8000 pulses, the entire textured area was entirely covered in debris. At higher fluence values, the debris is self-organized into clumps about 5 micrometers in size. Figure 2.3.5 shows the morphology of the surface debris.

The threshold fluence for texturing decreased with increasing pulse number, as in Section 2.2. With 8000 pulses, the surface is textured with a local fluence of  $0.8\text{--}0.9$

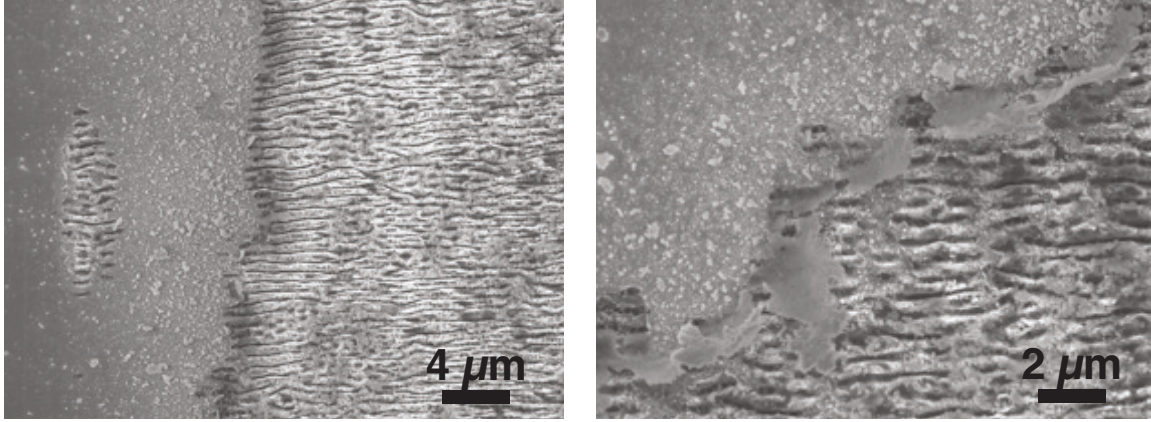


Figure 2.3.3: Left: Edge of sample with 1000 pulses and local fluence of  $1.2 \text{ kJ/m}^2$ . Transition from flat silicon to rippled silicon is abrupt at low fluences and high pulse numbers. For these conditions, the surface does not pass through an intermediate non-periodic texturing stage. Right: Edge of sample with 1500 pulses and local fluence of  $1.1 \text{ kJ/m}^2$ . Thin layer of material appears to delaminate from the surface as the ripples are formed.

$\text{kJ/m}^2$ . The threshold fluence decreases linearly with the logarithm of the number of pulses used, as shown in Figure 2.3.6. The slope of this dependence is the same as that measured in Section 2.2. However, for the same number of pulses, the threshold fluence measured here is offset by a constant value of  $0.18 \text{ kJ/m}^2$  relative to that measured in Section 2.2.

### 2.3.4 Discussion

Although surface ripples are observed after 500 pulses, we observe no surface texturing whatsoever after 10 or 100 pulses. However, even in the absence of visible surface textures, defects may be accumulating in the silicon surface, which could lead to increased heating with additional pulses. After 100 pulses, the presence of silicon debris with a Raman vibrational mode at  $504 \text{ cm}^{-1}$  is evidence that the surface is becoming highly strained in the absence of melting. For comparison, silicon nanowires

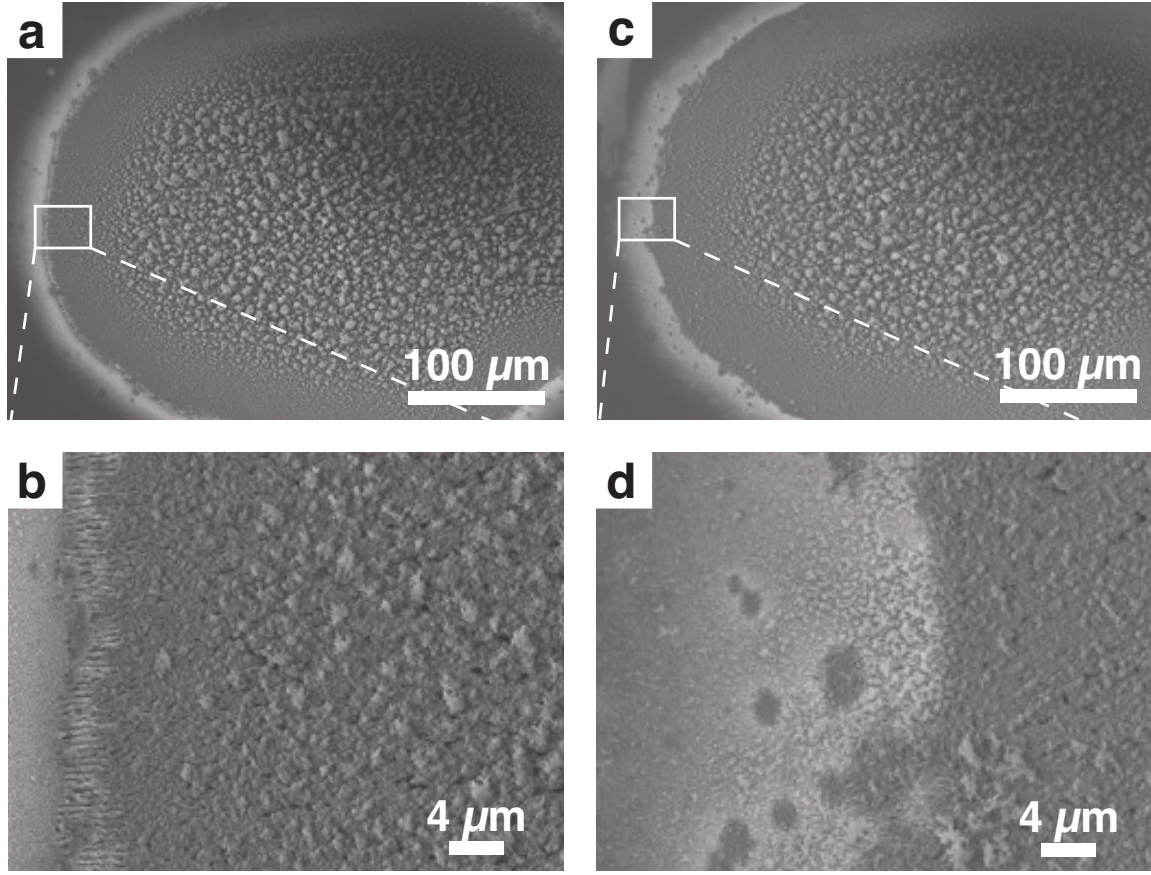


Figure 2.3.4: Accumulation of debris with increasing pulse number. a: 5000 pulses left only a small 2-micrometer-wide region at the edge of the textured area uncovered with debris (b: close-up of edge). c: 8000 pulses resulted in the entire textured area being covered in debris (d: close-up of edge). Edge of textured area has local fluence of  $0.9 \text{ kJ/m}^2$ .

with tensile strain of 4.5% (approximately 7.6 GPa tensile stress) show a Raman mode at  $506 \text{ cm}^{-1}$  [51]. Alternatively, the shift in Raman mode could indicate the formation of hexagonal (wurtzite) silicon, which has a Raman mode around  $500 \text{ cm}^{-1}$  [52, 53]. Hexagonal silicon has been reported from twin intersections in cubic silicon [54] and laser ablation of silicon [55]. The potential presence of hexagonal silicon is important for two reasons. First, the formation of hexagonal silicon through the accumulation of extended defects such as twin boundaries could be an incubation mechanism to



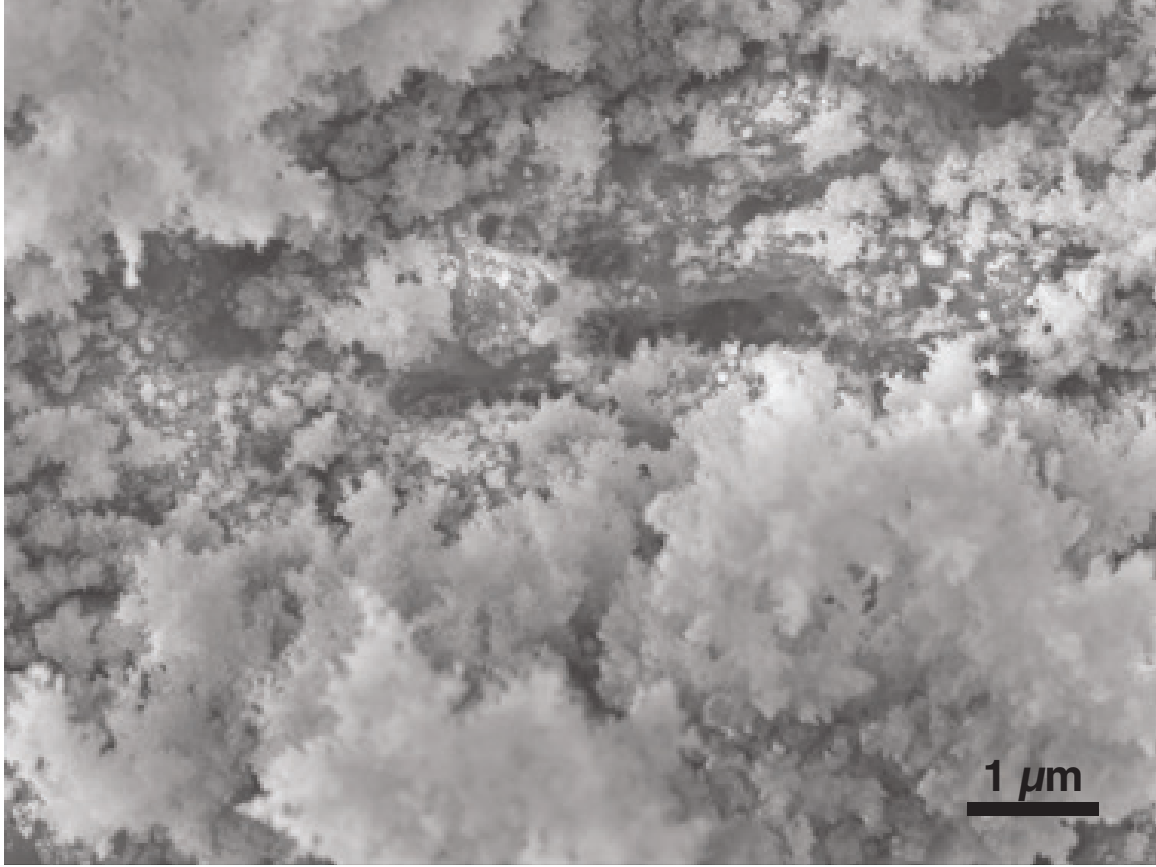


Figure 2.3.5: Close-up of surface debris after 8000 pulses at a local fluence of  $1.4 \text{ kJ/m}^2$ . Debris agglomerates into clumps around 5 micrometers in size.

explain the texturing of silicon below the single-pulse melting threshold. Second, hexagonal silicon could be useful for optoelectronic devices including photovoltaics [56].

Once ripples are formed, they propagate outward with additional laser pulses. At high pulse number and low local fluence, the growth of the ripples appears to be dependent on a feedback process that is initiated by the ripples themselves. For example, after 1000 pulses and with a local fluence of  $1.2 \text{ kJ/m}^2$ , no intermediate surface morphology exists between the flat silicon surface and the rippled texture. This indicates that after the surface texturing is initially seeded, it can propagate to

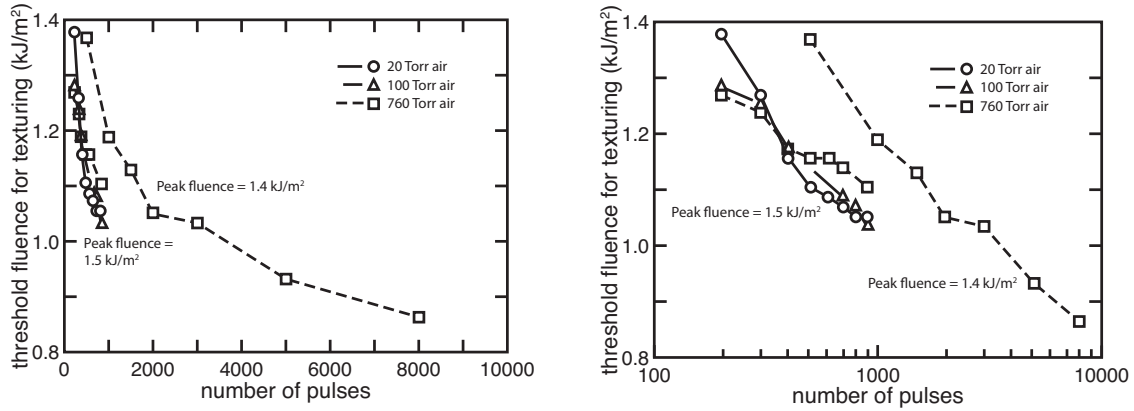


Figure 2.3.6: Decrease in local threshold fluence for texturing with increasing pulse number. Measurements from pulses with a peak fluence of  $1.4 \text{ kJ/m}^2$  are from this section; those from pulses with a peak fluence of  $1.5 \text{ kJ/m}^2$  are from Section 2.2.

areas with low local fluence through a feedback process based on surface morphology, such as local fluence enhancement through light trapping at the edge of the textured area.

We observe that the ripples are formed underneath of a thin, cohesive surface layer, which we can infer is the surface oxide. As the ripples are formed, the surface oxide no longer adheres the surface and is delaminated or ablated from the surface.

The fluffy surface debris is composed of sub-micrometer particles that continue to accumulate after thousands of pulses. Eventually, these particles aggregate into low-density structures about five micrometers in size, particularly at higher fluences. The morphology and structural density of the surface debris is similar to that of fumed or pyrogenic silica, which also forms micrometer-sized aggregates from sub-micrometer-sized silica particles [50]. It is possible that during the melting, ablation, and redeposition processes, oxygen and/or water vapor in the surrounding atmosphere produce silica or hydrated silica particles, which then agglomerate into larger

structures over repeated laser pulses.

The threshold fluence for surface texturing decreases approximately linearly with the logarithm of the pulse number, with a slope that is remarkably similar to that observed in Section 2.2. The curves between texturing fluence and pulse number between pulses with peak fluences of 1.4 and 1.5 kJ/m<sup>2</sup> (from this section and Section 2.2, respectively) are offset by a constant factor of about 0.18 kJ/m<sup>2</sup>. It is possible that this is due to uncertainty in estimating peak fluence. However, it is reasonable to expect that higher peak fluences lead to faster initiation of texturing and thus more rapid growth of the textured area with additional pulses through surface feedback processes. An empirical fit to the observed fluence thresholds for texturing is:

$$F = -0.4 * \log_{10}(N) - 1.8F_p + 4.92$$

Where  $F$  is the local fluence,  $N$  is the number of pulses, and  $F_p$  is the peak fluence of the pulse (in kJ/m<sup>2</sup>). Figure 2.3.7 shows this empirical relation for  $F_p = 1.4$ – $1.6$  kJ/m<sup>2</sup> in increments of 0.1 kJ/m<sup>2</sup>, where the line corresponding to  $F_p = 1.6$  kJ/m<sup>2</sup> is an extrapolation. The lines provide an estimate for the number of pulses required to initiate texturing for stationary pulses of a given peak fluence. For example, with a peak fluence of 1.5 kJ/m<sup>2</sup>, we expect texturing to be initiated after about  $10^{1.8} = 60$  pulses and grow in area to a local fluence of 1.0 kJ/m<sup>2</sup> after 1000 pulses. With a peak fluence of 1.4 kJ/m<sup>2</sup>, we expect texturing to be initiated after around  $10^{2.5} = 300$  pulses and grow in area to a local fluence of 1.2 kJ/m<sup>2</sup> after 1000 pulses, then to a local fluence of 1.0 kJ/m<sup>2</sup> after 3000 pulses, and then to a local fluence of 0.8 kJ/m<sup>2</sup> after 10000 pulses. Extrapolating this fit to a peak fluence of 1.6 kJ/m<sup>2</sup>, we expect texturing to be initiated after 10–20 pulses and, after 100 pulses, to grow to

a local fluence of around  $1.2 \text{ kJ/m}^2$ . At fluences above  $1.6 \text{ kJ/m}^2$ , the initiation of texturing may no longer be limited by fluence but rather by mass transfer during each melting event, in which case we would not expect texturing to be initiated faster than 10–20 pulses. Furthermore, at fluences well above the melting threshold, growth of the textured area would not be limited by surface feedback processes, but could be directly initiated over a large area. Thus, we expect that our empirical fits are valid only in the fluence regime around or below the single-pulse melting threshold of  $1.5 \text{ kJ/m}^2$ , and that texturing at  $1.6 \text{ kJ/m}^2$  and above would be limited by mass transfer and would occur after 10–20 pulses. It would be interesting to test these fits further for lower peak fluences. For example, we expect that with a peak fluence of  $1.3 \text{ kJ/m}^2$ , over 1000–2000 pulses would be required to initiate texturing.

Our empirical fits provide some guidance for future experiments in texturing silicon at or below the single-pulse melting threshold. First, they illustrate that it is possible to texture silicon below the single-pulse melting threshold through incubation and feedback effects. However, for peak fluences substantially below the melting threshold, initiating texturing may require thousands of pulses, as shown in Figure 2.3.7. Our fits also illustrate how sensitive the texturing process may be to peak fluence, a parameter that often contains considerable uncertainty (often at least 5–10%). Thus, it may be difficult to obtain good reproducibility in experiments performed in this low-fluence regime.

We close this discussion by considering the potential usefulness and challenges of low-fluence surface modification for technological applications. The possibility of structural defect incubation and the observation of silicon that is highly strained or

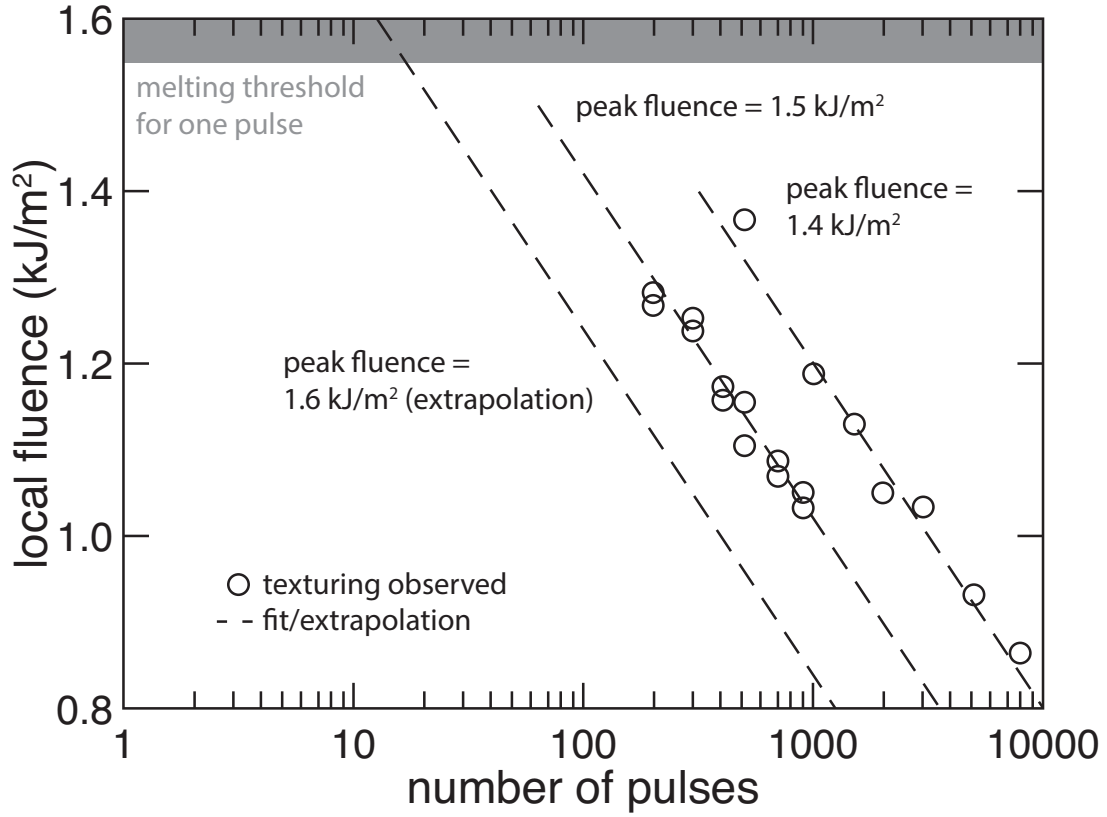


Figure 2.3.7: Empirical fits to the relationship between texturing fluence and pulse number. Experimental data (circles) from this section and Section 2.2. The line for a peak fluence of 1.6 kJ/m² is an extrapolation, which we verify in Section 2.5.

hexagonal in structure are of potential technological interest. Low-fluence fs laser pulses could potentially be used to produce highly strained or defect-rich silicon. At the same time, using low-fluence pulses to texture silicon entails a number of challenges. First, a large amount of debris is generated in ambient air at atmospheric pressure. It may be possible to reduce this debris by using dry air, flowing air over the surface as it is textured, or by using a controlled texturing atmosphere. Additionally, the surface texturing process, including the defect incubation process, appears to be



extremely sensitive to variations in peak fluence. Because it is difficult to reduce the uncertainty in the peak fluence to low levels, obtaining consistent results may be difficult in this low fluence regime.

### **2.3.5 Conclusions**

In this section, we investigated surface texturing using fs laser pulses with fluences below the single pulse melting threshold. We found that even if texturing is not initiated after many pulses (e.g., after 100 pulses), continued irradiation can nonetheless produce texturing, pointing to the presence of a non-thermal incubation mechanism at these fluences. Before texturing occurs, we observe the presence of highly strained or hexagonal silicon, which may result from the accumulation of structural defects arising from irradiation below the melting threshold. The accumulation of structural defects, strain, or hexagonal silicon may be the non-thermal incubation mechanism responsible for the initiation of texturing below the melting threshold fluence.

Once textures are initiated, the textured area grows with continued irradiation. Especially at high pulse numbers and low local fluences, the transition from flat to rippled silicon is abrupt and does not appear to pass through a transitional melting stage, indicating that the textured area grows at low local fluences through surface feedback mechanisms such as light trapping.

Surface debris continues to accumulate with increasing pulse number, eventually obscuring the entire textured area. Based on elemental and morphological analysis, this debris appears similar to fumed (pyrogenic) or hydrated silica and could arise from the interaction of ablated silicon material with the surrounding atmosphere.

After the surface texturing is initiated, the textured area grows larger, to increasingly lower local fluences with increasing pulse number. The local fluences associated with the appearance of texturing decreases remarkably linearly with the logarithm of the pulse number. For pulses with higher peak fluence, texturing is initiated after fewer pulses. After texturing is initiated, however, texture growth follows a similar behavior with the logarithm of the pulse number. An empirical fit to the observed data suggests that the number of pulses needed to initiate texturing is highly sensitive to the peak fluence when it is below the single-pulse melting threshold, requiring thousands of pulses for peak fluences below  $1.3 \text{ kJ/m}^2$ , while above the single-pulse melting threshold, only 10–20 pulses are needed to initiate texturing.

Irradiating silicon below the single-pulse melting threshold could be useful for generating highly strained, defective, or hexagonal silicon, as well as for forming surface textures. However, the effects on the surface appear to be highly sensitive to pulse fluence, which can entail considerable uncertainty in absolute terms, posing challenges for reproducibility. The formation of debris may also pose challenges in practice.

## **2.4 Initiation of surface textures**

### **2.4.1 Introduction**

In this section, we examine ripple formation in its early stages using fluence and pulse numbers near the onset of texturing. By examining ripple formation in its early stages, we can develop a phenomenological understanding of how surface textures are

formed from their earliest stages.

### **2.4.2 Methods**

A silicon wafer was irradiated with a series of stationary 800 nm fs pulses without translating the sample. A peak fluence of  $1.5 \text{ kJ/m}^2$  and pulse numbers of 110–190 were used in 10 pulse increments. The pulse diameter was 800x1000 micrometers and the pulse repetition rate was 100 Hz. Irradiation was carried out in three gases: ambient air,  $\text{N}_2$  gas, and  $\text{SF}_6$  gas. For each gas type, two gas pressures were used: 760 Torr (atmospheric pressure) and 20 Torr.

Samples were inspected using scanning electron microscopy and Raman spectroscopy. The presence of amorphous silicon was measured using Raman spectroscopy as in Section 2.2.

### **2.4.3 Results**

In air at 760 Torr, a non-periodic, random surface texture is present after 110 pulses and develops with additional pulses into periodic surface ripples, which are nearly formed after 190 pulses. These results are consistent with the surface texturing results presented in Section 2.3, in which surface ripples were formed under the same gas and fluence conditions after 200 pulses.

Different surface textures were produced in different gas types. Air produced surface ripples as discussed in Sections 2.2 and 2.3. Nitrogen produced a texture with thin, 200-nm-wide ridges separated by grooves running in a perpendicular direction approximately every 1 micrometer.  $\text{SF}_6$  produced an isotropic surface texture com-

posed of separated mounds. These surface textures are shown in Figure 2.4.1 for a local fluence of  $1.5 \text{ kJ/m}^2$  after 190 pulses in 760 Torr gas.

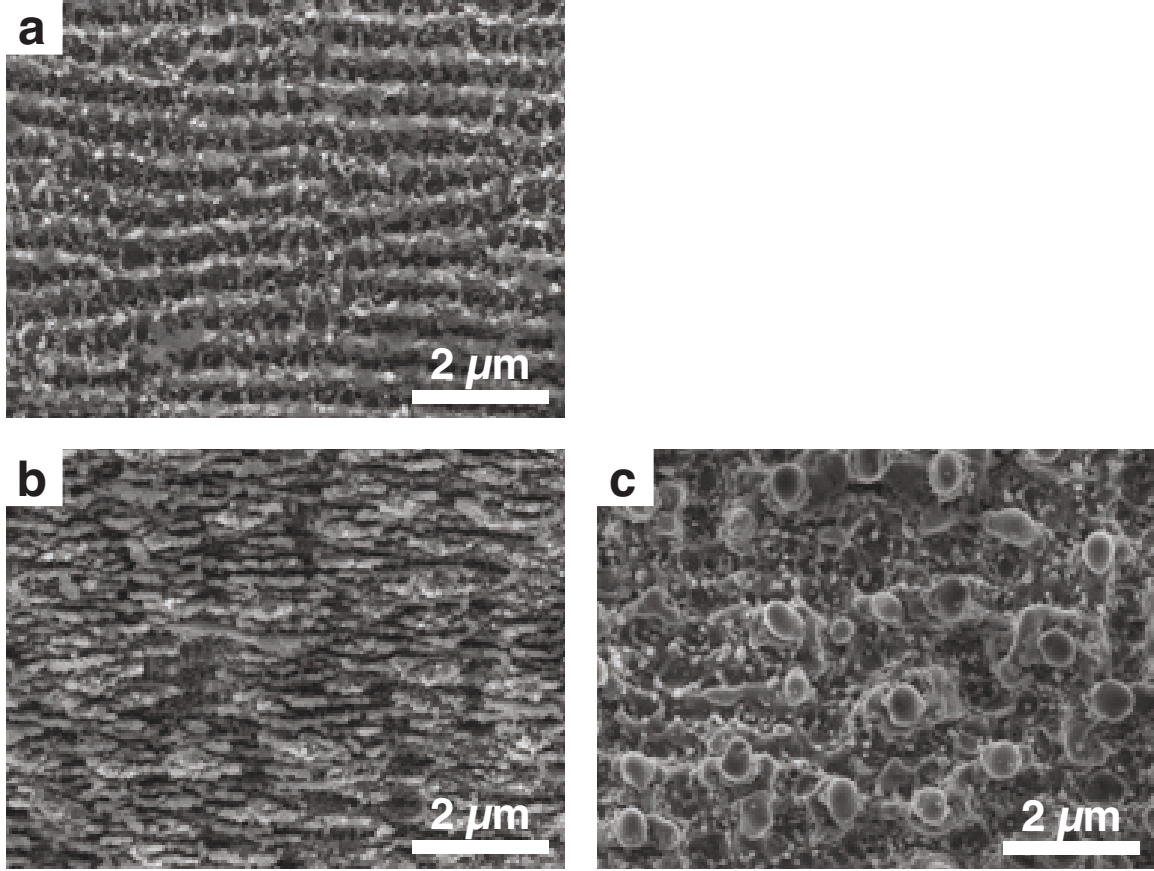


Figure 2.4.1: Surface textures produced by irradiation in various gases. a: ambient air. b: N<sub>2</sub> gas. c: SF<sub>6</sub> gas. All surfaces irradiated with a local fluence of  $1.5 \text{ kJ/m}^2$  and 190 pulses.

We report the evolution of the surface texture produced in N<sub>2</sub> gas at 760 Torr. Initially, at a local fluence of  $1.3 \text{ kJ/m}^2$  and 110 pulses, small mounds of material 10–100 nm in size cover the surface. At a higher local fluence of  $1.4 \text{ kJ/m}^2$ , an interconnected network of pits about 200 nm in diameter develops. Series of pits are aligned in rows perpendicular to the laser electric field polarization direction, similar to the orientation of surface ripples produced in air. With increasing fluence, these

pits coalesce into trenches, forming surface ripples with a period of about 400 nm. At a local fluence of  $1.5 \text{ kJ/m}^2$ , 1-micrometer-scale mounds appear, separated by trenches running both perpendicular and parallel to the laser polarization direction. Interfaces between surface morphology types are shown in Figure 2.4.2.

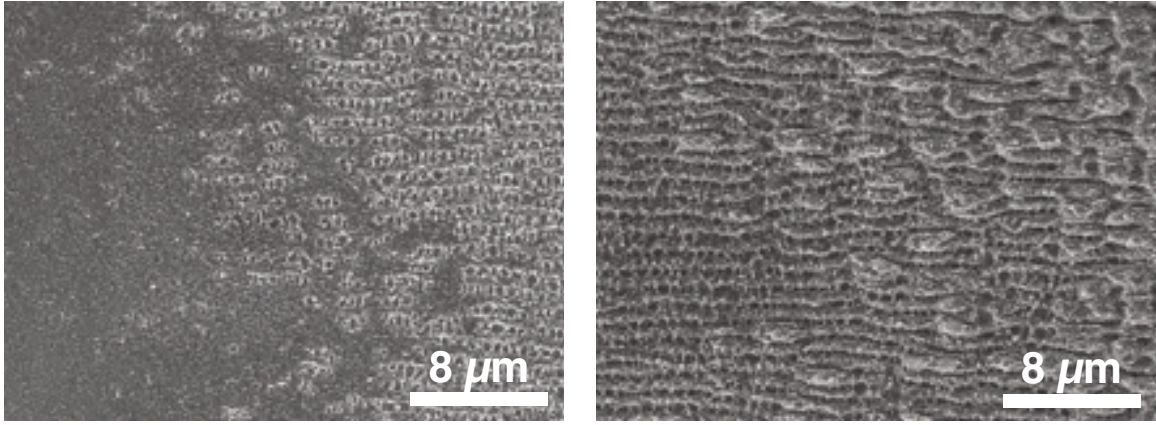


Figure 2.4.2: Development of surface texture in  $\text{N}_2$  gas at 760 Torr. Left: Interface between nanometer-scale surface mounds and interconnected network of pits about 200 nm in diameter (110 pulses, local fluence  $1.4 \text{ kJ/m}^2$ ). The interconnected network of pits develops into a surface ripple morphology. Right: Interface between surface ripples and 1-micrometer-scale surface mounds (110 pulses, local fluence  $1.5 \text{ kJ/m}^2$ ).

We found that gas pressure played a significant role in the formation of surface textures. Samples irradiated in a gas pressure of 760 Torr showed texturing over a roughly circular area corresponding to the laser pulse profile. However, samples irradiated in a gas pressure of 20 Torr showed much less texturing overall, as shown in Figure 2.4.3. The textures that were formed in low pressure gas, whether air,  $\text{N}_2$ , or  $\text{SF}_6$ , were composed of ripples extending perpendicular to the direction of laser polarization, as observed previously. However, the area covered by these ripples extended much farther in the direction parallel to the laser polarization than perpendicular to it. Multiple of these elongated textured strips were formed in each irradiated area,

and these textured strips grew larger with additional pulses, eventually merging to form interconnected textured areas that increasingly reflected the circular shape of the laser pulse profile.

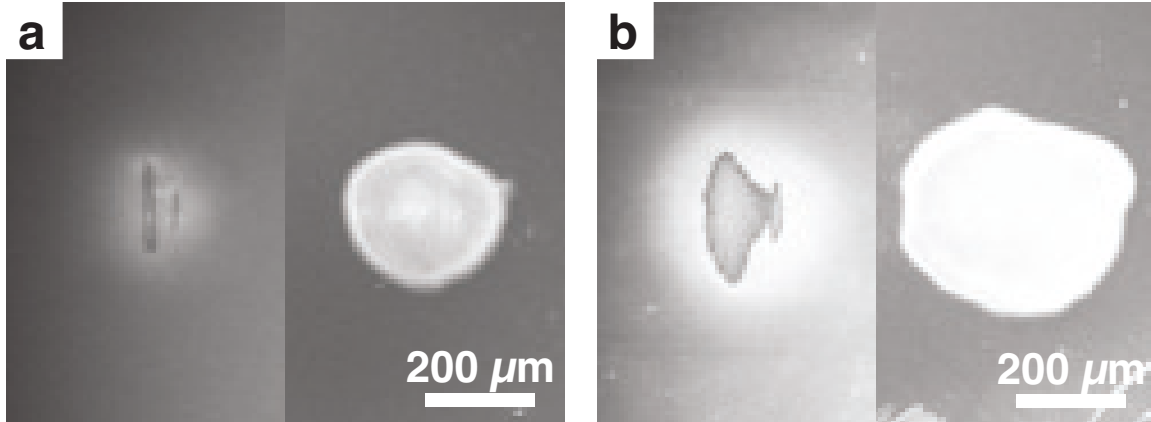


Figure 2.4.3: a: Comparison of areas textured with 110 pulses with peak pulse fluence of  $1.5 \text{ kJ/m}^2$  in  $\text{N}_2$  gas. Textured area on left irradiated in 20 Torr gas (texture present in elongated strip), and textured area on right irradiated in 760 Torr gas (texture present in circular area). b: Comparison of areas textured with 190 pulses with same parameters.

We now report the formation of surface textures in low-pressure (20 Torr) air and nitrogen in detail. Initially, small, sub-micrometer modified areas appear on the surface randomly. These areas produce laser-induced periodic surface structures extending parallel to the laser polarization (rather than perpendicular to it) that show a high spatial period of around 200 nm. These high-spatial-frequency ripples propagate perpendicular to the laser polarization. As they propagate, separate laser-induced periodic surface structures form, extending perpendicular to the laser polarization with a spatial period of around 400 nm. Once formed, these rapidly propagate in the direction of the laser polarization, forming an elongated strip of periodic surface ripples as shown in Figure 2.4.4.

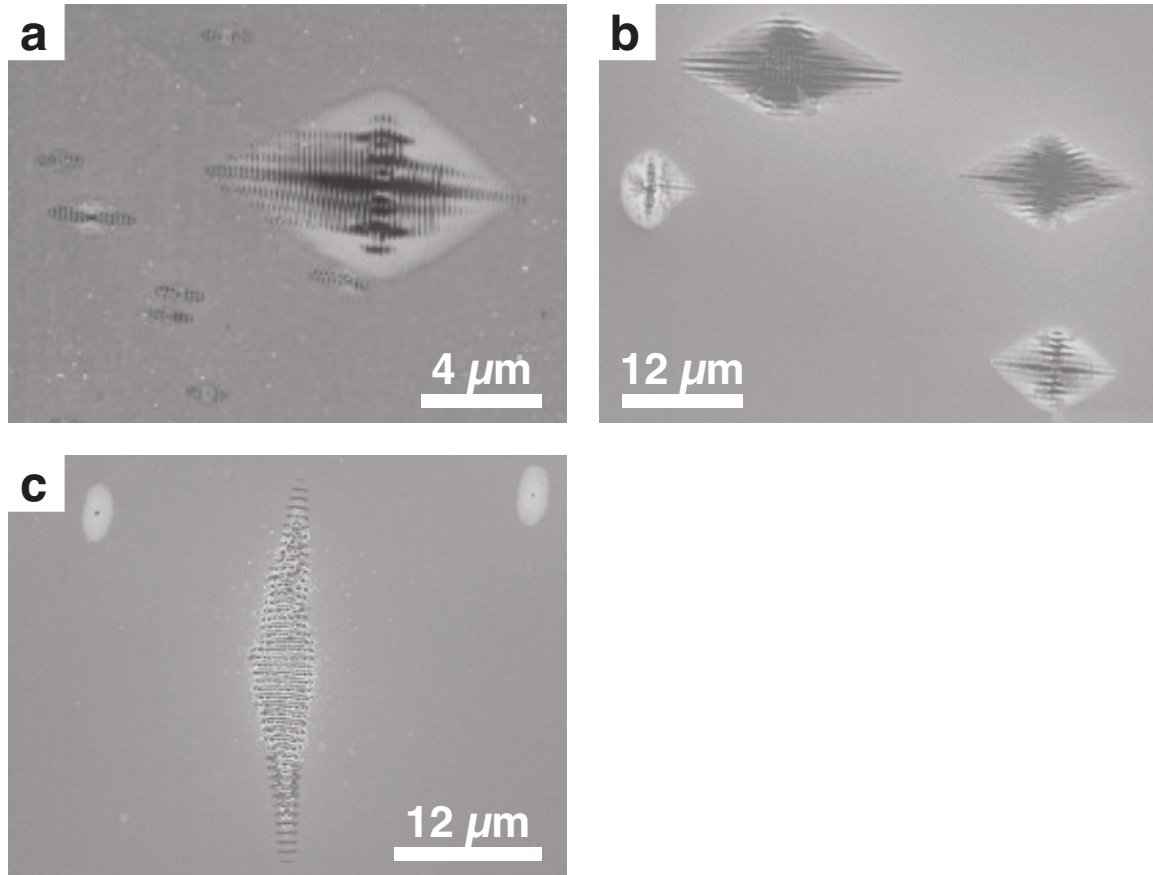


Figure 2.4.4: Initial formation of surface textures. Initial surface modification appears in sub-micrometer areas, apparently seeded by random surface defects (a and b). From these, high-frequency laser-induced periodic surface structures with period 200 nm form on the surface, with ripples extending parallel to laser polarization and propagating perpendicular to laser polarization. As these propagate, periodic surface structures with period 400 nm form, running perpendicular to laser polarization and propagating parallel to laser polarization. Once 400-nm surface structures form, they propagate rapidly in the direction of the laser polarization, forming an elongated strip of surface ripples (c). a: Random surface modification after 110 pulses, peak fluence 1.5 kJ/m<sup>2</sup>, 20 Torr N<sub>2</sub> gas. b: 150 pulses, 20 Torr N<sub>2</sub>. c: Textured strip in early stage of formation after 110 pulses, 20 Torr air.

With continued irradiation, the elongated strip of period surface ripples grows, primarily in the direction of laser polarization. For example, Figure 2.4.5 shows an elongated strip of ripples about width about 15 micrometers (perpendicular to laser

polarization) and height about 150 micrometers (parallel to laser polarization). The surface ripples typically extend uninterrupted across the entire width of the textured area. Figure 2.4.6 shows detail of another elongated strip of surface ripples.

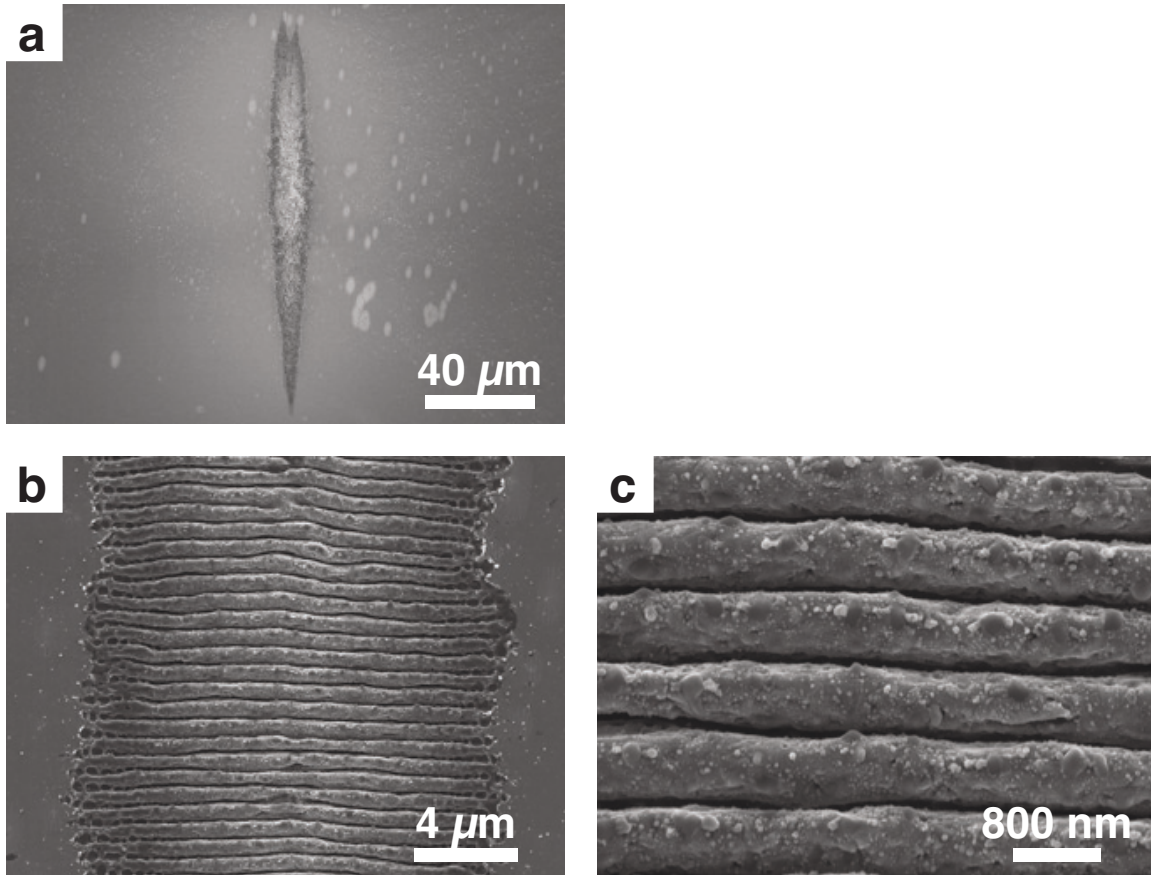


Figure 2.4.5: With continued irradiation, the strip of surface ripples grows primarily in the direction of the laser polarization (air, 140 pulses). The surface ripples typically extend uninterrupted across the entire width of the textured area. a: Textured area. b: Detail of texture. c: Close detail of texture.

With additional pulses, the elongated strips of surface ripples grow in width, and more strips form. As the strips merge together, an interconnected textured area forms which increasingly reflects the circular profile of the laser pulse as shown in Figure 2.4.7. Because the textured surface is formed by merging many individual



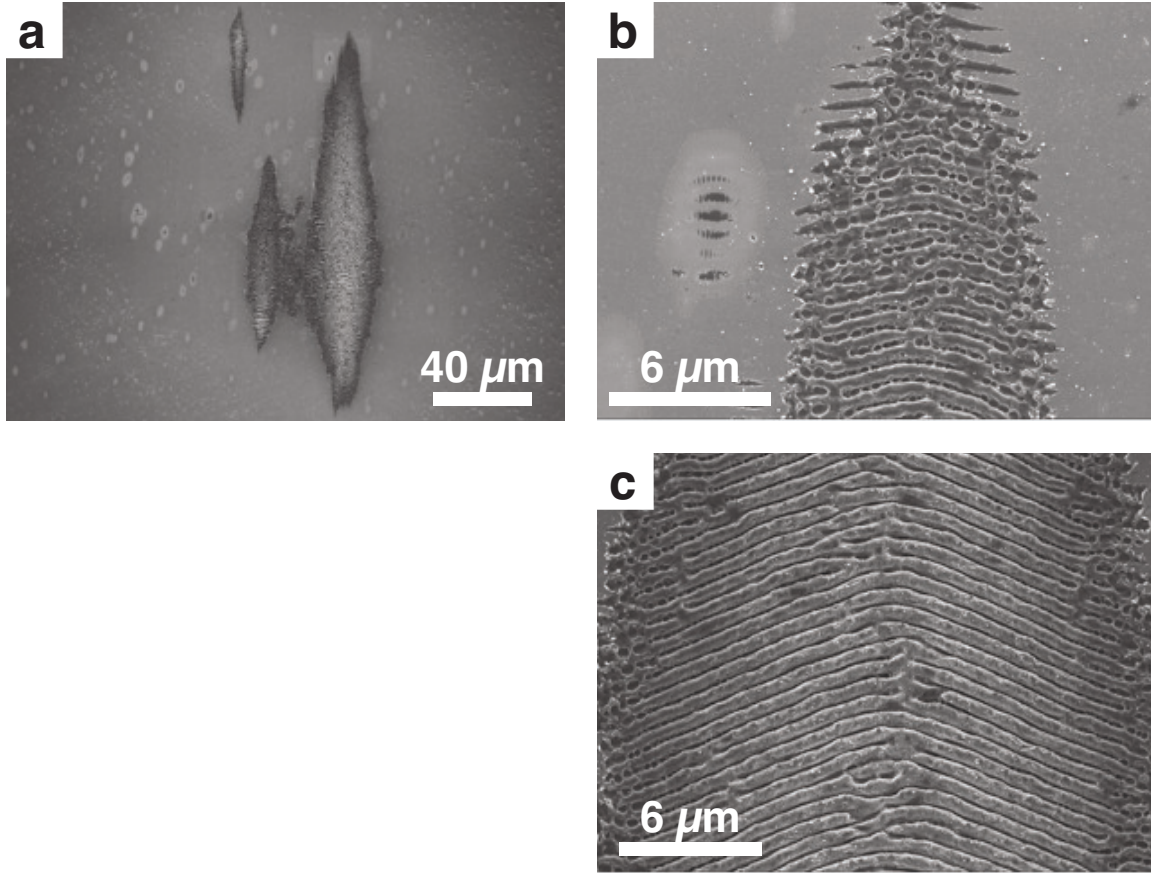


Figure 2.4.6: Area containing elongated strips of surface ripples. 120 pulses, 20 Torr air. a: Textured area. b: Detail of edge of textured area. c: Detail of central region of textured area.

strips of surface ripples, the resultant texture is also rippled, but the ripples merge and bifurcate to form a continuous network.

At the ends of each elongated area of surface ripples, additional periodic strips of melted silicon appear. These strips are separated by unmodified material. This unmodified material follows the same period and phase as the surface ripples, as shown in Figure 2.4.8.

In some of the elongated strips of surface ripples, a mound-like non-ripple structure was present in the center of the textured area, as shown in Figure 2.4.9.

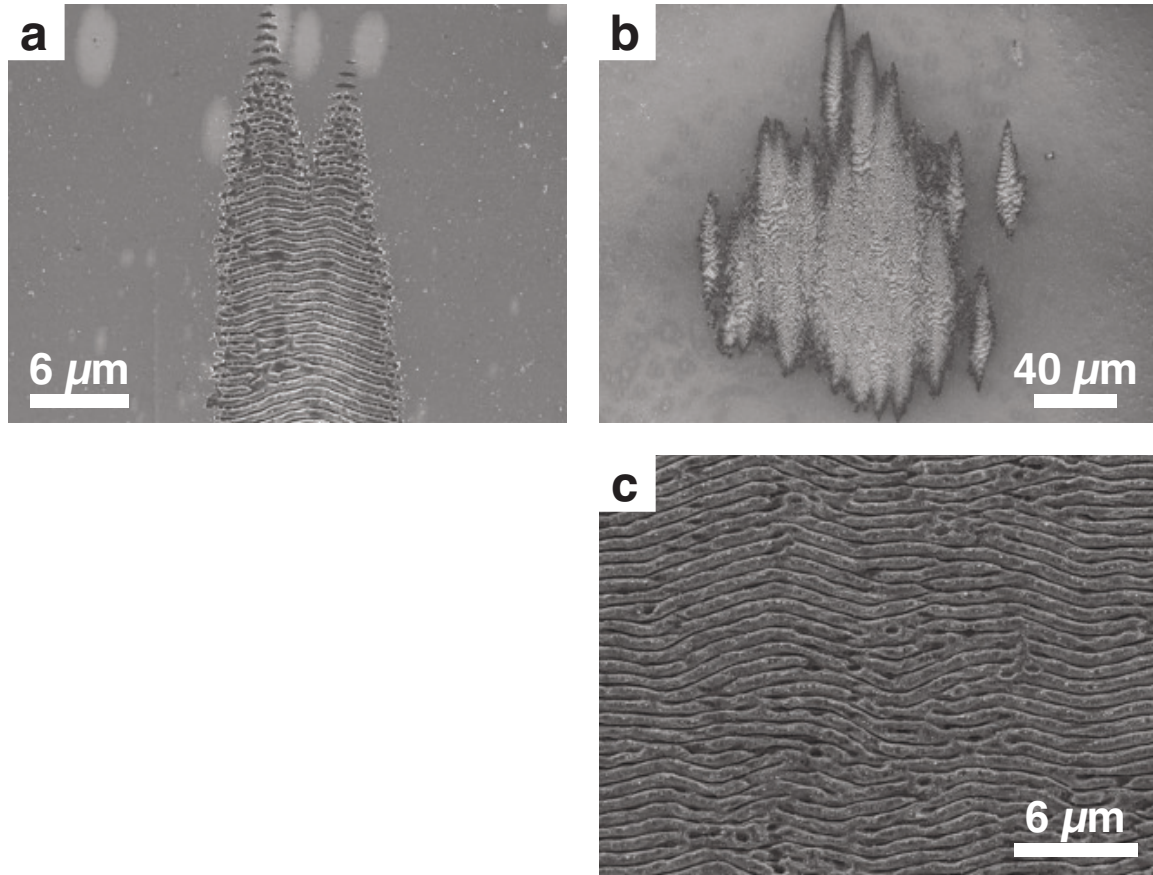


Figure 2.4.7: With additional pulses, the elongated strips of surface ripples grow in width, and more strips form. As the strips merge together, an interconnected textured area forms. a: Merging of two strips of surface ripples (140 pulses, air). b: Merging of many strips of surface ripples (150 pulses, air). c: Detail of central region of surface texture.

Raman spectroscopy showed amorphous silicon in the modified areas of the surface, including the areas with high-frequency laser-induced periodic surface structures (at the onset of surface modification) and areas near the edges of the elongated strips of surface ripples. Where the surface ripples are fully formed, however, only low levels of amorphous silicon were detected. Figure 2.4.10 shows maps indicating the location of the amorphous silicon on the surface as detected by Raman.

Fragments of silicon were found frequently near the textured areas. These frag-

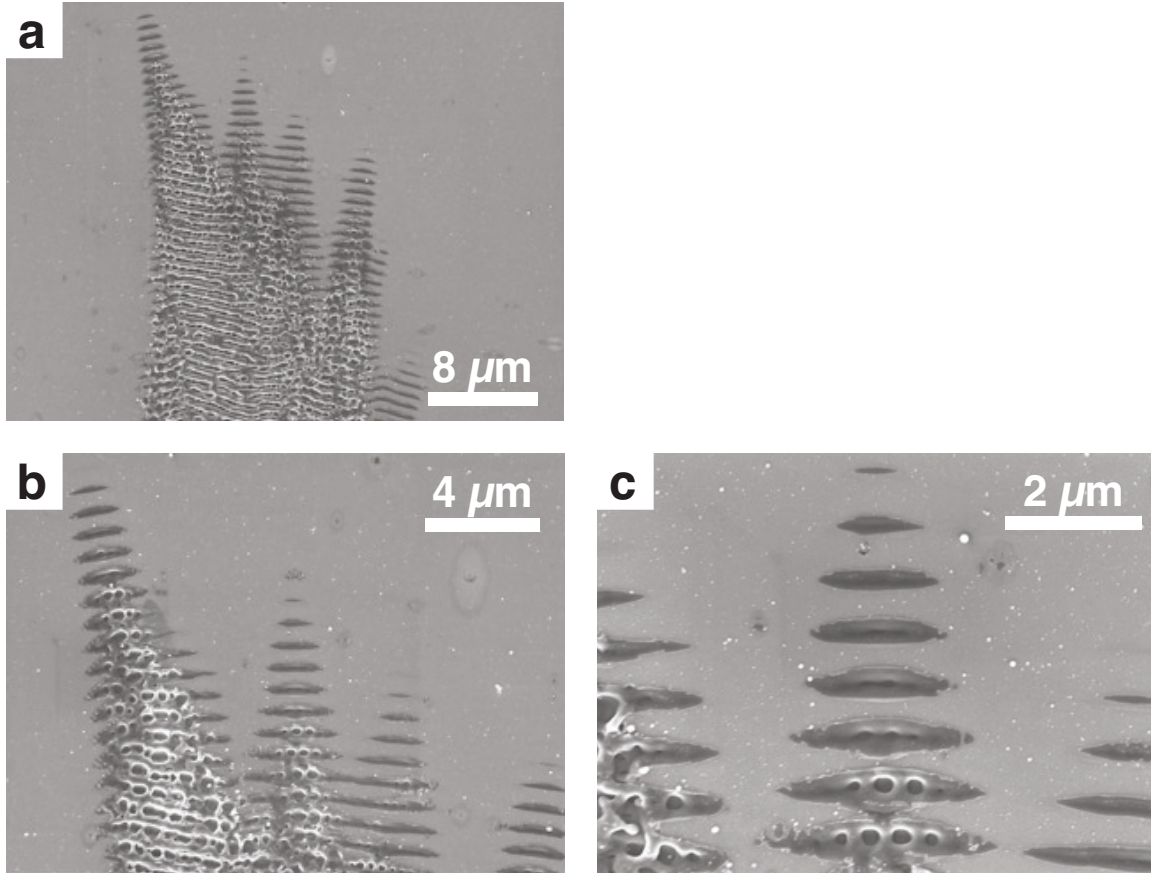


Figure 2.4.8: Example of melted strips of silicon extending from ends of textured areas. 20 Torr N<sub>2</sub>, 190 pulses. a: Ends of textured area. b: Detail. c: Close detail.

ments exhibited morphologies indicating high amounts of strain, such as plastic deformation and slip planes, as shown in Figure 2.4.11. Some of the debris appeared to degrade under the scanning electron beam during imaging; this debris exhibited highly deformed morphologies unusual for silicon; examples of such debris are shown in Figure 2.4.12.

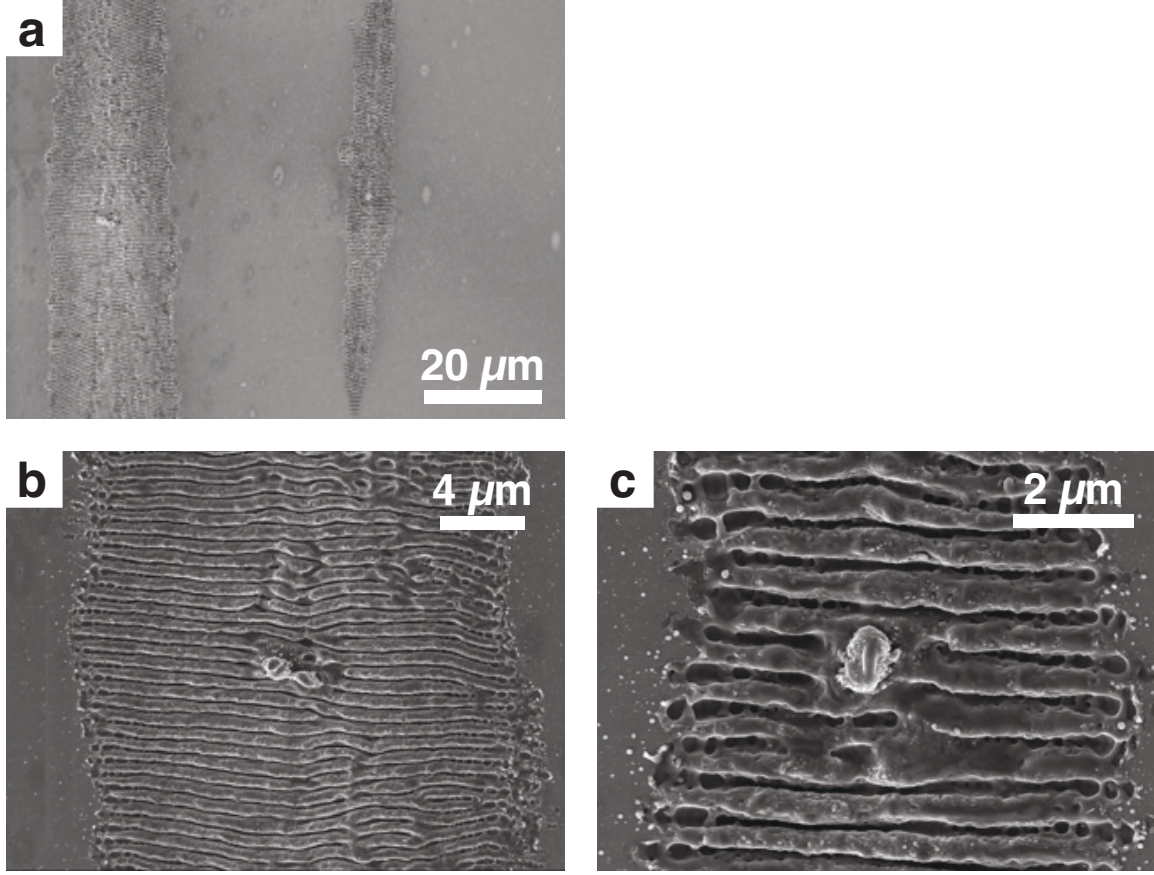


Figure 2.4.9: Mound-like structures present at the center of elongated strips of surface ripples. 190 pulses in 20 Torr N<sub>2</sub> gas. a: Textured area showing two elongated strips. b: Detail of left elongated strip. c: Detail of right elongated strip.

#### 2.4.4 Discussion

In this section, we are able to observe the initiation of ripple formation. First, small modifications of the surface occur over sub-micrometer areas without texturing, as shown in Figure 2.4.4. Because these modifications show the presence of amorphous silicon, we can infer that these are isolated areas of melting and resolidification. These modified areas appear randomly on the surface, indicating that they are seeded by random structural or morphological defects on the surface that experience enhanced



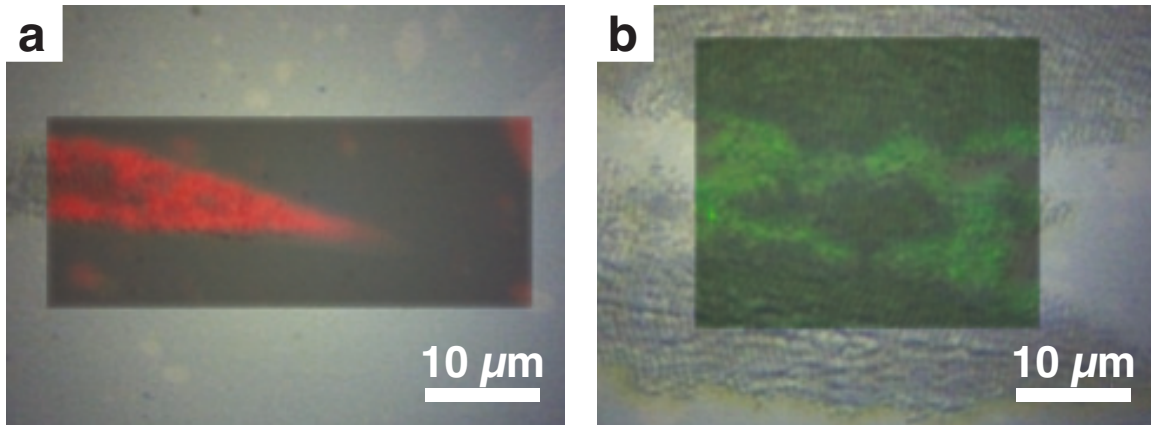


Figure 2.4.10: Maps showing the location of amorphous silicon on the surface, as detected by Raman spectroscopy. Colored areas show presence of amorphous silicon. a: 150 pulses in 20 Torr  $N_2$  gas. b: 120 pulses in 20 Torr air.

heating or depressed melting points [57]. Once these modified areas form, high-frequency laser-induced periodic surface structures appear with a period of about 200 nm. Unlike the larger ripples that form the surface texture, these periodic structures extend parallel to the laser polarization and propagate in a direction perpendicular to the laser polarization. It is possible that these are produced by interference between the incoming 800 nm laser pulse with 400 nm light produced by second harmonic generation at the surface [58,59]. Because these high-frequency laser-induced periodic

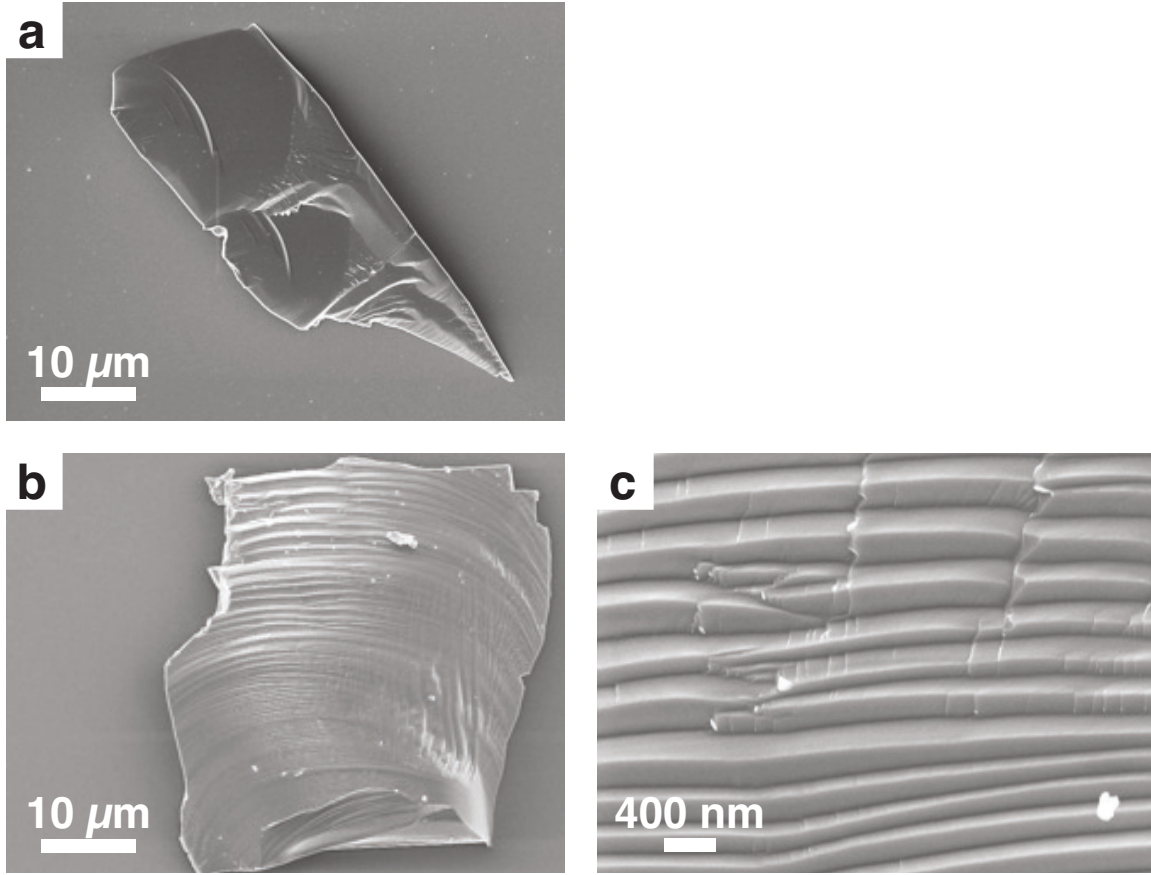


Figure 2.4.11: Examples of debris near texturing sites with morphologies suggesting high strain. a: 110 pulses in 20 Torr N<sub>2</sub>. b: 160 pulses in 760 Torr air. c: Detail of (b).

surface structures appear to be confined to the very top surface of the silicon (e.g., within the top  $\sim 10$  nm), it is possible that the surface oxide plays a role in their generation.

After the initial modification of the surface, deeper melting occurs in the modified area in strips separated by unmelted silicon with a period of about 400 nm. These strips extend perpendicular to the laser polarization and propagate in the direction of the laser polarization. These laser-induced periodic surface structures may be produced by surface plasmon polaritons from the fundamental frequency of the

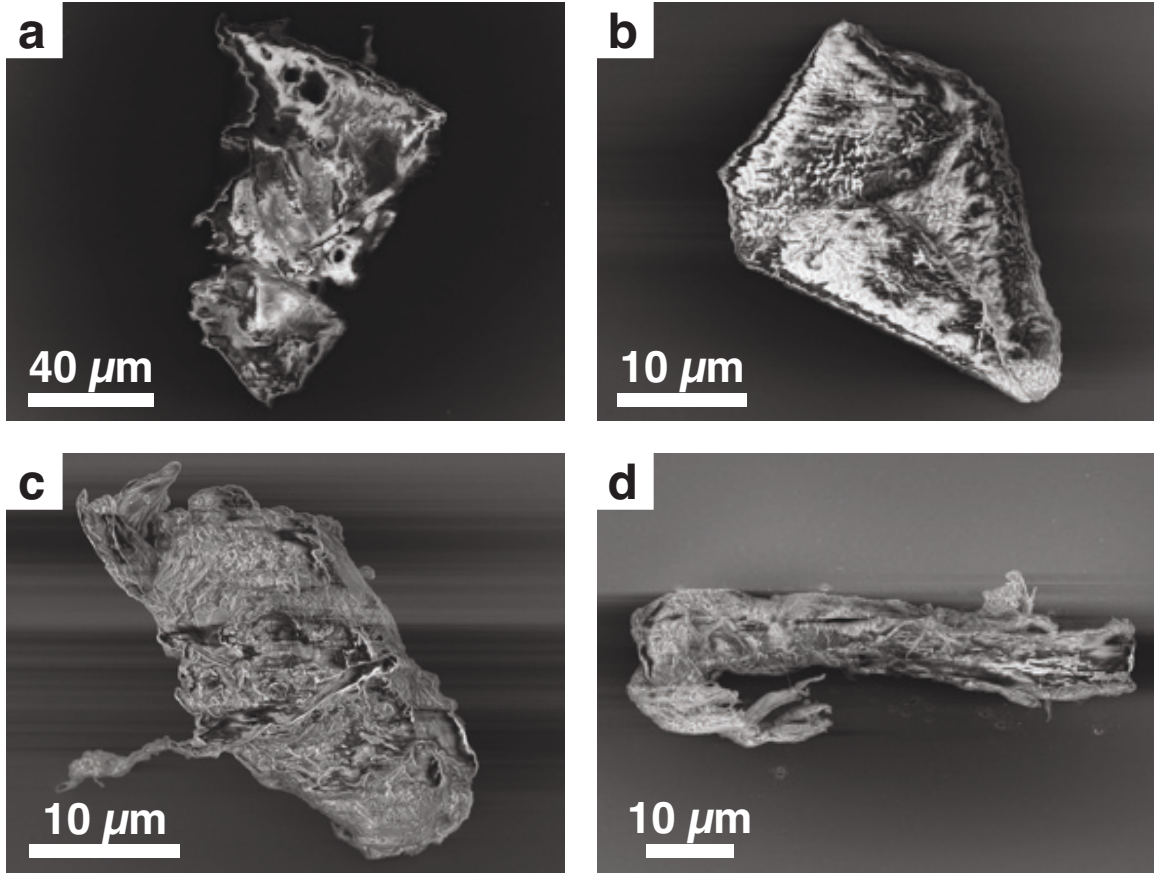


Figure 2.4.12: Examples of debris with unusual morphologies, which appeared to degrade under the scanning electron beam used for imaging. a: 120 pulses in 760 Torr air. b: 140 pulses in 760 Torr air. c and d: 130 pulses in 20 Torr air.

laser pulse (800 nm) seeded by the prior modification of the surface [60,61]. It appears that with successive laser pulses, material flows away from the melted strips to the areas between the strips, forming periodic ripples in the surface. Given that the surface ripples appear to be about 400 nm in depth and are formed after around 40 pulses after they are initiated (as estimated in Section 2.2), a change in surface roughness of only around 10 nm per melting event is required (the melt duration from fs laser irradiation on Si has been measured as around 5 ns [43]). As these ripples

form, successive pulses cause more melting between the ripples and the formation of additional melted strips in the direction of the laser polarization, as shown in Figure 2.4.8. The growth of the surface texture along the direction of the laser polarization is consistent with a surface plasmon polariton mechanism, because surface plasmon polaritons are launched primarily in the direction of the laser polarization [62]. With repeated laser pulses, the textured area grows rapidly in the direction of the laser polarization, forming elongated textured areas.

After strips of melted silicon are produced, what causes the mass transport necessary for ripple formation? Gradients in surface energy in the silicon melt could cause mass transport away from regions of low surface energy (the Marangoni effect). In the case of melted strips of silicon, two factors could contribute to mass transfer away from the melted strips through the Marangoni effect. The first is that the surface energy of silicon decreases with increasing temperature [63], so that the melted material will move away from the hottest region of the melt, which is presumably in the center of the melted strip (i.e., a thermo-capillary convection process). The second effect is that impurities can alter the surface energy of silicon as a function of impurity concentration. Both nitrogen and oxygen impurities decrease the surface energy of molten silicon at magnitudes that are similar to the effect of increased temperature [64, 65]. As the silicon surface becomes melted, impurity atoms enter the melt from the surrounding atmosphere. Upon subsequent melting the surface, previously melted regions will contain a relatively high concentration of impurities and thus a relatively low surface energy, leading to mass transport away from those regions. Thus, repeated melting would cause silicon to flow away from regions that



underwent melting earliest, which could correspond to molten strips produced by surface plasmon polaritons. Therefore, the reduction of surface energy with increasing temperature and with increasing impurity concentration both lead to mass transfer away from the molten periodic strips on the surface that are initially defined by surface plasmon polaritons. With repeated melting and resolidification, this process generates fully formed surface ripples.

Samples fabricated at 20 Torr and 760 Torr gas pressures exhibit some striking differences. First, the textured areas produced at 760 Torr are much larger than those produced at 20 Torr, and while textures produced at 760 Torr are present over the entire area of the laser pulse, textures produced at 20 Torr appear to propagate primarily in the direction of the laser polarization. Furthermore, while the surface morphologies produced at 20 Torr are similar for air, N<sub>2</sub>, and SF<sub>6</sub>, the morphologies produced in these gases at 760 Torr are considerably different. The effect of impurity concentration on surface energy again helps to explain some of these differences. At 760 Torr, significantly more impurity atoms are available to enter the silicon melt than at 20 Torr. This means that melting in general, even very shallow melting, will generate surface energy gradients from impurity concentration gradients produced by the infiltration of impurity atoms from the surrounding atmosphere. Once surface energy gradients are generated, irregularities in the surface morphology will be generated, as well, through the impurity Marangoni effect over repeated cycles of melting and resolidification. And once irregularities in the surface morphology are generated, surface plasmon polaritons can be generated, and the texture formation progresses through a feedback process.

On the other hand, at 20 Torr, fewer impurity atoms are available in the surrounding atmosphere. This means that the Marangoni effect is more dependent on thermal gradients rather than impurity gradients. Such thermal gradients can be produced by surface plasmon polaritons initiated by irregularities or defects on the surface. Such surface irregularities may be present randomly on the surface initially or may develop over many pulses, eventually allowing surface plasmon polaritons to be launched and texturing to be initiated. Indeed, some of the textured areas produced in 20 Torr gas show irregular mounds of material in their centers, presumably where the texturing process was initiated, as shown in Figure 2.4.9.

Thus, at low gas pressures we expect the Marangoni effect to be dependent on the presence of surface plasmon polaritons. Indeed, at low pressure (20 Torr), the textured areas, once initiated, grow rapidly in the direction of laser polarization but slowly in the orthogonal direction. (With continued irradiation, however, the textured areas eventually merge and form a roughly circular textured area.)

In addition to impurity concentration and temperature, surface energy is also affected by environmental gas pressure [66, 67]. However, we would not expect the environmental gas pressure to lead directly to a Marangoni effect, because the entire surface would be affected similarly, and the Marangoni effect requires surface energy gradients.

Surface morphologies between samples differ according to the type of gas at 760 Torr but not at 20 Torr. This also may reflect a distinction between polariton-driven texturing and impurity-driven texturing. At 20 Torr, the surface textures all consist of ripples that reflect the orientation and spacing of surface plasmon polaritons. At

760 Torr, however, air,  $N_2$ , and  $SF_6$  gas each produce distinct surface textures.

When mapping out the presence of amorphous silicon with Raman spectroscopy, we observe amorphous silicon at the onset of surface modification and near the edges of the textured areas, which is consistent with melting and rapid resolidification. Unexpectedly, however, the amorphous silicon signal decreases in the interior of the textured areas, where the surface ripples are well developed. One possibility is that after the surface ripples are formed, continued irradiation produces an annealing effect, increasing the crystallinity of the surface. Another possibility, however, is that structural defects are reduced through the inclusion of nitrogen atoms. Recently, it was reported that the crystallinity of fs-laser-textured silicon is increased by fabricating in nitrogen gas [48]. This effect of nitrogen atoms in silicon could also be responsible for the low amount of amorphous silicon we observed in fully formed surface ripples fabricated in air or nitrogen.

We now consider the silicon debris formed during irradiation. Two distinct kinds of debris were observed on the surface: silicon shards with crystallographic deformations, shown in Figure 2.4.11, and irregularly shaped debris that appeared to charge and deform under the electron beam used for electron microscope imaging, shown in Figure 2.4.12. The silicon shards show morphological features that resemble slip planes and other pressure-induced deformations. This is evidence that even in the absence of melting, fs laser irradiation can produce structural defects and high levels of strain in silicon. The accumulation of structural defects could be a mechanism for the initiation of melting and surface modification at local fluences below the single-pulse melting threshold. For example, hexagonal silicon, which is a direct-

bandgap semiconductor, has been reported at the intersection of twin boundaries in conventional cubic silicon. The debris objects observed in Figure 2.4.12 might be highly deformed, metastable forms of silicon, and their charging behavior indicates that they could be non-conducting. In the future, characterizing these debris objects could be an interesting area of study.

### **2.4.5 Conclusions**

In this section, we examined the onset of surface texture formation from the formation of scattered, sub-micrometer patches of melted material, to the production of high-frequency and conventional laser-induced periodic surface structures, to melting in periodic strips and the formation of surface ripples, to the propagation of surface ripples and growth of the textured area. The early stages of surface modification and the growth of textured areas along the direction of the laser polarization suggest that surface plasmon polaritons are responsible for the periodic structuring of the surface. We find that the initiation and growth of the surface textures are influenced heavily by the ambient gas pressure. We hypothesize that the formation of surface textures is driven by variations in surface energy and the resulting Marangoni effect. At low gas pressures, the Marangoni effect is driven by temperature gradients produced by surface plasmon polaritons, and the textured area grows primarily in the direction of surface plasmon polaritons propagation. At high gas pressures, the Marangoni effect is driven by impurity concentration gradients from ambient gas atoms entering the silicon melt, and the textured area grows in all directions within the irradiation area. At low gas pressures (e.g., 20 Torr), the texture morphology reflects the characteris-

tics of surface plasmon polaritons, regardless of the type of gas used in fabrication. At higher gas pressures, however (e.g., 760 Torr), the morphology of the surface texture is dependent on the type of gas used. When surface ripples are fully formed, they exhibit higher crystallinity than when they are initially formed, which may be due to thermal annealing or impurity annealing from nitrogen. During irradiation, silicon debris is produced, some of which shows evidence of no melting but high strain and structural defects, such as slip planes, and some of which appears to be unstable under the electron beam used for microscope imaging. Our observations in this section provide an explanation for periodic surface texturing, beginning with random patches of melting on the surface from surface defects and ending with an extended, interconnected area of fully formed surface ripples.

## **2.5 Fabrication with scanned pulses**

### **2.5.1 Introduction**

In Sections 2.2–2.4, we examined samples produced with stationary pulses. Here, we examine samples produced with scanned pulses. Just as with stationary pulse samples, for scanned pulse samples we use the metrics of fluence and pulse number—although these variables have more complicated definitions for scanned pulse samples than for stationary pulse samples. Scanned pulses and stationary pulses with the same fluence and pulse number parameters produce different texturing effects on the silicon surface. However, the understanding of texturing developed for stationary pulses still holds for scanned pulses. In this section, we show that the apparent

differences between stationary and scanned pulses are due to how fluence and pulse number are defined for each case.

When rastering laser pulses over an area to fabricate hyperdoped black silicon, pulse fluence and pulse number are representative metrics that describe the irradiation conditions in an approximate but not exact sense. The first approximation comes from expressing the fluence of a Gaussian pulse. Because the intensity profile of the pulse is not uniform but Gaussian, the effective fluence experienced by an irradiated spot on the sample surface depends on its distance from the center of the pulse. To approximate the fluence of a pulse, we approximate the pulse diameter as the width at  $1/e$  of the maximum intensity (denoted FW1/eM), rather than the commonly used full-width at half of the maximum intensity (denoted FWHM). This method results in a fluence value that is the same as the peak fluence  $F_0$  of the pulse (the effective fluence at the center of the pulse). The second approximation comes from expressing the number of pulses a spot on the surface is exposed to, called the pulse number or shots per area (s/a) [5]. For this, a threshold is chosen of half the peak fluence, so that, for example, a shots/area of 10 indicates each spot on the surface is exposed about 10 times to local fluences in the range between  $F_0/2$  and  $F_0$ . The number of times a spot is exposed to a fluence of, say,  $F_0/4$  is not reported. For a fuller mathematical discussion of pulse fluence and pulse number, see past work by Sher [14] or Smith et al. [5].

By reporting the parameters of fluence and pulse number, the irradiation conditions can be described economically, avoiding the need to report pulse diameter, pulse separation, scanning speed, or repetition rate. However, the fluence and pulse

number do not capture all of the information relevant for fabrication, such as the distribution of fluence exposures for a spot on the surface [5], and the separation of pulses on the surface, which may be relevant for understanding inhomogeneities on the surface such as patches of amorphous silicon.

Even if the two metrics of fluence and pulse number do not capture the irradiation conditions entirely, they condense those conditions into a manageable parameter space. In practice, fluence values for hyperdoped black silicon fabrication can vary from about 1.5–10 kJ/m<sup>2</sup>, and pulse number values typically vary from about 1–1000 pulses. This leaves a significant parameter space to investigate, which can consume a significant amount of experimental time and resources.

Large areas of hyperdoped black silicon are fabricated by scanning a pulsed ultrafast laser (e.g., a fs laser) beam across a silicon surface in the presence of a dopant. The scanning process can be accomplished by translating the sample stage using programmable stepper motors. However, the slow speed of the stepper motors often requires low laser pulse repetition rates in order to obtain the desired number of pulses on the surface. For example, a 1 cm<sup>2</sup> sample with pulse separation of 10 micrometers requires 10<sup>6</sup> pulses, which, at a pulse repetition rate of 100 Hz, requires 10<sup>4</sup> seconds or about three hours of laser scanning time.

In this section, we use a high-throughput fabrication system to reduce the fabrication time, making it feasible to explore the parameter space of hyperdoped black silicon experimentally. We map the parameter space according to the texture produced, and we quantitatively connect the observed threshold for texturing with scanned pulses with results obtained from stationary pulses.

## 2.5.2 Methods

For hyperdoped black silicon fabrication, we use a set of programmable galvanic mirrors to scan the laser pulse across the surface, obviating the need for translation of the sample by stepper motors. Otherwise, the fabrication process follows the methods described in previous theses [1, 14, 68]. The laser pulse train is passed through a focusing lens immediately before entering the scanning mirror system, after which it reflects off of a large mirror, through the sample chamber window, and into the sample chamber, as shown in Figure 2.5.1.

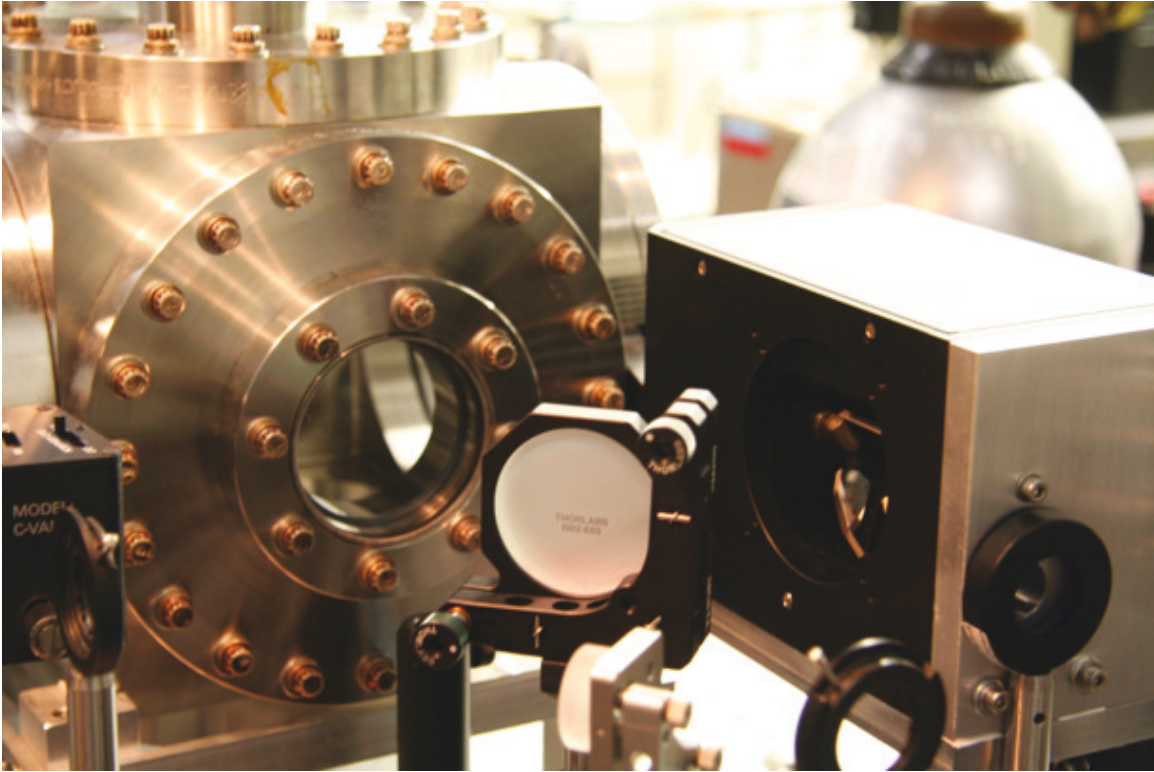


Figure 2.5.1: Galvanic scanning mirror system used for high-throughput fabrication. The laser pulse train is passed through a focusing lens into the mirror system (right), reflected to a large mirror (center), and reflected through the sample chamber window and into the sample chamber (left).

To survey the fabrication parameter space, a grid of  $3 \times 3 \text{ mm}^2$  samples were



fabricated with 800 nm fs laser pulses fluences of 1.6–3.8 kJ/m<sup>2</sup> (in 0.2 kJ/m<sup>2</sup> increments) and shots/area values of 5–200 (5, 15, 30, 50, 100, and 200 shots/area), for a total of 72 unique samples. The samples were fabricated in the presence of 500 Torr SF<sub>6</sub> gas and with a pulse diameter of 1 micrometer. The range of surface morphologies produced was investigated using optical and electron microscopy.

### **2.5.3 Results**

The scanning mirrors are capable of scanning the laser beam across the sample much faster than are the stepper motors (around 10 m/s vs. around 1 mm/s, respectively), allowing the maximum laser pulse repetition rate available in the fabrication system (1 kHz) to be used. This decreased the sample fabrication time by a factor of 1–2 orders of magnitude. The samples fabricated using the scanning mirrors appeared to be comparable to those fabricated using the stepper motors, with no effects observed from non-normal pulse incidence or the resulting small changes in focusing-lens-to-sample distance (and thus fluence).

The parameter space investigated produced a range of surface types, includes traditional hyperdoped black silicon (which is highly antireflective and appears black to the eye), textured silicon that is more optically reflective (which appears orange to the eye), and untextured silicon (which has a faint pink hue to the eye). We call these representative types of laser-irradiated silicon black silicon, orange silicon, and pink silicon for brevity. Black silicon is produced at high fluences and/or shots/area, orange silicon at lower fluences and shots/area, and pink silicon at even lower fluences and/or shots/area. Figure 2.5.2 shows the appearance of all 72 samples to the eye.

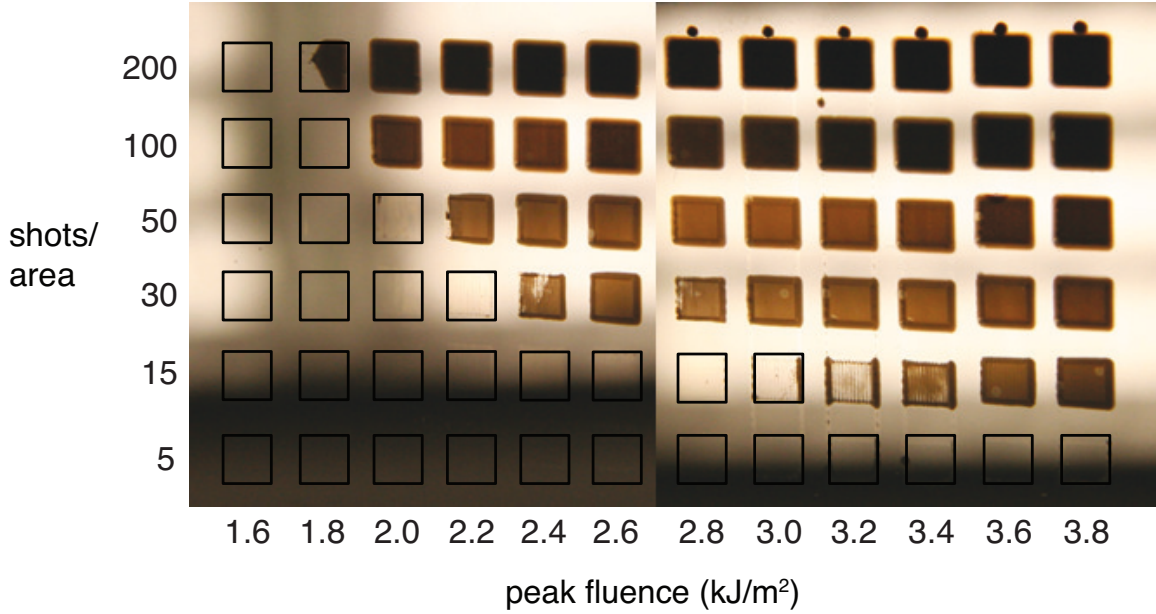


Figure 2.5.2: 72 samples showing the fluence and pulse number parameter space investigated in this section. Samples that remain untextured are not easily visible by eye and are outlined.

Both fluence and shots/area were important in determining whether pink, orange, or black silicon was fabricated by the irradiation process. Pink silicon was fabricated even at high fluence when low pulse number was used (e.g.,  $3.8 \text{ kJ/m}^2$  and 5 shots/area) and even at high pulse number when low fluence was used ( $1.6 \text{ kJ/m}^2$  and 200 shots/area). However, in both of these regions of the parameter space, the transition to black silicon (with increased pulse number or fluence, respectively) was abrupt. Orange silicon was fabricated when both fluence and pulse number were moderate (e.g.,  $2.2\text{--}3.4 \text{ kJ/m}^2$  and 30–50 shots/area). Thus, in fabricating pink, orange, or black silicon, there is some interaction between the the fluence and shots/area parameters in determining the texture.

Black, orange, and pink silicon showed significantly different surface morphologies. Black silicon is characterized by conical surface structures at least 1 micrometer

in size, orange silicon shows surface ripples less than 1 micrometer in size (here 400 nm in period), and pink silicon has a surface that is essentially flat, with some variation in surface structure (e.g., material phase or density) visible. In some of the black silicon surfaces, large spikes (around 10 micrometers in size) were interspersed among smaller spikes. Figure 2.5.3 shows representative images of these surface morphologies.

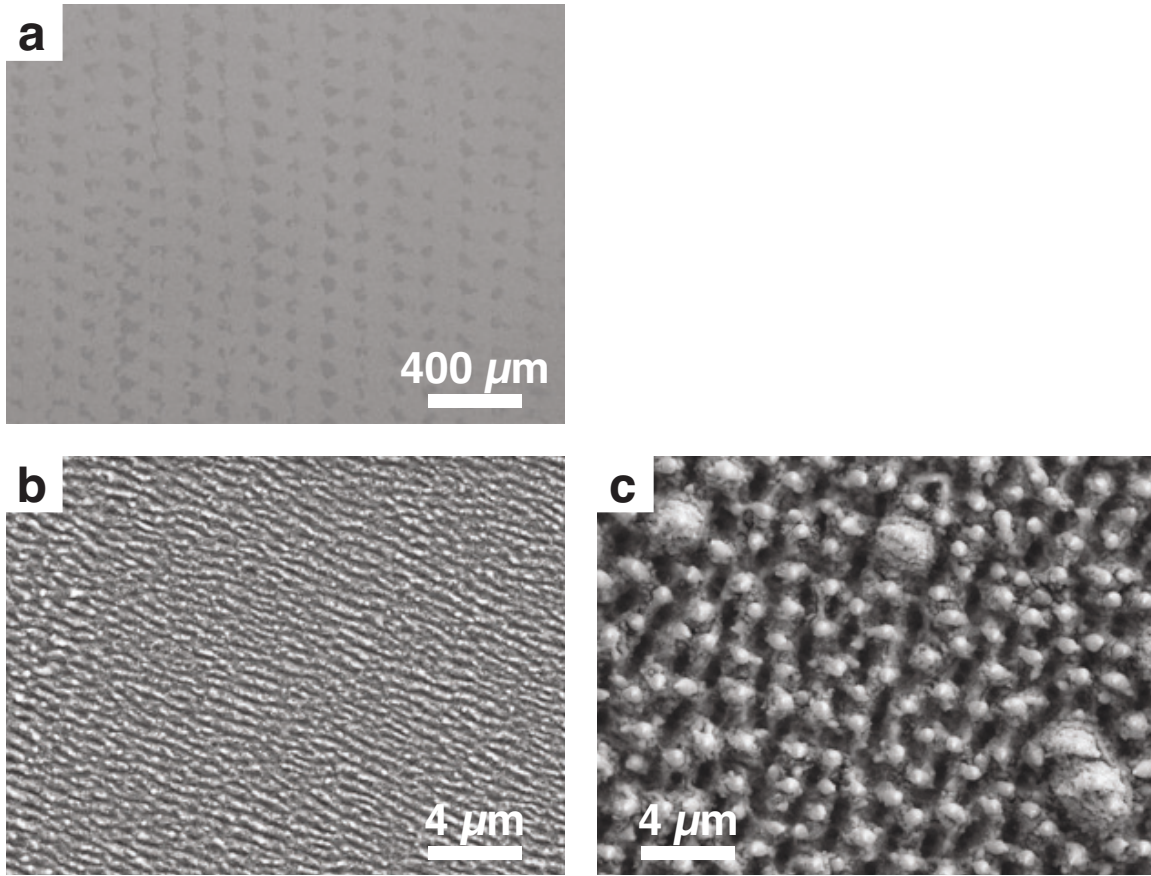


Figure 2.5.3: Electron microscope images of pink, orange, and black silicon (a, b, and c, respectively). Irradiation parameters were 2.2 kJ/m<sup>2</sup> and 15 shots/area, 2.8 kJ/m<sup>2</sup> and 30 shots/area, and 3.6 kJ/m<sup>2</sup> and 200 shots/area, respectively.

## 2.5.4 Discussion

In general, black silicon is produced at high fluence and pulse number, orange silicon at moderate fluence and pulse number, and pink silicon at low fluence and pulse number. However, to fabricate orange silicon, it appears that both fluence and pulse number must be moderate, because if either fluence or pulse number is high, then the transition from pink silicon to black silicon is sharp.

We can use the boundaries observed in the parameter space between pink, orange, and black silicon to model the fluence and shots/area requirements for fabricating a desired surface. The number of pulses  $P$  required to fabricate orange silicon reduces with increasing fluence  $F$ . A linear fit to the observed thresholds in the range 2.2–3.6 kJ/m<sup>2</sup> is:

$$P = 96 - 23F$$

(with R-squared of 0.90 and  $F$  in units of kJ/m<sup>2</sup>). Thus, we see that orange silicon can be fabricated when the number of pulses is around 10–50. For example, when  $F = 3.0$  kJ/m<sup>2</sup>, we expect 30 pulses to be the lower threshold for orange silicon fabrication, which is what we observe experimentally. We can also examine the total laser irradiation dose required to make orange silicon, where the dose  $D$  is the product of the pulse fluence and the pulse number. The total required dose for texturing decreases with increasing fluence, with a linear fit to the observed thresholds giving:

$$D = 184 - 37F$$

(with R-squared of 0.90,  $F$  in units of kJ/m<sup>2</sup>, and  $D$  in units of kJ/m<sup>2</sup>\*(shots/area)).

For black silicon, we can find a similar linear model for the fabrication require-

ments, with:

$$P = 243 - 59F$$

(with R-squared of 0.98). If  $F = 3.0 \text{ kJ/m}^2$ , for example, we expect 66 pulses to be the lower threshold for black silicon fabrication, which is consistent with our results (black silicon observed with 100 pulses, but not with 50 pulses). Similar to orange silicon, we find that the total dose required for fabrication decreases with increasing fluence, with a linear fit to the observed giving:

$$D = 537 - 119F$$

(with R-squared of 0.86).

Evidence of a feedback process during laser fabrication is present in the reduction in required irradiation dose with increasing fluence, because we expect feedback processes to be stronger at higher fluences. Interestingly, if we model how the required dose scales with the square of the fluence, we obtain:

$$D = 660 - 1.1F^2$$

for black silicon and:

$$D = 294 - 29F^2$$

for orange silicon. Especially for the black silicon threshold, the total dose is approximately constant with the square of the fluence. This could reflect the fact that a higher fluence melts and ablates more material than a lower fluence does, and also that it leaves behind a rougher surface morphology, enhancing the effect of the next pulse. Thus, the texturing process may rely upon a positive feedback process that goes as the square of the fluence.

The pulse number window for fabricating orange silicon is only tens of pulses at moderate fluences and decreases at lower fluences. For example, at a fluence of  $3.0 \text{ kJ/m}^2$ , we can fabricate orange silicon using 30–70 pulses (at higher pulse numbers, black silicon is fabricated). However, at a higher fluence of  $3.8 \text{ kJ/m}^2$ , we predict a lower threshold for orange silicon at only 9 pulses and a lower threshold for black silicon at 19 pulses—a sharp transition. Our analysis predicts that the pulse number window for fabricating orange silicon is wider at lower fluences, which is what we observe. In the fluence range of  $2.2\text{--}3.6 \text{ kJ/m}^2$ , our heuristic model is reasonably accurate in predicting the irradiation conditions necessary to fabricate orange and black silicon. Our experimental survey and model appear to capture the entire parameter space over which orange silicon can be fabricated using fs laser irradiation.

We can use our results from stationary pulse experiments to predict the onset of texturing for scanned pulse samples with very good accuracy. In Section 2.3, we predicted that for a local fluence of  $1.6 \text{ kJ/m}^2$  (above the single-pulse melting threshold), texturing would be initiated after 10–20 pulses. Texturing at fluences lower than this requires many more pulses (e.g., initiating texturing at  $1.5 \text{ kJ/m}^2$  requires around 60 pulses, and initiating texturing at  $1.4 \text{ kJ/m}^2$  requires around 300 pulses). For each sample fabricated with scanned laser pulses, we can simulate how many times a spot on the sample experiences a local fluence greater than  $1.6 \text{ kJ/m}^2$ , as shown in Figure 2.5.4.

We now consider what pulse number is required at each peak fluence for a spot on the sample to experience 15 pulses (about  $10^{1.1}\text{--}10^{1.1}$  pulses) with a local

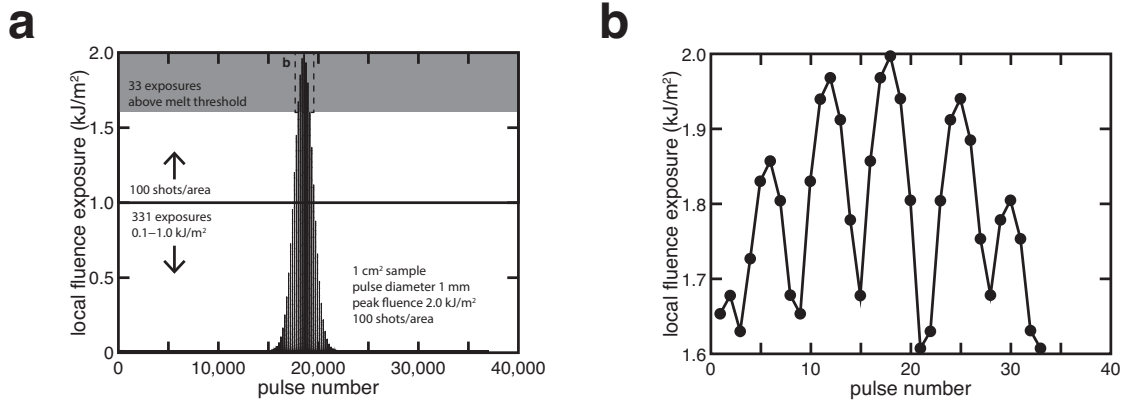


Figure 2.5.4: a: Simulation of local fluences experienced by a spot on the sample irradiated with scanned pulses with a peak fluence of  $2 \text{ kJ/m}^2$  and 100 shots/area. b: The simulation shows that the sample spot experiences only 33 pulses above the melting threshold of  $1.6 \text{ kJ/m}^2$ .

fluence of  $1.6 \text{ kJ/m}^2$  or greater; in Section 2.3, we predicted that this would be the approximate onset of surface texturing for pulses above the melting threshold. This many melting and resolidification events might be necessary in order to achieve the mass transfer necessary for texture formation. In Figure 2.5.5, we see the simulated texturing threshold (15 pulses above a local fluence of  $1.6 \text{ kJ/m}^2$ ) plotted as a function of pulse number and fluence. This simulated threshold agrees remarkably well with the observed threshold between untextured and textured silicon in the parameter space we investigated. We also plot the observed linear threshold between orange (textured) silicon and black (highly textured) silicon.

Figure 2.5.5 can be interpreted as a phase diagram for pink, orange, and black silicon fabrication. The onset of texturing appears to be determined by a minimum number of 10–20 melting and resolidification events, after which orange (textured) silicon forms. With continued irradiation, black silicon eventually forms. Recall that the total irradiation dose required to produce black silicon is approximately constant

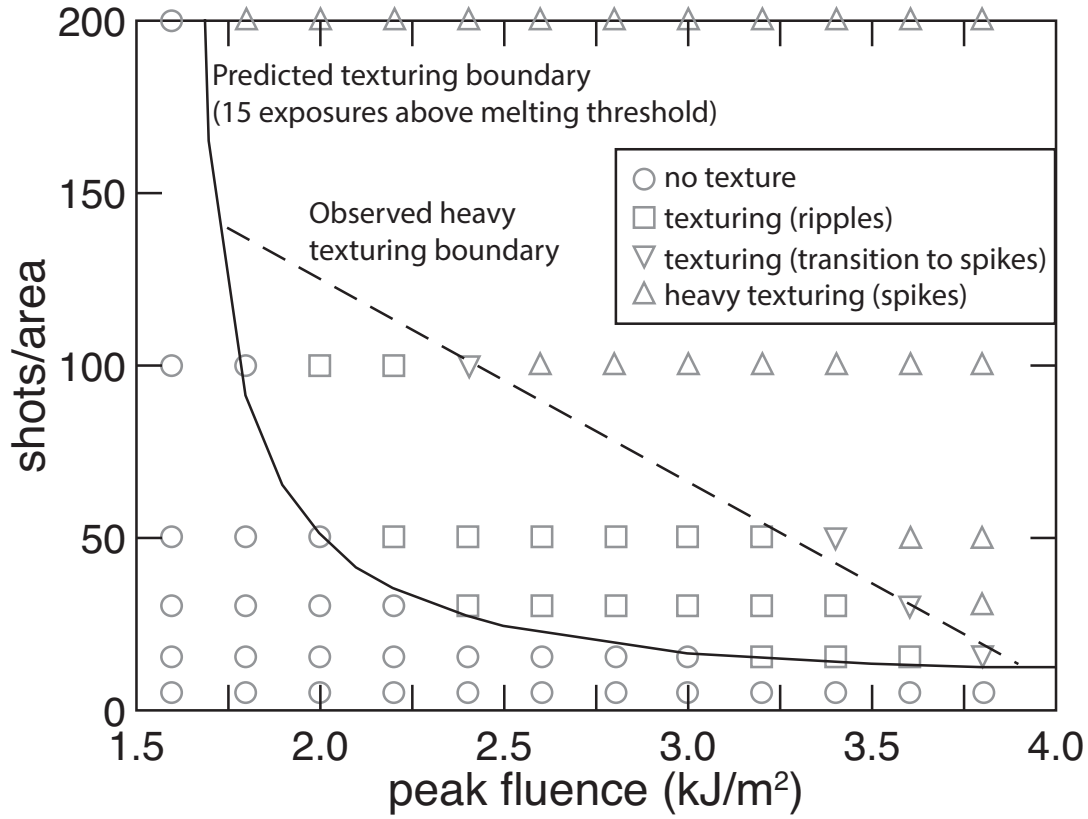


Figure 2.5.5: Fabrication phase diagram showing observed pink (no texture), orange (rippled texture), and black silicon (spiked texture) as a function of fluence (kJ/m<sup>2</sup>) and pulse number. The transition between pink and orange silicon is simulated by considering how many pulses are required at each peak fluence in order to obtain 15 exposures at local fluence of 1.6 kJ/m<sup>2</sup> or greater. The transition between orange and black silicon is a linear fit to the observed thresholds at various fabrication parameter values.

with the square of the laser fluence, indicating that black silicon is produced efficiently at high fluences, almost immediately after the onset of texturing. As the fluence decreases toward the single-pulse melting threshold, the number of pulses required to melt the surface 10–20 times grows very rapidly, and texturing again forms as black silicon rather than orange silicon. In sum, to produce orange silicon, the irradiation conditions must be such that the minimum melting condition is achieved for a pristine



surface but the irradiation dose required to produce black silicon is avoided. This can be achieved only within a limited parameter space, and is most easily achieved with peak fluences of 2–3 kJ/m<sup>2</sup>, as indicated by Figure 2.5.5. Because SF<sub>6</sub> assists in the fabrication of black silicon, we expect that the threshold line between orange and black silicon would shift to higher or lower pulse numbers as the SF<sub>6</sub> gas pressure is reduced or increased. It is interesting to note that the presence of SF<sub>6</sub> apparently does not affect the irradiation conditions necessary for the initial onset of texturing.

We can draw a few insights for fabrication from these results. First, the fabrication of orange silicon is possible only within a relatively small region in the fluence and pulse number parameter space. Second, the transition from pink to black silicon at low and high fluences is mostly direct, with little transition through an orange silicon surface. Third, the total dose required to fabricate black silicon decreases with increasing fluence and is constant with the square of the fluence, so that doubling the fluence decreases the number of pulses required by a factor of about four. This may be important in order to fabricate black silicon using the lowest number of pulses possible (e.g., to increase throughput).

### **2.5.5 Conclusions**

In this section, we used a scanning mirror system to increase the throughput of our laser processing system. This made feasible an experimental survey of the major fabrication parameters—fluence and shots/area. By surveying the parameter space with fluences of 1.6–3.8 kJ/m<sup>2</sup> and 5–200 pulses, we observed the region over which orange silicon (silicon textured with parallel, sub-micrometer ripples) can be fabricated. We

observed boundaries in parameter space between pink (flat) silicon, orange silicon, and black silicon. The boundary between pink and orange silicon can be predicted using the condition that the surface must be melted about 15 times for ripples to be formed, which is consistent with stationary pulse results contained in Section 2.3. The presence of  $\text{SF}_6$ , which is important for producing black silicon at these irradiation parameters, does not apparently affect the irradiation conditions necessary for initial texturing. The boundary between orange and black silicon can be modeled as a linear boundary in phase space based on observed thresholds. We used these predicted and observed boundaries to produce a phase diagram for laser texturing of silicon (treating pink, orange, and black silicon as phases), which can be useful for future fabrication. We found that orange silicon can only be fabricated using moderate fluences and pulse numbers, with low and high fluences not yielding orange silicon. We found that the total laser dose required to fabricate orange and black silicon decreases with increasing fluence, indicating the presence of feedback mechanisms in texturing, and that for black silicon, the total required dose is approximately constant with the square of the fluence, so that doubling the fluence decreases the required number of pulses by a factor of about four. These insights can guide future fabrication of laser-doped and -textured silicon in this parameter range.

## **2.6 Low-fluence fabrication with selenium thin films**

### **2.6.1 Introduction**

In Sections 2.2 and 2.3, we saw that texturing of silicon could be achieved using low fluences and many pulses, with fluences below the melting threshold requiring hundreds or thousands of pulses to modify silicon. In this section, we again investigate fluences at and below the melting threshold, but here using a selenium (Se) thin film. We find that using a thin film, it is possible to texture and dope the silicon surface with fluences far below the melting threshold, and we observe very small (150-nm) surface ripples that appear to be silicon hyperdoped with selenium.

### **2.6.2 Methods**

A silicon wafer was coated in a 80-nm thin film of Se by thermal evaporation. 800 nm fs laser pulses were then scanned across the sample. Five  $1\text{ cm}^2$  samples were fabricated using fluences of  $1.5\text{ kJ/m}^2$  (100 shots/area),  $1.0\text{ kJ/m}^2$  (100 and 1000 shots/area), and  $0.8\text{ kJ/m}^2$  (1000 and 5000 shots/area). The pulse diameter was 990x860 micrometers and the pulse repetition rate was 1 kHz. The samples were irradiated in an atmosphere of 500 Torr  $\text{N}_2$  in order to prevent debris from coating the chamber walls.

The surface textures present on the resulting samples were characterized using scanning electron microscopy, and optical absorptance was measured using an UV-VIS-NIR spectrophotometer with an integrating sphere.

### 2.6.3 Results

To achieve uniform coverage of the silicon wafer with the Se thin film, a minimum thin film thickness was required. A 20-nm thin film of Se did not wet the silicon surface but showed beading, as shown in Figure 2.6.1 [20]. The 80-nm thin film used for fabrication completely covered the surface, although some surface variations ( $<100$  nm in area) were visible.

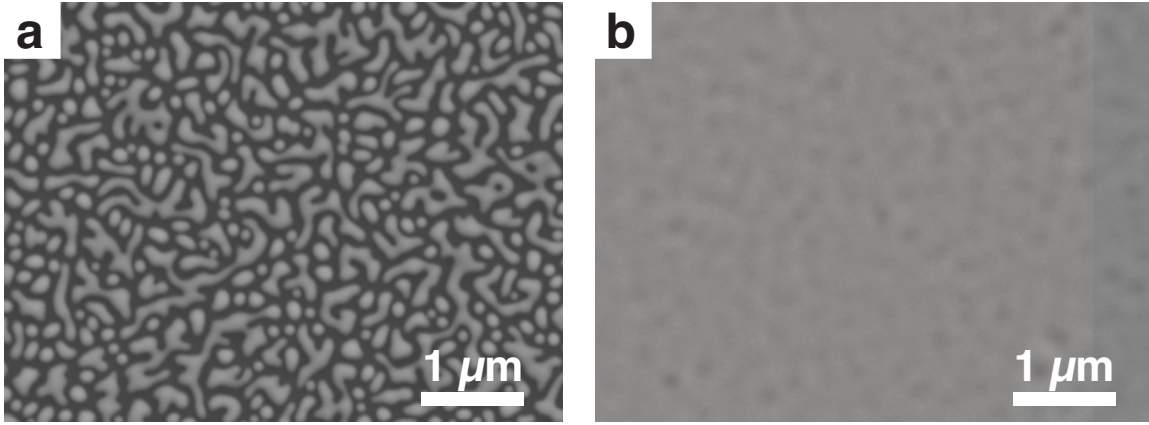


Figure 2.6.1: Se thin films on silicon. a: 20 nm thin film shows beading. b: 80-nm thin film covers surface entirely.

We report the surface morphologies of our samples first at a fluence of  $1.5 \text{ kJ/m}^2$  and then at progressively lower fluences down to  $0.8 \text{ kJ/m}^2$ . With  $1.5 \text{ kJ/m}^2$  and 100 shots/area, we obtain a rippled surface texture similar to that obtained without a thin film in previous sections, with periodic surface structures showing a period of about 600 nm (as opposed to about 400 nm without a thin film). No remnants of the Se thin film are visible on the surface. The sample showed increased above-bandgap absorptance and sub-bandgap absorptance. We note for comparison that a silicon wafer irradiated with the same fluence and pulse number values but without a Se thin film (in Section 2.5) showed no surface texturing.

Next, we consider a pulse fluence of  $1.0 \text{ kJ/m}^2$  again at 100 shots/area. The texturing effect on the surface was not uniform, perhaps due to the varying local fluence as the laser pulses were scanned across the surface. The Se thin film was disrupted but still apparent on the surface, with surface ripples appearing in the Se thin film itself with periods of 200 and 800 nm. The surface showed no sub-bandgap absorptance. When the pulse number was increased to 1000 shots/area, periodic surface ripples with a period of about 600 nm were formed on the surface, similar to the sample fabricated at  $1.5 \text{ kJ/m}^2$ , and the surface showed sub-bandgap absorptance.

At a fluence of  $0.8 \text{ kJ/m}^2$  and 1000 shots/area, the texturing effect was again not uniform, with the Se film disrupted with surface ripples with periods of about 200 nm and 800 nm. The surface showed no sub-bandgap absorptance. Representative images for the sample surfaces are shown in Figure 2.6.2.

When the shots/area value was increased to 5000 at  $0.8 \text{ kJ/m}^2$ , the surface developed a new morphology. The texturing effect was again non-uniform, with debris-covered areas on the surface interspersed with rippled areas. The rippled areas were composed of highly uniform ripple structures with a period of 150 nm, shown in Figure 2.6.3. Some debris was apparent on the surface of these structures as well. The surface showed increased above-bandgap and sub-bandgap absorptance. Figure 2.6.4 shows the absorptance spectra of the samples in this section.

#### **2.6.4 Discussion**

With a fluence of  $1.5 \text{ kJ/m}^2$  and 100 shots/area, the surface shows fully developed laser-induced periodic surface structures. We can compare this to the sample made

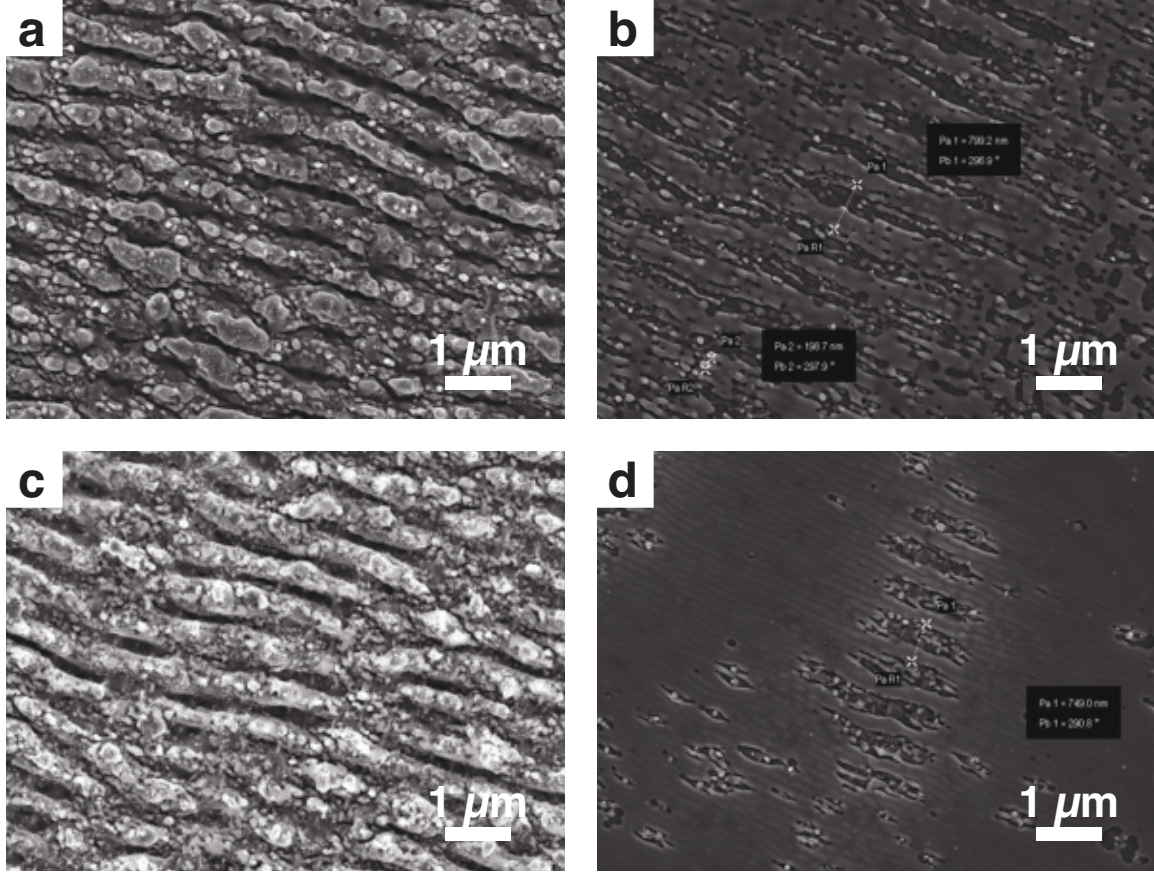


Figure 2.6.2: Surface morphologies of irradiated silicon with a Se thin film. a: 100 shots/area with a peak fluence of  $1.5 \text{ kJ/m}^2$ . b: 100 shots/area with a peak fluence of  $1.0 \text{ kJ/m}^2$ . c: 1000 shots/area with a peak fluence of  $1.0 \text{ kJ/m}^2$ . d: 1000 shots/area with a peak fluence of  $0.8 \text{ kJ/m}^2$ . (a) and (c) show sub-bandgap optical absorptance, while (b) and (d) do not.

with  $1.6 \text{ kJ/m}^2$  and 100 shots/area in Section 2.5, which was made in  $\text{SF}_6$  without a thin film and which showed no surface texturing. This difference indicates that the Se thin film somehow reduces the modification threshold of the silicon. Selenium has a melting temperature of 221 deg. C and a boiling temperature of 685 deg. C, much lower than silicon's melting temperature of 1414 deg. C (Royal Society of Chemistry). Thus, we would expect the Se film to be heavily modified at fluences just below the melting threshold of silicon. As the Se film is modified, surface irregularities arise,

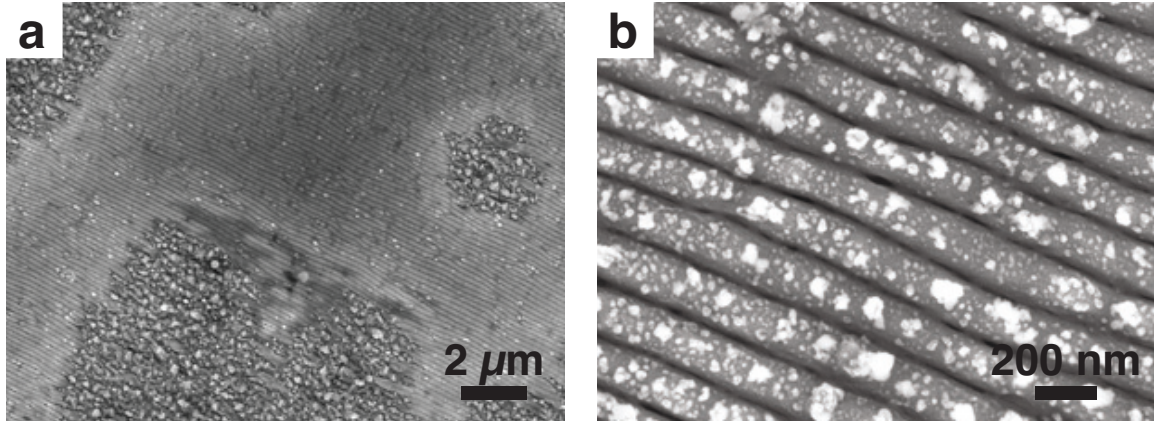


Figure 2.6.3: Scanning electron microscope images of surface after 5000 shots/area with a peak fluence of  $0.8 \text{ kJ/m}^2$ . Surface showed sub-bandgap optical absorbance. a: Overview of surface showing non-uniform modification of surface. b: Ripples on surface were highly uniform with a period of 150 nm.

which could enhance localized heating and melting of silicon, initiating the texturing process. Furthermore, the melting temperature of silicon may be depressed as it is mixed with the Se film. These mechanisms could be responsible for the reduction of the modification threshold of the surface with the presence of the Se film.

We observe a wide range of periodic surface structures in the Se thin film and in the silicon. In the Se thin film, we observe periodic structures before the silicon becomes fully textured, with periods of about 200 and 800 nm. The 800 nm structures could be due to the interference of scattered surface waves with the incoming laser pulse or to surface plasmon polaritons that experience an effective index similar to that of air. The 200 nm structures could be due to surface waves derived from second harmonic generation at the surface that experience an effective index from the selenium-silicon interface. Even when the Se film is modified with periodic structures, it appears that no selenium is incorporated into the silicon, because no



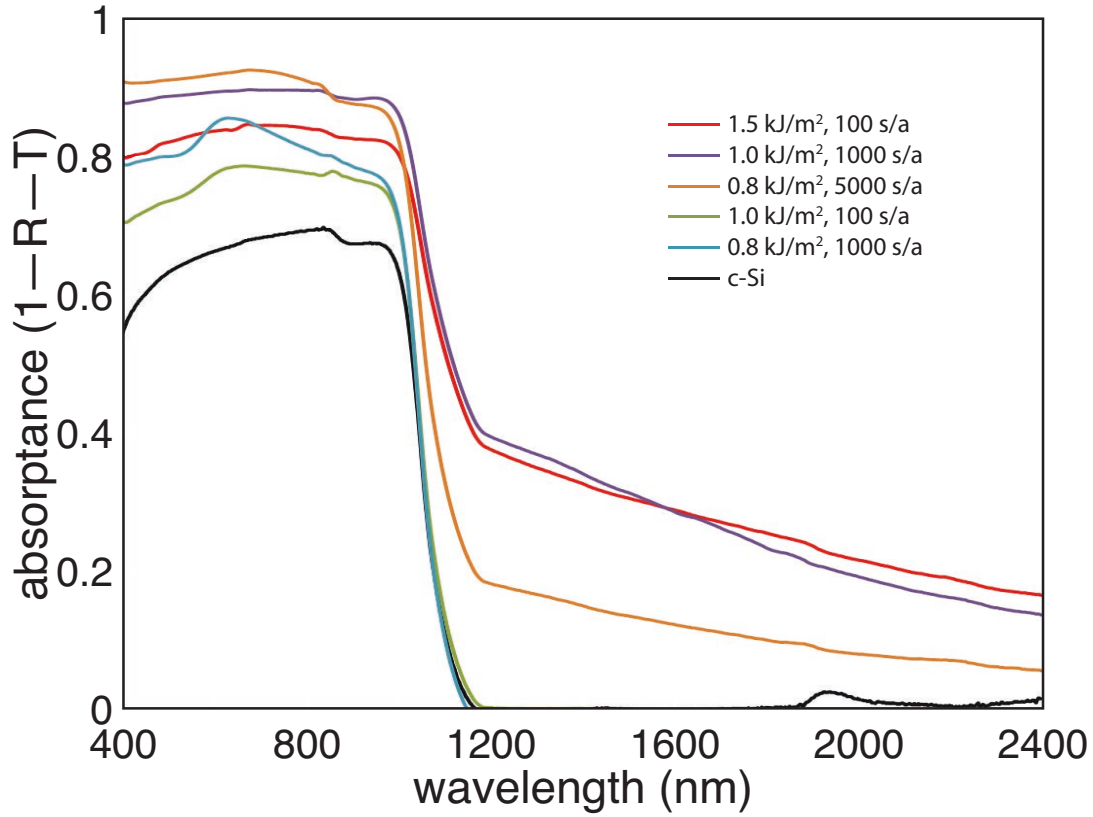


Figure 2.6.4: Optical absorbance shown by samples fabricated with Se thin film and low fluence. Sub-bandgap absorbance was observed with silicon texturing at 1.5 kJ/m<sup>2</sup> and 100 shots/area, 1.0 kJ/m<sup>2</sup> and 1000 shots/area (but not at 100 shots/area), and 0.8 kJ/m<sup>2</sup> and 5000 shots/area (but not at 1000 shots/area).

sub-bandgap absorbance is observed. When periodic surface structures appear in the silicon substrate, however, sub-bandgap absorbance appears. This is consistent with sub-bandgap absorbance requiring the melting and doping of the silicon surface. We can see that the period of the surface structures in silicon is about 600 nm, which is larger than the 400-nm ripples observed on silicon irradiated in air and nitrogen. This may be due to a decrease in the effective index experienced by surface plasmon polaritons from the presence of the Se film or from the incorporation of selenium into



the silicon surface.

It is interesting to note that melting and doping of the silicon surface with a thin film can occur even at fluences far below the silicon melting threshold if a sufficient number of pulses is used. For example, a fluence of  $1.0 \text{ kJ/m}^2$  and 100 shots/area modifies only the Se film overlying the silicon and does not lead to sub-bandgap absorptance. When the pulse number is increased to 1000 shots/area, however, surface ripples appear in the silicon and sub-bandgap absorptance is observed. (Recall that for scanned laser pulse samples, 1000 shots/area at  $1.0 \text{ kJ/m}^2$  means that for each spot on the surface, about 1000 pulses produce a local fluence of  $0.5\text{--}1.0 \text{ kJ/m}^2$ , with the distribution weighted toward the lower end of the fluence range.) With a fluence of  $0.8 \text{ kJ/m}^2$  and 1000 shots/area, we again see modification only of the Se thin film, not the underlying silicon, and we observe no sub-bandgap absorptance, but when the pulse number is increased to 5000 shots/area, sub-bandgap absorptance is observed, indicating that modification of the silicon surface has occurred. Modifying silicon far below the melting threshold is interesting because it suggests that a thin film and low pulse fluences can be used to selectively modify just the top surface of the silicon, without melting or affecting the silicon below the doped layer.

The periodic surface structures produced with a fluence of  $0.8 \text{ kJ/m}^2$  and 5000 shots/area do not appear to have been reported in the literature before. These structures have a small period of about 150 nm and are highly smooth and uniform. Other than debris on the surface, the structures appear to be composed of a single material phase, and because the sample shows sub-bandgap absorptance, it appears that the Se film has been integrated into the silicon surface. No deep melting of the silicon

surface is apparent. Future work could investigate the structure of these features further. In some areas of the sample surface, the debris coverage is heavy. It is possible that debris accumulation could be reduced by reducing the gas pressure used during the fabrication process or by flowing gas over the surface during fabrication.

### **2.6.5 Conclusions**

In this section, we investigated the fabrication of large-area samples using low fluences and a Se thin film. The presence of the Se film reduces the modification threshold of the silicon significantly, with sub-bandgap absorptance indicative of silicon doping achieved with peak fluences as low as  $0.8 \text{ kJ/m}^2$ . Before surface structures and sub-bandgap absorptance arise in the silicon substrate, we observe periodic surface structuring of the Se thin film, which by itself is not sufficient for sub-bandgap absorptance to occur. At  $0.8 \text{ kJ/m}^2$  and 5000 shots/area, we observe highly uniform surface ripples with a period of about 150 nm, which have not been reported before. These surface ripples appear to be composed of hyperdoped silicon, because they are associated with sub-bandgap absorptance. It would be interesting to further characterize the structure of these ripples in future work.

## 2.7 Controlling the dopant concentration in hyper-doped black silicon

### 2.7.1 Introduction

One of the main challenges in fabricated intermediate band devices with impurities is to ensure that the band produced by the impurities is truly an intermediate band—that is to say, that it is not degenerate with either the valence or conduction bands. The impurity band produced by chalcogens in silicon grows with increasing doping concentration, becoming degenerate with the conduction band above 0.4 at. % [13]. However, the dopant concentrations produced by fs-laser doping can easily exceed 1 at. % [1]. Lower dopant concentrations can be achieved with fs-laser irradiation, but few pulses must be used [14], meaning no or little surface texture is produced by the irradiation process. Yet the surface texture is integral to the design of an efficient intermediate band device, because without light-trapping, the doped layer is only weakly absorbing [34]. Thus, a central challenge in fabricating efficient intermediate band devices is to keep the dopant concentration below the degeneracy threshold (i.e., the semiconductor-to-metal transition threshold) while also obtaining strong light trapping in the surface.

In this section, we approach this challenge by separating the laser-texturing and laser-doping steps in the irradiation process. We texture a silicon substrate in  $\text{N}_2$  gas using a high fs laser fluence and many pulses, then dope the textured surface in  $\text{SF}_6$  gas using a lower laser fluence and fewer pulses. The texturing enhances the optical absorptance of the dopants through light-trapping, and we can directly

observe the growth of a sub-bandgap absorption band with increased sulfur doping by using spectrophotometry and FTIR spectroscopy. With increased doping, we observe changes in the sub-bandgap absorption band that we associate with the onset of degeneracy (a semiconductor-to-metal transition). Our results indicate that laser doping of textured substrates could be a successful approach for fabricating efficient intermediate band devices.

### **2.7.2 Methods**

Silicon was laser-textured in  $N_2$  gas, then laser-doped with  $SF_6$ . First, a silicon wafer was irradiated with scanned 800 nm fs laser pulses at a fluence of  $8.0 \text{ kJ/m}^2$  and 50 shots/area in order to produce a light-trapping surface texture. An atmosphere of 20 Torr  $N_2$  was used as a buffer gas to prevent ablated particles from coating the fabrication chamber. The  $N_2$  gas was flowed through the irradiation chamber at a constant pressure of 20 Torr in order to carry away debris as the silicon was irradiated. Following this, the textured silicon was irradiated with the same laser at a fluence of  $2.5 \text{ kJ/m}^2$  in 500 Torr  $SF_6$  gas using 5, 10, 20, 40, 60, and 80 shots/area.

The optical absorptance of the hyperdoped black silicon was measured using an ultraviolet-visible-near infrared (UV-VIS-NIR) spectrophotometer (for wavelengths of  $0.4\text{--}2.5 \mu\text{m}$ ) and a Fourier transformed infrared (FTIR) spectrometer (for wavelengths of  $2.4\text{--}10.0 \mu\text{m}$ ). Reflectance (R) and transmittance (T) spectra were measured with integrating spheres and were used to calculate the optical absorptance ( $A = 1 - R - T$ ). The FTIR spectra were matched to the spectrophotometer spectra in the overlapping wavelength range ( $2.4\text{--}2.5 \mu\text{m}$ ). To observe the effect of the  $SF_6$  doping

on the optical absorptance, absorptance spectra from samples not doped with  $\text{SF}_6$  were subtracted from spectra from samples doped with  $\text{SF}_6$ .

### 2.7.3 Results

When texturing samples in  $\text{N}_2$  gas, large amounts of debris accumulated on the surface unless the gas was flowed through the chamber during the irradiation process. When texturing in flowing gas, the surface was textured while remaining free of debris.

After texturing in  $\text{N}_2$  but before doping with  $\text{SF}_6$ , the surface showed increased optical absorptance both above the bandgap energy (with absorptance of about 80%) and below the bandgap energy (with absorptance decreasing from 1.1–0.4 eV), consistent with other studies of silicon texturing in  $\text{N}_2$  gas [43].

After additional irradiation in  $\text{SF}_6$  gas, the optical absorptance was increased further. With 20–60 pulses in  $\text{SF}_6$ , the sub-bandgap absorptance increased while retaining a similar lineshape to the absorptance before  $\text{SF}_6$  doping, while the above-bandgap absorptance remained constant. With 80 pulses in  $\text{SF}_6$ , however, the sub-bandgap absorptance increased significantly while changing its lineshape, and the above-bandgap absorptance increased to 90%, as shown in the Figure 2.7.1, with detail at low photon energies shown in Figure 2.7.2.

By subtracting the spectrum of the undoped sample from those of the doped samples, we can observe the effect of  $\text{SF}_6$ , as shown in Figures 2.7.1 and 2.7.2. After 20 shots/area in  $\text{SF}_6$ , an absorption band appears with a peak around 0.7 eV. With additional pulses, the band grows larger with a peak around 0.6–0.8 eV. The absorption bands due to  $\text{SF}_6$  decline to zero around 0.1–0.3 eV. After 80 shots/area in  $\text{SF}_6$ ,

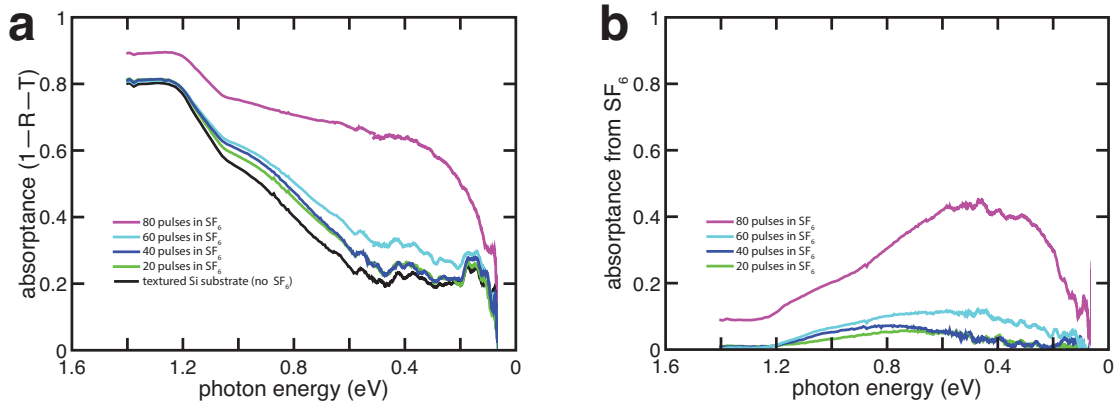


Figure 2.7.1: a: Optical absorption spectra of silicon textured in  $N_2$  gas and subsequently irradiated in 500 Torr  $SF_6$  gas using 20, 40, 60, and 80 shots/area (fluence of  $2.5 \text{ kJ/m}^2$ ). b: Absorbance on textured substrate attributed to  $SF_6$  doping.

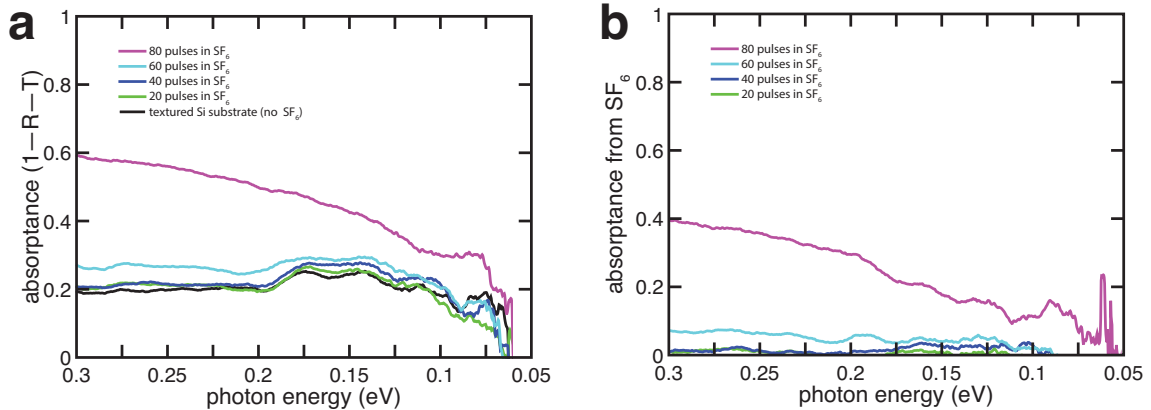


Figure 2.7.2: a: Detail of optical absorption spectra from 0.05–0.3 eV. b: Absorbance attributed to  $SF_6$  doping from 0.05–0.3 eV. For samples irradiated with 20–60 shots/area in  $SF_6$ , the absorbance due to  $SF_6$  approaches zero between 0.3–0.1 eV. For the sample irradiated with 80 shots/area in  $SF_6$ , however, sub-bandgap absorbance is observed all the way to the detection limit at around 0.05 eV.

the absorption due to  $SF_6$  is no longer symmetric, but grows from the band edge to 0.6 eV with upward concavity, plateaus, and then decreases rapidly below 0.3 eV, with significant absorption still observed at the low-energy detection limit at 0.05 eV. In

the range of 0.3 eV to 0.05 eV (our detection limit), the samples irradiated with 20–60 shots/area in SF<sub>6</sub> no sub-bandgap absorptance below around 0.1 eV, while the sample irradiated with 80 shots/area in SF<sub>6</sub> shows SF<sub>6</sub>-induced sub-bandgap absorptance all the way to the detection limit at 0.05 eV.

### 2.7.4 Discussion

To produce a highly textured substrate in N<sub>2</sub>, a high fluence and shots/area were used, which generated a large amount of debris. Samples that were fabricated as described above but without flowing gas were coated in debris after fabrication. Flowing the N<sub>2</sub> gas through the chamber was effective in preventing this debris from building up on the silicon surface and could be a useful technique for producing debris-free samples in the future.

What dopant concentrations are achieved in our samples? The increase in dopant concentration as a function of pulse number (for 1–6 pulses) and SF<sub>6</sub> pressure (for 10–500 Torr) have been measured with a pulse fluence of 2.5 kJ/m<sup>2</sup> (Sher thesis) and indicate that, in 500 Torr SF<sub>6</sub>, 4 pulses produce a peak dopant concentration of around  $8 \times 10^{18}$  S atoms/cm<sup>3</sup>. The growth in peak dopant concentration with additional pulses is approximately linear from 1–6 pulses, so we estimate an average increase in peak dopant concentration of around  $2 \times 10^{18}$  S atoms/cm<sup>3</sup> per pulse. To achieve a dopant concentration of 0.1–0.4 at. % ( $5 \times 10^{19}$ – $2 \times 10^{20}$  S atoms/cm<sup>3</sup> in Si), which has been indicated as the doping range producing an intermediate band [13], our estimate implies that 25–100 pulses are needed. At around 100 pulses, we expect to exceed a dopant concentration of 0.4 at. %, producing a semiconductor-to-metal

transition and free-carrier absorption. Although the increase in dopant concentration with additional pulses eventually plateaus around 1 at. % [8], we expect to be below this limit with our irradiation conditions.

These estimates of dopant concentration are consistent with the absorption spectra we observe. After 20 shots/area in  $\text{SF}_6$ , we expect the dopant concentration to be close to 0.1 at. %, and we see an absorption band develop with a peak at around 0.7 eV; this is consistent with an intermediate band centered at 0.7 eV above the valence band, which is the region of the band gap corresponding to the substitutional donor levels of sulfur in silicon [69]. We observe that the enhanced absorptance drops to zero at energies below around 0.3 eV, which is consistent with a gap between the intermediate band and the conduction band. The width of the absorption band suggests intermediate band absorption rather than absorption from isolated impurities. Thus, both our estimate of the dopant concentration and our absorption measurements after 20 shots/area are consistent with silicon that exhibits an intermediate band but has not undergone a semiconductor-to-metal transition. After 40 shots/area, the  $\text{SF}_6$  absorption band grows but is still zero below around 0.3 eV. After 60 shots/area, the absorption band grows further and extends to lower energies, reaching zero only for energies below around 0.1 eV. This is consistent with the energy range of the intermediate band growing in width and nearly becoming degenerate with the conduction band. After 80 shots/area, we see a sharp transition to increased absorptance. The absorptance band is no longer symmetric but drops off abruptly, which may be due to a reduction in light-trapping efficiency at long wavelengths (Sher, Lin, 2014). Furthermore, the enhanced absorptance stays above zero all the way to the detection



limit at around 0.05 eV, indicating that free-carrier absorption may be occurring. These features could indicate a semiconductor-to-metal transition.

What is the sulfur dose that we expect in our samples? Again, the increase in dose as a function of pulse number and gas pressure has been measured (see thesis), but because the dose appears to grow nonlinearly with increased pulse number under some conditions, and because the pulse numbers we use here are significantly larger than those measured in the literature, it is difficult to estimate the total dose. However, we make a rough estimate by assuming that the dose grows linearly with pulse number. The dose reported for 6 pulses at a fluence of 2.5 kJ/m<sup>2</sup> in 500 Torr SF<sub>6</sub> is about  $3 \times 10^{13}$  atoms/cm<sup>2</sup> [14]. This implies a dose of around  $3 \times 10^{14}$  atoms/cm<sup>2</sup> for our sample with 60 shots/area. The product of absorption coefficient  $\alpha$  and depth  $d$  reported for this dose is around 0.04 at 0.7 eV [34], which corresponds to only 4% light absorption. In our sample, however, we have about 10% light absorption from sulfur doping. This could be due to an increase in optical path length due to texturing by a factor of about two, or it could be due to an underestimate of the sulfur dose (for example, a dose of  $10^{15}$  atoms/cm<sup>2</sup> has been reported with an  $\alpha d$  product at 0.7 eV of 0.1, which would yield an absorptance of 10%). It is reasonable to expect that the optical path length is increased on our textured surface relative to a flat surface simply due to the fact that the doped layer is not oriented normally to the incoming light.

We can obtain a rough idea of the anti-reflective effectiveness of the N<sub>2</sub>-textured surface by considering the increase in above-bandgap absorptance. After texturing, we see the above-bandgap absorptance increase from 70% to 80%. Because above-

bandgap absorptance losses comes from surface reflectivity, we can determine that texturing reduces the effective reflectivity from 0.3 to 0.2, equivalent to 1.3 normal-incidence reflection events per photon at the surface (instead of 1 reflection event for a flat surface). Greater reductions in reflectivity have been achieved using textures produced by fs-laser irradiation in fluorine-bearing gases (such as  $\text{SF}_6$ ). For example, black silicon produced in  $\text{SF}_6$  can exhibit above-bandgap reflectivity as low as 5% (see Chapter 4, for example), equivalent to 2.5 reflection events per photon. Future work could attempt to control the dopant concentration on substrates with similarly strong light-trapping properties.

Similarly, we can estimate the increase in optical path length produced by our textured surface by considering the absorptance below the bandgap. The sulfur dose we estimate for our sample with 60 pulses is  $3 \times 10^{14}$  atoms/cm<sup>2</sup>, associated with an  $\alpha d$  product of 0.05 for a 250 nm thick layer [34], or an absorption coefficient  $\alpha = 2 \times 10^5$  m<sup>-1</sup>. For a 100-nm thick layer produced by laser doping, we would expect absorption of only 2% without light trapping. In our samples, if we have a 100-nm thick doped layer and an absorption coefficient of  $2 \times 10^5$  m<sup>-1</sup> after 60 shots/area in  $\text{SF}_6$ , then our sulfur absorption band with 10% absorptance would correspond to a light-trapping factor of about 5. This is much lower than the Lambertian limit, which is  $4n^2/\sin(2\theta)$ , where  $n$  is the refractive index and  $\theta$  is the angle of the emission cone in the medium surrounding the cell [46]. For silicon, if  $n = 3.5$  and  $\theta = 90$  degrees, then path-length enhancement factors of 50 can be achieved. If we were to increase the optical path length by a factor of 50 through Lambertian light trapping on our sample doped with 60 shots/area, then we would expect sub-bandgap absorption of over 60%.

It may be possible to achieve even higher absorption levels by using nanophotonic light trapping tuned to the intermediate band absorption wavelength [46]. Thus, we expect that textured surfaces with greater light-trapping factors could result in much higher intermediate band absorptance than what we observe here at doping levels below the semiconductor-to-metal transition.

Here we demonstrated the separation of the texturing and doping steps, so that the dopant concentration could be controlled on a light-trapping surface. This is ultimately an important task for producing efficient intermediate band devices. However, the level of sub-bandgap absorptance we achieve through sulfur doping is only about 10% before reaching what appears to be the semiconductor-to-metal transition. This indicates that to achieve strong sub-bandgap absorptance while staying below the semiconductor-to-metal transition, very strong light-trapping surfaces should be used. Because the doped layer must be thin to allow carrier transport, effective light-trapping surfaces would utilize optical path length enhancement. Thus, a future direction is to use substrates with much greater optical path length enhancement factors while controlling the dopant concentration to form an intermediate band. There are multiple strategies that could be used to achieve this, such as doping pre-textured substrates (e.g., nanowire substrates) or fabricating black silicon in  $\text{SF}_6$ , removing the doped skin layer (e.g., through chemical texturing or laser ablation), and then doping the surface in a controlled way.

### **2.7.5 Conclusions**

In this section, we investigated the separation of texturing and doping steps in laser processing of silicon. We find that we can texture a silicon substrate in  $N_2$  gas, then laser-dope the textured surface with sulfur. After sulfur doping with a small number of laser pulses (20 shots/area), we observe an optical absorption band emerge with a peak at 0.7 eV and which drops to zero below photon energies of 0.3 eV, consistent with the formation of an intermediate band. With increasing shots/area, the absorption band grows in strength and extends to lower photon energies, consistent with an increase in the density of states and width of the intermediate band. After 80 shots/area, we observe an abrupt transition to much greater absorption, the sulfur absorption band is no longer symmetric, and the band remains above zero for photon energies down to the detection limit of our experiment (0.05 eV), consistent with a semiconductor-to-metal transition caused by an increase in sulfur dopant concentration beyond the transition threshold, which has been reported as 0.4 at. % in the literature [13]. The pulse numbers at which we observe the emergence of the sulfur band and the emergence of metallic absorption are broadly consistent with those expected to produce dopant concentrations above 0.1 and 0.4 at. %, respectively. These results show that it is possible to laser-dope a textured substrate while controlling the dopant concentration, an important step for fabricating efficient intermediate band devices. Based on an estimate of the doped layer thickness and the sulfur dose, we estimate that our light-trapping surface increases the optical path length at the intermediate band absorption wavelength by a factor of about 5. We estimate that by using substrates with light-trapping factors at the Lambertian limit, the strength of

the intermediate band absorption could be increased to above 60% without exceeding the semiconductor-to-metal transition. A future direction is to use substrates with high light-trapping factors while controlling the dopant concentration to form an intermediate band.

## **2.8 Surface cleaning with hydrofluoric acid**

### **2.8.1 Introduction**

In Sections 2.2 and 2.3, we observed the accumulation of surface debris when fabricating laser-textured silicon at low fluences. In this section, we investigate the use of hydrofluoric acid (HF) for removing this debris.

### **2.8.2 Methods**

Samples described in Section 2.2 were used to investigate the effect of HF treatment. A silicon wafer was irradiated with a series of stationary 800 nm fs pulses without translating the sample. A peak fluence of  $1.5 \text{ kJ/m}^2$  and pulse numbers of 200–900 were used in 100 pulse increments. The pulse diameter was 840x1000 micrometers, the pulse duration was 50 fs, and a pulse repetition rate was 100 Hz. Replicate samples were prepared in ambient air at atmospheric pressure, 100 Torr, and 20 Torr.

To test the effect of hydrofluoric acid, samples were placed in 10 HF solution for 2 minutes.

Samples were imaged with a scanning electron microscope at all local fluences for which texturing was present in local fluence increments of  $0.1 \text{ kJ/m}^2$ . Local fluence

was determined as a function of position as described in Section 2.2. Samples were imaged before and after HF treatment.

The presence of amorphous silicon in the laser-irradiated area was measured using Raman spectroscopy as in Section 2.2. A baseline was subtracted from the Raman spectra by fitting and subtracting a 2nd-degree polynomial through a series of spectral values that are nominally zero for silicon (70, 80, 600, 700, 800, 1100, 1200, 1300, and 1400  $\text{cm}^{-1}$  were used). Then, the spectral area from 460–510  $\text{cm}^{-1}$  (associated with the broad amorphous silicon peak centered at 480  $\text{cm}^{-1}$ ) was divided by the spectral area from 515–525  $\text{cm}^{-1}$  (associated with the sharp crystalline silicon peak centered at 520  $\text{cm}^{-1}$ ). This procedure yielded an indicator of amorphous silicon content that was insensitive to variations in overall spectral strength. The amorphous silicon content was then mapped out radially over the textured area of the sample. The amorphous silicon content was measured in this way both before and after HF treatment.

### **2.8.3 Results**

HF treatment removed almost all visible debris from the surface. The effect was greatest for samples fabricated at higher gas pressures, because those samples exhibited higher levels of surface debris to begin with, as shown in Figure 2.8.1. Samples fabricated at low pressure (20 Torr) did not have surface debris present after fabrication; for these samples, HF treatment had no visible effect on the surface morphology, as shown in Figure 2.8.2.

The effect of HF treatment on the amorphous silicon content depended on the

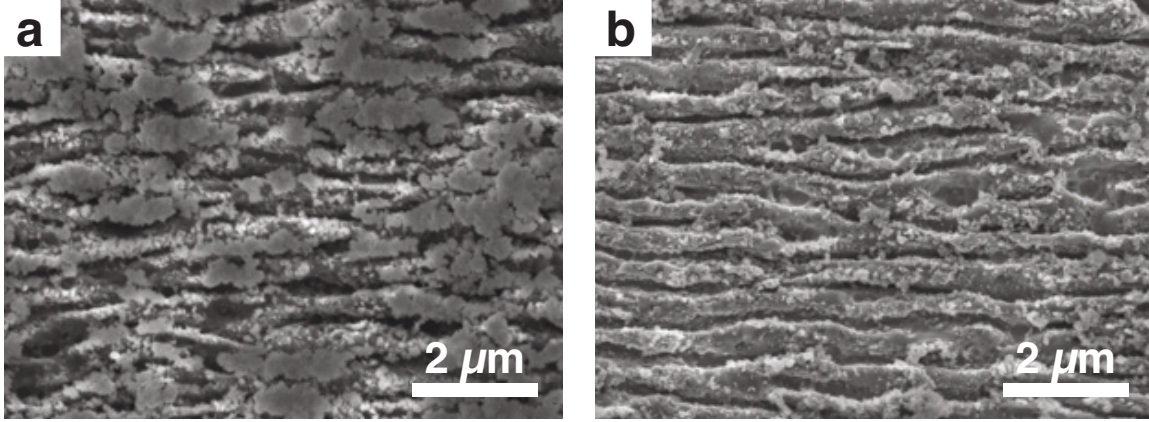


Figure 2.8.1: Removal of heavy surface debris with HF treatment. 400 pulses with local fluence of  $1.4 \text{ kJ/m}^2$ . a: before HF treatment. b: after HF treatment.

fabrication gas pressure. For samples fabricated at atmospheric pressure, HF treatment reduced the amorphous silicon content at the edge of the textured area (where the amorphous silicon content was highest before HF treatment). However, HF treatment did not significantly reduce the amorphous silicon content throughout the rest of the textured area, despite the visible reduction in surface debris. For samples fabricated at a pressure of 20 Torr, HF treatment reduced the amorphous silicon content throughout the textured area by about a factor of two. The amorphous signal as measured by Raman is shown as a function of texturing radius in Figure 2.8.3.

#### 2.8.4 Discussion

HF treatment was highly effective at removing surface debris without altering the morphology of the surface texture. This may be due to the fact that HF selectively etches silica rather than silicon. In Section 2.2, x-ray spectroscopy showed that the surface debris is oxygen-rich, which is consistent with its removal by HF. The fact

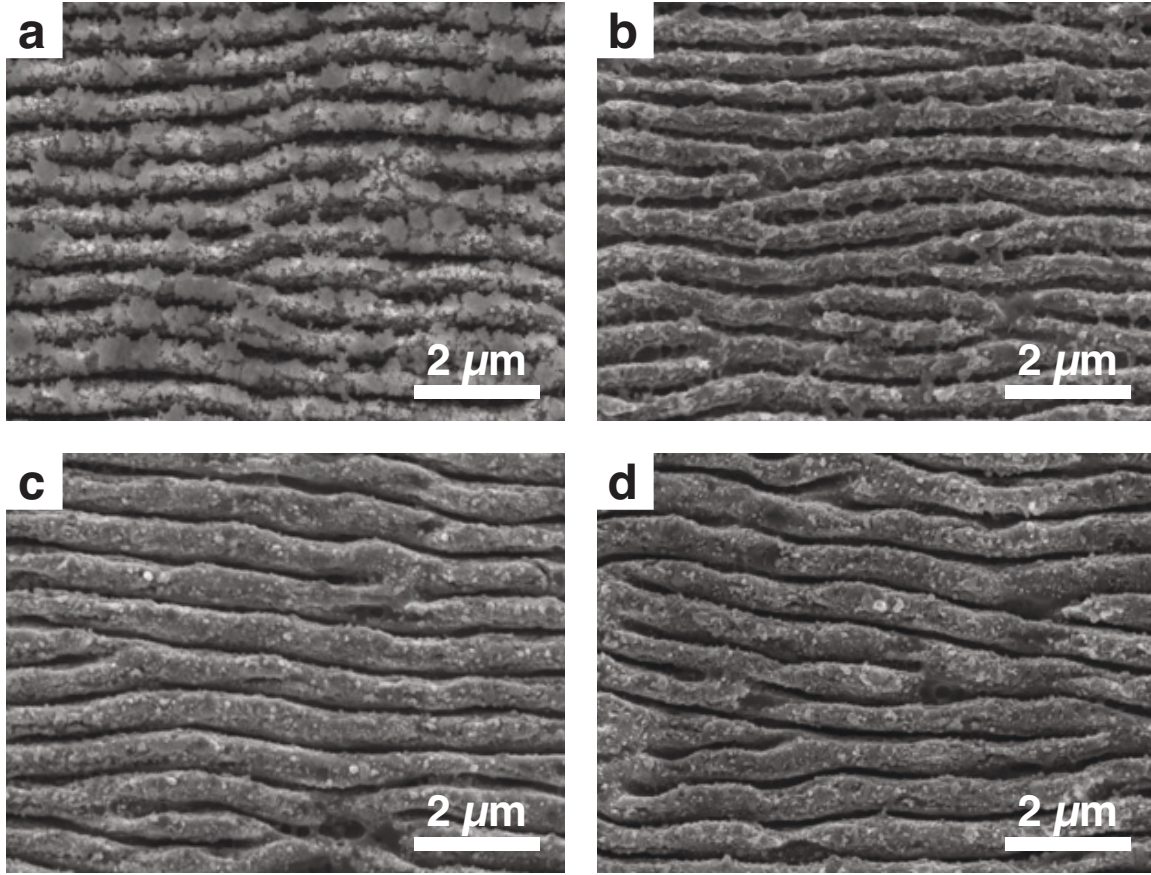


Figure 2.8.2: HF removes surface debris when present and otherwise has no discernible effect on the surface morphology. All images 200 pulses with local fluence of  $1.4 \text{ kJ/m}^2$ . Top: fabrication in air at atmospheric pressure (a: before HF treatment; b: after HF treatment). Bottom: fabrication in 20 Torr air (c: before HF treatment; d: after HF treatment).

that the removal of surface debris did not correlate with a reduction in amorphous silicon (in fact, the opposite was the case) indicates that the debris is not composed of amorphous material. The morphology of the debris, its chemistry, and its removal by HF all suggest that it is some kind of silica material, perhaps similar to fumed silica.

Amorphous silicon was removed by HF treatment, but only under some conditions. For example, when no debris was initially present on the surface, then HF treat-



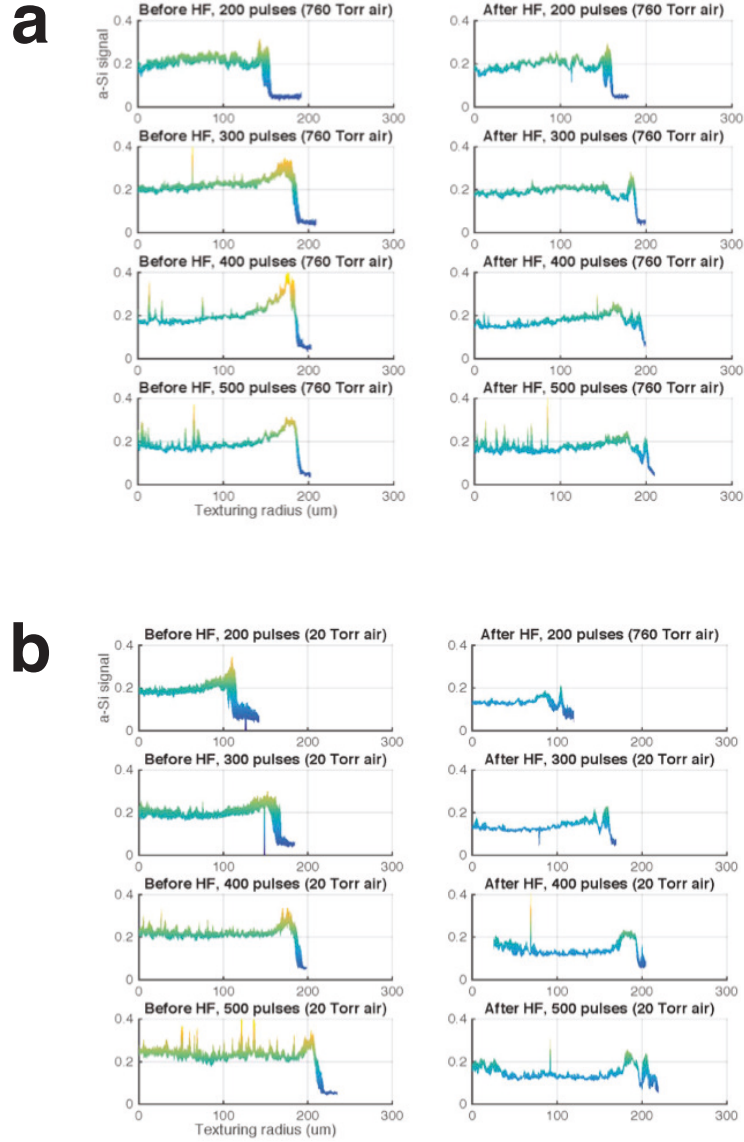


Figure 2.8.3: The effect of HF treatment on amorphous silicon content (left: before HF treatment; right: after HF treatment). Average amorphous silicon signal shown as a function of distance from the center of the irradiated area. Samples fabricated at atmospheric pressure (top 8 plots) showed no significant reduction in amorphous silicon content after HF treatment except for at the edge of the textured area (although visible surface debris was removed). Samples fabricated at 20 Torr (bottom 8 plots) showed a reduction in amorphous silicon content by about a factor of two throughout the textured area.

ment removed some amorphous silicon. Similarly, when surface debris was present, HF treatment removed some amorphous silicon near the edge of the textured area that is debris-free, but did not remove amorphous silicon in the textured area covered by debris. Because HF rapidly etches  $\text{SiO}_2$  but not Si, it is possible that these differences in amorphous silicon removal are due to differences in the incorporation of oxygen into the surface. For example, the accumulation of debris on the surface might reduce the amount of oxygen incorporated into the amorphous silicon surface during melting and resolidification. If less oxygen is incorporated into the amorphous silicon surface, then that amorphous silicon would be more resistant to removal by HF. Conversely, we see that HF removes amorphous silicon when surface debris does not accumulate (e.g., at low fabrication pressures and near the edge of the textured area). The lack of surface debris may facilitate incorporation of oxygen into the surface, which is amorphous, and thus removal of that surface by HF. The remaining amorphous silicon detected by Raman spectroscopy could be left on the surface or could be sub-surface pockets of amorphous silicon that HF treatment cannot reach.

Even after amorphous silicon is removed, the surface morphology appears unaltered. This could be due to the fact that the amorphous skin on laser-textured silicon is typically less than 100 nm thick, so its removal would not alter the surface morphology significantly.

HF treatment could be useful for laser-processed silicon surfaces. Particularly if irradiation is performed in air (or in any oxygen-bearing gas), HF treatment would remove any oxygenated material on the surface, including debris. The removal of the oxygenated skin on the surface could be useful because this skin tends to be

amorphous and thus undesirable, and also because this skin would contain impurities from the irradiation atmosphere, which may also be undesirable. Thus, HF treatment could be useful for cleaning laser-textured silicon for photovoltaics or photodetectors. If the doped skin is functional (e.g., if it is hyperdoped for the purpose of producing sub-bandgap absorptance), then HF treatment could be less useful, because the etching process would remove this layer.

### **2.8.5 Conclusions**

In this section, we investigated the use of HF for cleaning laser-textured silicon after fabrication in air. We found that HF removes the surface debris that accumulates during irradiation. We also found that when debris is not present, HF reduces the amorphous silicon content of the surface by about a factor of two. The overall surface morphology, which here consists of periodic ripples, is not altered by HF treatment. The effect of HF treatment may be attributed to the inclusion of oxygen in the debris and the amorphous skin during irradiation. HF treatment could be useful for removing undesirable material from the surface of laser-textured silicon while keeping the morphology intact.

## **2.9 Conclusions of chapter**

In this chapter, we explored a range of experimental advances in the fabrication of laser textured and laser doped silicon.

In Section 2.2, we investigated the texturing of silicon under simple conditions—in air near the melting threshold fluence using stationary pulses. We observed laser-

induced periodic surface structures, which became fully formed at particular fluence and pulse number combinations, and which became damaged by continued irradiation. Debris, which is oxygen-rich and similar in morphology to fumed silica, accumulates on the surface with continued irradiation, but can be mitigated by using a low-pressure environment. We find that oxygen is incorporated into the surface of the ripples, and that the formation of surface textures is associated with a sharp increase in the presence of amorphous silicon, which decreases slightly with increased irradiation. With increased pulse number, the threshold fluence for surface texturing decreases, and the surface feedback effects leading to texturing at low fluences—from initial modification of the surface to fully developed surface textures—occur over about 40 pulses irrespective of local fluence.

In Section 2.3, we investigated the texturing of silicon below the single-pulse melting threshold. We found that before texturing occurs, debris is generated that appears to be highly strained silicon and/or hexagonal (wurtzite) silicon. The generation of hexagonal silicon and extended defects could be one of the incubation mechanisms leading to eventual melting and surface texturing below the single-pulse melting threshold. We observe the surface ripples to form beneath a thin surface layer, which is likely the native oxide layer and which delaminates from the surface as the textures are formed. This delaminated layer may be the origin of the oxygen-rich debris we observe in Section 2.2. We again find that the threshold fluence for surface texturing decreases with increasing pulse number, yet we also find that it is sensitive to not just the local fluence but the peak fluence, as the peak fluence determines how quickly incubation effects accumulate, how quickly texturing is initiated, and thus

how quickly surface feedback mechanisms can produce texturing at lower local fluences. We describe the initiation and propagation of surface texturing as a function of fluence and pulse number, which predicts that peak fluences above the melting threshold require 10–20 pulses for texture formation, whereas lower peak fluences require many more pulses to initiate texturing (e.g., hundreds of pulses with a peak fluence of  $1.4 \text{ kJ/m}^2$ ).

In Section 2.4, we use irradiation conditions that allow us to observe the formation of surface textures from the earliest stages of surface modification. We use a range of gases (air, nitrogen, and sulfur hexafluoride) as well as a range of gas pressures, and we find that the surface texture formation process is highly sensitive to gas pressure in general. Surface textures appear to initiate as localized areas of melting, which at low fluence are randomly distributed over the surface and are likely due to defects or small particles on the surface. Some of these localized areas of melting produce melting strips that propagate over the surface, likely due to surface plasmon polaritons. As these melting strips propagate, mass transfer occurs away from the areas of greatest melting, which we attribute to surface energy gradients from temperature gradients (thermocapillary effects) and impurity gradients arising from the ambient gas (impurity Marangoni effects). Once surface ripples are formed from mass transfer, growth of the textured region occurs in the direction of laser polarization, again likely due to the generation of surface plasmon polaritons from the textured surface. At low gas pressures, highly elongated regions of surface texturing can be formed. These regions eventually merge to form an interconnected textured network. At increased gas pressures, the textured area forms over a region that reflects the shape of the

laser pulse rather than the direction of surface plasmon polaritons, which may be due to the dominance of impurity Marangoni effects over thermocapillary effects. Again, we find that amorphous silicon forms as the textures are generated, but that textures that receive additional irradiation exhibit slightly less amorphous silicon, similar to Section 2.2. In some textured areas, we observe silicon debris that appears highly strained, as well as debris that appears to be modified by the the electron beam used for imaging and therefore may be metastable.

In Section 2.5, we move from stationary pulses to scanned pulses. We use a high-throughput fabrication system to explore the fabrication parameter space experimentally. In sulfur hexafluoride gas, we find three typical surface morphologies: flat, textured with ripples, and textured with spikes. These morphologies have distinct appearances to the eye. Treating these morphologies as phases, we generate a phase diagram as a function of pulse number and fluence. We are able to predict the boundary in the phase diagram between flat and textured silicon using the results from stationary pulses obtained in Section 2.3. We find an empirical boundary between rippled and spiked textures that appears to be sensitive to surface feedback effects. The fabrication phase diagram we generate is a useful step toward predictive fabrication of laser-textured silicon.

In Section 2.6, we used scanned pulses to fabricate samples with selenium thin films. We find that using low fluences, the Se film is initially textured with ripple structures, and with additional pulses, the silicon surface is textured with ripple structures as well, at which point the surface shows sub-bandgap optical absorptance, which indicates the incorporation of Se into the silicon surface. At very low fluence

(0.8 kJ/m<sup>2</sup>) and high pulse number (5000 pulses), we observe highly uniform ripples with a period of only 150 nm, which show sub-bandgap optical absorptance. The results suggest that the presence of Se strongly reduces the texturing threshold of silicon, which can be utilized to dope and texture the surface of silicon without modifying the substrate.

In Section 2.7, we explore how to control the doping concentration when performing laser doping of textured surfaces. To accomplish this, we separate the laser texturing and laser doping steps, texturing silicon in nitrogen with a high fluence and subsequently doping the textured surface with sulfur hexafluoride at a lower fluence. With sulfur doping, we observe the formation of a symmetric optical absorptance band with a peak around 0.7 eV, which corresponds to the valence band to intermediate band transition energy. This absorption band drops to zero at photon energies below around 0.3 eV, indicating that the sulfur forms a true intermediate band. With continued sulfur incorporation, the absorption band grows in intensity and to lower energies, consistent with expected intermediate band characteristics. Above a certain doping threshold, we observe an abrupt shift in the sulfur absorption to an asymmetric shape and to increased absorption at very low photon energies (0.05 eV), consistent with a semiconductor-to-metal transition. The estimated sulfur concentrations from our laser doping parameters agree well with the concentrations associated with the formation of an intermediate band and the semiconductor-to-metal transition. This is the first demonstration of control of doping concentration on textured surfaces using fs laser doping to form an intermediate band.

In Section 2.8, we investigate the use of hydrofluoric acid (HF) on the surface of

laser-textured silicon fabricated in air. HF is highly effective at removing the oxygen-rich debris from the surface after texturing without altering the surface morphology. When fabrication is performed at low pressures, surface debris is avoided, but oxygen is incorporated into the surface of the texture. In this case, HF removes about half of the amorphous silicon detected by Raman spectroscopy, again without altering the surface morphology. Thus, HF treatment could be a useful technique for general cleaning of laser-textured silicon surfaces.



## Chapter 3

# The material microstructure of hyperdoped black silicon

### 3.1 Introduction to chapter

In this chapter, we review two research papers in which I participated as a coauthor [5, 6]. The papers were led by Matthew Smith at the Massachusetts Institute of Technology [2] and describe the complex material microstructure of hyperdoped black silicon. The microstructure of hyperdoped black silicon provides information on the conditions produced by fs laser irradiation, such as pressure induced during the irradiation process, and is important in determining the properties of resultant devices [70]. Because the details of each study are available in the published literature, here I review only the major results of each paper.

## 3.2 The origins of pressure-induced phase transformations during the surface texturing of silicon using femtosecond laser irradiation

### 3.2.1 Introduction

Here, we discuss the main results from "The origins of pressure-induced phase transformations during the surface texturing of silicon using femtosecond laser irradiation" (Journal of Applied Physics 112, 2012) [5]. In this paper, we investigate the origins of silicon polymorphs in hyperdoped black silicon: amorphous silicon (a-Si), Si-XII, and Si-III. These phases are present both as a skin on the surface (a-Si from melting and fast resolidification) and as pockets below the surface, usually concentrated in the cores of black silicon spikes (a-Si, Si-III, and Si-XII, apparently from high pressures induced during the irradiation process). Although it is sometimes difficult to detect Si-XII and Si-III visually in cross-sectional microscope images, these phases can be detected by Raman spectroscopy [42]. Amorphous silicon can be detected both with Raman spectroscopy and visually with cross-sectional microscopy. In this study, to understand the origin of these phases, their presence is correlated with the mechanisms resulting from fs irradiation at various fluences.

Amorphous silicon, Si-XII, and Si-III can be produced by high pressures. At pressures above 10–12 GPa, conventional, diamond cubic silicon (Si-I) transforms to Si-II. As the pressure is released, Si-II transforms first to Si-XII, then to Si-III around 2 GPa. If the pressure is released sufficiently quickly (faster than microseconds), how-

ever, then a-Si is formed instead of Si-XII and Si-III. The purpose of this study was to determine the pressure generation mechanism responsible for these high-pressure phases in black silicon. There are at least three potential mechanisms that can produce pressures on the order of GPa in laser-irradiated silicon. First is thermoelastic pressure, which occurs because during fs laser irradiation, the silicon is heated so quickly that it remains at constant volume. This cycle of pressure generation and release occurs on the order of picoseconds. Second is pressure from recoil shock waves generated during ablation of the surface, which also occurs over picoseconds. And third is pressure from melting and resolidification of the surface, which develops over nanoseconds; residual stress from this mechanism remains locked into the surface after irradiation.

### **3.2.2 Measuring pressure-induced phases**

A silicon wafer was irradiated with 88 stationary pulses with a peak fluence of 4.0 kJ/m<sup>2</sup>, and the intensity of Si-XII signal was mapped out over the irradiated area. The Si-XII signal is measured by Raman spectroscopy, as Si-XII exhibits a Raman peak around 350 cm<sup>-1</sup>. The onset of Si-XII generation occurs at a local fluence of about 1.6 kJ/m<sup>2</sup>, which corresponds to the melting threshold of silicon under fs laser irradiation. At local fluences above about 3.2 kJ/m<sup>2</sup>, which is close to the ablation threshold for fs laser irradiation of silicon, the Si-XII signal drops to near zero. These results show that Si-XII is associated with melting and resolidification. The reduction in the Si-XII signal at fluences above 3.2 kJ/m<sup>2</sup> contradicts the hypotheses of Si-XII being formed by thermoelastic pressure or recoil shock waves, both of which would

be expected to increase with increasing pulse fluence.

For comparison, a silicon wafer was irradiated with 88 stationary pulses with a peak fluence of  $3.2 \text{ kJ/m}^2$ , and the Si-XII signal was again mapped out using Raman spectroscopy, as shown in Figure 3.2.1. As expected, the Si-XII signal was not suppressed in the center of the irradiated area, presumably because the local fluence never exceeded  $3.2 \text{ kJ/m}^2$ . However, the onset of Si-XII formation occurred at about  $1.9 \text{ kJ/m}^2$  rather than  $1.6 \text{ kJ/m}^2$ . To explain this, we observe that for both of the irradiated areas (with peak fluences of  $4.0$  and  $3.2 \text{ kJ/m}^2$ ), the surface texturing extends to lower local fluences than the Si-XII formation. Because surface texturing at low fluences is associated with surface melting and resolidification, this is evidence that surface melting alone is not sufficient to produce Si-XII. Rather, it appears that Si-XII develops only after textures are formed and then subsequently irradiated at fluences that produce melting and resolidification. If the local fluence corresponding to the onset of texturing is reduced for higher peak fluences (consistent with results reported in Chapter 2), then we would also expect the local fluence corresponding to additional cycles of melting on the surface texture, and thus the generation of Si-XII, to be reduced, as well, which is consistent with what we observe here.

When scanning the laser pulse train across the sample, Si-XII is present throughout the surface, even when the peak fluence of the pulse is above  $3.2 \text{ kJ/m}^2$ . For example, after scanning a silicon surface with 88 shots/area and a peak fluence of  $4.0 \text{ kJ/m}^2$ , the Si-XII signal is much greater than that produced by 88 stationary pulses with a local fluence of  $4.0 \text{ kJ/m}^2$ . This is explained by the fact that when scanning pulses across a surface to achieve 88 shots/area using a peak fluence of  $4.0 \text{ kJ/m}^2$ ,

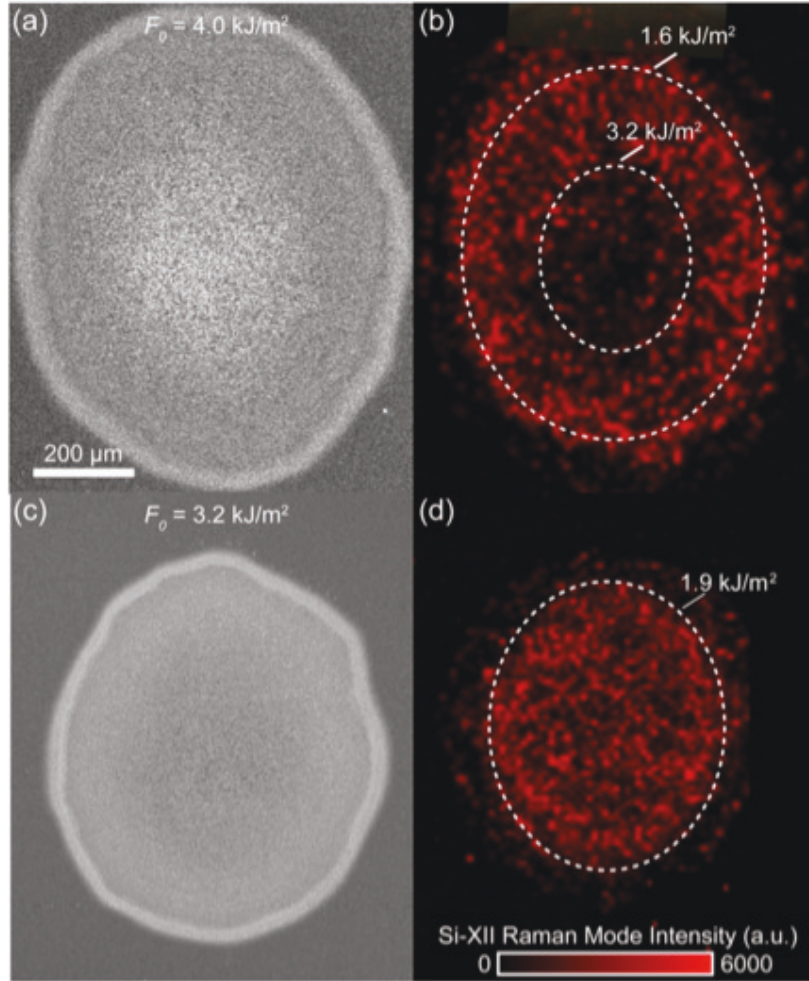


Figure 3.2.1: Map of Si-XII on irradiated silicon as determined by Raman spectroscopy. From [5].

the average site on the surface receives 88 exposures to local fluences between 2.0–4.0  $\text{kJ/m}^2$ , but over 300 pulses in the range 0.1–2.0  $\text{kJ/m}^2$ . Thus, the irradiation conditions between the stationary pulse sample and the scanned pulse sample are quite different, even though the irradiation parameters appear similar. To investigate this, a silicon surface was irradiated with a series of tranches of stationary pulses. After each tranche of pulses, the surface texture was imaged, the Si-XII content was mea-

sured, and the pulse fluence was reduced. In this way, we can observe the connection between pulse fluence, texturing, and Si-XII production. Figure 3.2.2 shows the fluence and number of pulses in each tranche, the texture produced after each tranche, and the Si-XII signal after each tranche. After 5 pulses at  $4.0 \text{ kJ/m}^2$  and 8 pulses at  $3.6 \text{ kJ/m}^2$ , the texture is poorly developed and no Si-XII is observed. Subsequently, after 12 pulses at  $3.2 \text{ kJ/m}^2$ , the surface texture is almost fully formed, but Si-XII is still not observed. Then, after 12 pulses at  $2.8 \text{ kJ/m}^2$ , the surface texture is fully developed, and a small amount of Si-XII (just above the noise floor) is detected. Finally, after 20 pulses at  $2.4 \text{ kJ/m}^2$ , 12 pulses at  $2.0 \text{ kJ/m}^2$ , and 20 pulses at  $1.6 \text{ kJ/m}^2$ , the surface texture is unchanged, but the Si-XII signal grows substantially. Again, these results show that it is not texturization per se that produces Si-XII, but rather low-fluence irradiation (sufficient to produce melting) on the textured surface. Indeed, through the texture formation process itself, little or no Si-XII is observed. Thus, if Si-XII is produced by stresses incurred during resolidification, then the surface morphology may be important in determining the magnitude and spatial distribution of such stresses.

In Figure 3.2.2, samples FM4 and FM5 have very similar surface morphologies, yet quite different amounts of Si-XII. To investigate whether this difference is apparent with microscopy, cross-sectional transmission electron microscope images were prepared from each sample, shown in Figure 3.2.3. We can see a 50–100 nm skin of amorphous silicon produced directly by melting and resolidification. Below this, within the core of the surface peaks, we see pockets of amorphous silicon, which are presumably pressure-induced. The fact that pressure-induced phase transformations

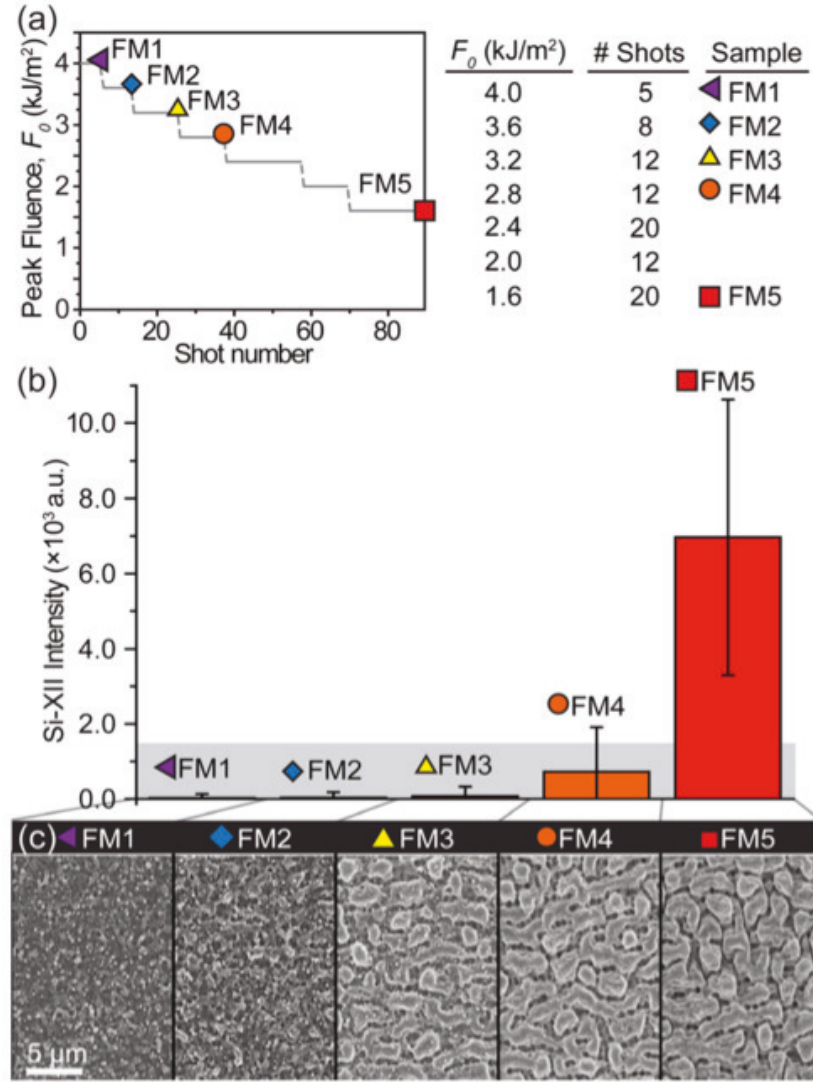


Figure 3.2.2: Tranches of stationary pulses with decreasing fluences, showing the surface texture and the Si-XII signal after each tranche. From [5].

are observed only within the surface peaks (and not below, for example, the surface valleys) indicates that the surface morphology plays an important role in giving rise to sufficient stresses to generate pressure-induced phases such as a-Si and Si-XII. Simulations of resolidification on textured surfaces are consistent with the formation of compressive stress at each side of the surface peak [71]. Although we can detect

Si-XII in FM5 using Raman spectroscopy, we are not able to identify it visually in the micrograph. Past, similar work has indicated that Si-XII forms in the same regions as a-Si, but can be difficult to detect visually due to its small volume and metastability [42]. Overall, the cross-sectional micrographs consistent with the hypothesis that Si-XII is formed by residual stresses produced by melting and resolidification on the textured silicon surface, with the region of greatest compressive stress localized in the core of the surface peaks.

### **3.2.3 Conclusions**

In this section, we reviewed the main results of a study on the origins of pressure-induced phase transformations in laser-irradiated silicon [5]. We saw that after fs-laser irradiation, amorphous silicon, Si-XII, and Si-III are often present in the silicon surface and be detected using Raman spectroscopy. Si-XII is associated with the melting and resolidification of the silicon surface after it has been textured and is suppressed at local fluences above  $3.2 \text{ kJ/m}^2$ . Scanned pulse samples and stationary pulse samples with the same apparent irradiation parameters are actually quite different in terms of the number and range of fluence exposures experienced by an average site on the surface. Because scanned pulse samples experience a large number of exposures at low fluences compared to exposures near the peak fluence, these samples often exhibit high levels of pressure-induced phases relative to stationary pulse samples. By irradiating a silicon surface with a sequence of stationary pulses, and reducing the fluence after each tranche of pulses, we see that the surface texture forms with little or no Si-XII present, and then subsequent irradiation at low fluences (sufficient



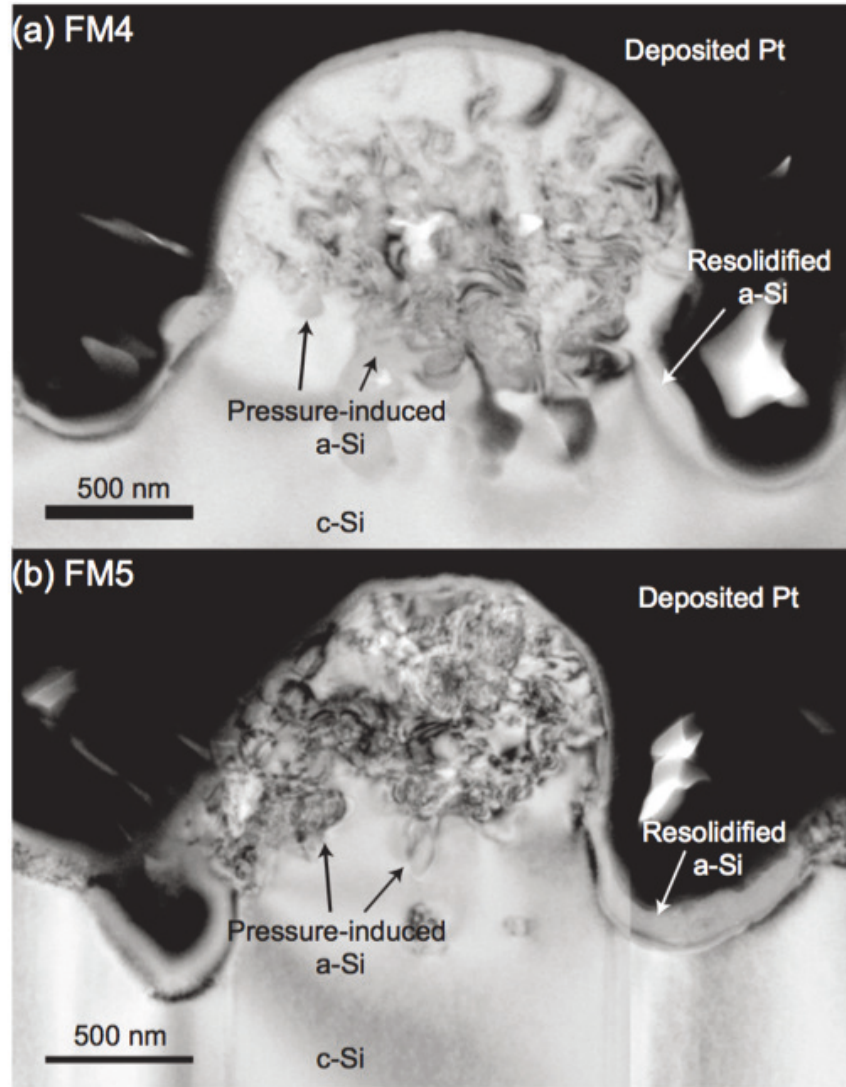


Figure 3.2.3: Cross-sectional transmission electron microscope images from samples FM4 and FM5 from Figure 3.2.2. Surface and pressure-induced amorphous silicon are visible in both samples. Raman spectroscopy shows the presence of Si-XII in FM5 although it cannot be seen visually in the micrograph. From [5].

to melt the surface) do not alter surface texture but do generate Si-XII. This Si-XII is detectable by Raman spectroscopy but is not easily visible in cross-sectional transmission electron micrographs. These micrographs show pockets of a-Si within

the core of the surface peaks, which is consistent with compressive stress generated by melting and resolidification on the textured surface. Overall, our results indicate that residual stresses from surface melting and resolidification are responsible for pressure-induced phases observed in fs-laser-irradiated silicon, rather than other pressure-generating mechanisms such as thermoelastic pressure or recoil shockwaves from surface ablation. It appears that for subsurface pressure-induced phases to form, such melting and resolidification must occur on a textured surface, rather than a flat surface. These results are relevant for the manufacture of optoelectronic devices with fs laser processing of silicon (for surface texturing and hyperdoping, for example), because pressure-induced phases are expected to affect the optoelectronic properties of the surface and can be difficult to remove from the surface due to their subsurface location.

### **3.3 Improving dopant incorporation during femtosecond-laser doping of Si with a Se thin-film dopant precursor**

#### **3.3.1 Introduction**

Here, we discuss the main results from “Improving dopant incorporation during femtosecond-laser doping of Si with a Se thin-film dopant precursor” (Applied Physics A 114, 2014) [6]. In this paper, we investigate the incorporation of a selenium (Se) thin film into the surface of silicon during fs laser irradiation in two fluence regimes: high

fluence ( $4.0 \text{ kJ/m}^2$ ) and low fluence ( $<1.5 \text{ kJ/m}^2$ ). The incorporation of Se into the surface, the surface morphologies, and the surface microstructures are distinct for these fluence regimes. At high fluences, the Se film is substantially removed before any texturing of the surface occurs. With increasing pulse number, nm-scale nodules are formed on the surface, which are doped with Se and contain a-Si, polycrystalline silicon (pc-Si), and crystalline silicon (c-Si). With additional pulses, the nodules transform to micrometer-scale mounds, which are largely composed of large-grained crystalline silicon but also contain pc-Si and a-Si. The mounds appear to form through the accumulation of material from melting and resolidification; after formation, however, it appears that material is removed from between the mounds by ablation. At low fluences, a portion of the Se film remains continuously intact on the surface, and irradiation by many pulses generates surface ripples with a period of around 600 nm. The surface ripples exhibit a 10–20 nm skin of Se-doped silicon, which is crystalline, with a Se doping concentration of around 1 at. %. This study illustrates the process by which Si is doped with thin films during fs laser irradiation and shows that different fs laser fluence regimes lead to different texture formation mechanisms, microstructures, and doping outcomes.

### **3.3.2 High fluence regime**

In the high fluence regime, a silicon wafer covered in a 75-nm thin film of Se was irradiated with 1, 2, 5, 10, 15, 20, 30, 50, and 100 stationary pulses with a peak fluence of  $4.0 \text{ kJ/m}^2$  in an atmosphere of 500 Torr  $\text{N}_2$ . After 1 pulse, much of the Se thin film had been removed, and the underlying silicon remained flat. Cross-sectional

transmission electron microscopy showed that a 2-nm Si oxide layer present beneath the Se layer, and below the oxide layer was a 10-nm layer of a-Si. The presence of a-Si indicates that the silicon surface was melted and resolidified while the native Si oxide layer remained intact, as shown in Figure 3.3.1. This is consistent with the observation in Chapter 2 that the surface texture appears to form underneath of the native oxide layer. The preservation of the oxide layer after melting suggests that for the Se to enter the underlying silicon, the oxide layer must be disrupted (e.g., through surface texturization). The removal of part of the Se film may be due to evaporation, because the evaporation temperature of Se is only 685 deg. C, compared to silicon's melting temperature of 1414 deg. C. Because much of the Se film is removed from the surface before texturization occurs, it is likely that subsequent doping of the surface is non-uniform.

After 5 pulses, we observe surface texturing consisting of nanometer-scale nodules on the surface, as shown in Figure 3.3.2. Transmission electron microscopy shows that these nodules are composed of c-Si, pc-Si, and a-Si, and energy-dispersive x-ray spectroscopy indicates that the nodules are doped with high concentrations of Se (2 at. %). The surface oxide layer is no longer visually apparent.

From 10–100 pulses, the surface morphology continues to evolve. After 10 pulses, some of the nodules transform to mounds about 1 micrometer in size. From 20–100 pulses, these mounds grow in size and cover the surface, as shown in Figure 3.3.3. After about 50 pulses, nm-scale nodules are no longer present. Profilometry shows that after 30 pulses these mounds grow to height of about 1.5 micrometers above the original silicon surface, indicating that they are formed by melting and

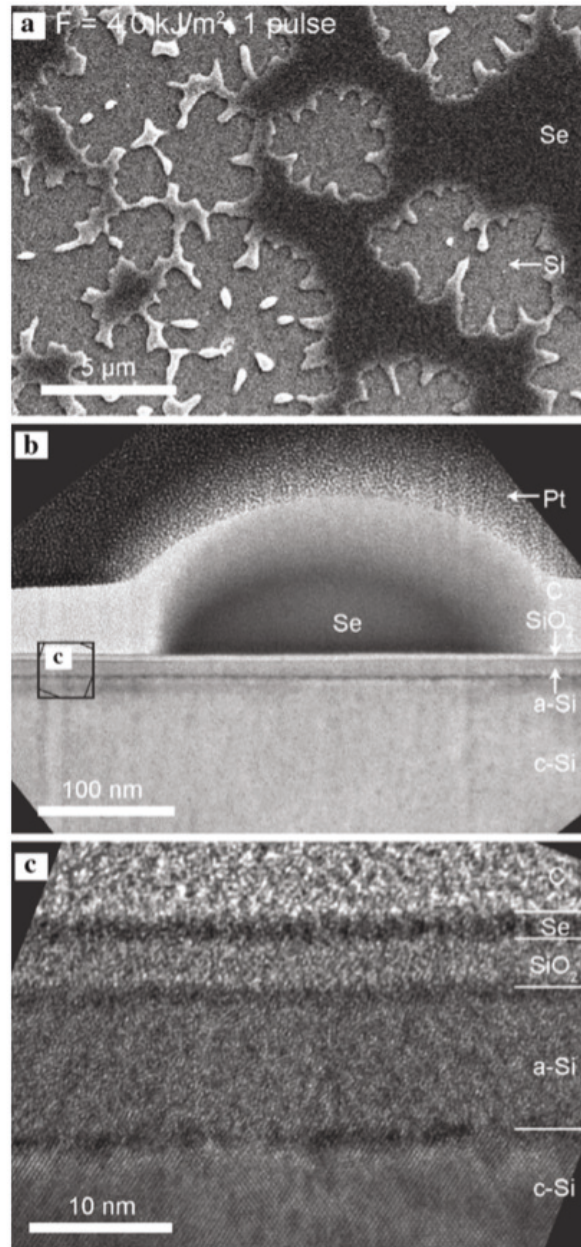


Figure 3.3.1: Scanning electron and transmission electron micrographs showing effect of one fs laser pulse at a fluence of  $4.0 \text{ kJ/m}^2$  on a silicon wafer covered with a 75-nm Se film. Much of the Se film is removed. Below the Se film is a 2-nm Si oxide layer overlying a 10-nm a-Si layer. From [6].

mass transfer rather than ablation. From 30–100 pulses, the apparent peak–valley height of the mounds continues to grow, although the absolute height of the mounds

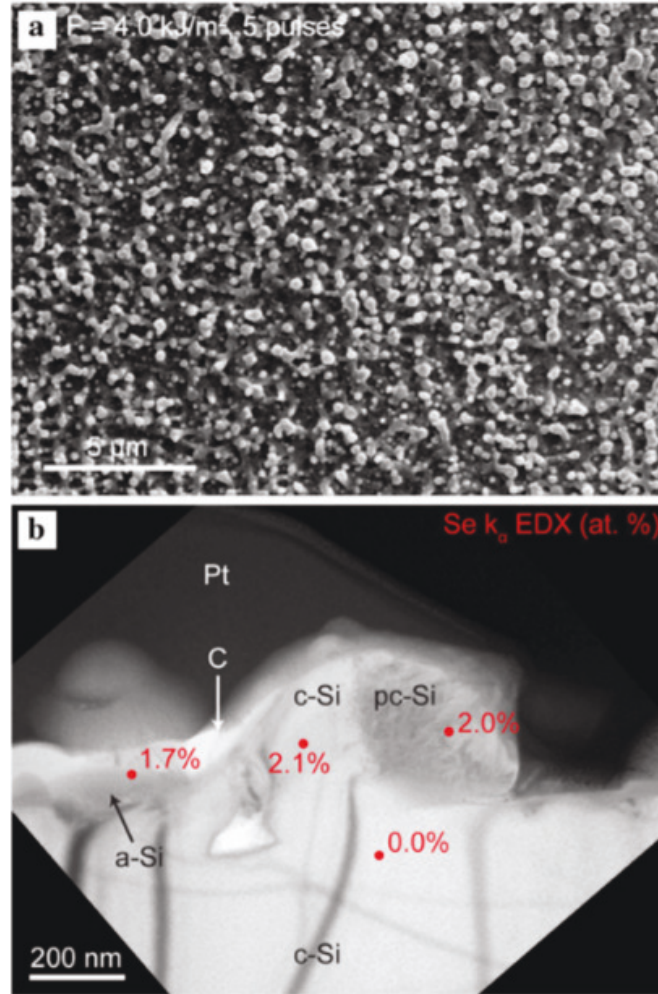


Figure 3.3.2: Scanning electron and transmission electron micrographs showing effect of five fs laser pulses at a fluence of 4.0 kJ/m<sup>2</sup> on a silicon wafer covered with a 75-nm Se film. Nanometer-scale nodules are formed, consisting of c-Si, pc-Si, and a-Si, and doped with 2 at. % Se. From [6].

compared to the original silicon surface declines by a few hundred nm, indicating that preferential ablation is occurring in the valleys between the mounds. Cross-sectional images of the mounds after 10, 20, and 50 pulses (shown in the figure below) show a similar microstructure for each of the mounds: micrometer-scale crystalline grains are predominant in the mounds, with small nm-scale crystalline grains at the base.



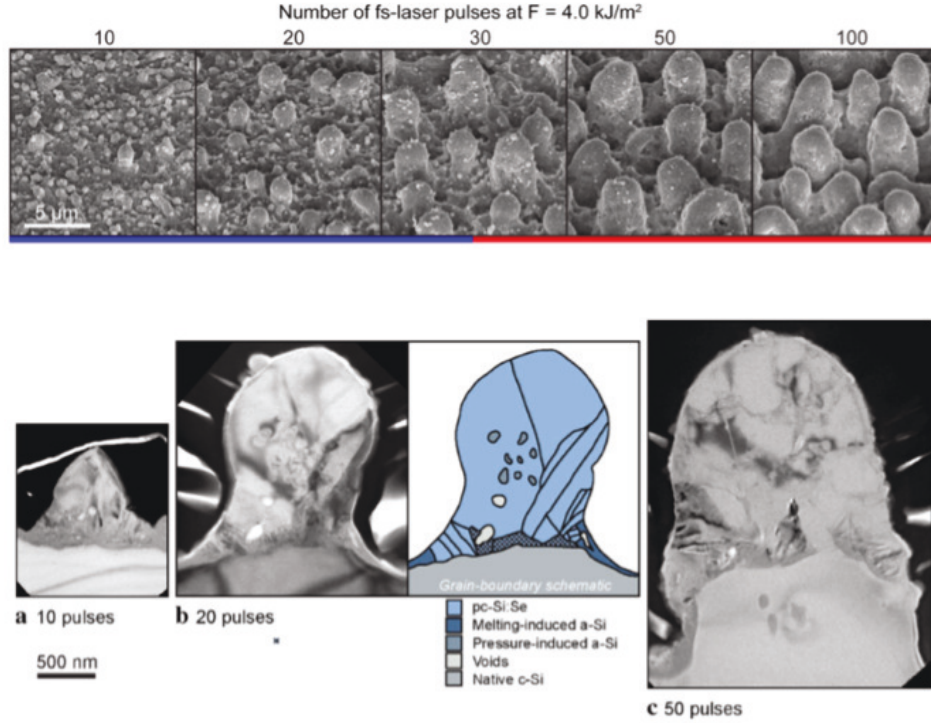


Figure 3.3.3: Top: Scanning electron micrographs (45 deg. angle) of surface showing evolving morphology from 10–100 pulses. Bottom: Transmission electron micrographs of surface mounds after 10, 20, and 50 pulses showing polycrystalline microstructure. From [6].

### 3.3.3 Low fluence regime

In the low fluence regime, a silicon wafer covered in a 75-nm thin film of Se was irradiated with 10 and 100 pulses with a fluence range of 1.3–1.7  $\text{kJ/m}^2$ . After 10 pulses at a local fluence of 1.3  $\text{kJ/m}^2$ , a 10-nm Se layer remained on the surface, overlying 2-nm Si oxide layer, overlying a 3-nm a-Si layer. Again, this indicates that a thin layer of Si has melted and resolidified, but the Si oxide layer acts as a barrier between the Se and the Si substrate. Although the Se film is reduced in thickness to 10 nm, it shows uniform coverage of the surface, indicating that subsequent doping of the surface may be uniform. After 100 pulses at a local fluence of 1.4  $\text{kJ/m}^2$ , we

observe laser-induced periodic surface structures (ripples) with a period of around 600 nm and a height of around 250 nm, as shown in Figure 3.3.4. The ripples are covered in a thin, 10–20 nm layer of Si doped to around 1 at. % with Se. The entire ripple structure, including the doped layer, appears to be crystalline, although the doped layer contains {111} stacking faults and some isolated nodules of a-Si are present overlying the doped layer. The doped layer appears to grow in thickness from about 10 nm to 20 nm between local fluences of 1.25 kJ/m<sup>2</sup> and 1.40 kJ/m<sup>2</sup>. The observation of doped and textured silicon that is crystalline indicates that the presence of Se might slow the resolidification velocity of the melt, leading to crystalline resolidification, or there might be some other mechanism that avoids the formation of a-Si. It is also interesting to note that this surface modification occurs below the single-pulse melting threshold of silicon of  $\sim 1.5$  kJ/m<sup>2</sup>, which is consistent with the greatly reduced modification threshold observed when using a Se thin film in Section 2.6.

### **3.3.4 Conclusions**

In this section, we discussed the main results from a study on the modification of silicon covered in a Se thin film. We saw that in the high fluence regime (4.0 kJ/m<sup>2</sup>), fs laser irradiation first removes much of the Se film, then produces doped textures on the surface which begin as nodules at the nm scale and grow to mounds at the micrometer scale over around 30 pulses. Beyond 30 pulses, material is ablated from the valleys between the mounds. The surface textures are composed primarily of polycrystalline material, with large grains near the top of the mounds and nm-scale



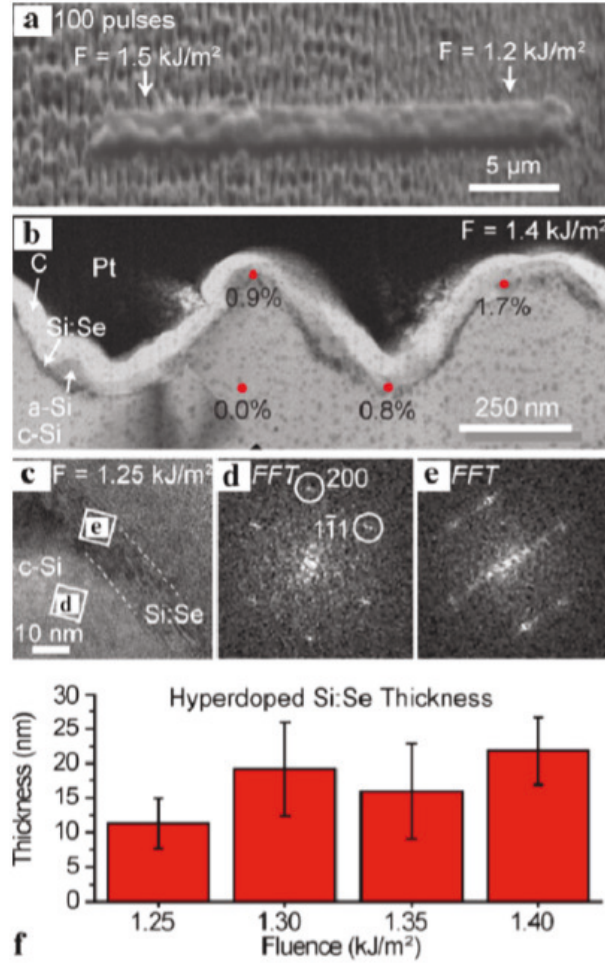


Figure 3.3.4: Irradiation of silicon covered in a 75-nm layer of Se with 100 pulses at local fluences of 1.3–1.7 kJ/m<sup>2</sup>. The transmission electron micrograph shows a cross-section of the ripple structure formed, which is crystalline and contains a 10–20 nm layer of Si doped with Se to around 1 at. %. The fast-Fourier transform (FFT) of the micrograph shows that the doped layer is crystalline but contains {111} stacking faults. From [6].

grains near the bottom of the mounds. Before texturization occurs, the silicon surface appears to be melted and resolidifies as a-Si, but the native Si oxide layer remains intact, separating the Se film from the underlying Si substrate. In the low-fluence regime (1.3–1.7 kJ/m<sup>2</sup>), the Se thin film is reduced in thickness to about 10 nm after 10 pulses but remains uniform over the silicon surface. After 100 pulses, periodic

surface ripples are generated, which exhibit an overlying 10–20 nm doped Si layer (1 at. % Se). The ripple structure, including the doped layer, appears to be crystalline. This study demonstrates that it is possible to uniformly dope a Si substrate with a thin film using fs laser irradiation, which could be useful for hyperdoped devices requiring dopant precursors in thin film form. Furthermore, in some fluence regimes, the surface may be textured and doped without substantial loss of crystallinity.

### **3.4 Conclusions of chapter**

In this chapter, we described two studies in which I participated as a coauthor [5,6]. Both studies examine the microstructures generated by fs laser irradiation of Si. The first study examines the mechanisms that produce pressure-induced Si phases during fs laser irradiation of Si in a nitrogen gas environment. The second study examines the microstructure produced by fs laser irradiation of Si covered in a Se thin film. Both studies show that, generally, fs laser irradiation produces a range of material phases before and during texturization, including amorphous silicon, polycrystalline silicon, and sometimes pressure-induced phases such as Si-XII and Si-III. These material phases present challenges for device fabrication, because they can interfere with desired device properties. In Chapter 4, we investigate how to regain high crystallinity after producing these multi-phase structures.

## Chapter 4

# Laser annealing of hyperdoped black silicon

### 4.1 Introduction to chapter

In this chapter, we investigate the use of laser annealing for improving the crystallinity of laser-processed silicon. High crystallinity is important for obtaining favorable optical and electronic properties [70], but traditional methods for obtaining high crystallinity in materials can be problematic for hyperdoped silicon. Thermal annealing, for example, causes dopant diffusion and optical deactivation of the hyperdoped material [47]. Chemical etching, another approach, often flattens the surface texture and may also remove the hyperdoped layer, which is typically coincident with the non-crystalline layer [43]. Laser annealing, in contrast, does not require removal of material and is based on melting and fast resolidification to a crystalline structure.

Here, we investigate the use of nanosecond lasers for laser annealing (Sections

4.2–4.4) as well as femtosecond lasers for laser annealing (Section 4.5). We also investigate annealing on a variety of surface textures, from 10-micrometer structures (Section 4.2) to 1-micrometer structures (Section 4.3) to sub-micrometer structures (Section 4.4). We use a variety of laser pulse durations and wavelengths, and we investigate the effects of laser annealing on the crystallinity, microstructure, electrical properties, and optical properties.

In general, we find that ns laser pulses smooth and crystallize the surface, remove amorphous and pressure-induced silicon phases, and maintain the material’s high sub-bandgap optical absorptance and light-trapping surface morphology. We find that if the fluence of the ns laser pulse is too high, then the surface textures are destroyed. However, we find that some ns laser fluences result in essentially complete crystallization of the surface without damaging the surface textures. Additionally, if thermal annealing is used (e.g., to increase the electrical rectification or material crystallinity)—thereby deactivating the sub-bandgap optical absorptance—ns laser annealing can be used subsequently to reactivate the sub-bandgap optical absorptance while maintaining high crystallinity. We also find that ns laser annealing does not interfere with the rectifying homojunction in hyperdoped black silicon. Thermal annealing and ns laser annealing can be combined in series to fabricate hyperdoped black silicon that has high crystallinity, high above-bandgap and sub-bandgap optical absorptance, and a rectifying homojunction. Because nanosecond laser annealing is based on physical processes of melting and fast resolidification, it could potentially be applied to other non-equilibrium material systems beyond hyperdoped black silicon [72, 73]. In contrast, with fs laser irradiation, we were not able to improve the

crystallinity of hyperdoped black silicon, but we estimate irradiation parameters for which such annealing might be possible.

The results in this chapter represent significant progress in addressing one of the longstanding challenges in fabricating laser-processed silicon: obtaining highly crystalline material. The nanosecond laser annealing process in particular is straightforward, robust to laser pulse duration and wavelength, and can be performed with high-throughput laser scanning systems. Thus, ns laser annealing of laser-textured and laser-doped silicon could be useful in experimental materials and device research as well as in industrial applications.

## **4.2 Nanosecond laser annealing of 10-micrometer surface textures**

### **4.2.1 Introduction**

Hyperdoped black silicon surface structures of size approximately 10 micrometers show strong light-trapping properties, yielding near-total optical absorptance both above and below the bandgap energy. Thus, these surface structures could be useful for efficient light collection in optoelectronic devices. However, after fabrication, these structures show the presence of amorphous silicon and pressure-induced phases typical of laser-fabricated black silicon. In this section, we use nanosecond laser pulses to remove these phases.

After nanosecond laser annealing, we find that the surface structures regain essentially complete crystallinity. They undergo nanometer-scale smoothing but largely

maintain their overall surface morphology and high optical absorptance. Additionally, after deactivating the sub-bandgap optical absorptance with thermal annealing, the absorptance is reactivated to near its original level by nanosecond laser annealing. Thermal annealing and nanosecond laser annealing can be combined in sequence to fabricate hyperdoped black silicon that simultaneously shows high crystallinity, high above-bandgap and sub-bandgap absorptance, and a rectifying electrical homojunction.

The content of this section has been previously published [7] and forms the basis of a patent application (see citations to previously published work on page ix of this thesis).

### **4.2.2 Methods**

We fabricated hyperdoped black silicon by irradiating a silicon wafer with fs laser pulses in the presence of sulfur hexafluoride ( $\text{SF}_6$ ) gas. A monocrystalline silicon wafer (p-type, boron-doped, 7–14 ohm-cm) was placed in a vacuum chamber which was evacuated to  $< 0.1$  Torr and then filled with sulfur hexafluoride gas to a pressure of 500 Torr. Femtosecond laser pulses (800 nm, 100-fs pulse duration, 1 kHz repetition rate) were output by a Ti:sapphire regenerative amplifier, passed through a computer-controlled mirror galvanometer, directed into the vacuum chamber, and focused onto the silicon surface so that a pulse diameter of 0.5–1 mm (full width at half maximum (FWHM) of the Gaussian pulse) was obtained. Each pulse had a peak fluence of  $8 \text{ kJ/m}^2$ , and the pulses were scanned across the silicon surface (as described by [5]) to obtain 200 shots/area. Each time  $4 \text{ cm}^2$  of the surface was irradiated, the vacuum

chamber was evacuated and refilled with new sulfur hexafluoride gas in order to prevent ablated particles from the silicon surface from accumulating in the chamber. The hyperdoped black silicon samples fabricated for this study were  $1 \times 1 \text{ cm}^2$  in area. Between batches of samples (groups of samples made on different days), we noticed some variation in the size and shape (e.g., the aspect ratio) of the resulting surface structures when using the same nominal fs laser irradiation parameters, which might result from uncertainties in estimating the fs laser pulse fluence or instabilities in our fs laser. These variations in surface structures caused variations in the optical absorptance between batches of samples. Therefore, we only directly compare samples from the same batch in optical absorptance measurements.

We irradiated the hyperdoped black silicon with ns laser pulses. Nanosecond laser pulses were generated by ArF (193 nm) and XeCl (308 nm, 25 ns FWHM pulse duration) excimer lasers and a Nd:YAG laser (355 nm, 4 ns FWHM pulse duration). The laser pulse fluence was controlled by focusing the beam to increase the fluence or by reflecting a portion of the beam off of a quartz window to decrease the fluence, and the pulses were passed through a metal mask with a  $2.5 \times 2.5 \text{ mm}^2$  square opening to improve the uniformity of the pulse intensity profile, resulting in uniform pulses with fluences of  $0.6\text{--}2.2 \text{ J/cm}^2$ . The laser pulses were scanned across the hyperdoped black silicon surface in ambient air. Typically, each site on the hyperdoped black silicon surface was exposed to a single nanosecond laser pulse, though exposures of up to 40 pulses were carried out to determine the effects of multiple exposures.

We measured the crystallinity of the hyperdoped black silicon surface using Raman spectroscopy. For Raman spectrum measurements, a 10 mW HeNe laser beam

(632.8 nm) was passed through a 50x objective lens (resulting in a spot diameter of 5 micrometers on the hyperdoped black silicon surface) and projected onto a CCD using a diffraction grating with 1200 grooves/mm, producing Raman spectra with a spectral wavenumber resolution of  $2.0 \text{ cm}^{-1}$ . After subtracting a baseline from the measured spectrum, the relative crystallinity of the hyperdoped black silicon surface was determined by dividing the area under the spectral curve from 470–490  $\text{cm}^{-1}$  (containing the broad transverse-optical vibrational mode of amorphous silicon centered at 480  $\text{cm}^{-1}$  [74]) by the area under the spectral curve from 515–525  $\text{cm}^{-1}$  (containing the sharp optical vibrational mode of crystalline silicon at 520  $\text{cm}^{-1}$  [75]). We also measured the width (FWHM) of the crystalline silicon peak at 520  $\text{cm}^{-1}$ . Results from pristine monocrystalline silicon wafers were used as references. Measurements from each sample were averaged between 100 spectra collected within a  $15 \times 15 \text{ }\mu\text{m}^2$  grid in order to account for possible variations over the surface.

We investigated the surface morphology of the hyperdoped black silicon using a field emission scanning electron microscope (FESEM). Samples were imaged at an angle of 45 degrees without foreshortening correction, using an accelerating voltage of 3 kV and a working distance of 16 mm.

We investigated the microstructure of the hyperdoped black silicon using cross-sectional bright field transmission electron microscopy (BF-TEM) and selected area diffraction (SAD). TEM samples were prepared by lift-out in a dual-beam FIB/SEM. Protection layers of carbon and platinum were deposited in situ prior to lift-out. Thinning steps were performed at 30 kV with the final thinning at 5 kV, which has been shown to leave 2.5 nm of amorphous surface damage in silicon [76]. TEM and



SAD were performed with a field emission TEM operated at 200 kV. For imaging of bend contours, BF-TEM images were obtained several degrees off the  $[110]$  zone axis with an objective aperture to enhance diffraction contrast.

We measured the optical absorptance of the hyperdoped black silicon using an ultraviolet-visible-near infrared (UV-VIS-NIR) spectrophotometer (for wavelengths of 0.4–2.5  $\mu\text{m}$ ) and a Fourier transformed infrared (FTIR) spectrometer (for wavelengths of 2.4–10.0  $\mu\text{m}$ ). Reflectance ( $R$ ) and transmittance ( $T$ ) spectra were measured with integrating spheres and were used to calculate the optical absorptance ( $A = 1 - R - T$ ). The FTIR spectra were matched to the spectrophotometer spectra in the overlapping wavelength range (2.4–2.5  $\mu\text{m}$ ).

We measured the current-bias behavior of the hyperdoped black silicon with a probe station and parametric analyzer. To apply metal electrodes to the samples, we cleaned the samples in solvents (acetone, isopropanol, and water), defined four 2x2 mm<sup>2</sup> square regions with photoresist on the hyperdoped black silicon surface, carried out a plasma clean to remove organic debris (75 W, 40 sec., 40 sccm O<sub>2</sub>), dipped the sample in hydrofluoric acid (HF) to remove the native surface oxide (5% HF solution, 1 min.), used electron beam evaporation to deposit Ti, Ni, and Ag (20 nm, 20 nm, and 200 nm thicknesses, respectively) on the hyperdoped black silicon surface in sequence, used thermal evaporation to deposit Al (200 nm thickness) on the silicon wafer surface reverse of the hyperdoped black silicon surface, lifted off the remaining photoresist in heated acetone (80 deg. C), and cleaned the samples in solvents (acetone, isopropanol, and water). After electrode deposition, rapid thermal annealing (200–500 deg. C., 30 sec., N<sub>2</sub> atmosphere) was used to obtain ohmic contact between the electrodes and

the silicon surface. To measure the current-voltage behavior of the hyperdoped black silicon, samples were placed on a metal chuck (with the Al electrode in contact with the chuck), and a tungsten probe was placed in contact with one of the Ti-Ni-Ag electrodes on the hyperdoped black silicon surface. The bias between the chuck and the probe was swept from  $-20$  V to  $+20$  V and the resulting current was measured. The four electrodes on each hyperdoped black silicon sample were used to check the consistency of the measurements. A pristine silicon wafer with Al electrodes on both sides was used as a reference.

We used thermal annealing to crystallize the hyperdoped black silicon and deactivate its sub-bandgap optical absorptance. Samples were thermally annealed in a tube furnace at  $700$  deg. C for  $30$  min. in forming gas ( $95\%$   $N_2$ ,  $5\%$  H,  $300$  sccm).

To test the effects of combining thermal annealing and ns laser annealing in sequence, we fabricated hyperdoped black silicon with fs laser irradiation, thermally annealed the sample ( $700$  deg. C.,  $30$  min., forming gas atmosphere), performed ns laser annealing ( $355$  nm Nd:YAG pulse,  $1.1$  J/cm<sup>2</sup> fluence), deposited metal electrodes onto the sample, rapidly thermally annealed the sample ( $500$  deg. C.,  $30$  sec.,  $N_2$  atmosphere), and performed ns laser annealing again. Between each step, we measured the sample's crystallinity and current-bias behavior. We also measured the optical absorptance between each step on an identical sample that underwent the same process without deposition of metal electrodes, which would have interfered with the optical absorptance measurements.

### 4.2.3 Results

Fabrication with a fs-laser pulse fluence of  $8 \text{ kJ/m}^2$  yielded hyperdoped black silicon with a rough surface morphology consisting of nm-scale granular structures overlying  $\mu\text{m}$ -scale conical structures, as shown in Figure 1. The nm-scale granular structures might have originated as particulate debris generated by laser ablation and deposited onto the silicon surface during the fs laser irradiation process [77,78]. The  $\mu\text{m}$ -scale conical structures in our hyperdoped black silicon were about  $10 \mu\text{m}$  tall and  $5 \pm 2 \mu\text{m}$  wide at the base, with variation between individual cones. The cones had an elliptical base, perhaps due to the linear polarization of the laser beam, with the base width about twice as great in one dimension as in the orthogonal dimension. BF-TEM images showed a thin, 50–100 nm skin layer of amorphous material on the surface of the conical structures as well as contrast-producing features within the conical structures, which may be small pockets of amorphous silicon [42]. Consistent with previous studies, the hyperdoped black silicon showed amorphous silicon and pressure-induced crystalline silicon phases in Raman spectra [5,42], near-unity optical absorptance of above- and below-bandgap photon energies [8], and deactivation of sub-bandgap absorptance after thermal annealing [8].

Nanosecond laser annealing of hyperdoped black silicon resulted in nm-scale smoothing of the surface, leaving the  $10\text{-}\mu\text{m}$ -scale conical structures intact, as shown in Figure 4.2.1. After ns laser annealing, diffraction contrast imaging and SAD indicated that the surface was single-crystalline. Nanosecond laser annealing also removed most of the contrast-producing features within the conical structures.

Nanosecond laser annealing removed the amorphous and pressure-induced crys-

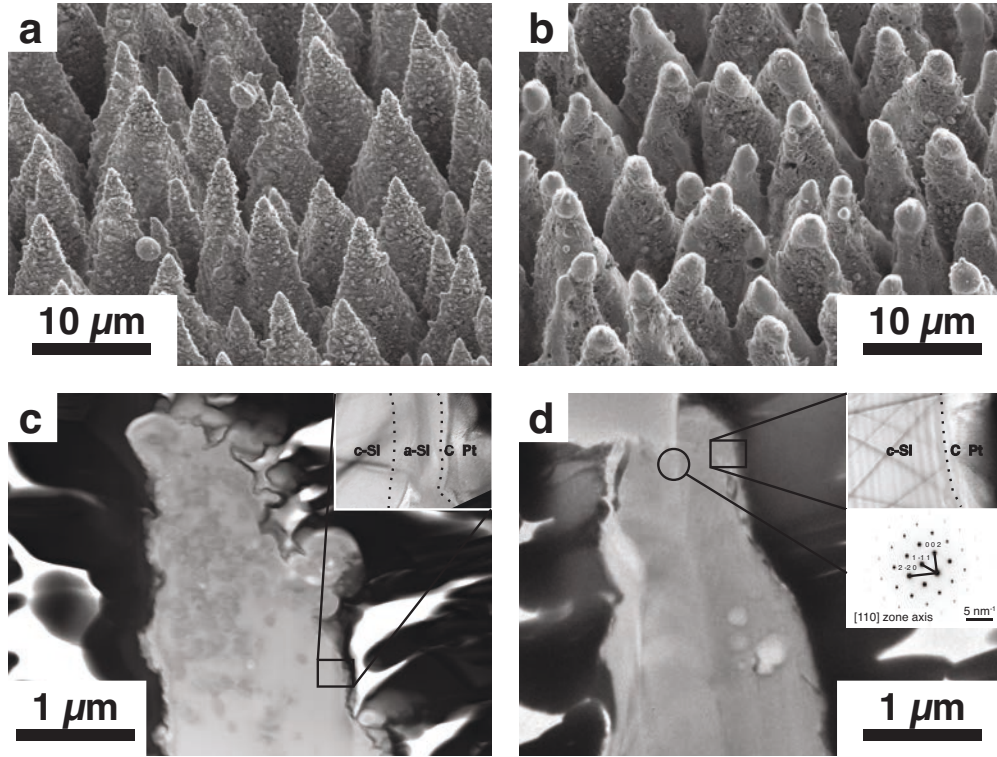


Figure 4.2.1: a: Hyperdoped black silicon (fabricated with a fs-laser pulse fluence of  $8 \text{ kJ/m}^2$ ) with nm-scale granular structures overlying conical structures about  $10 \text{ }\mu\text{m}$  in height and  $5 \pm 2 \text{ }\mu\text{m}$  in width. (Image obtained at 45-degree angle without foreshortening correction.) b: Nanosecond laser annealing (here, with a fluence of  $2.2 \text{ J/cm}^2$ ) causes smoothing of the nm-scale granular structures while keeping the  $10\text{-}\mu\text{m}$ -scale conical structures intact. c: Cross-section of a conical surface structure before ns laser annealing shows nm-scale surface roughness and contrast-producing pockets within the conical surface structure. BF-TEM imaging of the surface with enhanced diffraction contrast (inset indicated by box  $300 \text{ nm}$  wide) shows an amorphous skin (a-Si)  $50\text{--}100 \text{ nm}$  thick between the crystalline core (c-Si) and the protective carbon and platinum layers (C, Pt). In this imaging mode, bend contours are observed in the crystalline core but do not appear in the amorphous skin. d: Cross-section of a conical surface structure after ns laser annealing (again, with a fluence of  $2.2 \text{ J/cm}^2$ ) shows smoothing of nm-scale surface roughness and removal of contrast-producing pockets within the conical surface structure. BF-TEM imaging of the surface (upper inset indicated by box  $300 \text{ nm}$  wide) shows crystalline material throughout. Selected area electron diffraction (lower inset indicated by circled area) indicates that the core is single crystalline ([110] zone axis). From [7].

talline silicon phases shown in Raman spectra, as shown in Figure 4.2.2 [42]. The lowest ns pulse fluence we investigated ( $0.6 \text{ J/cm}^2$ ) was adequate to remove the pressure-induced crystalline silicon phases completely. The amount of amorphous silicon shown in Raman spectra decreased as the ns pulse fluence was increased, with pulse fluences greater than about  $1.0 \text{ J/cm}^2$  yielding nearly undetectable amounts of amorphous silicon, shown in Figure 4.2.3. The decrease in amorphous silicon did not depend on the number of pulses (1–40 pulses), the pulse wavelength (193, 308, or 355 nm), or the pulse duration (4 or 25 ns). Nanosecond laser annealing also reduced the width (FWHM) of the crystalline silicon peak at  $520 \text{ cm}^{-1}$  by about  $1 \text{ cm}^{-1}$ , as shown in Figure 4.2.3 inset. For example, the FWHM of the crystalline silicon peak was reduced from  $8.4 \pm 0.3 \text{ cm}^{-1}$  (before ns laser annealing) to  $7.3 \pm 0.3 \text{ cm}^{-1}$  (after ns laser annealing at fluences above  $1.5 \text{ J/cm}^2$ ). Even after ns laser annealing, the peak width remained greater than that measured from pristine monocrystalline silicon ( $6.8 \pm 0.1 \text{ cm}^{-1}$ ). The peak width we measured in monocrystalline silicon was greater than values reported in the literature [75], which could be due to the low spectral resolution of our Raman measurements. Nonetheless, we consistently observed a reduction in peak width after ns laser annealing of about  $1 \text{ cm}^{-1}$ .

The optical absorptance of hyperdoped black silicon, including its sub-bandgap optical absorptance, remained high after ns laser annealing, as shown in Figure 4.2.4. For example, after ns laser annealing with a pulse fluence of  $2.2 \text{ J/cm}^2$  (the highest fluence we investigated), the above-bandgap absorptance (which was about 95%) remained unchanged, and the sub-bandgap absorptance (which was greater than 90%) increased slightly.

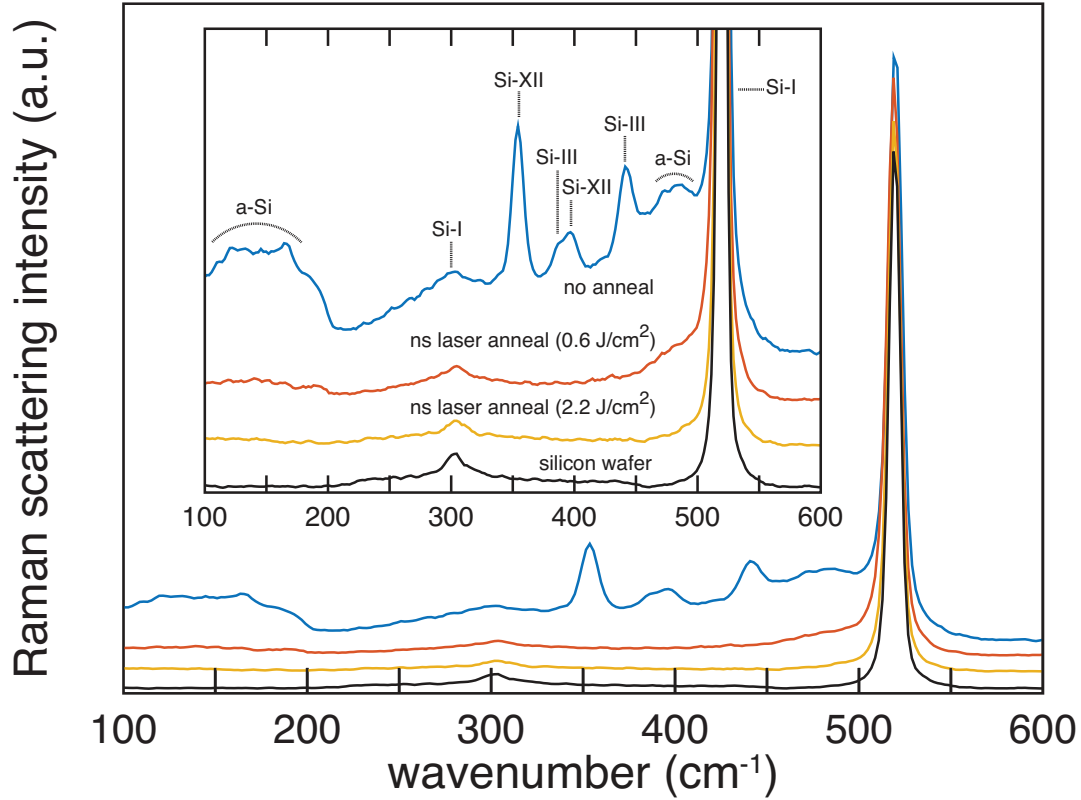


Figure 4.2.2: Stokes Raman spectra of hyperdoped black silicon (fabricated with a fs-laser pulse fluence of  $8 \text{ kJ/m}^2$ ) before and after ns laser annealing (normalized and offset to show individual spectra). The rescaled inset highlights Raman modes corresponding to amorphous silicon (a-Si), pressure-induced crystalline phases (Si-III and Si-XII), and conventional crystalline silicon (Si-I). (Smith, Lin et al., 2011) Nanosecond laser annealing at low fluence ( $0.6 \text{ J/cm}^2$ ) removed the pressure-induced crystalline phases and much of the amorphous silicon, while ns laser annealing at high fluence ( $2.2 \text{ J/cm}^2$ ) removed the pressure-induced crystalline phases and nearly all of the amorphous silicon. From [7].

Obtaining consistent current-bias measurements required rapid thermal annealing at  $500 \text{ deg. C}$  for 30 sec. after electrode deposition. This rapid thermal annealing shifted the diode turn-on voltage (defined as the point of greatest curvature in the current-bias curve) from  $0.2 \pm 0.1 \text{ V}$  to  $0.5\text{--}1.5 \text{ V}$  (with some variation between sam-

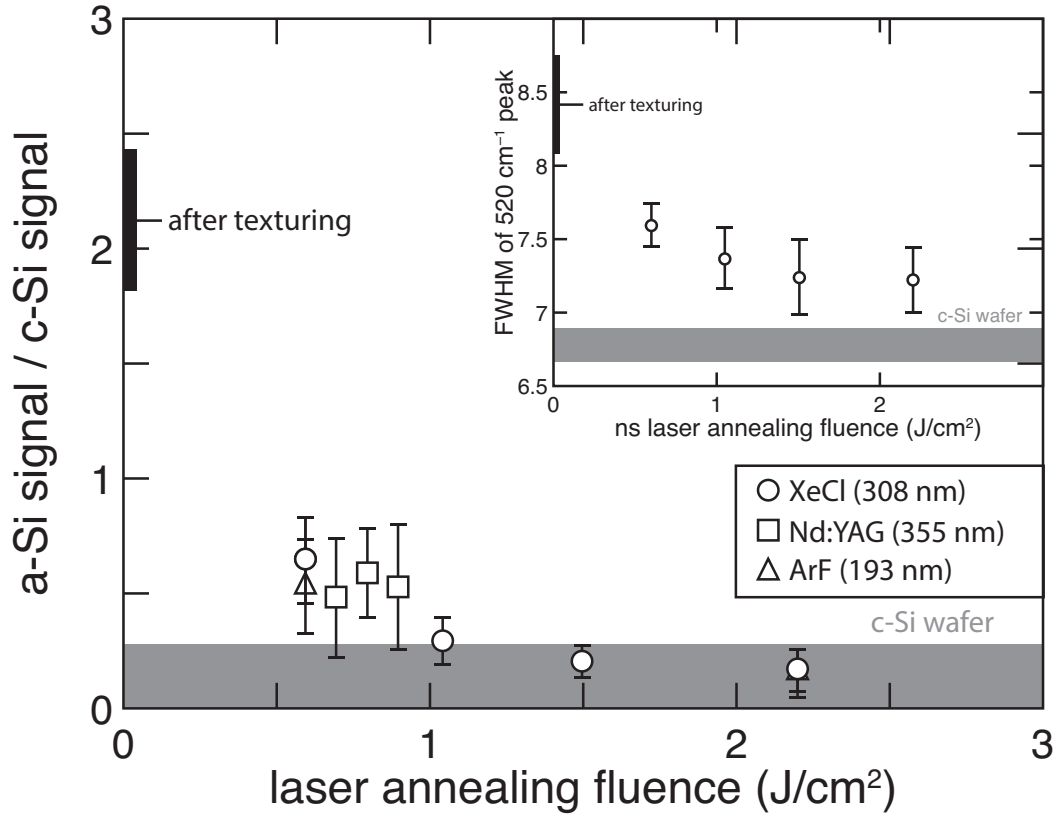


Figure 4.2.3: Raman spectra indicate that ns laser annealing can increase the crystallinity of hyperdoped black silicon (fabricated with a fs-laser pulse fluence of 8 kJ/m²) near to that of monocrystalline silicon (gray box). The amount of crystallization increases with the ns laser pulse fluence. Additionally, the width (FWHM) of the crystalline silicon Raman peak at 520 cm⁻¹ decreases with increasing ns laser pulse fluence (inset). From [7].

ples), shown in Figure 4.2.5. Rapid thermal annealing before electrode deposition had no effect on the current-bias measurements. Rapid thermal annealing did not decrease the presence of amorphous silicon, but it did decrease the sub-bandgap optical absorptance, with higher annealing temperatures decreasing the absorptance further. Nanosecond laser annealing did not affect electrical current-bias behavior, as shown in Figure 4.2.6. Rectification ratios of  $50 \pm 20$  at  $\pm 10$  V were obtained.

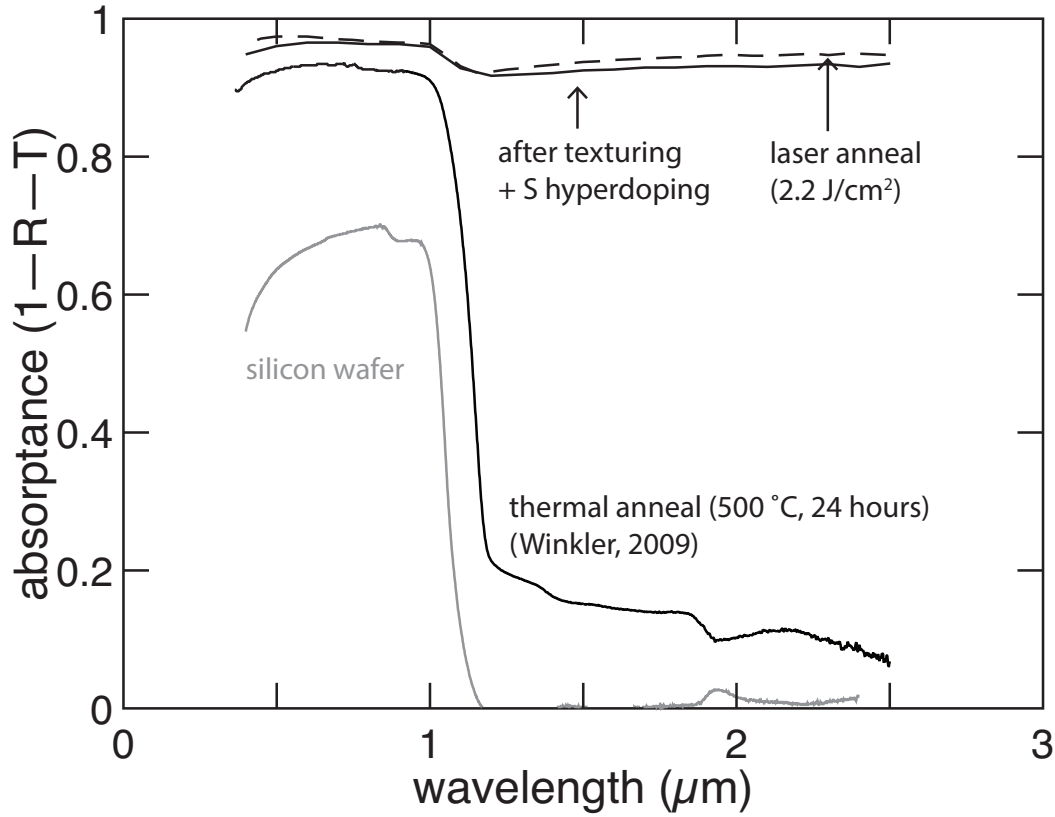


Figure 4.2.4: Nanosecond laser annealing (here, with a fluence of  $2.2 \text{ J/cm}^2$ ) preserves the high above-bandgap and sub-bandgap optical absorbance produced by the light-trapping surface as long as the surface structures are sufficiently large (here, around  $10 \text{ } \mu\text{m}$  tall and  $5 \pm 2 \text{ } \mu\text{m}$  wide at the base). This is in contrast to thermal annealing (Winkler, 2009 [1]), which deactivates the sub-bandgap optical absorbance. From [7].

After thermal annealing deactivated the sub-bandgap optical absorbance, ns laser annealing reactivated the sub-bandgap optical absorbance near to its original level. For example, after thermal annealing at  $700 \text{ deg. C}$  for 30 min., the sub-bandgap optical absorbance ( $1.2\text{--}4.0 \text{ } \mu\text{m}$  wavelengths) was reduced from about 80% to about 20%, as shown in Figure 4.2.7, and the amount of amorphous silicon was reduced to an undetectable level. Subsequent ns laser annealing with a pulse fluence of  $1.1$



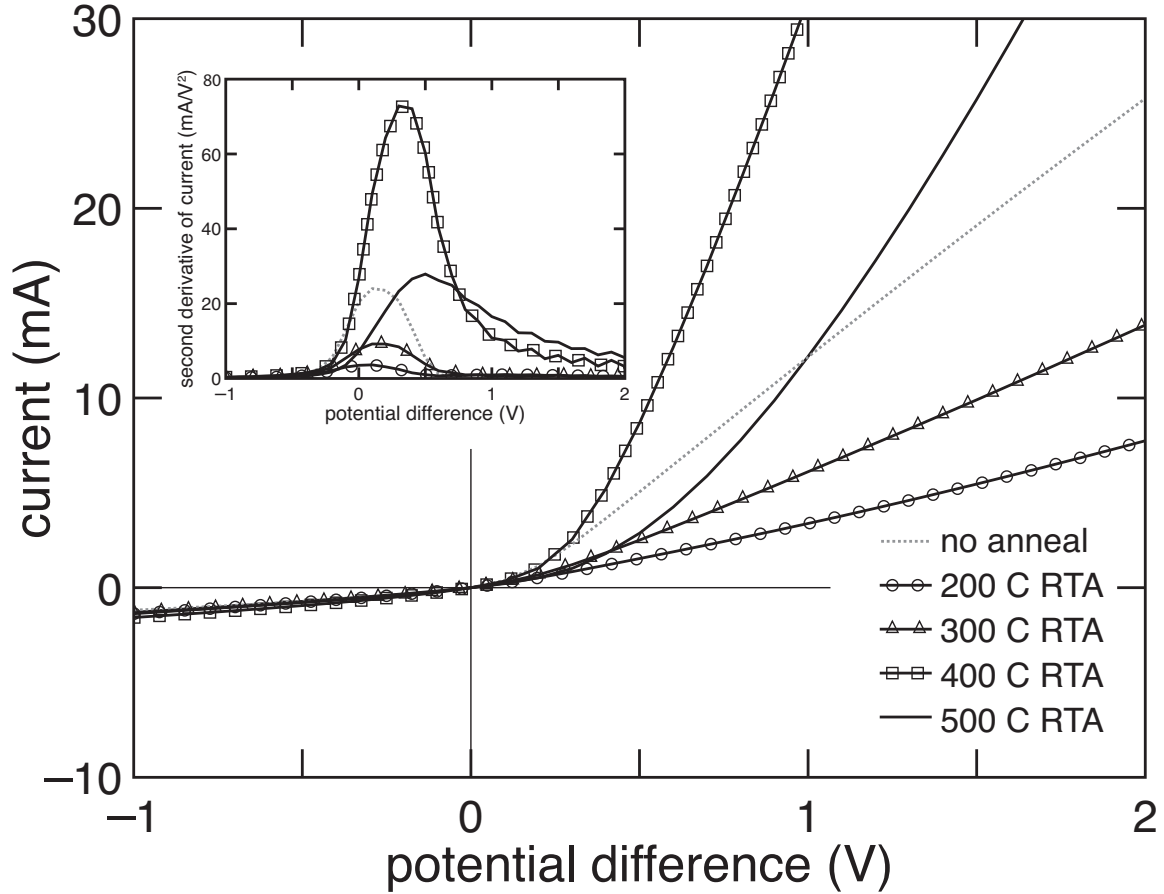


Figure 4.2.5: The turn-on voltage of hyperdoped black silicon diodes (fabricated with a fs-laser pulse fluence of  $8 \text{ kJ/m}^2$ ) is increased by rapid thermal annealing (RTA) after electrode deposition. Higher rapid thermal annealing temperatures up to 500 deg. C (for 30 sec.) produce higher turn-on voltages (inset). Turn-on voltages of around 0.2 V are typical of Schottky diodes (Card and Rhoderick, 1971), while turn-on voltages of around 0.7 V are typical of silicon homojunction diodes (Pearson and Sawyer, 1952). From [7].

$\text{J/cm}^2$  restored the sub-bandgap optical absorptance to 70-80% (with a broad sub-bandgap absorption peak at a wavelength of  $2.0 \pm 0.8$  micrometers) while maintaining high crystallinity. Subsequently, rapid thermal annealing reduced the sub-bandgap absorptance to about 60%. Finally, ns laser annealing again restored the sub-bandgap absorptance to 70–80%. The samples in Figure 4.2.7 exhibit slightly lower optical

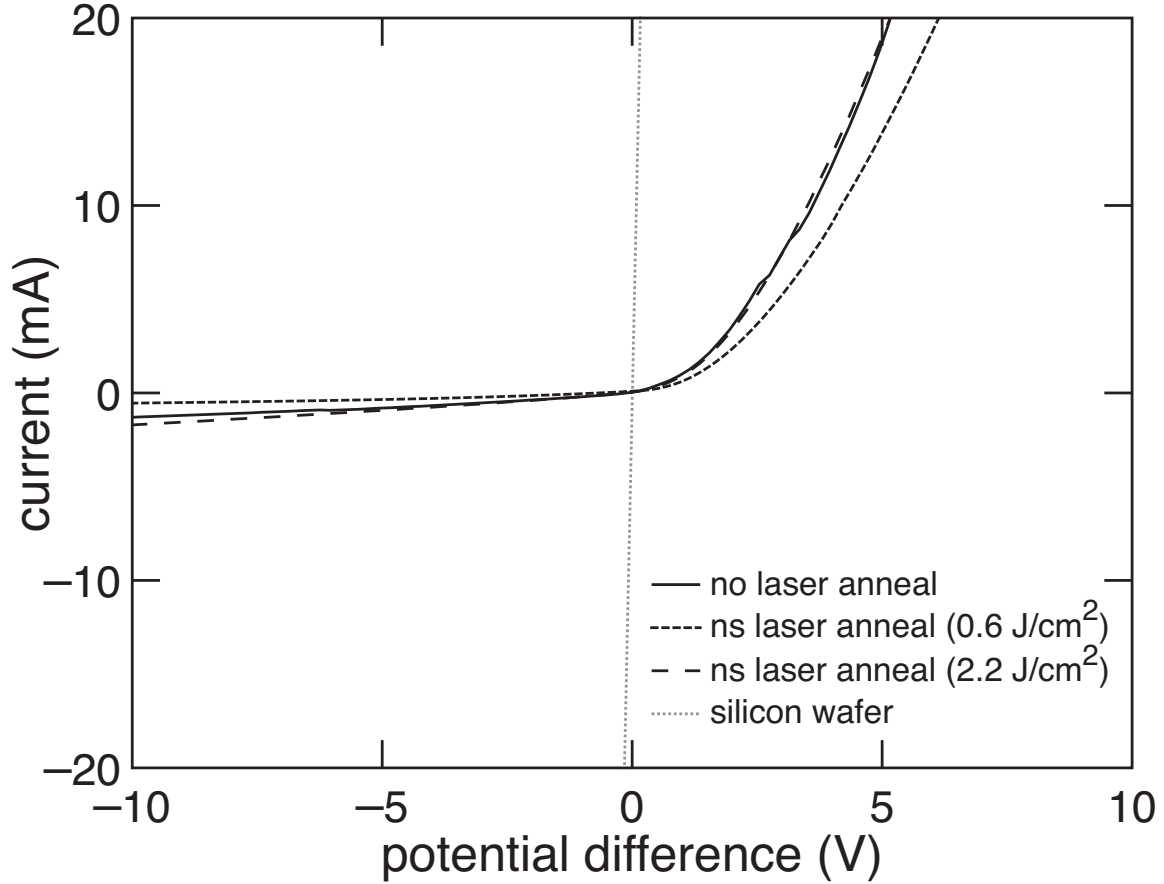


Figure 4.2.6: Electrical rectification in hyperdoped black silicon diodes (fabricated with a fs-laser pulse fluence of  $8 \text{ kJ/m}^2$ ) is maintained after ns laser annealing. All diodes underwent rapid thermal annealing (RTA) at 500 deg. C (for 30 sec.) after electrodes were deposited. From [7].

absorptance than the samples in Figure 4.2.4 due to variations in surface structure size between batches of samples. As a result, we only directly compare samples from the same batch.

#### 4.2.4 Discussion

Nanosecond laser annealing produces three notable effects: smoothing the surface on the nm scale, converting amorphous and pressure-induced silicon phases to con-

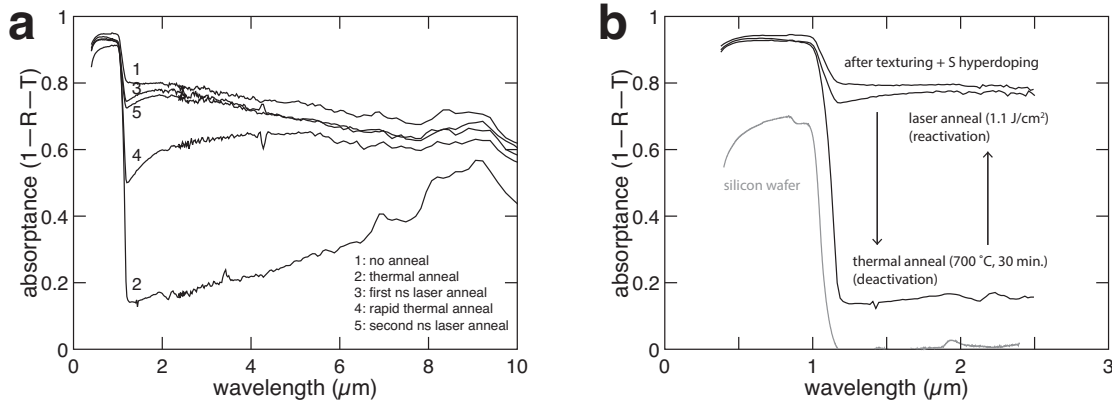


Figure 4.2.7: a: The effects of thermal and ns laser annealing in sequence on the optical absorbance. 1) Femtosecond-laser-fabricated hyperdoped black silicon exhibits high above-bandgap and sub-bandgap optical absorbance. 2) Thermal annealing (700 deg. C, 30 min.) crystallizes the hyperdoped black silicon but deactivates its sub-bandgap optical absorbance. 3) Nanosecond laser annealing (here, with a fluence of  $1.1 \text{ J/cm}^2$ ) maintains the high crystallinity while reactivating the sub-bandgap optical absorbance near to its original level. 4) Rapid thermal annealing (500 deg. C, 30 sec.) after depositing electrodes again deactivates (partially) the sub-bandgap optical absorbance. 5) Nanosecond laser annealing again reactivates the sub-bandgap optical absorbance near to its original level. The final hyperdoped black silicon diodes are highly crystalline, highly optically absorbing, and electrically rectifying. b: Detail of deactivation and reactivation of absorbance. From [7].

ventional crystalline silicon (Si-I), and placing or maintaining the dopant atoms in optically active, non-equilibrium positions. These effects are analogous to the effects of ns pulsed laser melting on flat silicon hyperdoped by ion implantation, which also include crystallizing the surface and placing or maintaining the dopant atoms in optically active, non-equilibrium positions. In flat silicon hyperdoped by ion implantation, a series of ns laser pulses can be used to melt the surface (which is amorphous after ion implantation) to a depth reaching the non-hyperdoped, crystalline silicon substrate. Resolidification of the melt initiates from the substrate-liquid interface,

moves toward the surface (under some conditions epitaxially), and traps the dopant atoms in optically active, non-equilibrium positions within the crystal, producing crystalline hyperdoped silicon. The key to obtaining crystalline hyperdoped silicon that exhibits sub-bandgap optical absorptance is to produce a resolidification velocity that is less than the amorphization velocity of silicon (15 m/s [79]) but still sufficiently high to produce solute trapping [23]. With this method, a thin layer (e.g., 200 nm) of single-crystal hyperdoped silicon can be obtained. Processes that can interfere with the formation of single-crystal hyperdoped silicon include cellular breakdown (which can result in columnar crystals separated by dopant-rich boundaries) [80,81] and explosive crystallization of amorphous silicon (which can result in polycrystalline silicon containing nanometer-scale grains) [82]. The physical processes that occur during ns laser annealing of hyperdoped black silicon appear similar to but more complex than these processes that occur during ns pulsed laser melting of flat hyperdoped silicon.

From cross-sectional TEM images of the conical surface structures (Figure 4.2.1), we estimate that after fabrication with fs laser irradiation, the surface is covered with a 50–100 nm skin of amorphous, sulfur-bearing silicon. Below this skin layer and within the conical surface structures, contrast-producing features are visible, which could be pockets of amorphous silicon within the crystalline silicon matrix, as indicated by previous studies [42]. The removal of these contrast-producing features could be the result of heat diffusion into the conical surface structures during ns laser annealing. We infer that after ns laser annealing, the black silicon surface contains a skin of crystalline hyperdoped silicon, because BF-TEM imaging, SAD, and Raman spectra all indicate that the surface is crystalline, and the strong sub-bandgap optical

absorptance indicates that the surface is hyperdoped. In future work, it would be interesting to investigate the effect of ns laser annealing on the distribution of dopant atoms by using, for example, three-dimensional atom probe or other tomographic methods [83].

We estimate the melting depth from ns laser annealing with a fluence of  $1.0 \text{ J/cm}^2$  to be about 100 nm on hyperdoped black silicon with  $10\text{-}\mu\text{m}$ -scale structures, because the amorphous skin on the surface after fabrication with fs laser irradiation appears to be 50–100 nm thick, and after ns laser annealing at fluences above  $1.0 \text{ J/cm}^2$ , little-to-no amorphous silicon is detected (Figure 4.2.3). To verify this estimate, we compare it to the average melting depth expected from geometric optics. We stress that the laser intensity at the surface might be very inhomogeneous due to surface reflections and other effects. We do not discuss these effects in detail here; our aim, rather, is to determine whether 100 nm is a reasonable estimate for the average melting depth. The melting threshold fluence for ns laser irradiation of flat amorphous silicon (248 nm wavelength) has been reported as  $0.1\text{--}0.2 \text{ J/cm}^2$  [84–86], which we have verified in laser-induced melting simulations. However, the conical surface structures increase the surface area of black silicon relative to flat silicon and thus reduce the average effective fluence of the laser pulse, in this case by a factor of about 4 (because surface cones with a height of  $10 \mu\text{m}$  and a diameter of  $5 \mu\text{m}$  increase the surface area by a factor of 4). At the same time, the surface reflectance of the amorphous silicon is decreased from 0.6 [86] to 0.1 due to light-trapping, indicating that about twice as much energy is absorbed by a hyperdoped black silicon surface than by a flat amorphous silicon surface for a given laser pulse fluence. Therefore,

we estimate an average melting threshold fluence for our hyperdoped black silicon of 0.2–0.4 J/cm<sup>2</sup>, and that a ns laser pulse fluence of 1.0 J/cm<sup>2</sup> on the hyperdoped black silicon we examined produces an average melting depth similar to that produced by a ns laser pulse with a fluence of 0.25–0.5 J/cm<sup>2</sup> on flat amorphous silicon. Indeed, reported simulations and experiments indicate that this fluence range on flat amorphous silicon yields melting depths of 50–150 nm [84], in agreement with our estimate of 100 nm. The melting depths at the peaks of the conical surface structures and in the valleys between the structures could be expected to be greater than our estimate, as these surfaces are closer to normal incidence to the ns laser pulses than are the side walls of the conical surface structures. Indeed, the most prominent melting visible in SEM images of the surface after ns laser annealing appears at the peaks of the surface structures. Because crystalline silicon has a higher melting threshold than amorphous silicon (0.7–0.8 J/cm<sup>2</sup> compared to 0.1–0.2 J/cm<sup>2</sup>), as well as a higher heat of fusion [85], we expect fluences greater than those required to melt the amorphous skin (i.e., greater than about 1.0 J/cm<sup>2</sup>) not to produce melting depths extending far beyond the amorphous skin depth, although high fluences could be effective at crystallizing amorphous silicon pockets within the conical surface structures through heat diffusion. The result that additional ns laser pulses do not lead to additional increases in crystallinity suggests that the first ns pulse produces a melting depth that is similar to or greater than the melting depth produced by subsequent ns pulses, which is consistent with the higher melting threshold and latent heat of fusion of crystalline silicon relative to amorphous silicon. The melting depths and dynamics may not depend significantly on the laser wavelength within the range we investigated

(193–355 nm), because the optical absorption depth in silicon is fairly uniform in this range (5–10 nm) [87], and the amount of crystallization we measured after ns laser annealing did not depend on the ns laser wavelength.

Nanosecond laser annealing also smoothed the surface on the nm scale while leaving the 10- $\mu\text{m}$ -scale structures intact. We speculate that nm-scale smoothing could improve conformality during subsequent deposition of electrodes or additional semiconductor layers. Maintaining the  $\mu\text{m}$ -scale structures, on the other hand, leaves the geometric light-trapping properties of the surface intact (Figure 4.2.4).

Nanosecond laser annealing also reduced the width of the Raman crystalline silicon peak at  $520\text{ cm}^{-1}$  (Figure 4.2.3 inset). Lattice stress and small grain sizes can both increase the width of the  $520\text{ cm}^{-1}$  peak as well as shift the peak to lower wavenumbers [88, 89]. Thus, the reduction in peak width after ns laser annealing could indicate a reduction in lattice stress and/or an increase in grain size. Because the spectral resolution of our Raman measurements is only  $2.0\text{ cm}^{-1}$ , peak shifts to lower wavenumbers might result in an apparent increase in peak width. After ns laser annealing, the peak width is still greater than that from a pristine silicon wafer, indicating the presence of residual lattice stress, perhaps from the above-equilibrium concentration of dopant atoms.

The increase in the turn-on voltage of the hyperdoped black silicon diodes after rapid thermal annealing (Figure 4.2.5) could be due to the removal of Schottky barriers that form at the metal-semiconductor interface during electrode deposition. Consistent with this interpretation, the turn-on voltage of  $0.2\pm 0.1\text{ V}$  we observed after electrode deposition is typical of Schottky diodes [90], while the turn-on voltage

after rapid thermal annealing of 0.5–1.5 V is more consistent with the turn-on voltage of around 0.7 V that is typical of silicon homojunction diodes [91]. Furthermore, when rapid thermal annealing was performed before the electrodes were deposited, the turn-on voltage remained at  $0.2 \pm 0.1$  V, and no changes in crystallinity were detected after rapid thermal annealing, indicating that the increase in turn-on voltage was not due to structural changes in the hyperdoped black silicon itself, but rather changes within the electrode or at the electrode-silicon interface. Indeed, rapid thermal annealing has been reported to reduce significantly the density of defect states at silicon interfaces [92]. The fact that the current-bias curves showed rectification both before and after ns laser annealing (Figure 4.2.6) suggests that in hyperdoped black silicon containing amorphous regions, a rectifying junction can still be formed, perhaps in localized crystalline regions.

Nanosecond laser annealing reactivated the sub-bandgap optical absorptance after it was deactivated by thermal annealing, as shown in Figure 4.2.7. The deactivation of sub-bandgap optical absorptance, which is associated with an increase in electron mobility and changes in sheet carrier concentration, has been explained using the Johnson-Mehl-Avrami-Kolmogorov framework describing diffusion-mediated changes in metastable supersaturated solid solutions such as hyperdoped silicon [36]. However, the reactivation of the sub-bandgap optical absorptance after heating and fast cooling suggests that the degree of departure from room-temperature equilibrium of the dopant atoms, as reflected by the placement of the dopant atoms within the lattice, is reversible and important in describing the properties of hyperdoped silicon, similarly to the way in which fictive temperature is important in describing the prop-



erties of glasses—another non-equilibrium material. Reactivation has been previously reported when deactivated hyperdoped silicon was irradiated with fs laser pulses or heated to temperatures above 1350 K followed by fast cooling (e.g., in silicone oil, yielding estimated cooling rates of about 250 K/s) [37]. The reactivation we observe after ns laser annealing, however, is more complete than what has been previously reported and produces or maintains high crystallinity, unlike reactivation by fs laser pulses, which typically produces a layer of amorphous silicon [5].

We combined thermal and ns laser annealing in sequence to demonstrate the design flexibility provided by combining equilibrium with non-equilibrium processing techniques (Figure 4.2.7). In practice, an initial thermal annealing step can be useful for increasing crystallinity or obtaining electrical rectification [24], but it leads to deactivation of sub-bandgap optical absorptance [37]. Subsequent ns laser annealing can then reactivate the optical absorptance while maintaining high crystallinity. Similarly, rapid thermal annealing can be necessary to obtain ohmic contact after electrode deposition, but, again, some deactivation of the optical absorptance occurs. Another application of ns laser annealing can then reactivate the optical absorptance near to its original level. Overall, we noticed a small drop in above-bandgap absorptance after ns laser annealing of about 5% absolute due to an increase in surface reflectance, which is probably due to smoothing of the surface, and the final ns laser annealing step removed our metal electrodes. In practice, removal of the electrodes might be avoided by using thicker electrodes, more robust electrode materials, transparent electrodes, or by shielding the electrodes with a mask during ns laser annealing. The combination of thermal and ns laser annealing can produce hyperdoped black silicon that is

highly crystalline, highly absorptive to above- and below-bandgap wavelengths, and electrically rectifying. The process we carried out is not a prescription for a specific device, but is meant to be illustrative of the design flexibility provided by combining thermal and ns laser annealing.

We conclude our discussion by commenting on some of the remaining challenges in fabricating hyperdoped black silicon for sub-bandgap optoelectronic devices. The main challenge we address in this work is to obtain high crystallinity and high sub-bandgap optical absorptance concurrently, which we accomplish with ns laser annealing. However, before researchers can expect hyperdoped materials to find widespread use for sub-bandgap optoelectronic devices, some additional challenges need to be addressed. One of those challenges is to obtain doping concentrations within the range needed to produce an intermediate band. In silicon hyperdoped with sulfur, selenium or tellurium, this range is below 0.4 at. %, with the best figures of merit obtained below 0.1 at. % [15, 32]. Silicon that is hyperdoped with sulfur, selenium, or tellurium above 0.4 at. % is metallic and therefore not expected to produce significant optoelectronic (photoconductive or photovoltaic) response. Yet hyperdoped silicon fabricated with ion implantation or with femtosecond laser irradiation often contains dopant concentrations of 1 at. % or more, including much of the hyperdoped silicon reported in the literature and, likely, the hyperdoped black silicon we examined in this work. It is possible to fabricate hyperdoped silicon with dopant concentrations of  $< 0.4$  at. % with fs laser irradiation (by using a low number of pulses and a low pulse fluence [24, 30]) or with ion implantation (by reducing the implanted ion dose [31]), but the resultant hyperdoped silicon is typically flat, so it does not show

light trapping effects and therefore is not a strong optical absorber of sub-bandgap wavelengths. Addressing this challenge will require methods to control the dopant concentration and light-trapping properties of hyperdoped silicon independently.

Another challenge in fabricating hyperdoped black silicon for sub-bandgap optoelectronic devices is in controlling the hyperdoped layer thickness so that charge carriers can be extracted efficiently. Charge carriers in hyperdoped silicon have short carrier lifetimes on the order of picoseconds [32], so the hyperdoped layer must be thin enough to allow carriers to be transported out of the layer before recombination occurs. The transport length for holes in sulfur-hyperdoped silicon was estimated in one study to be around 100 nm [29], but in general the transport length can be expected to depend on a number of factors, including the dopant concentration, the material microstructure, and electrostatic fields set up by the dopant concentration gradient. If the electrostatic fields set up by the dopant concentration gradient prove to be a limiting factor in carrier transport, then it might necessary to control the dopant concentration gradient [40,41] (e.g., obtaining a monotonic dopant concentration profile with depth) in order to fabricate efficient hyperdoped intermediate band photovoltaics or sub-bandgap photodetectors. Developing methods for meeting these device requirements are important areas of future research.

#### **4.2.5 Conclusions**

Nanosecond laser annealing can crystallize and remove pressure-induced phases from the surface of hyperdoped black silicon while maintaining a light-trapping surface morphology and high sub-bandgap optical absorptance. Additionally, ns laser annealing

can reactivate the sub-bandgap optical absorptance after it has been deactivated by thermal annealing. Furthermore, we find that ns laser annealing does not interfere with the formation of rectifying homojunctions in hyperdoped black silicon. Thermal annealing and ns laser annealing can be combined in sequence to produce hyperdoped black silicon that is highly crystalline, shows high above-bandgap and sub-bandgap optical absorptance, and is electrically rectifying. The effects of ns laser irradiation on hyperdoped black silicon are not highly sensitive to laser wavelength, pulse duration, or number of pulses used. Because ns laser annealing is based on physical processes of melting/heating and fast resolidification/cooling, it could potentially be applied to other non-equilibrium material systems beyond hyperdoped black silicon. The combination of equilibrium processing techniques (e.g., thermal annealing) with non-equilibrium processing techniques (e.g., ns laser annealing) could be a useful approach for controlling the properties of non-equilibrium materials in general.

Fabricating optoelectronic devices using hyperdoped black silicon presents a number of challenges, including concurrently controlling the crystallinity, optical absorptance, dopant concentration, and hyperdoped layer thickness. Here, we use ns laser annealing on hyperdoped black silicon to obtain high crystallinity and optical absorptance while also maintaining electrical rectification. Beyond this, developing methods to control the dopant concentration and hyperdoped layer thickness in hyperdoped black silicon may be important for fabricating sub-bandgap optoelectronic devices.

## 4.3 Nanosecond laser annealing of 1-micrometer surface textures

### 4.3.1 Introduction

In this section, we expand upon Section 4.2 by carrying out ns laser annealing on surface textures only 1 micrometer in size. These surface textures are highly effective at light trapping, but they require lower laser fluence in fabrication, have less surface area, and may be easier to integrate into devices than 10-micrometer textures. Thus, these textures with high crystallinity could have applications in optoelectronic devices.

The content of this section has been published as supplementary material in [7].

### 4.3.2 Methods

To fabricate hyperdoped black silicon with conical surface structures approximately 1 micrometer in size, we carried out the same fabrication procedure described in Section 4.2 but used a laser pulse fluence of  $2.5 \text{ kJ/m}^2$  instead of  $8 \text{ kJ/m}^2$ .

### 4.3.3 Results

Fabrication with a fs-laser pulse fluence of  $2.5 \text{ kJ/m}^2$  yielded hyperdoped black silicon with smaller conical surface structures, which were about  $1 \mu\text{m}$  in size (as shown in Figure 4.3.1). Before ns laser annealing, these samples exhibited amorphous and pressure-induced crystalline phases similar to unannealed hyperdoped black silicon with  $10\text{-}\mu\text{m}$  surface structures, above-bandgap optical absorptance of 90%, and sub-bandgap optical absorptance of 80% (as shown in Figure 4.3.2). After ns laser anneal-

ing with a fluence of  $0.6 \text{ J/cm}^2$ , the  $1\text{-}\mu\text{m}$  conical surface structures remained intact, the amorphous and pressure-induced crystal phases were reduced to an undetectable level, and the sub-bandgap optical absorptance increased to 80–90%. After ns laser annealing with a higher fluence of  $2.2 \text{ J/cm}^2$ , the conical surface structures were largely destroyed, the above-bandgap optical absorptance dropped to 80–90%, and the sub-bandgap optical absorptance dropped to 60% (the amorphous and pressure-induced crystal phases were again reduced to an undetectable level).

#### **4.3.4 Discussion and conclusions**

In contrast to the  $10\text{-}\mu\text{m}$ -scale conical surface structures discussed in Section 4.2, the  $1\text{-}\mu\text{m}$ -scale conical surface structures fabricated with a fs-laser fluence of  $2.5 \text{ kJ/m}^2$  were destroyed by high-fluence ns laser annealing ( $2.2 \text{ J/cm}^2$ ), which reduced their light-trapping effectiveness. However, ns laser annealing at a lower fluence of  $0.6 \text{ J/cm}^2$  resulted in high crystallinity while preserving the surface texture. In fact, annealing at this fluence increased the sub-bandgap absorptance, which may be due to an increase in the population of dopants in a crystalline environment. Further investigation of ns laser annealing on  $1\text{-}\mu\text{m}$ -scale conical surface structures could be interesting, because such structures produce considerable light-trapping effects, can be crystallized without being destroyed by using low-fluence ns laser annealing, could potentially be fabricated on thin silicon substrates, and could be easier to integrate into devices (e.g., easier to contact electrically) than  $10\text{-}\mu\text{m}$ -scale structures.

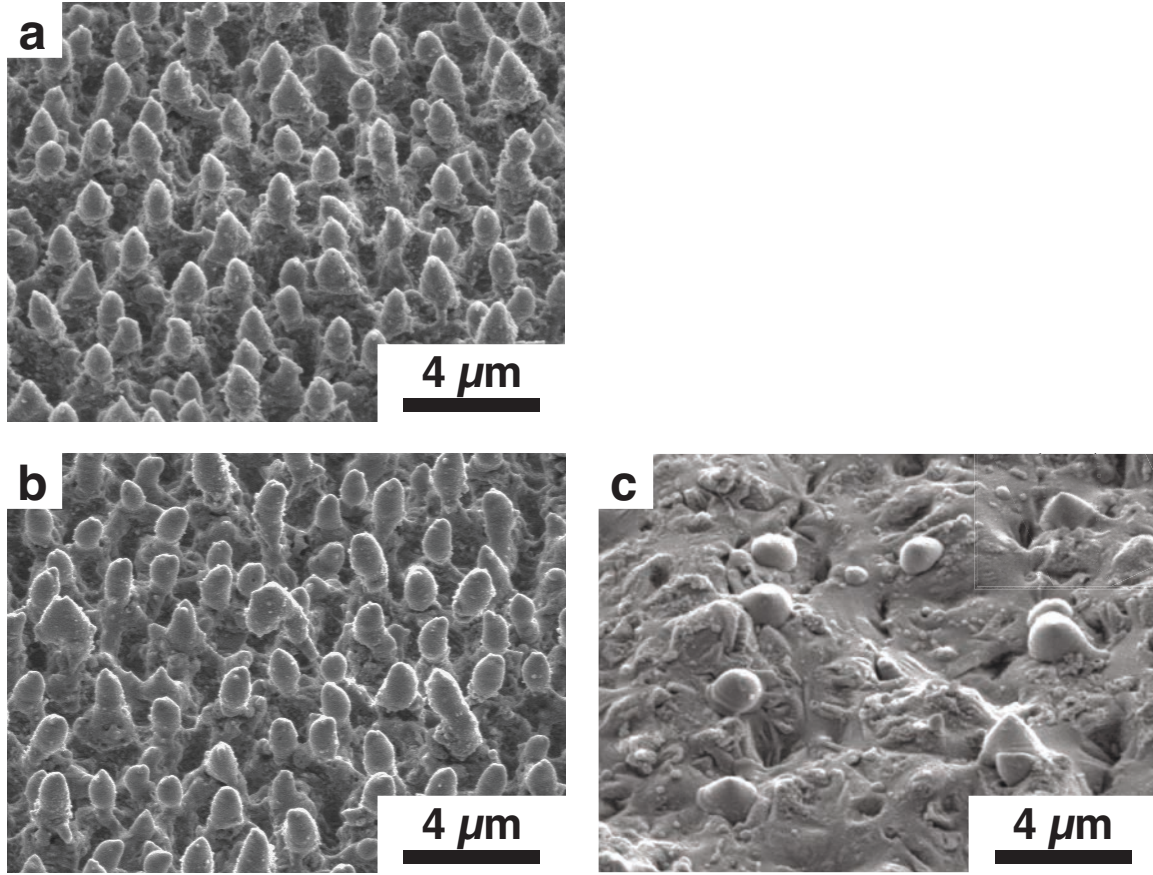


Figure 4.3.1: a: Hyperdoped black silicon (fabricated with a fs-laser pulse fluence of  $2.5 \text{ kJ/m}^2$ ) with light-trapping conical surface structures about  $1 \mu\text{m}$  in size. (Image obtained at 45-degree angle without foreshortening correction). b: Nanosecond laser annealing at low fluences (here,  $0.6 \text{ J/cm}^2$ ) kept the surface structures intact while crystallizing the surface. c: Nanosecond laser annealing at high fluences (here,  $2.2 \text{ J/cm}^2$ ) destroyed the surface structures. From [7] supplemental material.

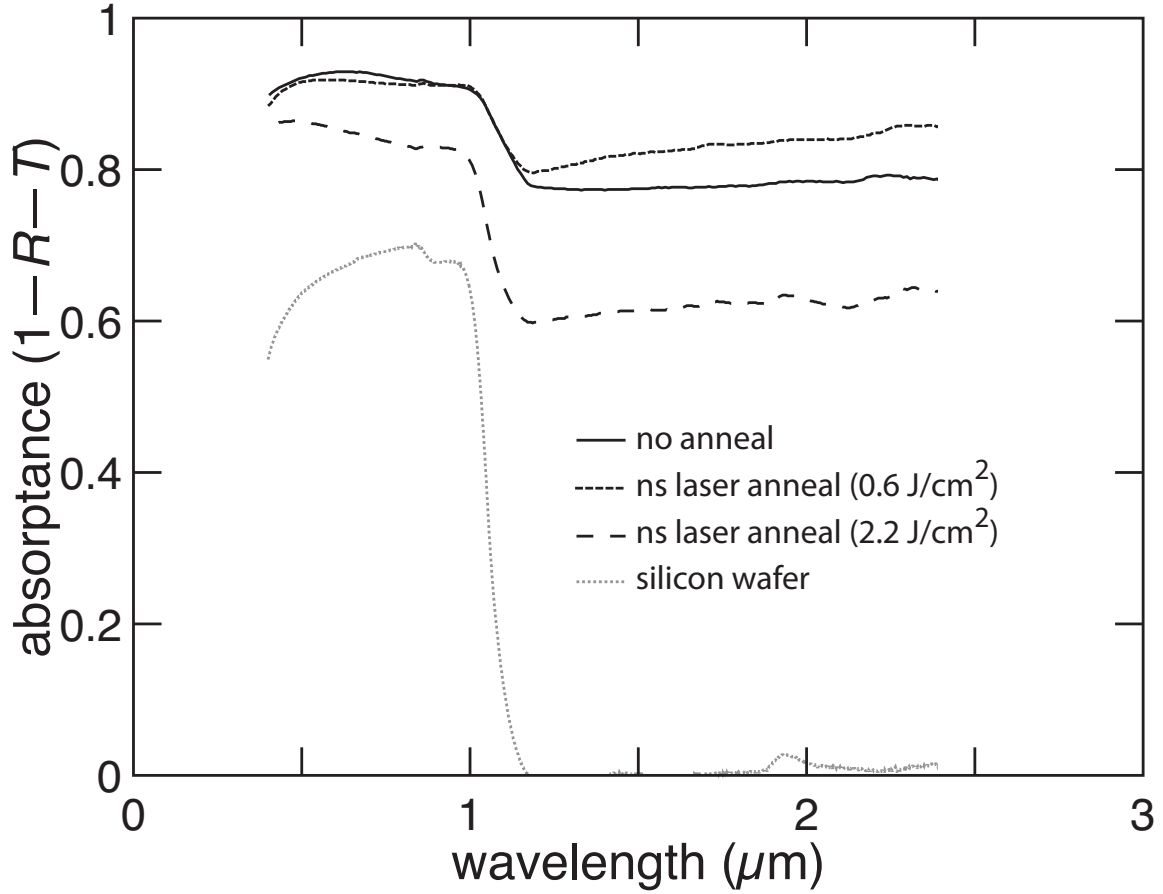


Figure 4.3.2: Nanosecond laser annealing at low fluences (e.g.,  $0.6 \text{ J/cm}^2$ ) on  $1\text{-}\mu\text{m}$ -scale surface structures maintained or increased the optical absorbance, but annealing at high fluences (e.g.,  $2.2 \text{ J/cm}^2$ ) decreased the optical absorbance due to the removal of the light-trapping surface structures. From [7] supplemental material.

## 4.4 Nanosecond laser annealing of sub-micrometer surface textures

### 4.4.1 Introduction

Here, we examine ns laser annealing of hyperdoped silicon with sub-micrometer surface structures, including surface ripples and flat hyperdoped silicon. Surface ripples,



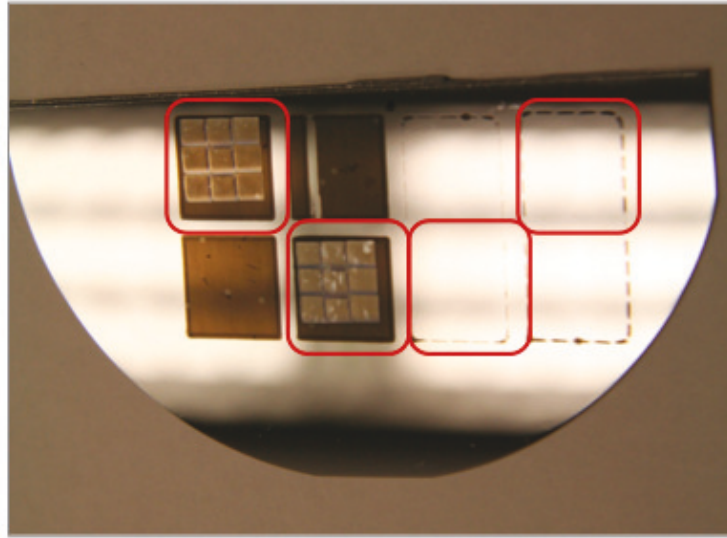
or laser-induced periodic surface structures (LIPSS), are characteristic of silicon—as well as metals and dielectrics—irradiated with fs laser pulses. Controlling the crystallinity of these structures could be useful for functional anti-reflective surfaces and surface catalysts (such as laser-processed titanium dioxide or other water-splitting photocatalysts [93]). Flat doped silicon made with ultrafast laser irradiation could be a more economical alternative to making flat doped silicon with ion implantation, and laser doping of semiconductors could be useful for creating shallow junctions in general. However, the tendency for ultrafast laser processing to generate amorphous material at the surface is a challenge for devices. Nanosecond laser annealing could potentially address this challenge.

#### **4.4.2 Methods**

Hyperdoped silicon was fabricated using 100-fs, 800-nm pulses on p-type (7–14 Ohm-cm) silicon ( $\langle 100 \rangle$  orientation). The wafer was immersed in 500 Torr  $\text{SF}_6$  gas during irradiation. A fluence of  $2.8 \text{ kJ/m}^2$  and 25 and 30 shots/area were used to produce a doped surface with ripple-like structures (sometimes called orange silicon due to its golden-orange appearance to the eye, as shown in Figure 4.4.1). Similarly, a fluence of  $3.0 \text{ kJ/m}^2$  with 5 shots/area and a fluence of  $3.4 \text{ kJ/m}^2$  with 3 shots/area were used to produce a doped but flat surface (sometimes called pink silicon due to the pink appearance of the amorphous layer at the surface following fs laser irradiation). The samples were each  $1 \text{ cm}^2$  in area.

The hyperdoped samples were annealed using a single ns laser pulse (308 nm XeCl excimer laser, 25 ns FWHM pulse duration) at a fluence of  $1.8 \text{ J/cm}^2$ . The melt

depth simulated for this fluence was around 400 nm, which is roughly the size of the surface structures. The pulses were passed through a square mask ( $3 \times 3 \text{ mm}^2$  opening) to obtain a uniform pulse profile and were tiled across the surface to obtain a  $9 \times 9 \text{ mm}^2$  annealed area, as shown in Figure 4.4.1. The effects of ns laser annealing were investigated using Raman spectroscopy, optical and scanning electron microscopy, and spectrophotometry.



|                              |     |     |     |     |
|------------------------------|-----|-----|-----|-----|
| fluence ( $\text{kJ/m}^2$ ): | 2.8 | 2.8 | 3.0 | 3.4 |
| shots/area:                  | 30  | 25  | 5   | 3   |

Red outline: Sample underwent ns laser annealing.  
(Each sample  $1 \text{ cm}^2$ .)

Figure 4.4.1: Photograph of laser-irradiated samples used in this section. Samples outlined in red were ns laser annealed. Rippled samples appear gold colored, whereas untextured samples remain reflective.

### 4.4.3 Results

Before ns laser annealing, the samples fabricated with a fluence of  $2.8 \text{ kJ/m}^2$  and 25 or 30 shots/area exhibited ripple-like surface structures with a period of 400 nm, as shown in Figure 4.4.2. The silicon irradiated with fluences of  $3.0$  and  $3.4 \text{ kJ/m}^2$  with 5 or 3 shots/area remained flat. However, for these flat samples, regular patches of contrast were visible under optical and scanning electron (side-detector) microscopy, which, consistent with previous studies [14], could be amorphous regions on the surface. In contrast, examining these flat samples with backscattered electron microscopy revealed patterns of contrast associated with the shape of each fs laser pulse rastered across the surface, as shown in Figure 4.3.3. The features revealed by side-scattered electrons are located between the features visible with back-scattered electrons.

Compared to a pristine silicon wafer, the rippled silicon showed enhanced above-bandgap and sub-bandgap optical absorptance, with above-bandgap absorptance of around 80% and sub-bandgap absorptance of 10–20%. The flat, laser-irradiated samples showed no difference in optical absorptance from a pristine silicon wafer.

We now report the effects of ns laser annealing. First, we consider the effects of ns laser annealing on the rippled surface. After ns laser annealing, the surface ripples were destroyed, leaving behind a rough, cratered surface morphology, shown in Figure 4.4.4. Despite this alteration of the surface, the optical absorptance remained largely the same, with the sub-bandgap absorptance becoming flat, as shown in Figure 4.4.5. The laser annealing process also resulted in the disappearance of the amorphous silicon signal detected by Raman spectroscopy, consistent with Section 4.2. Note that only the rippled surface showed detectable amorphous silicon prior to ns laser annealing.

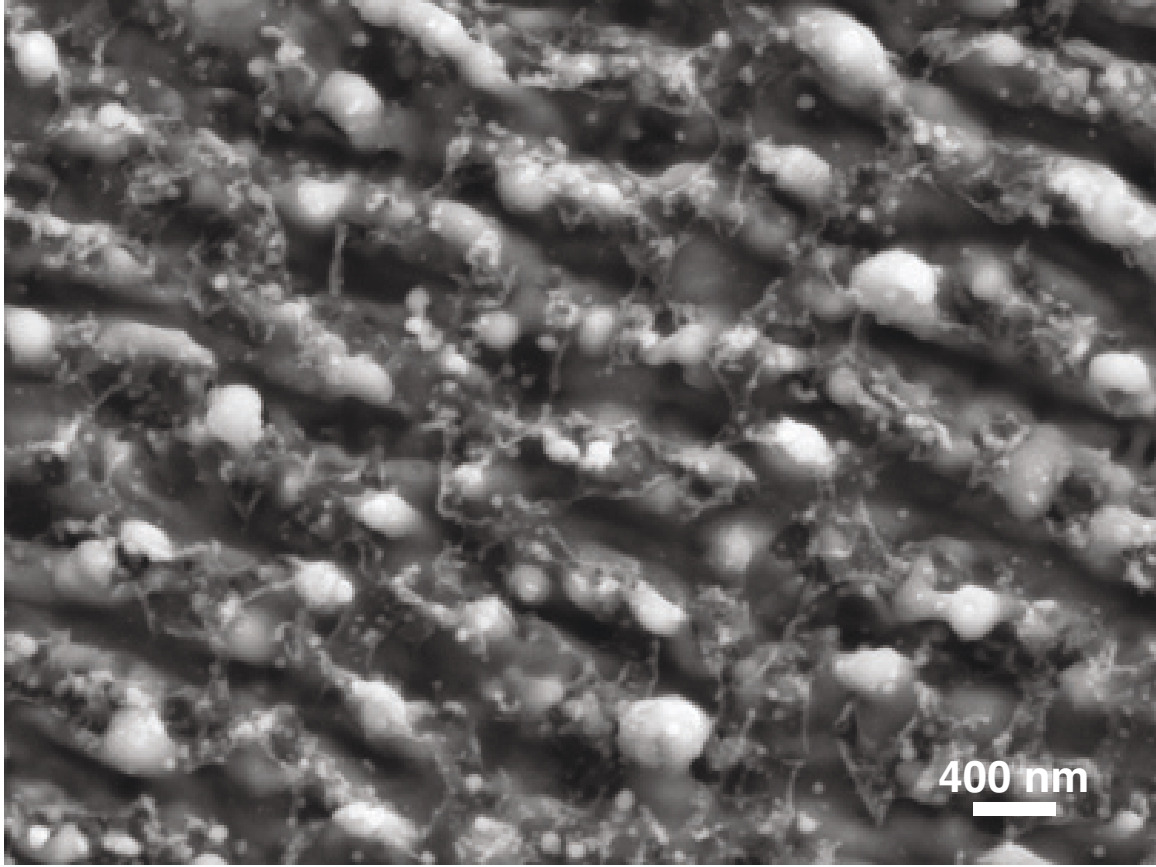


Figure 4.4.2: Surface of hyperdoped silicon with surface ripples fabricated using a fluence of  $2.8 \text{ kJ/m}^2$  and 30 shots/area.

On the untextured laser-irradiated samples, ns laser annealing removed the periodic surface contrast shown by optical and side-scattering electron microscopy, shown in Figure 4.4.6. The periodic surface contrast shown by backscattered electron microscopy, however, remained intact and unaltered.

#### **4.4.4 Discussion**

First we consider the properties of the rippled and flat silicon before ns laser annealing. The rippled silicon shows enhanced optical absorptance, even though its

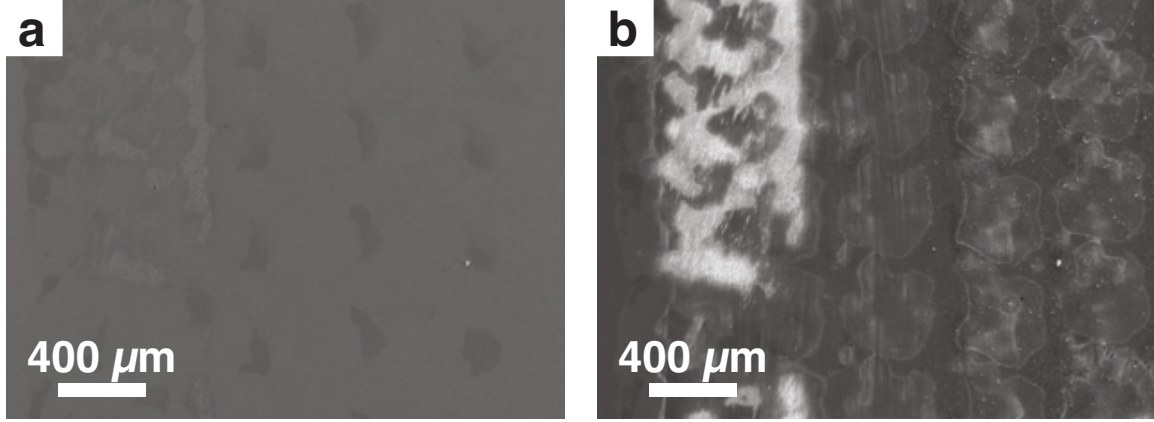


Figure 4.4.3: Surface of laser-irradiated but untextured silicon fabricated using a fluence of  $3.0 \text{ kJ/m}^2$  and 5 shots/area. a: Side-scattered electrons reveal periodic surface contrast which may be due to amorphous Si on the surface. b: Backscattered electrons reveal periodic surface contrast associated with the shape of each fs laser pulse.

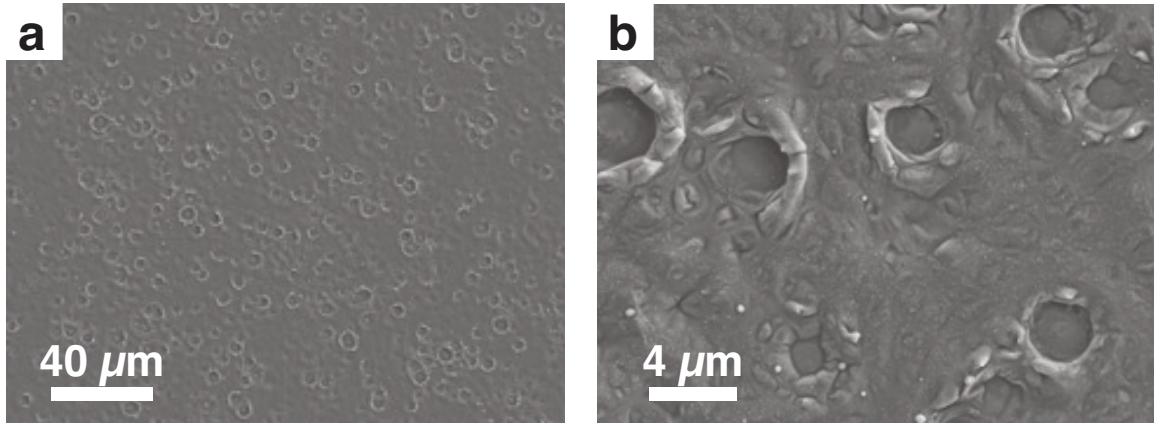


Figure 4.4.4: a: After ns laser annealing, the rippled surface is transformed to a crater-like surface. b: Detail of surface.

surface structures are only about 400 nm in size. The sub-bandgap optical absorbance, which reduces with increasing wavelength, could be due to surface defects or sulfur doping. The presence of amorphous silicon shown by Raman spectroscopy is consistent with hyperdoped black silicon with 1–10 micrometer surface structures, although the rippled silicon in this section did not show evidence of pressure-induced

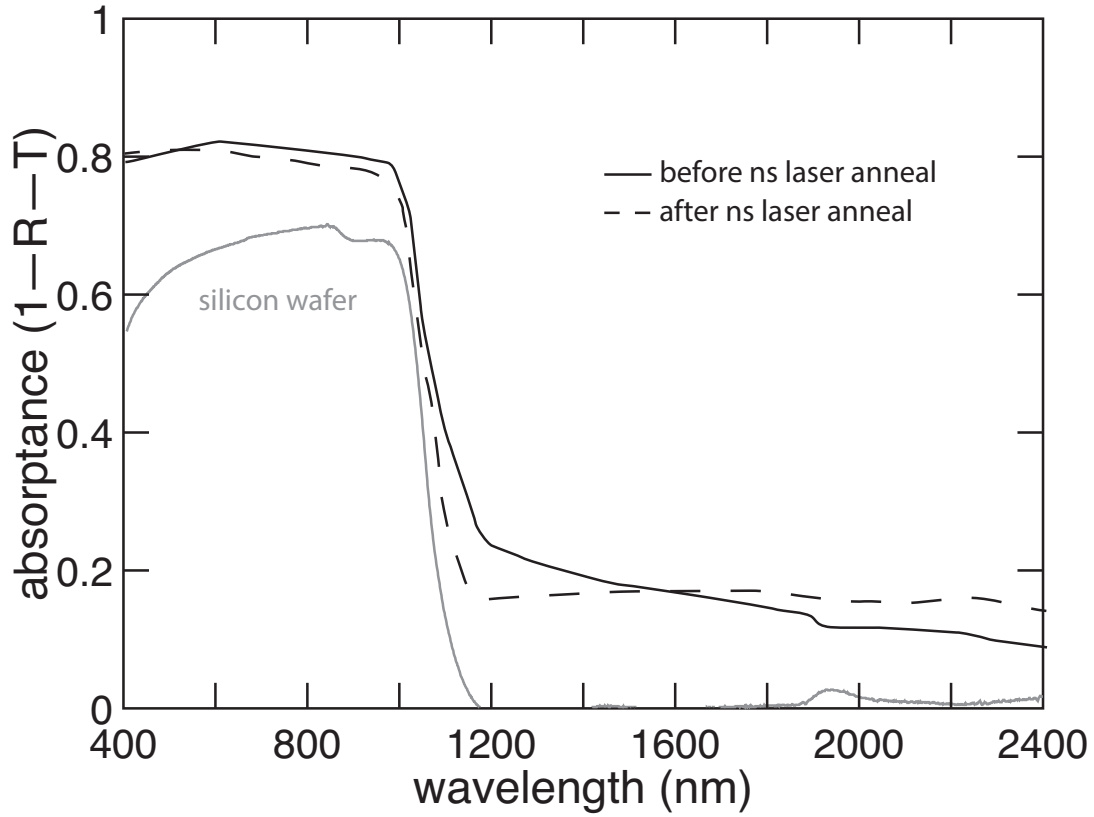


Figure 4.4.5: Optical absorbance of rippled hyperdoped silicon before and after ns laser annealing.

crystalline silicon phases such as Si-III and Si-XII.

The periodic surface contrast seen with optical and side-scattered electron microscopy on flat laser-irradiated silicon has also been observed in past studies of hyperdoped flat silicon [1]. Although no amorphous signal appeared in Raman spectroscopy, it is nonetheless possible that these pockets of contrast are amorphous regions on the surface, and that their Raman signal is low due to their small volume. Alternatively, it is possible that the observed contrast is due to small variations in surface morphology. The additional periodic contrast revealed by backscattered electron microscopy appeared to be an outline of each laser pulse (above a local fluence



Figure 4.4.6: Optical microscope image of untextured laser-irradiated silicon. Nanosecond laser annealing (right side of image) removed the periodic surface contrast visible before annealing (left side of image).

value on the Gaussian pulse). To explain these contrast features, we consider the fluence of the fs pulses:  $3.0 \text{ kJ/m}^2$ . Within a fs pulse fluence range of about  $2.5\text{--}3.5 \text{ kJ/m}^2$ , silicon melts and resolidifies as crystalline silicon [14], whereas between about  $1.5\text{--}2.5 \text{ kJ/m}^2$ , silicon melts and resolidifies as amorphous silicon. It is possible that the outline revealed by backscattered electrons corresponds to the boundary between amorphous and crystalline resolidification. Alternatively, the outline may be due to local strain at the interface where the melt stops growing and begins solidifying, or from strain or defects produced by pressure waves resulting from fs laser irradiation.

Of note is the fact that the features revealed by optical and side-scattered electron microscopy are located at the edge of each of the features revealed by backscattered electron microscopy. This is consistent with the optical, side-scattered electron features being amorphous silicon, because at the edge of each Gaussian fs laser pulse, the local fluence decreases to below  $2.5 \text{ kJ/m}^2$ , which we can expect to produce a region of amorphous silicon upon resolidification.

Nanosecond laser annealing had the basic effect already discussed in this chapter: melting and resolidification of the surface, resulting in high crystallinity. In the case of our rippled hyperdoped silicon, the  $1.8 \text{ J/cm}^2$  ns laser pulse destroyed the original surface morphology, leaving behind a rough, cratered surface that, coincidentally, showed similar optical absorptance as the original rippled surface. This may not be surprising given that the characteristic size scales of the surface roughness before and after ns laser annealing were somewhat similar (0.4–1 micrometer), even though the shape of the texture had changed. Lower ns pulse fluences (e.g.,  $0.6 \text{ J/cm}^2$ ) might be able to crystallize the rippled surface without destroying it, as shown in Section 4.3. Although the surface morphology was altered, the sulfur dopants appeared to remain intact, as evidenced by the similar levels of sub-bandgap optical absorptance before and after ns laser annealing. Of note, however, is that after ns laser annealing, the sub-bandgap optical absorptance became flat (instead of declining with increasing wavelength). One possibility is that the alteration of the surface morphology changed the light-trapping properties as a function of wavelength (e.g., the cratered surface may be more effective than the rippled surface at absorbing long wavelengths). Another possibility is that the ns annealing process changed the optical properties of the



dopants by changing their local atomic environment. Along this line of reasoning, the declining sub-bandgap absorptance before ns laser annealing may be due to structural defects in the silicon separate from the activity of the dopant, and ns laser annealing may have removed these defects and activated the dopant atoms by placing them in a crystalline environment.

On flat silicon irradiated with fs laser pulses, ns laser annealing had no discernible effect on optical absorptance or the Raman spectrum, because both of these were indistinguishable from a crystalline silicon wafer to begin with. However, the surface contrast visible with optical and side-scattered electron microscopy disappeared after ns laser annealing, as shown in Figure 4.4.6. This would be consistent with this surface contrast arising from amorphous silicon and being removed by ns laser annealing. The contrast visible with backscattered electron microscopy, on the other hand, was unaltered by ns laser annealing. This suggests that such contrast arises from structural effects other than the presence of amorphous silicon, and that these structural effects are located below the melt depth produced by the ns laser pulse, because melting and resolidification would presumably erase any structural modifications previously present.

What are potentially useful applications of ns laser annealing on fs-laser processed surfaces with sub-micrometer surface structures? Like other hyperdoped black silicon, silicon with sub-micrometer surface features has anti-reflective properties but typically contains amorphous regions after fs laser irradiation. Nanosecond laser annealing can produce a highly crystalline surface, but for surfaces with sub-micrometer surface features, low ns laser fluences should be used to avoid destroying the surface

texture. For comparison, Section 4.3 showed that hyperdoped black silicon with 1-micrometer surface structures could be annealed with ns laser pulses without destroying the surface texture when low ns laser fluences were used (in that case,  $0.6 \text{ J/cm}^2$ ). Similar or lower ns pulse fluences could be investigated for hyperdoped black silicon with sub-micrometer ripples.

Using ns laser pulses to anneal sub-micrometer hyperdoped ripples has interesting potential beyond silicon, because these structures are produced by fs laser irradiation on a wide range of materials, including metals and insulators. For example, past studies have investigated using ultrafast laser processing to fabricate doped, textured surface catalysts, such as heavily doped titanium dioxide [93]. Yet ultrafast laser processing often leaves material phases that are undesirable for functional devices, necessitating some form of annealing. Conventional thermal annealing, however, can be incompatible with maintaining the properties of heavily doped materials. So ns laser annealing could play a role in tailoring the structural properties of a range of functional surfaces prepared by ultrafast laser irradiation.

For flat hyperdoped silicon produced by ultrafast laser irradiation, ns laser annealing could also have useful applications. With appropriate laser irradiation parameters, ultrafast laser processing can produce flat, hyperdoped silicon, which could be a more economical approach than ion implantation, which is a batch process requiring high vacuum. A problem with the ultrafast laser irradiation approach, however, is the production of amorphous silicon on the surface (which also occurs during ion implantation). Nanosecond laser annealing can crystallize this amorphous material. That being said, the presence of amorphous material is not the only challenge asso-

ciated with producing flat, doped layers with ultrafast laser irradiation: Controlling the dopant concentration profile, depth, and uniformity are also challenges.

#### **4.4.5 Conclusions**

In this section, we investigated the use of ns laser annealing on hyperdoped silicon with surface structures less than one micrometer in size. For hyperdoped silicon with ripples (laser-induced periodic surface structures), ns laser annealing can crystallize the surface while keeping the dopant atoms present. Low ns laser pulse fluences must be used, however, to avoid destroying the rippled surface texture. Nanosecond laser annealing on flat, fs laser-irradiated silicon resulted in the removal of surface contrast features revealed by optical and side-scattered electron microscopy, which may be due to amorphous Si, but not contrast features revealed by backscattered electron microscopy, which may be structural features below the melt depth of the ns laser pulse. Nanosecond laser annealing on doped, sub-micrometer surface structures could be useful for antireflective surfaces, surface catalysts, and shallow doped layers prepared by ultrafast laser irradiation.

### **4.5 Femtosecond laser annealing of hyperdoped black silicon**

#### **4.5.1 Introduction**

When a femtosecond laser pulse melts silicon, the melt often resolidifies faster than 15 m/s, which yields an amorphous silicon structure [43]. However, under some

conditions, femtosecond laser pulses can produce crystalline silicon. For example, at fluences above around  $2.5 \text{ kJ/m}^2$ , femtosecond laser pulses (at 800 nm) produce resolidification velocities slow enough to yield crystalline silicon [14,43]. Alternatively, femtosecond laser pulses could potentially be used to perform laser annealing by heating amorphous silicon to the point of crystal nucleation without melting the bulk silicon (for example, by initiating explosive crystallization) [94,95]. In this section, we investigate fs laser annealing on hyperdoped black silicon using femtosecond laser pulses at 1300 nm.

### **4.5.2 Methods**

We fabricated hyperdoped black silicon by irradiating a silicon wafer with fs laser pulses in the presence of sulfur hexafluoride ( $\text{SF}_6$ ) gas. A monocrystalline silicon wafer (p-type, boron-doped, 7–14 ohm-cm) was placed in a vacuum chamber which was evacuated to  $< 0.1$  Torr and then filled with sulfur hexafluoride gas to a pressure of 500 Torr. Femtosecond laser pulses (800 nm, 100-fs pulse duration, 1 kHz repetition rate) were output by a Ti:sapphire regenerative amplifier, passed through a computer-controlled mirror galvanometer, directed into the vacuum chamber, and focused onto the silicon surface so that a pulse diameter of 0.5–1 mm (full width at half maximum (FWHM) of the Gaussian pulse) was obtained. We fabricated samples using pulse fluences of  $8 \text{ kJ/m}^2$  and  $2.5 \text{ kJ/m}^2$ , which produced hyperdoped black silicon with conical surface structures approximately 10 micrometers and 1 micrometer in height, respectively. The pulses were scanned across the silicon surface to obtain 200 shots/area [5]. Each time  $4 \text{ cm}^2$  of the surface was irradiated, the vacuum cham-

ber was evacuated and refilled with new sulfur hexafluoride gas in order to prevent ablated particles from the silicon surface from accumulating in the chamber. The hyperdoped black silicon samples fabricated for this study were each  $1\text{ cm}^2$  in area.

In order to test fs laser annealing, the hyperdoped black silicon samples were mounted on a translation stage and irradiated with a series of 110-fs laser pulses at 1300 nm. The fs laser pulses were generated by a Ti:sapphire regenerative amplifier at 800 nm, then passed through a optical parametric amplifier to produce fs laser pulses at 1300 nm. The beam had a diameter of 74 micrometers (FWHM) at the sample surface.

Before annealing, the melting threshold fluence at the hyperdoped black silicon surface was determined (using black silicon with 1-micrometer surface structures), because the goal of the fs laser annealing was to produce a solid-state phase transformation rather than melting. The 1300-nm fs laser pulses were scanned across the surface at a repetition rate of 1 kHz using a range of pulse energies (3–30 microjoules/pulse). An infrared camera was used to observe reflections from the hyperdoped black silicon surface, with high reflectivity interpreted as melting.

Once the melting threshold fluence was determined, the hyperdoped black silicon samples were exposed to fs laser pulses in order to attempt laser annealing. Fluences lower than the melting threshold were used in order to avoid melting the silicon (which could produce amorphous silicon upon resolidification). The samples were reversed so that the 1300 nm laser pulses were incident on the flat backside of the silicon substrate and transmitted to the interface between the crystalline substrate and the amorphous hyperdoped silicon. The purpose of irradiating the samples from the backside was to

promote crystal nucleation and epitaxial crystal growth at the crystalline–amorphous interface, because the 1300 nm wavelength undergoes linear absorption only within the hyperdoped layer.

Although silicon is nominally transparent to 1300 nm light, two-photon absorption can occur for intense fields, such as those within fs laser pulses. Therefore, the two-photon absorption occurring within the silicon wafer was measured, as this represents energy not incident on the hyperdoped layer. To determine the two-photon absorption, the 1300 nm pulses were passed through a pristine section of the silicon wafer and the transmittance was measured. The transmittance  $T$  can be approximated by  $T = (1 - R)(1 - A)(1 - R)$ , where  $R$  is the reflectivity at the air/silicon interface (0.3 at 1300 nm), and  $A$  is the two-photon absorptance in the silicon. Note that  $A$  is a function of the pulse intensity and thus the pulse energy and pulse fluence.

Once the two-photon absorption was measured, the fs laser pulses were scanned across the hyperdoped black silicon samples, with the pulses incident on the pristine backside of the silicon wafer as described above. The pulse fluence  $F_1$  incident at the hyperdoped silicon/silicon substrate interface was estimated as  $F_1 = F_0(1 - R)(1 - A)$ , where  $F_0$  was the pulse fluence before entering the silicon. In estimating  $F_1$ , we did not estimate the change in pulse area due to scattering or self-focusing. Annealing fluences of  $F_1 = 0.6$  and  $0.9 \text{ kJ/m}^2$  were used. The laser pulses were incident at a repetition rate of 10 Hz, and the stage was translated to obtain 5 shots/area.

In order to measure changes in crystallinity resulting from fs laser annealing, Raman Stokes scattering spectra were obtained and analyzed as described in Section 4.2. The presence of amorphous silicon and high-pressure silicon phases (Si-III and

Si-XII) were measured before and after fs laser annealing.

### 4.5.3 Results

In order to avoid melting the hyperdoped silicon with the 1300 nm fs laser pulses, the melting threshold on hyperdoped black silicon with 1-micrometer surface structures was determined. The onset of melting was observed at a fluence of approximately 3 kJ/m<sup>2</sup>, which is about twice the fluence required to melt pristine crystalline silicon using an 800 nm fs laser pulse [1].

Table 4.5.1 shows the incident fs laser pulse fluence  $F_0$ , the measured two-photon absorption occurring within the silicon substrate  $A$ , and the estimated fs laser pulse fluence at the hyperdoped silicon interface  $F_1$ . The reflectivity  $R$  at the silicon/air interface was assumed to be  $R = 0.3$  in accordance with the Fresnel equations. A fluence  $F_1$  of 0.9 kJ/m<sup>2</sup> was the highest annealing fluence achieved with the experimental setup.

| $F_0$                 | $A$  | $F_1$                 |
|-----------------------|------|-----------------------|
| 3.6 kJ/m <sup>2</sup> | 0.76 | 0.6 kJ/m <sup>2</sup> |
| 7.1 kJ/m <sup>2</sup> | 0.82 | 0.9 kJ/m <sup>2</sup> |

Table 4.5.1: Femtosecond laser pulse fluence  $F_0$  incident on the backside of the hyperdoped black silicon wafer, the measured two-photon absorptance  $A$  within the wafer, and the estimated fluence  $F_1$  at the sub-surface interface between the hyperdoped layer and the substrate.

Raman spectroscopy showed no change in amorphous silicon, Si-III, or Si-XII content

after fs laser annealing for both the 1-micrometer-surface-structure hyperdoped black silicon and the 10-micrometer-surface-structure hyperdoped black silicon.

#### **4.5.4 Discussion**

First we consider the measured melting fluence threshold of  $3 \text{ kJ/m}^2$  on hyperdoped black silicon with 1-micrometer surface structures, which is twice as large as the melting threshold of about  $1.5 \text{ kJ/m}^2$  for flat crystalline silicon. To compare these values, we consider the amount of energy absorbed by the surface and the differing surface geometries and material properties between hyperdoped black silicon and flat crystalline silicon. At 1300 nm, the hyperdoped black silicon surface we examined (with 1-micrometer surface structures) absorbs 80% of incident light, reflecting about 10% and transmitting about 10% (Section 4.3). Furthermore, the surface structures increase the surface area by a factor of about 2–3 (approximating the surface structures as pillars with height and diameter both equal to 1 micrometer covering half the surface). Thus, the effective absorbed fluence at the hyperdoped black silicon surface for an incident  $3 \text{ kJ/m}^2$  pulse is only 0.8–1.2  $\text{kJ/m}^2$ . This is comparable to the absorbed fluence at a flat crystalline silicon surface of  $1 \text{ kJ/m}^2$  for an incident pulse with fluence  $1.5 \text{ kJ/m}^2$  (taking into account surface reflection). Thus, a pulse fluence of  $3 \text{ kJ/m}^2$  at 1300 nm deposits roughly as much energy per unit surface area in the sample of hyperdoped black silicon as a pulse fluence of  $1.5 \text{ kJ/m}^2$  at 800 nm on flat crystalline silicon.

Although the energy density absorbed from a 1300 nm,  $3 \text{ kJ/m}^2$  pulse on our hyperdoped black silicon is roughly equal to that from a 800 nm,  $1.5 \text{ kJ/m}^2$  pulse



on flat crystalline silicon, the surface of our hyperdoped black silicon is amorphous, not crystalline. This does not introduce a discrepancy into our analysis, however, because the melting threshold fluences for crystalline and amorphous silicon from fs pulses are similar. In the literature, the melting of amorphous silicon by fs laser pulses is described as an ultrafast lattice destabilization process driven by the excitation of a large fraction of valence electrons ( $\sim 10^{22}/\text{cm}^3$ , about one excited valence electron per atom), which also produces high optical reflectivity similar to that of liquid silicon [95]. This excitation and resulting lattice disorder can be produced by fs laser fluences of 1–2 kJ/m<sup>2</sup>, similar to the melting threshold fluence for crystalline silicon from fs laser pulses, which is typically measured to be 1.5–2.0 kJ/m<sup>2</sup> [43, 96]. For longer laser pulses (e.g., ns laser pulses), the melting threshold fluence for crystalline silicon increases (7–8 kJ/m<sup>2</sup>) while that for amorphous silicon remains fixed (1–2 kJ/m<sup>2</sup>) [85]. This difference is consistent with the fact that the thermal conductivity of amorphous silicon thin films (typically in the range of 1–3 W/mK) is about two orders of magnitude lower than that of crystalline silicon, which is due to high rates of phonon scattering from amorphous silicon’s disordered atomic structure [97] and which prevents heat diffusion from the amorphous silicon film over the pulse duration.

What fluence conditions are required to modify amorphous silicon selectively? The divergence of the melting threshold fluences for amorphous and crystalline silicon at ns pulse lengths suggests that ns pulses could be used to melt amorphous silicon selectively. With fs pulses, however, the melt threshold fluences for amorphous and crystalline silicon are quite similar, making selective melting more difficult. Nonetheless, amorphous silicon does have a melting temperature about 200 K below that of

crystalline silicon (about 1460 K for amorphous silicon vs. 1685 K for crystalline silicon), meaning it should in principle be possible to initiate selective melting using fs laser pulses, which can then initiate an explosive crystallization process [94]. Experiments on fs laser-induced crystallization of amorphous silicon have shown that a fs pulse fluence of  $1.2 \text{ kJ/m}^2$  can crystallize 100-nm-thick amorphous silicon films, yielding crystal grain sizes of around 50 nm, whereas neither  $0.8 \text{ kJ/m}^2$  nor  $1.5 \text{ kJ/m}^2$  result in crystallization [95]. Thus, there is a rather narrow fluence window for obtaining crystallization in hyperdoped black silicon using fs laser pulses, particularly when considering the irregular surface morphology of black silicon, which affects the effective fluence at the surface. Both fluences we obtained experimentally at the amorphous, hyperdoped interface ( $F_1 = 0.6$  and  $0.9 \text{ kJ/m}^2$ ) were below that needed for crystallization. Indeed, when considering the surface morphology, which increases the surface area by a factor of 2–3 for black silicon with 1-micrometer surface structures, the effective fluence would be even less than indicated by the nominal annealing fluence  $F_1$ .

We did not obtain crystallization with our fs pulses. To what degree, though, did we heat the amorphous layer? Nominally, the change in temperature  $\Delta T$  of the amorphous layer can be estimated by:

$$\Delta T = \frac{FA}{c_p \rho d G}$$

where  $F$  is the pulse fluence at the amorphous silicon surface,  $A$  is the optical absorptance of the amorphous layer,  $c_p$  is the heat capacity of amorphous silicon ( $0.992 \text{ J/g/K}$ ),  $\rho$  is the mass density of amorphous silicon ( $2330 \text{ kg/m}^3$ ),  $d$  is the thickness of the amorphous layer, and  $G$  is a geometric factor that indicates the increase in surface

area due to the surface morphology [97]. To initiate melting of the amorphous silicon (and subsequent explosive crystallization),  $\Delta T$  must be greater than approximately 1100 K (from an initial temperature of 300 K).

First, we consider if we can use this expression to obtain estimates consistent with the experimental literature. Crystallization of 100-nm-thick amorphous silicon films can be achieved using a 90-fs pulse at 800 nm with a fluence of 1.2 kJ/m<sup>2</sup> [95]. Because these films are flat,  $G = 1$ . Estimating  $A$  is more complicated, because both linear and nonlinear absorption occur in the amorphous film. At 800 nm, amorphous silicon has reflectivity  $R = 0.35$ , linear absorption coefficient  $\alpha = 2.36 \times 10^4 \text{ cm}^{-1}$ , and two-photon absorption coefficient  $\beta = 37 \text{ cm/GW}$  [95]. We can model the linear and nonlinear absorption separately as:

$$A_{\text{linear}} = (1 - R)(1 - e^{-\alpha t})$$

and

$$A_{\text{nonlinear}} = (1 - R)\left(1 - \frac{1}{1 + (1 - R)^2 \frac{F}{\tau} \beta d}\right)$$

where  $F$  is the fluence and  $\tau$  is the pulse duration. At  $d = 100 \text{ nm}$ , we obtain  $A_{\text{linear}} = 0.14$  and  $A_{\text{nonlinear}} = 0.11$ . However, to sum these overestimates the total absorptance, because linear absorption reduces nonlinear absorption and vice-versa. Therefore, we can estimate the total absorptance as:

$$A_{\text{total}} = A_{\text{linear}}(1 - A_{\text{nonlinear}}) + A_{\text{nonlinear}}(1 - A_{\text{linear}})^2$$

which gives us  $A_{\text{total}} = 0.21$  for the explosive crystallization fluence of  $F = 1.2 \text{ kJ/m}^2$ . Indeed,  $A=0.21$  precisely gives us the required temperature increase for melting of  $\Delta T = 1100 \text{ K}$ —a remarkably good agreement between this simple model and experiment.

Of course, this is the average  $\Delta T$  in the thin film. In reality, absorption is strongest near the surface. Using this model, we would estimate that  $\Delta T = 1500$  K near the surface, declines to 1100 K at a depth of 40 nm, and declines further to 700 K at a depth of 100 nm. (To initiate explosive crystallization of the entire film, however, only a small layer of it needs to be melted by the laser pulse [94].) The consistency of our model with experimental literature provides some confidence that we can estimate the change in temperature produced by our infrared fs laser pulses on hyperdoped black silicon.

To estimate  $\Delta T$  for the amorphous silicon in our samples, we must estimate  $A$ ,  $G$ , and  $d$ . For hyperdoped black silicon with 1-micrometer surface structures,  $A_{linear} = 0.8$  from spectrophotometer measurements, and we can estimate  $G = 2$ –3. If  $\Delta T = 1100$  K is produced by  $1.2 \text{ kJ/m}^2$  on flat amorphous silicon (i.e., 80% of the melting threshold fluence), then we estimate that  $\Delta T = 1100$  K would be produced by  $2.4 \text{ kJ/m}^2$  on our hyperdoped black silicon (80% of our measured melting threshold fluence of  $3 \text{ kJ/m}^2$ ), which implies  $d = 300$ –400 nm. This agrees generally with measured amorphous layer thicknesses in hyperdoped black silicon with 1-micrometer surface structures, which vary over the surface between around 100 nm and 1 micrometer [5]. Using these values for  $A$ ,  $G$ , and  $d$ , we obtain  $\Delta T = 200$ –300 K for  $F_1 = 0.6 \text{ kJ/m}^2$  and  $\Delta T = 300$ –400 K for  $F_1 = 0.9 \text{ kJ/m}^2$ . These estimates are consistent with the fact that we did not observe structural changes (e.g., crystallization) after fs laser annealing.

Interestingly, the  $\Delta T$  values we estimate for the hyperdoped black silicon with 10-micrometer surface structures are larger:  $\Delta T = 600$  K for  $F_1 = 0.6 \text{ kJ/m}^2$  and

$\Delta T = 900$  K for  $F_1 = 0.9$  kJ/m<sup>2</sup>. This is because although  $G$  is larger ( $G = 4$  for surface cones of height 10 micrometers and diameter 5 micrometers),  $A$  is also larger (0.9 from spectrophotometer measurements), and, most importantly,  $d$  is smaller ( $d = 100$  nm from cross-sectional TEM images). We still did not attain high enough  $\Delta T$  to initiate crystallization, but our estimates suggest we were close. To attain  $\Delta T = 1100$  K, we estimate  $F_1 = 1.1$  kJ/m<sup>2</sup>, or that the incident pulse fluence would need to be  $F_0 = 10$  kJ/m<sup>2</sup>, assuming two-photon absorption in the wafer of about 0.9. Although these are only general estimates, they suggest that it may in some cases be easier to anneal large surface textures than small surface textures, because the amorphous layers in large surface textures fabricated with high fs laser fluences can be relatively thin.

In practice, what fluence values are required for fs laser annealing of amorphous silicon? At present there are two methods to crystallize amorphous silicon using fs laser pulses: 1) Irradiation with pulses below the melting threshold (e.g., 1.2 kJ/m<sup>2</sup> on flat amorphous silicon) to initiate explosive crystallization or 2) irradiation with pulses significantly above the melting threshold (e.g., 2.5–3.5 kJ/m<sup>2</sup> on flat amorphous silicon) to produce resolidification velocities sufficiently slow to yield crystalline silicon [14, 43]. (At fluences of 1.5–2.5 kJ/m<sup>2</sup>, the material is melted and resolidifies as amorphous silicon. At fluences below 1 kJ/m<sup>2</sup>, no apparent structural modification occurs, and at fluences above 3.5 kJ/m<sup>2</sup>, significant surface ablation occurs [98].) Thus, it appears that fs laser annealing can be obtained only within these two fluence windows (around 1.2 kJ/m<sup>2</sup> and 2.5–3.5 kJ/m<sup>2</sup>).

In our experiments, we attempted to anneal the amorphous, hyperdoped layer

not at the surface but at the amorphous/crystal interface. This may be an impracticable approach going forward. First, to attain sufficiently high fluences at the amorphous/crystal interface, very high incident fluences (around 10x larger) must be used, because two-photon absorption in the silicon substrate can be high. Second, even if sufficiently high fluences are attained at the interface to initiate explosive crystallization, such crystallization might not be epitaxial to the substrate, although it would be interesting to investigate this. A more straightforward approach to fs laser annealing would be to irradiate the hyperdoped or textured surface directly using pulses with fluences of 2.5–3.5 kJ/m<sup>2</sup>, potentially melting to the crystalline substrate and yielding crystalline (perhaps epitaxial) resolidification.

Is fs laser annealing a viable approach for improving the material properties of hyperdoped black silicon? Femtosecond laser irradiation can indeed crystallize amorphous silicon films. However, for optoelectronic devices, fs laser annealing might have some practical limitations. Initiating explosive crystallization with fluences below the melting threshold produces nanometer-scale crystal grains, which may result in low carrier mobility or high recombination rates in devices. Producing crystalline silicon using fluences in the range 2.5–3.5 kJ/m<sup>2</sup> might yield lower grain boundary densities. However, if Gaussian pulses are used, their low-fluence edges will produce amorphous silicon, although it may be possible to obtain purely crystalline material by using non-Gaussian pulses (e.g., uniform pulse profiles). Thus, obtaining high-quality crystalline material using fs pulses would require specially designed pulses within a particular fluence window. If this can be achieved, there could be advantages to using fs laser annealing compared to ns laser annealing, because less energy would be deposited

into the material during the annealing process.

#### **4.5.5 Conclusions**

Here, we investigated the viability of using fs laser pulses to anneal, or improve the crystallinity of, hyperdoped black silicon. Using 1300-nm fs laser pulses, we measured the melting threshold fluence on hyperdoped black silicon, and we laser-heated the hyperdoped, amorphous layer at the subsurface interface, taking into account two-photon absorption in the substrate. Although we were unable to initiate crystallization in the amorphous layer, we described a simple annealing model that is consistent with the literature and used it to estimate the heating produced by our fs pulses. Our results and analysis indicate that fs laser annealing may be most practicable when the pulses are incident at the amorphous surface, obviating the need for fs laser pulse wavelengths transparent to crystalline silicon. Annealing using uniform fs pulses in the 2.5–3.5 kJ/m<sup>2</sup> fluence window could be straightforward approach for crystallizing the surface of hyperdoped black silicon. Femtosecond laser annealing could be useful for devices, because very little energy would be deposited below the annealing zone during the process.

### **4.6 Conclusions of chapter**

In this chapter, we investigated the use of pulsed laser irradiation for annealing of hyperdoped black silicon. We explored laser annealing using ns and fs lasers, a range of laser wavelengths, and a variety of surface textures. In general, ns laser annealing is a robust process for obtaining highly crystalline laser-processed silicon while preserving

the surface texture and the supersaturated dopant states.

In Section 4.2, we investigated the use of ns laser annealing on hyperdoped black silicon with surface textures about 10 micrometers in size. Nanosecond laser annealing smoothed the surface on the nm scale, but kept the micrometer-scale surface textures intact. No loss of optical absorptance was observed. The ns laser pulses resulted in essentially complete crystallization of the surface, removing amorphous and pressure-induced silicon phases. Transmission electron microscopy and selected area diffraction of the surface textures show a complete absence of non-crystalline material, and the material appears to be single-crystalline. The ns laser annealing process also does not interfere with the formation of an electrical diode at the dopant-substrate interface. The use of ns laser annealing was also shown to reactivate the optical activity of the dopants after deactivation by thermal annealing. This is useful because thermal processes, such as rapid thermal annealing to improve electrode contact, are sometimes unavoidable. The deactivation-reactivation cycle can be repeated multiple times.

In Section 4.3, we investigated the use of ns laser annealing on hyperdoped black silicon with surface textures about 1 micrometer in size. Again, ns laser annealing resulted in full crystallization of the surface. At some ns laser fluences, the surface texture was destroyed, which reduced its optical absorptance. However, we found that some laser fluences can crystallize the surface while preserving the surface texture. In fact, crystallizing the surface led to an increase in sub-bandgap absorptance, possibly due to an increase in the population of dopants in a crystalline environment.

In Section 4.4, we explore the use of ns laser annealing on hyperdoped silicon



with sub-micrometer surface textures, specifically nanometer-scale ripples and flat laser-doped silicon. Again, ns laser annealing removed the amorphous silicon detected in the nanometer-scale surface ripples. However, the ns laser annealing fluence was too high to preserve the texture, so that after ns annealing, the texture was heavily modified. Nanosecond laser annealing also appeared to remove amorphous silicon from flat laser-doped silicon. The amorphous material in this flat silicon could not be detected before or after annealing by Raman spectroscopy, but before annealing, optical and side-scattered electron microscopy showed pockets of contrast associated with amorphous silicon. After ns annealing, these pockets were removed.

In Section 4.5, we explore the use of fs laser annealing on hyperdoped black silicon. We used fs laser pulses at 1300 nm to heat the amorphous, doped layer from within the surface (at the hyperdoped-substrate interface). However, in transmitting the fs laser pulses through the undoped portion of the silicon wafer, significant multi-photon absorption was measured. We estimated the heating effect produced by our fs laser pulses, finding that it is most practicable to perform fs laser annealing from the surface of the hyperdoped layer, either at a fluence of around 80% of the crystalline silicon melting threshold (e.g.,  $1.2 \text{ kJ/m}^2$ ) to initiate explosive crystallization of the amorphous layer [95] or at a fluence of  $2.5\text{--}3.5 \text{ kJ/m}^2$  to produce melting and crystalline resolidification [14].

# Chapter 5

## Conclusions of thesis

### 5.1 Advances in this thesis

In this thesis, we report a range of advances in laser processing of silicon. In Chapter 2, we document the texturing effect of fs laser irradiation of silicon in air at low fluences, determining the fluence and pulse number combinations that produce fully formed surface ripples with a minimum of debris. We find that the debris is oxygen-rich and determine conditions that mitigate its accumulation. We find that surface texturing is strongly associated with the presence of amorphous silicon and that amorphous silicon content is highest immediately after texture formation. Moving to fluences below the single pulse melting threshold, we observe incubation behavior, and we document the presence of silicon before texturing occurs that appears to be highly strained and/or hexagonal in structure, which is a possible incubation mechanism for surface modification at low fluences. We observe that the surface textures form underneath of a thin surface layer which may be the native silicon oxide layer and which may be a

source of oxygen-rich surface debris seen on the surface after fabrication. We measure the reduction in local texturing fluence with increased pulse number and find that the texturing fluence decreases linearly with the logarithm of the pulse number. We find that the number of pulses needed to initiate texturing is sensitive to the peak fluence of the pulse, and we predict that 10–20 pulses are needed above the melting threshold to initiate texturing, while peak fluences of around  $1.4 \text{ kJ/m}^2$  require hundreds of pulses to initiate texturing. We observe the progression of the texturing process from its earliest stages and find that the growth of the textured area is sensitive to the gas pressure. At low gas pressures, we infer that thermocapillary effects from surface plasmon polaritons are responsible for mass transfer leading to surface ripples, while at high gas pressures, we infer that an impurity-gradient-driven Marangoni effect dominates. Moving to scanning pulses, we verify our prediction that 10–20 pulses are needed above the melting threshold for texturing, which holds for scanned pulses over a wide range of fluences. We experimentally map out the fluence and pulse number parameter space for hyperdoped black silicon fabrication in  $\text{SF}_6$ , reporting our results in a phase diagram. We begin to quantify the effects of surface feedback for black silicon formation empirically. We continue to investigate scanned pulses and move to selenium thin films on silicon. We report the formation of ripple-like structures in both the selenium film and the silicon substrate and that the presence of the selenium film substantially reduces the texturing threshold fluence of silicon. At low fluence and high shots/area, we report highly uniform, very small (150-nm) surface ripples of Se-doped silicon. We then show that by separating the laser texturing and laser doping steps of hyperdoped black silicon fabrication, the doping concentration can

be controlled on textured surfaces, and we use optical absorption measurements to observe what appears to be intermediate band formation and a semiconductor-to-metal transition at different irradiation conditions. Finally, we investigate the use of hydrofluoric acid (HF) for surface cleaning of laser-textured silicon and find that HF can remove both surface debris as well as amorphous silicon without altering the surface morphology.

In Chapter 3, we focus on the microstructure of hyperdoped black silicon and its relationship to irradiation and doping conditions. We show that the formation of pressure-induced Si-XII is correlated with melting and resolidification on a textured surface and is suppressed at high fluences (e.g., above  $3.2 \text{ kJ/m}^2$ ). We show that if low-fluence irradiation of the textured surface is avoided, then textured surfaces can be formed without generating significant amounts of Si-XII. We then report results using selenium thin films, showing that high-fluence irradiation removes much of the film. During irradiation, silicon melts beneath the native silicon oxide layer, which separates the silicon substrate from the film. Thus, texturization or some other method of removing or disrupting the native silicon oxide layer appears necessary to mix selenium into the silicon surface. We find that selenium is incorporated at very high concentrations (around 2 at. %) and that the surface textures are composed of fine- and large-grained polycrystalline silicon. At low fluences below the single-pulse melting threshold, the surface is textured with sub-micrometer structures that are crystalline and that contain a thin, 10–20 nm skin of Se-doped silicon.

In Chapter 4, we report results from laser annealing of hyperdoped black silicon. We demonstrate that ns laser annealing results in essentially complete crystallization

of the surface and removes pressure-induced phases. The annealing process preserves the optical absorptance and the electrical rectification properties. After thermal annealing that deactivates the sub-bandgap absorptance, ns laser annealing reactivates the sub-bandgap absorptance. Larger surface textures can undergo annealing at higher fluences than smaller structures without losing their surface morphology. We identify ns annealing fluences that crystallize 10-micrometer and 1-micrometer surface textures without loss of surface morphology and light trapping. We also carry out ns laser annealing on sub-micrometer textures and flat surfaces. We investigate the use of fs laser pulses for annealing hyperdoped black silicon. We find that annealing through the backside of the silicon wafer using infrared laser pulses is largely impracticable due to nonlinear absorption inside of the silicon substrate. We identify fluence ranges that may be useful for direct fs laser annealing of the surface. Nanosecond laser annealing addresses one of the longstanding challenges in the field: obtaining high crystallinity and high sub-bandgap absorptance simultaneously in laser-hyperdoped black silicon.

## 5.2 Outstanding challenges

We consider the important outstanding challenges facing hyperdoped black silicon fabrication for creating useful devices. One of the longstanding challenges—low material crystallinity—is largely resolved in this thesis through the use of ns laser annealing. Another major challenge—controlling the dopant concentration on textured surfaces—is addressed in this thesis (Section 2.7) but not yet resolved. Controlling the dopant concentration is probably the most immediate research challenge that needs to

be addressed for laser-doped intermediate band devices to be fabricated. Fortunately, there exists a range of approaches for addressing this challenge, including separation of laser texturing and laser doping fabrication steps (Section 2.7), laser doping of pre-textured substrates, or even ion implantation of textured substrates followed by ns laser annealing.

Obtaining a hyperdoped layer thin enough for carrier extraction is more a requirement than an outstanding challenge, insofar as it is feasible with current laser doping or implantation methods. However, this requirement is frequently ignored in the literature, with hyperdoped layers 200–300 nm thick often fabricated by ion implantation. Basic hole transport calculations indicate that this is too thick for hole extraction (as shown in Figure 1.4.1); hyperdoped layers 50–150 nm thick are more appropriate. Fabricating hyperdoped layers of these thicknesses is possible using both ion implantation and laser doping. Indeed, fs laser doping typically produces doped layers in this thickness range. Researchers using ultrafast lasers (picosecond and shorter) to perform laser doping often search for a justification for using ultrafast pulses rather than, say, ns pulses. The need for very thin doped layers in prospective hyperdoped devices is one realistic justification. Another is that with ultrafast pulses, the melting and resolidification process occurs rapidly enough that the dopant concentration may be controlled using individual pulses.

Obtaining high optical absorptance in hyperdoped silicon is not challenging alone, but it is challenging to obtain while meeting all the other requirements for an intermediate band device (controlled doping concentration, controlled doped layer thickness, etc.) For example, if the dopant concentration is controlled through ion

implantation, then the hyperdoped material is typically flat. The main challenge with regard to laser texturing is probably how to obtain a highly textured surface without introducing too many impurities into the surface (e.g., impurities from air,  $\text{SF}_6$ , or  $\text{NF}_3$ ). One approach could be to laser-texture the surface while introducing the impurities, then to remove the impurity layer (which is typically only 50–100 nm thick) through laser ablation or chemical etching. The textured surface can then be doped controllably with ion implantation or laser doping (using irradiation parameters designed to produce the desired doping concentration).

Thermal stability of the dopant is largely addressed by ns laser annealing, because such annealing can reactivate the dopant after thermal deactivation. However, in practical device fabrication, ns laser annealing may not be possible after thermal treatment, such as after rapid thermal annealing. Thus, the use of dopant atoms with lower thermal diffusivities (such as tellurium) is attractive. Methods for introducing low-diffusivity dopants through gas precursors would be useful, because it is difficult to control the doping concentration and dopant distribution using thin films.

One outstanding challenge that has received very little attention is to embed the hyperdoped layer within conventional p- and n-type silicon layers. Because very little work has been done in this area, it is difficult to speculate how this could best be achieved. However, an initial approach could be to use chemical vapor deposition to deposit conventional doped silicon on top of hyperdoped black silicon. Because the deposition process typically involves high temperatures, thermal deactivation of the dopant will likely occur. To address this, ns laser annealing could be carried out following the deposition process, which would reactivate the dopant and also presum-

ably blend the conventional and hyperdoped layers together somewhat. Alternatively, a low-diffusivity dopant could be used so that less or no thermal deactivation occurs during silicon deposition.

## 5.3 Outlook

We close this thesis by discussing an outlook for hyperdoped black silicon research. A great deal of excitement has been generated over the past decade by the prospect of intermediate band devices, yet useful hyperdoped devices have yet to be made. The absence of useful hyperdoped devices is not entirely surprising, however, because numerous outstanding challenges for device fabrication remain unresolved (Sections 1.4 and 5.2). Commercialization of laser-textured and laser-doped silicon might be accelerated if researchers were to identify and address these challenges directly. Fortunately, all of the challenges identified appear resolvable in principle.

In the realm of optoelectronic devices, laser-textured and hyperdoped silicon have various potential applications. One area of application which we do not discuss here in detail is light-emitting diodes and lasing, which take advantage of the ability of hyperdoping to transform indirect bandgap semiconductors to direct bandgap semiconductors [99]. Another area of application encompasses intermediate band photodetectors and photovoltaics, which take advantage of prospective sub-bandgap photoresponse [16]. And another area of application is laser texturing for light-trapping surfaces, which does not necessarily entail doping. Below, we discuss sub-bandgap photoresponse applications and laser texturing applications in more detail.

The prospect of sub-bandgap photoresponse has generated a great deal of excite-



ment over the last decade, based mostly on the prospect of using inexpensive materials like silicon to produce high-efficiency photovoltaics [16] and infrared-sensitive photodetectors. In hyperdoped materials research, these applications are often lumped together. However, to realistically assess the prospects of these applications, it may be useful to recognize their differences. At least three reasons exist why hyperdoped materials may be more promising for photodetectors than for photovoltaics, at least in the prospective term. First, the commercial markets for these products are distinct. Photovoltaics produce a commodity (electricity), meaning new technologies compete on the basis of a single or perhaps a few metrics (in the case of photovoltaics, most typically cost/Watt). This can make it difficult for niche products with low production volumes and unique functionalities to enter the market. Photodetectors, in contrast, compete on the basis of a wide range of performance characteristics, such as sensitivity to particular spectral bands and dynamic range. Thus, niche products with low production volumes can enter the market in particular application areas (such as low-light night vision, consumer electronics, or specific military applications). This difference in markets is one reason why photodetector applications may be nearer than photovoltaic applications for hyperdoped silicon. The second reason photodetector applications may be more promising is technological. Hyperdoping interferes with carrier transport (reducing lifetime and mobility) [32], which may reduce overall photovoltaic efficiency. These efficiency losses might be overcome with precise material and device engineering, but this may translate to increased cost. Photodetectors, on the other hand, could be operated under increased bias regimes to compensate for poor carrier transport. The third obstacle for the prospects of

hyperdoped photovoltaic applications is that the intermediate band concept focuses on increasing the efficiency limit of single-semiconductor photovoltaic devices. It is possible that large efficiency improvements are necessary to grow the solar industry [100]. However, in recent practice, photovoltaic cost reductions have been driven significantly by economies of scale rather than by very large photoconversion efficiency improvements—let alone large improvements in theoretical maximum efficiency limits [101]. In practice, such theoretical maximum efficiency limits might not be a limiting factor to continued growth of the photovoltaics industry, and increasing such limits might not be directly relevant to the continued growth of the photovoltaics market (especially if improvements in theoretical limits are not accompanied by increases in actual operating efficiency—and at competitive cost). Given that improved efficiencies in hyperdoped photovoltaic devices have not yet been demonstrated in the lab, it is reasonable to expect that demonstrating such improvements in industrial settings may be distant, and demonstrating such improvements economically may be more distant. Thus, there are multiple reasons to expect hyperdoping to be more applicable to photodetectors than to photovoltaics, at least in the foreseeable term.

However, another application of laser processing of silicon is laser texturing (without hyperdoping). Laser texturing of silicon has already been used to produce enhanced infrared response near the bandgap energy in silicon-based photodetectors and enhanced efficiencies in silicon-based photovoltaics [45]. And promisingly, black silicon photovoltaic cells fabricated with non-laser methods, such as metal assisted etching, have been shown to exhibit enhanced photoconversion efficiencies [12, 102]. Laser texturing may have some advantages over other texturing approaches (such

as reactive ion etching, metal-assisted chemical etching, and electrochemical etching [103]) in terms of throughput, silicon and process waste, and cost. Some noteworthy challenges facing the use of laser texturing for photovoltaics include material quality, cost of laser texturing systems, and design of laser texturing systems for industrial settings. In the near future, however, these challenges could be resolved through advances in material processing (e.g., laser annealing discussed in Chapter 4) and cost, performance, and design of ultrafast laser systems [104]. Commercial use of laser texturing for photovoltaics may be possible in the foreseeable future and could be facilitated by technology transfer from academic laboratories to commercial settings [7].

# Bibliography

- [1] Mark T. Winkler, Thesis, Harvard University, 2009.
- [2] Matthew J. Smith, Thesis, Massachusetts Institute of Technology, 2012.
- [3] J. T. Sullivan, Thesis, Massachusetts Institute of Technology, 2013.
- [4] Meng-Ju Sher, Mark T. Winkler, and Eric Mazur, MRS Bull. **36**, 439 (2011).
- [5] Matthew J. Smith, Meng-Ju Sher, Benjamin Franta, Yu-Ting Lin, Eric Mazur, and Silvija Gradecak, J. Appl. Phys. **112**, 083518 (2012).
- [6] Matthew J. Smith, Meng-Ju Sher, Benjamin Franta, Yu-Ting Lin, Eric Mazur, and Silvija Gradecak, Appl. Phys. A **114**, 1009 (2014).
- [7] Benjamin Franta, David Pastor, Hemi H. Gandhi, Paul H. Rekemeyer, Silvija Gradecak, Michael J. Aziz, and Eric Mazur, Journal of Applied Physics **118**, 225303 (2015).
- [8] C.H. Crouch, J.E. Carey, M. Shen, E. Mazur, and F.Y. GÃ¶nner, Appl. Phys. A **79**, 1635 (2004).
- [9] L. L. Ma, Y. C. Zhou, N. Jiang, X. Lu, J. Shao, W. Lu, J. Ge, X. M. Ding, and X. Y. Hou, Appl. Phys. Lett. **88**, 171907 (2006).
- [10] Howard M. Branz, Vernon E. Yost, Scott Ward, Kim M. Jones, Bobby To, and Paul Stradins, Appl. Phys. Lett. **94**, 231121 (2009).
- [11] Barada K. Nayak, Vikram V. Iyengar, and Mool C. Gupta, Prog. Photovoltaics **19**, 631 (2011).
- [12] Hele Savin, Paivikki Repo, Guillaume von Gastrow, Pablo Ortega, Eric Calle, Moises Gariñn, and Ramon Alcubilla, Nat. Nanotechnology **10**, 624 (2015).
- [13] E. Ertekin, M.T. Winkler, D. Recht, A.J. Said, M.J. Aziz, T. Buonassisi, and J.C. Grossman, Phys. Rev. Lett. **108**, 026401 (2012).
- [14] M.-J. Sher, Thesis, Harvard University, 2013.

- [15] J.T. Sullivan, C.B. Simmons, J.J. Krich, A.J. Akey, D. Recht, M.J. Aziz, and T. Buonassisi, *J. Appl. Phys.* **114**, 103701 (2013).
- [16] Antonio Luque, Antonio Marti, and Colin Stanley, *Nat. Photonics* **6**, 146 (2012).
- [17] Si H. Pan, Daniel Recht, Supakit Charnvanichborikarn, James S. Williams, and Michael J. Aziz, *Appl. Phys. Lett.* **98**, 121913 (2011).
- [18] James E. Carey, Catherine H. Crouch, Mengyan Shen, and Eric Mazur, *Optics Letters* **30**, 1773 (2005).
- [19] Aurore J. Said, Daniel Recht, Joseph T. Sullivan, Jeffrey M. Warrender, Tonio Buonassisi, Peter D. Persans, and Michael J. Aziz, *Appl. Phys. Lett.* **99**, 073503 (2011).
- [20] Malek Tabbal, Taegon Kim, David N Woolf, Byungha Shin, and Michael J Aziz, *Appl. Phys. A* **98**, 589 (2010).
- [21] Matthew J. Smith, Mark T. Winkler, Meng-Ju Sher, Yu-Ting Lin, Eric Mazur, and Silvija Gradecak, *Appl. Phys. A* **105**, 795 (2011).
- [22] T. G. Kim, Jeffrey M. Warrender, and Michael J. Aziz, *Appl. Phys. Lett.* **88**, 241902 (2006).
- [23] Brion P. Bob, Atsushi Kohno, Supakit Charnvanichborikarn, Jeffrey M. Warrender, Ikurou Umezu, Malek Tabbal, James S. Williams, and Michael J. Aziz, *J. Appl. Phys.* **107**, 123506 (2010).
- [24] Mark T. Winkler, Meng-Ju Sher, Yu-Ting Lin, Matthew J. Smith, Haifei Zhang, Silvija Gradecak, and Eric Mazur, *J. Appl. Phys.* **111**, 093511 (2012).
- [25] Svetoslav Koynov, Martin S. Brandt, and Martin Stutzmann, *Appl. Phys. Lett.* **88**, 203107 (2006).
- [26] D. Zielke, D. Sylla, T. Neubert, R. Brendel, and J. Schmidt, *IEEE J. Photovolt.* **3**, 656 (2013).
- [27] Malcolm Abbott and Jeffrey Cotter, *Prog. Photovoltaics* **14**, 225 (2006).
- [28] M. Halbwax, T. Sarnet, Ph Delaporte, M. Sentis, H. Etienne, F. Torregrosa, V. Vervisch, I. Perichaud, and S. Martinuzzi, *Thin Solid Films* **516**, 6791 (2008).
- [29] P.D. Persans, N.E. Berry, D. Recht, D. Hutchinson, H. Peterson, J. Clark, S. Charnvanichborikarn, J.S. Williams, A. DiFranzo, M.J. Aziz, and J.M. Warrender, *Appl. Phys. Lett.* **101**, 111105 (2012).

- [30] Mark T. Winkler, Daniel Recht, Meng-Ju Sher, Aurore J. Said, Eric Mazur, and Michael J. Aziz, *Phys. Rev. Lett.* **106**, 178701 (2011).
- [31] J. T. Sullivan, R. G. Wilks, M. T. Winkler, L. Weinhardt, D. Recht, A. J. Said, B. K. Newman, Y. Zhang, M. Blum, S. Krause, W. L. Yang, C. Heske, M. J. Aziz, M. BĀdr, and T. Buonassisi, *Appl. Phys. Lett.* **99**, 142102 (2011).
- [32] M.-J. Sher, C.B. Simmons, J.J. Krich, A.J. Akey, M.T. Winkler, D. Recht, T. Buonassisi, M.J. Aziz, and A.M. Lindenberg, *Appl. Phys. Lett* **105**, 053905 (2014).
- [33] Christie B. Simmons, Austin J. Akey, Jonathan P. Mailoa, Daniel Recht, Michael J. Aziz, and Tonio Buonassisi, *Adv. Funct. Mater.* **24**, 2852 (2014).
- [34] Ikurou Umezu, Jeffrey M. Warrender, Supakit Charnvanichborikarn, Atsushi Kohno, James S. Williams, Malek Tabbal, Dimitris G. Papazoglou, Xi-Cheng Zhang, and Michael J. Aziz, *J. Appl. Phys.* **113**, 213501 (2013).
- [35] Michael A. Sheehy, Luke Winston, James E. Carey, Cynthia M. Friend, and Eric Mazur, *Chem. Mater.* **17**, 3582 (2005).
- [36] C.B. Simmons, A.J. Akey, J.J. Krich, J.T. Sullivan, D. Recht, M.J. Aziz, and T. Buonassisi, *J. Appl. Phys.* **114**, 243514 (2013).
- [37] Bonna K. Newman, Meng-Ju Sher, Eric Mazur, and Tonio Buonassisi, *Appl. Phys. Lett.* **98**, 251905 (2011).
- [38] J.P. Mailoa, A.J. Akey, C.B. Simmons, D. Hutchinson, J. Mathews, J.T. Sullivan, D. Recht, M.T. Winkler, J.S. Williams, J.M. Warrender, P.D. Persans, M.J. Aziz, and T. Buonassisi, *Nat. Commun.* **5**, 3011 (2014).
- [39] Kay-Michael Guenther, Thomas Gimpel, Jens W. Tomm, Stefan Winter, Augustinas Ruibys, Stefan Kontermann, and Wolfgang Schade, *Applied Physics Letters* **104**, 042107 (2014).
- [40] Meng-Ju Sher, Niall M. Mangan, Matthew J. Smith, Yu-Ting Lin, Sophie Marbach, Tobias M. Schneider, Silvija Gradecak, Michael P. Brenner, and Eric Mazur, *J. Appl. Phys.* **117**, 125301 (2015).
- [41] Yu-Ting Lin, Niall Mangan, Sophie Marbach, Tobias M. Schneider, Guoliang Deng, Shouhuan Zhou, Michael P. Brenner, and Eric Mazur, *Appl. Phys. Lett.* **106**, 062105 (2015).
- [42] Matthew J. Smith, Yu-Ting Lin, Meng-Ju Sher, Mark T. Winkler, Eric Mazur, and Silvija Gradecak, *J. Appl. Phys.* **110**, 053524 (2011).

- [43] Yu-Ting Lin, Thesis, Harvard University, 2014.
- [44] Haibin Sun, Cong Liang, Guojin Feng, Zhen Zhu, Jun Zhuang, and Li Zhao, *Optical Materials Express* **6**, 1321 (2016).
- [45] C. Vineis, M. Levy-Finklshtein, J. Carey, E. Knight, E. Wefringhaus, and R. Harney, Ultrafast laser texturing for enhanced solar cell performance and lower cost.
- [46] Zongfu Yu, Aaswath Raman, and Shanhui Fan, *Proceedings of the National Academy of Sciences* **107**, 17491 (2010).
- [47] Brian R. Tull, Mark T. Winkler, and Eric Mazur, *Applied Physics A* **96**, 327 (2009).
- [48] Xiao Dong, Ning Li, Zhen Zhu, Hezhu Shao, Ximing Rong, Cong Liang, Haibin Sun, Guojin Feng, Li Zhao, and Jun Zhuang, *Applied Physics Letters* **104**, 091907 (2014).
- [49] D.L. Flamm, *Mechanisms of Silicon Etching in Fluorine- and Chlorine-Containing Plasmas*, 1990.
- [50] A. R. Patel, B. Mankoc, M. D. Bin Sintang, A. Lesaffer, and K. Dewettinck, *RSC Advances* **5**, 9703 (2015).
- [51] R. A. Minamisawa, M. J. Suess, R. Spolenak, J. Faist, C. David, J. Gobrecht, K. K. Bourdelle, and H. Sigg, *Nat Commun* **3**, 1096 (2012).
- [52] Ilaria Zardo, Gerhard Abstreiter, and Anna Fontcuberta i Morral, in *Nanowires*, edited by Paola Prete (INTECH, Croatia, 2010), .
- [53] Hakon Ikaros T. Hauge, Marcel A. Verheijen, Sonia Conesa-Boj, Tanja Etzelstorfer, Marc Watzinger, Dominik Kriegner, Ilaria Zardo, Claudia Fasolato, Francesco Capitani, Paolo Postorino, Sebastian KÄlling, Ang Li, Simone As-sali, Julian Stangl, and Erik P. A. M. Bakkers, *Nano Letters* **15**, 5855 (2015).
- [54] U. Dahmen, C. J. Hetherington, P. Pirouz, and K. H. Westmacott, *Scripta Metallurgica* **23**, 269 (1989).
- [55] Yan Zhang, Zafar Iqbal, Sankaran Vijayalakshmi, and Haim Grebel, *Applied Physics Letters* **75**, 2758 (1999).
- [56] C. Rodl, T. Sander, F. Bechstedt, J. Vidal, P. Olsson, S. Laribi, and J. F. Guillemoles, *Physical Review B* **92**, 045207 (2015).
- [57] David Zubia, Stella Quinones, Noel Marquez, Jose Mireles, and Ernest J. Garcia, *Nanotexturing of Surfaces to Reduce Melting Point*, 2011.

- [58] T. Q. Jia, H. X. Chen, M. Huang, F. L. Zhao, J. R. Qiu, R. X. Li, Z. Z. Xu, X. K. He, J. Zhang, and H. Kuroda, *Physical Review B* **72**, 125429 (2005).
- [59] D. Dufft, A. Rosenfeld, S. K. Das, R. Grunwald, and J. Bonse, *Journal of Applied Physics* **105**, 034908 (2009).
- [60] J. E. Sipe, Jeff F. Young, J. S. Preston, and H. M. van Driel, *Physical Review B* **27**, 1141 (1983).
- [61] Jorn Bonse, Arkadi Rosenfeld, and Jorg Krueger, *Journal of Applied Physics* **106**, 104910 (2009).
- [62] B. Hecht, H. Bielefeldt, L. Novotny, Y. Inouye, and D. W. Pohl, *Physical Review Letters* **77**, 1889 (1996).
- [63] F. Millot, V. Sarou-Kanian, J. C. Rifflet, and B. Vinet, *Materials Science and Engineering: A* **495**, 8 (2008).
- [64] Kazutaka Terashima, Mitsuyoshi Sakairi, Muneyuki Hirai, and Tomohisa Tsuchiya, *Solid State Phenomena* **95-96**, 659 (2004).
- [65] Z Niu, K Mukai, Y Shiraishi, T Hibiya, K Kakimoto, and M Koyama, *Effects of temperature and oxygen on the surface tension of molten silicon*, 2005.
- [66] A. V. Shishkin and A. S. Basin, *Theoretical Foundations of Chemical Engineering* **38**, 660 (2004).
- [67] Zhang Fu Yuan, Kusuhiro Mukai, and Wen Lai Huang, *Langmuir* **18**, 2054 (2002).
- [68] Brian R. Tull, Thesis, Harvard University, 2007.
- [69] Sokrates Pantelides, *Deep Centers in Semiconductors*, 2nd revised ed. edition ed. (CRC Press, USA, 1992), .
- [70] Martin Otto, Matthias Kroll, Thomas Kasebier, Roland Salzer, Andreas TÄijn-nermann, and Ralf B. Wehrspohn, *Applied Physics Letters* **100**, 191603 (2012).
- [71] A. Borowiec, D. M. Bruce, Daniel T. Cassidy, and H. K. Haugen, *Applied Physics Letters* **83**, 225 (2003).
- [72] Michael J Aziz, *Metall. Mater. Trans. A* **27**, 671 (1996).
- [73] J. A. Kittl, P. G. Sanders, M. J. Aziz, D. P. Brunco, and M. O. Thompson, *Acta Mater.* **48**, 4797 (2000).



- [74] R. L. C. Vink, G. T. Barkema, and W. F. van der Weg, Phys. Rev. B **63**, 115210 (2001).
- [75] H. Richter, Z. P. Wang, and L. Ley, Solid State Commun. **39**, 625 (1981).
- [76] Joachim Mayer, Lucille A. Giannuzzi, Takeo Kamino, and Joseph Michael, MRS Bull. **32**, 400 (2007).
- [77] B. R. Tull, J. E. Carey, M. A. Sheehy, C. Friend, and E. Mazur, Appl. Phys. A **83**, 341 (2006).
- [78] N. G. Semaltianos, S. Logothetidis, W. Perrie, S. Romani, R. J. Potter, S. P. Edwardson, P. French, M. Sharp, G. Dearden, and K. G. Watkins, J. Nanopart. Res. **12**, 573 (2010).
- [79] Michael O. Thompson, J. W. Mayer, A. G. Cullis, H. C. Webber, N. G. Chew, J. M. Poate, and D. C. Jacobson, Phys. Rev. Lett. **50**, 896 (1983).
- [80] A.G. Cullis, D. T. J. Hurle, H. C. Webber, N. G. Chew, J. M. Poate, P. Baeri, and G. Foti, Appl. Phys. Lett. **38**, 642 (1981).
- [81] Austin J. Akey, Daniel Recht, James S. Williams, Michael J. Aziz, and Tonio Buonassisi, Adv. Funct. Mater. doi: 10.1002/adfm.201501450 (2015).
- [82] Michael O. Thompson, G. J. Galvin, J. W. Mayer, P. S. Peercy, J. M. Poate, D. C. Jacobson, A. G. Cullis, and N. G. Chew, Phys. Rev. Lett. **52**, 2360 (1984).
- [83] Georg Haberfehlner, Matthew J. Smith, Juan-Carlos Idrobo, Geoffroy Auvert, Meng-Ju Sher, Mark T. Winkler, Eric Mazur, Narciso Gambacorti, Silvija Gradecak, and Pierre Bleuet, Microscopy and Microanalysis **19**, 716 (2013).
- [84] Jan Forster and H. Vogt, in *2011 COMSOL Conference in Stuttgart* (COMSOL, Stuttgart, 2011), .
- [85] J. Narayan, C. W. White, M. J. Aziz, B. Stritzker, and A. Walthuis, J. Appl. Phys. **57**, 564 (1985).
- [86] C. J. Shih, C. H. Fang, C. C. Lu, M. H. Wang, M. H. Lee, and C. W. Lan, J. Appl. Phys. **100**, 053504 (2006).
- [87] Martin A. Green and Mark J. Keevers, Prog. Photovoltaics **3**, 189 (1995).
- [88] Norbert H Nickel, *Laser Crystallization of Silicon-Fundamentals to Devices* (Academic Press, USA, 2003), Vol. 75.
- [89] Ingrid De Wolf, Semiconductor Science and Technology **11**, 139 (1996).

- [90] H C Card and E H Rhoderick, J. Phys. D: Appl. Phys. **4**, 1589 (1971).
- [91] G. L. Pearson and B. Sawyer, Proc. IRE **40**, 1348 (1952).
- [92] Y. Ma, T. Yasuda, and G. Lucovsky, J. Vac. Sci. Technol. A **11**, 952 (1993).
- [93] Elizabeth Landis, Kasey Phillips, Eric Mazur, and Cynthia M. Friend, J. Appl. Phy. **112**, (2012).
- [94] A. Polman, S. Roorda, P. A. Stolk, and W. C. Sinke, Journal of Crystal Growth **108**, 114 (1991).
- [95] Tae Y. Choi, David J. Hwang, and Costas P. Grigoropoulos, Optical Engineering **42**, 3383 (2003).
- [96] D. P. Korfiatis, K. A. Th Thoma, and J. C. Vardaxoglou, Journal of Physics D: Applied Physics **40**, 6803 (2007).
- [97] Seungjae Moon, Mutsuko Hatano, Minghong Lee, and Costas P. Grigoropoulos, International Journal of Heat and Mass Transfer **45**, 2439 (2002).
- [98] Harald O. Jeschke, Martin E. Garcia, Matthias Lenzner, Jorn Bonse, Jorg Krueger, and Wolfgang Kautek, Applied Surface Science **197-198**, 839 (2002).
- [99] Zhen Zhu, Hezhu Shao, Xiao Dong, Ning Li, Bo-Yuan Ning, Xi-Jing Ning, Li Zhao, and Jun Zhuang, Scientific Reports **5**, 10513 (2015).
- [100] D. M. Powell, M. T. Winkler, H. J. Choi, C. B. Simmons, D. Berney Needleman, and T. Buonassisi, Energy & Environmental Science **5**, 5874 (2012).
- [101] Alan C. Goodrich, Douglas M. Powell, Ted L. James, Michael Woodhouse, and Tonio Buonassisi, Energy & Environmental Science **6**, 2811 (2013).
- [102] Jihun Oh, Hao-Chih Yuan, and Howard M. Branz, Nat Nano **7**, 743 (2012).
- [103] Martin Otto, Michael Algasinger, Howard Branz, Benjamin Gesemann, Thomas Gimpel, Kevin Fuchsel, Thomas Kasebier, Stefan Kontermann, Svetoslav Koynov, Xiaopeng Li, Volker Naumann, Jihun Oh, Alexander N. Sprafke, Johannes Ziegler, Matthias Zilk, and Ralf B. Wehrspohn, Advanced Optical Materials **3**, 147 (2015).
- [104] Ron Schaeffer, Industrial Laser Solutions (2014).